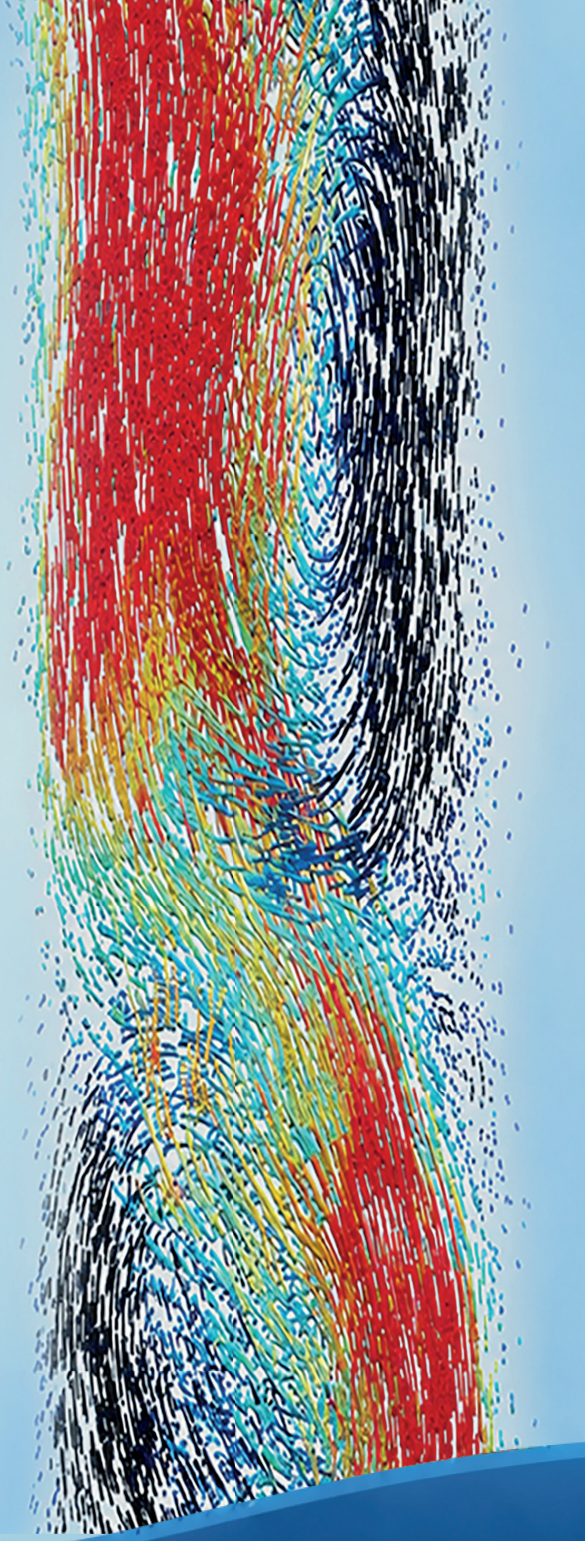
Multiphase Flow Behavior

of

Anaerobic Granular Sludge Reactors



Hooman Eslami

2026

Propositions

1. Quantifying shear stress and mass transfer at microbial granule-scale requires more than reactor-scale hydrodynamic characterization.
   (This Thesis)

2. Liquid spatial and temporal turbulent velocity fluctuations are primary hydrodynamic drivers in shaping anaerobic granular sludge properties.
   (This Thesis)

3. In the age of generative AI, the value of education lies in training students to question answers rather than to answer questions.

4. In science for impact, synthesizing relevant knowledge across various research fields is more important than producing new knowledge within individual fields.

5. PhD candidates who operate biological reactors for months deserve parental benefits.

6. Time reserved for hobbies enhances sustained productivity more than extended working hours.

7. Algorithm-controlled social media platforms amplify human bias.

Propositions belonging to the thesis, entitled

Multiphase flow behavior of anaerobic granular sludge reactors

Hooman Eslami

Wageningen, 2026

Multiphase Flow Behavior of Anaerobic Granular Sludge Reactors

Hooman Eslami

Thesis Committee

Promotor

Prof. Dr ir. H.H.M. Rijnaarts

Professor of Environmental Technology

Wageningen University & Research

Co-promotors

Dr H. Bruning

Associate Professor in Environmental Technology

Wageningen University & Research

Dr D. Sudmalis

Assistant Professor in Environmental Technology

Wageningen University & Research

Other members:

Prof. Dr D. Batstone, The University of Queensland, Australia

Prof. Dr ir. R.G.M. van der Sman, Wageningen University & Research

Dr C. Terenzi, Wageningen University & Research

Dr ir. T. Hendrickx, Paques Global B.V., Balk

This research was conducted under the auspices of the Graduate School for Socio-Economic and Natural Sciences of the Environment (SENSE).

Multiphase Flow Behavior of Anaerobic Granular Sludge Reactors

Hooman Eslami

Thesis

submitted in fulfilment of the requirements for the degree of doctor
at Wageningen University
by the authority of the Rector Magnificus,
Prof. Dr C. Kroeze,
in the presence of the
Thesis Committee appointed by the Academic Board
to be defended in public
on Wednesday 4 November 2026
at 10:30 a.m. in the Omnia Auditorium

Hooman Eslami

Multiphase Flow Behavior of Anaerobic Granular Sludge Reactors

228 pages.

PhD thesis, Wageningen University, Wageningen, The Netherlands (2026)

With references, with summary in English

ISBN: 978-94-6534-726-4

DOI: 10.18174/681531

Table of Contents

Chapter 1 General Introduction 11

1.1 Anaerobic granular sludge technology for wastewater treatment . 13

1.2 The role of hydrodynamics and mass transfer in biofilm, and granular sludge formation and development 14

1.3 Hydrodynamics of anaerobic granular sludge reactors (AGSRs) . 17

1.3.1 Granules are exposed to varying flow dynamics of AGSRs 17

1.3.2 Different types of AGSRs 18

1.3.3 Factors affecting the multiphase flow in AGSRs 21

1.4 Approaches to study the hydrodynamics of AGSRs 23

1.4.1 Modeling approaches 23

1.4.2 Experimental approaches 25

1.5 Calcification of anaerobic granules and role of hydrodynamics . . 29

1.6 Overview of the thesis 31

Chapter 2 Theoretical background on turbulence and transport in multiphase flows 35

2.1 Introduction 37

2.2 Statistical description of turbulence 38

2.3 The scales of turbulent motions 39

2.4 Turbulence in multiphase flows 43

2.5 Transport phenomena in multiphase turbulent flows 44

Chapter 3 3D Hydrodynamic Characterization in Anaerobic Granular Sludge Reactors. Part 1: Application of 3D-PTV in Dense Two-phase Flows 47

3.1 Introduction 49

3.2 Material and Methods 53

3.2.1 Flow system and experimental conditions 53

3.2.2 Refractive index matching 55

3.2.3 Experimental setup for 3D-particle tracking velocimetry (3D-PTV) . . . 56
3.2.4 Calculation of hydrodynamic dispersion coefficients . . 60
3.3 Results and Discussion . . . 61
3.3.1 Index Matching and 3D Particle Tracking . . . 61
3.3.2 Flow pattern visualization . . . 65
3.3.3 Quantitative flow analysis . . . 66
3.4 Conclusions . . . 72
Supplementary Information . . . 73
S.3.1 Image preprocessing steps . . . 73
S.3.2 Particle tracking statistics . . . 74
S.3.3 Bin size sensitivity analysis . . . 75
S.3.4 Single-phase flow velocity profile . . . 76

Chapter 4 3D Hydrodynamic Characterization in Anaerobic Granular Sludge Reactors. Part 2: Effect of Gas Superficial Velocity and Solid Volume Fraction . . . 79

4.1 Introduction . . . 81
4.2 Materials and methods . . . 85
4.2.1 Reactor setup, material properties, and operating conditions . . . 85
4.2.2 Imaging system . . . 87
4.2.3 Experimental procedure, data acquisition and processing . . . 87
4.2.4 Post-processing . . . 88
4.3 Results and discussion . . . 90
4.3.1 Particle tracking results and flow visualization . . . 90
4.3.2 Effect of increasing gas superficial velocity and solid VOF on liquid mean velocity . . . 91
4.3.3 Effect of gas superficial velocity at different solid VOFs on axial and lateral liquid velocity components . . . 93

4.3.4 Effect of solid VOF at different gas superficial velocity on liquid axial and lateral velocity components 96
4.3.5 Effect of varying gas superficial velocity and solid VOF on mixing performance 98
4.4 Conclusion 102
Supplementary Information 103
S.4.1 Raw images 103
S.4.2 STB settings and statistics 103
S.4.3 Effect of gas flow rate on liquid velocity and acceleration 106
S.4.4 Effect of solid VOF on liquid velocity and acceleration 109

Chapter 5 Mechanistic Effects of Hydrodynamic Shear and Turbulence on Anaerobic Granule Properties in Calcium-Rich Wastewater 113

5.1 Introduction 115
5.2 Materials and methods 118
5.2.1 Reactor setup 118
5.2.2 Operating condition and flow control 118
5.2.3 Experimental setup for 3D-particle tracking velocimetry (3D-PTV) 122
5.2.4 Analytical methods 126
5.3 Results 129
5.3.1 Flow characteristics in shear-dominated reactors 129
5.3.2 Pseudo-turbulence characterization 132
5.3.3 Granule properties characterization 135
5.4 Discussion 142
5.4.1 Effects of gas bubbles on the hydrodynamics and mass transfer 142
5.4.2 Interdependent effect of hydrodynamics and Ca^{2+} on the properties of granules 143
5.5 Limitations and future work 146

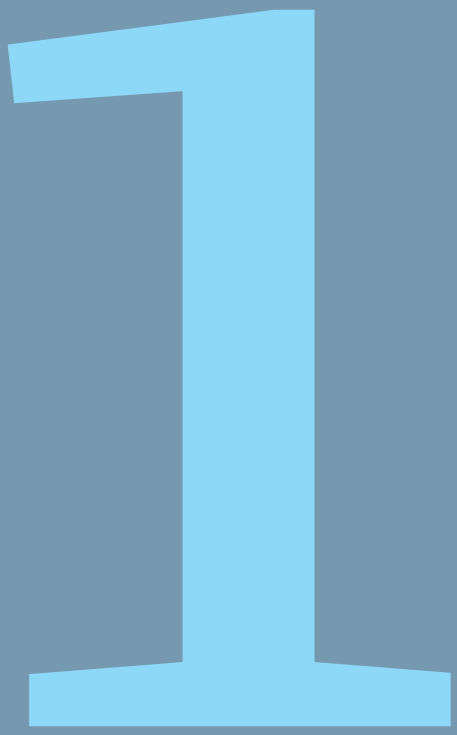
5.6 Conclusions . . . 147
Supplementary Information . . . 148
S.5.1 Recirculation tank design . . . 148
S.5.2 Biofilm diffusion–reaction model for spherical granules 148
S.5.3 Reactor process performance . . . 150
S.5.4 Camera calibrations and image prepossessing . . . 150
S.5.5 Particle tracking settings . . . 151
S.5.6 Effect of averaging time interval on PDF of velocity and shear rate in shear-dominated reactors . . . 151
S.5.7 Real-time axial velocity at three different points in the reactors and flow time-scale calculation using FFT. . . . 153
S.5.8 Shear rate distribution across the reactor's diameter . . 156
S.5.9 Post-experiment flow measurement . . . 157
S.5.10 Effect of gas and liquid on shear intensities . . . 157
S.5.11 Macroscopic images of surface and cross-section of granules . . . 159
S.5.12 Precipitation on surfaces of cells in LSR . . . 160
S.5.13 EDS spectra of sliced HSR and LSR granules . . . 161
S.5.14 SEM and SEM-EDS of granules analysed with MRI as "calcified" . . . 162
S.5.15 Internal structure of granules . . . 164
S.5.16 Mechanical strength of the granules . . . 166

Chapter 6 General Discussion . . . 169

6.1 Introduction . . . 171
6.2 Overview of the thesis findings: from black box reactor to resolved local hydrodynamics . . . 172
6.3 Scientific insights practical implications and research limitations . 174
6.3.1 Parameters affecting key hydrodynamic variables and the transport phenomena in AGSRs . . . 174
6.3.2 Turbulence characteristics as the missing puzzle piece in hydrodynamics studies of AGSRs . . . 182

6.4 Future perspectives 190
6.4.1 Hydrodynamic characterization approaches for three-phase flow in AGSRs 190
6.4.2 Turbulence characteristics in AGSRs 195
References 197
Summary 219
Acknowledgements 223
About the Author 225

Chapter 1



Chapter 1

General Introduction

1.1. Anaerobic granular sludge technology for wastewater treatment

Water is essential for life, the environment, and health. Urbanization and industrialization have resulted in a significant increase in water use, mainly for food production and industrial activities. Furthermore, due to rapid population growth and increased water demand, the quality of surface water and groundwater has become a major concern in industrialized countries, largely impacted by increased wastewater discharge (Weissbrodt (2024)). While sanitation and sewage treatment are central to protecting aquatic ecosystems and public health, modern wastewater treatment is shifting toward holistic principles aimed at achieving sustainability beyond merely environmental protection (Kehrein et al. (2020)). This shift requires improvements in conversion capacities, resource recovery, energy efficiency, and minimizing land use, while reducing investment and operating costs (Zhou et al. (2011)).

Anaerobic digestion (AD) has emerged as a promising technology that converts organics contained in (waste)water into biogas and has become a key technology to support this transition, especially in the industrial sector. AD is a biological process in which complex organic matter is degraded by microorganisms under anaerobic conditions, resulting in the production of biogas and enabling the recovery of nutrients (e.g., nitrogen and phosphorus) (Duan et al. (2025)). Notably, the produced biogas can be used as an energy source (e.g., heat, electricity, cogeneration, and compressed natural gas) (Li et al. (2022)).

AD has been widely applied for the treatment of municipal and industrial wastewaters. Until the 1960s, anaerobic wastewater treatment systems were predominantly based on completely mixed reactor configurations, in which the hydraulic retention time (HRT) was approximately equal to the solids retention time (SRT) (van Lier et al. (2015)). In such systems, treatment capacity is directly constrained by the growth kinetics of anaerobic microorganisms. Given the inherently low growth rates of these microorganisms, such systems required long HRTs and large reactor volumes to maintain sufficient biomass concentrations. These systems are typically referred to as “low-rate” reactors (Rittmann and McCarty (2001), Van Lier (2008)).

A major breakthrough in anaerobic wastewater treatment was achieved through the immobilization of anaerobic biomass in the form of anaerobic granules, which can be described as dense spherical biofilms. Granule formation enabled the decoupling of the STR from the HRT, allowing anaerobic reactors to retain high concentrations of

active biomass. This fundamental development marked the emergence of "high-rate" anaerobic reactors, suitable for industrial wastewaters with low solids content. These "high-rate" reactors can be operated at substantially higher organic loading rates (OLR) while achieving much smaller reactor volumes and improved treatment efficiency (Lettinga et al. (1980)).

The design and operation of these reactors depend on multiple physical, chemical, and biological processes that interact dynamically and collectively, thereby determining overall reactor performance. Among the many governing parameters (e.g., wastewater characteristics, OLR, upflow velocity, HRT, SRT, temperature, pH) (Batstone et al. (2004), Kundu et al. (2014a), Uemura and Harada (2000), Gao et al. (2024a,b)), hydrodynamics plays a key role in regulating the processes that control granule properties and pollutant removal efficiency. In these systems, the hydrodynamic behavior is governed by the complex interactions between the biogas, wastewater), and anaerobic granules, which together define the local flow environment. This thesis focuses on the hydrodynamic characterization of these three-phase reactors and aims to elucidate the mechanisms by which local flow dynamics influence the properties of anaerobic granules in saline wastewater.

1.2. The role of hydrodynamics and mass transfer in biofilm, and granular sludge formation and development

High-rate anaerobic granular sludge reactors rely on the formation and long-term stability of anaerobic granules, which can be described as spherical moving bed biofilms formed without supporting carrier materials. These granules consist of microbial consortia embedded in a highly hydrated extracellular polymeric substance (EPS) matrix which forms hydrogels (Figure 1.1a) (Atmakuri et al. (2024)). Anaerobic granules in well-operating plants typically exhibit several distinguishing characteristics: (i) regular, smooth, and nearly spherical shape, (ii) excellent settleability, (iii) dense and mechanically strong microbial structure, (iv) high biomass concentration, (v) the ability to withstand high organic loading rates, and (vi) tolerance to a range of toxic or inhibitory compounds (Tay et al. (2001b), Weissbrodt (2024)). Of paramount importance contributing to the above properties is the EPS matrix, which accounts for approximately 70–95 % of the biofilm's mass (Show et al. (2020), Flemming et al. (2016)). Here, the intrinsic

properties of EPS hydrogel matrix, including porosity, density, water content, charge density of the polymers, sorption capacity (e.g., for nutrients and trace element) , hydrophobicity, and mechanical stability, define the local microenvironment, granules overall mechanical properties, and govern microbial activity within the granules by influencing mass transfer of substrates and metabolic byproducts as described below (Flemming et al. (2007)) Because of the hydrogel nature of EPS matrix, diffusion phenomena and mass transfer limitations are a main characteristic of biofilms and granules, when considering microbial activity and growth. This differentiates them from suspended cultures (van den Berg et al. (2021), van den Berg (2022)). Such diffusion limitations within biofilms and granules lead to spatial gradients in substrate and metabolic product concentrations. As a consequence, microorganisms within biofilms form different types of habitats and differentiate their ecological niches along chemical gradients that develop across the biofilm depth. Depending on substrate gradients and growth rates, biofilms may develop as homogeneous structures or as heterogeneous architectures (Picioreanu et al. (2000)).

Transport of solutes from the bulk flow towards microbial cells in anaerobic granules consists of two main mass transfer steps: external and intragranular mass transfer (Figure 1.1b) (Guimerà et al. (2016)). Solutes are exchanged across the external mass transfer diffusive boundary layer (liquid film) near the liquid–granule interphase and may subsequently be sorbed onto the EPS matrix, after which they diffuse through the internal granule structure (intragranular diffusion) toward microbial clusters (Baeten et al. (2019)). Although water channels within the granule can facilitate convective transport of solutes into and out of deeper regions, they do not guarantee direct access to the interior of dense cell aggregates. Consequently, substrate and product transport within anaerobic granules is largely governed by diffusion (Pan et al. (2016), Weissbrodt (2024)).

The interaction between a biofilm and the surrounding fluid flow plays a pivotal role in determining both internal and external mass transfer efficiencies. This is because they directly influence the external mass transfer resistance by altering the diffusive boundary layer and affect internal diffusion by modifying the biofilm structure (Baeten et al. (2019), Liu and Tay (2002)). In particular, shear stress can modify biofilm thickness (granule size), porosity, permeability, density, and EPS properties (Feng et al. (2019), Nguyen et al. (2021), Pechaud et al. (2022), Pizzi

et al. (2025)). These modifications in the properties of biofilms and granules feed back into mass transport efficiency, which highlights the strong coupling between hydrodynamics and biofilm function (Huang et al. (2023)). Hence, biofilms exhibit distinct structural responses under different flow regimes.

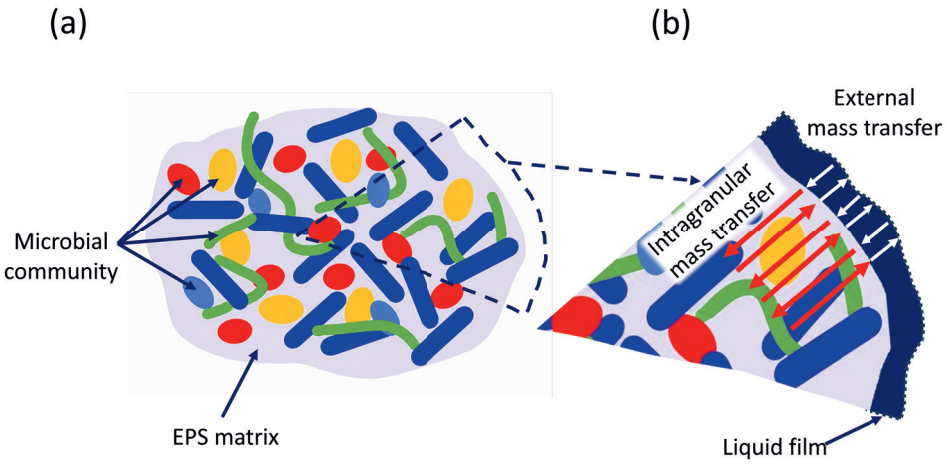


Figure 1.1: Graphical illustration of (a) an anaerobic granule and (b) mass transfer across the liquid boundary layer (liquid film) and within the granule (biofilm).

The hydrodynamic forces responsible for above effects originate from both mean (bulk) flow and turbulent velocity pulsations (fluctuations) (Pizzi et al. (2025), Liu and Tay (2002)). Recent studies have investigated the distinct contributions of turbulent fluctuations and quantified their individual roles in substrate and nutrient transport and mechanical stress on biofilms (Huang et al. (2023)). These investigations have demonstrated that turbulence pulsations alone, even in the absence of a mean flow, can substantially modify biofilm thickness, density, and EPS content (Luo et al. (2021)). It has also been observed that increasing turbulence intensity initially promotes biofilm growth and increases thickness due to enhanced substrate and nutrient flux into the biofilm. However, at higher turbulence intensities, shear-induced erosion dominates, leading to biomass detachment, resulting in thinner but denser biofilms (Tsagkari et al. (2022), Pizzi et al. (2025)). In a recent study, the frequency of turbulence fluctuations was identified as another key parameter affecting biofilm characteristics. It was reported that, at a fixed mean shear stress, low-frequency fluctuations promote biofilm growth, whereas high-frequency

fluctuations suppresses it. The authors argued that biofilms require a characteristic adaptation time to recover and grow following a shift from high to low shear stress. Hence, when the fluctuation frequency is too high, the duration of the low-shear phase becomes insufficient for significant growth (Wei and Yang (2023)).

As explained above, in granular sludge reactors for wastewater treatment, the development of compact and dense granules with high mechanical strength is often desirable for stable treatment performance. However, solute diffusivity is inversely related to biofilm density (Liu and Tay (2002), Guimerà et al. (2016)). Therefore, to achieve high treatment efficiency, operational conditions should be designed such that shear stress and mass transfer jointly fall within an optimal range (Wu et al. (2020)). Despite the recognized importance of local hydrodynamics on the properties of biofilm, such as anaerobic granular sludge, only a limited number of studies have systematically investigated the effects of hydrodynamic variables on granule characteristics. In particular, the role of turbulent pulsations on mass transfer, shear stress, and the mechanisms through which they influence key granule properties, e.g., size, density, strength, internal structure, EPS composition, and methanogenic activity, has remained largely unexplored.

1.3. Hydrodynamics of anaerobic granular sludge reactors (AGSRs)

1.3.1. Granules are exposed to varying flow dynamics of AGSRs

Granular sludge reactors operate as gas–liquid–solid three-phase systems, where interactions among rising gas bubbles, the liquid phase, and the granules generate dynamic and spatially variable flow fields. The flow conditions in these reactors are inherently heterogeneous, and anaerobic granules are continuously exposed time-varying hydrodynamic forces originating from different sources.

Due to continuous gas production and buoyancy-driven bubble rise as well as reactor-scale circulation, the flow in these reactors is essentially turbulent, and granules develop in a turbulent environment (Wu et al. (2015), Huang et al. (2023)). A fundamental characteristic of turbulence is the pulsation of flow parameters, with motion occurring over a wide range of spatial and temporal scales (Xia et al. (2013)). Because of the stochastic nature of turbulence, the instantaneous velocity is commonly decomposed into time-averaged and pulsating (fluctuating) components.

Both components coexist and interact with dispersed phases (granules and gas bubbles). Hence, anaerobic granules experience varying local flow dynamics which determine the mass transfer and mechanical stresses at the granule–liquid interface (Rodi (2017), D' Bastiani et al. (2023)).

The mechanical forces experienced by microbial granules arise from multiple hydrodynamic interactions. The primary contributors include relative motion between granules and the surrounding fluid (drag force), local velocity gradients (shear rates) in the liquid phase, and turbulent velocity fluctuations. Additionally, granule–granule interactions contribute to mechanical stress by exerting both normal and tangential forces on granule surfaces (Ren et al. (2009b)). The relative dominance of these mechanisms depend on the hydrodynamic characteristics of the reactor.

The hydrodynamics of such systems are complex and depend on multiple interrelated parameters. In particular, the hydrodynamic characteristics of these three-phase reactors (i.e., flow regime, gas holdup, liquid velocity, bubble size and spatial distribution, and the relative velocity between rising gas bubbles and the bulk liquid) mainly depend on the following factors: structural parameters (i.e., reactor geometry, internal configurations, and inlet design); physical properties of the liquid–solid phases (i.e., rheological properties of the wastewater, granular sludge size and concentration (solid volume fraction)); and operational conditions (i.e., OLR (gas production rate), upflow velocity, temperature, and pressure) (Yang et al. (2022), D' Bastiani et al. (2023), An et al. (2024b), Gonçalves et al. (2025)). The influence of these various factors is further discussed in Section 1.3.3.

Although the underlying multiphase flow principles are shared among AGSRs, their hydrodynamic behavior depends on the three phase flow regime (e.g., packed bed, fluidized bed). Different reactor design and operational strategies generate distinct flow regimes in the reactor and flow dynamics around granules and must be studied in the context of each reactor type. In what follows, the differences between these various reactors are described.

1.3.2. Different types of AGSRs

The most widely applied high-rate anaerobic granular sludge reactors (AGSRs) in modern industrial wastewater treatment are the Upflow Anaerobic Sludge Blanket (UASB), Expanded Granular Sludge Bed (EGSB), and Internal Circulation (IC)

reactors (Figure 1.2), including their modified configurations. Although these reactor types rely on the same general principle, the retention of anaerobic granular sludge, they differ substantially in reactor design, hydrodynamic regime, and operating conditions (Aragón-Barroso et al. (2026)).

UASB reactors (Figure 1.2A) typically operate at relatively low superficial upflow velocities of 0.5–1.5 m/h (Rittmann and McCarty (2001)). The hydrodynamic conditions in these reactors are highly heterogeneous. This is because a UASB reactor can be divided into three main zones: (i) the sludge bed zone, (ii) the sludge blanket zone, and (iii) the three-phase separator zone (Gonçalves et al. (2025)). The sludge bed zone at the bottom consists of densely packed, relatively large granules through which influent wastewater and biogas rise. Above this region there is a sludge blanket zone, characterized by suspended biomass particles, liquid, and rising gas bubbles. At the top, the three-phase separator, a zone with relatively low turbulence, collects the produced biogas and ensures retention of biomass in the reactor. In UASB reactors, mixing is predominantly induced by the rising biogas bubbles, making them a self-mixing system (D' Bastiani et al. (2023)).

EGSB reactors (Figure 1.2B) are considered second-generation sludge bed reactors. In contrast to UASB systems, the granular sludge bed in EGSB reactors is partially fluidized rather than densely packed. To achieve bed expansion, a higher upflow velocities are applied, typically exceeding 6 m/h. Despite the moderate expansion of the sludge bed, EGSB reactors can still exhibit heterogeneous hydrodynamics, due to sludge concentration gradients along the reactor height and granule clustering Wang et al. (2009)

IC reactors (Figure 1.2C) are regarded as third-generation high-rate AGSR systems. They operate with an expanded granular sludge bed in the lower section and feature multiple three-phase separators positioned at different heights along the reactor. The produced biogas is directed upward through an internal riser to a degassing tank. In this unit, the gas–liquid mixture is separated, and the biogas is discharged from the system. Subsequently, the degassed liquid–sludge mixture flows downward through an internal downcomer located inside the reactor, thereby establishing a continuous internal circulation. In some IC reactors, the superficial upflow velocity, resulting from both liquid upflow and gas flow, may range from 25 to 30 m/h, causing nearly complete mixing of the reactor medium and biomass (van Lier et al. (2015)).

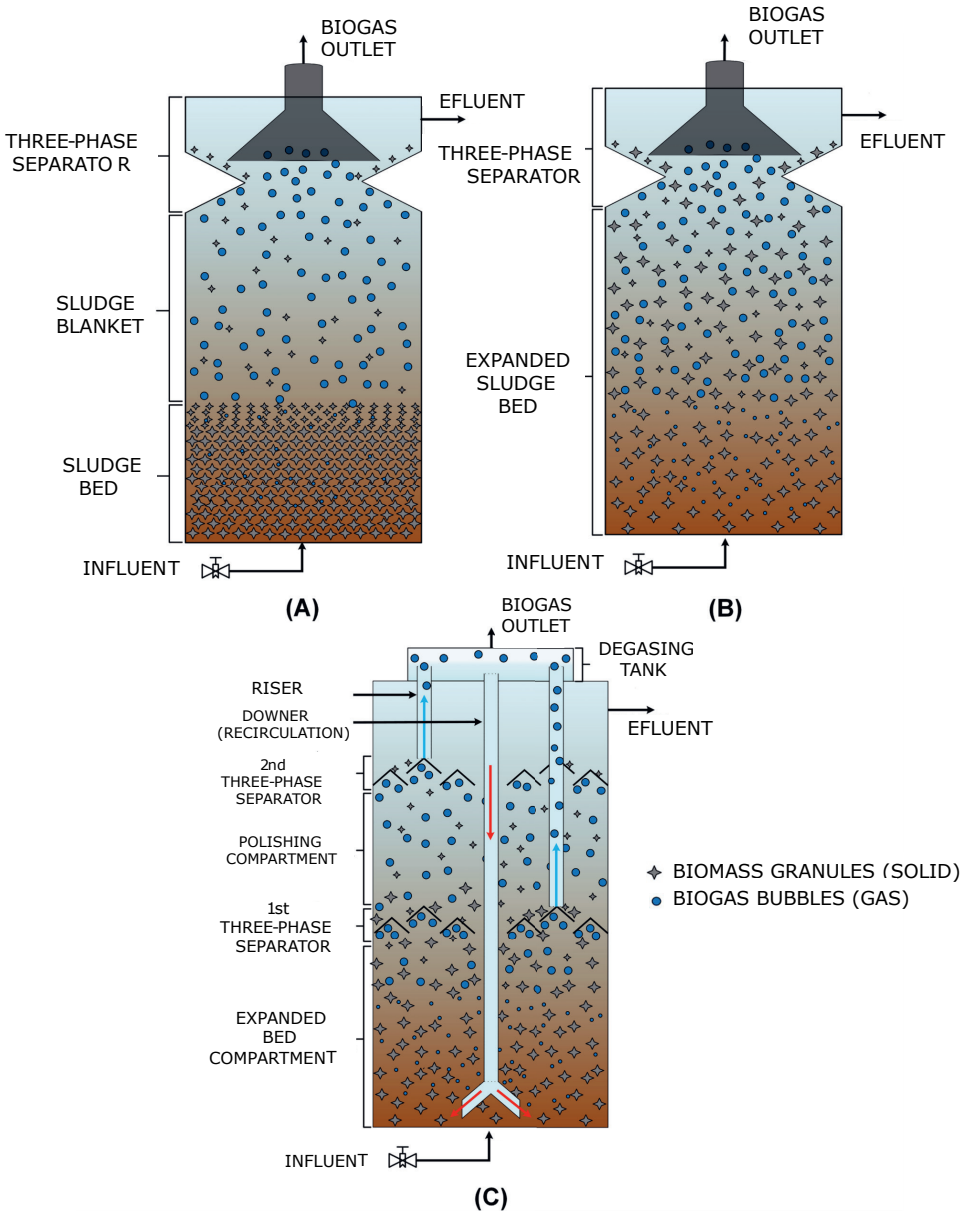


Figure 1.2: Schematic representation of (A) UASB reactor (B) EGSB reactor (C) IC reactor (D' Bastiani et al. (2023)).

1.3.3. Factors affecting the multiphase flow in AGSRs

As explained in section 1.3.2, flow dynamics in AGSRs, operated as gas–liquid–solid three-phase systems (Yang et al. (2022)), are governed by multiple interdependent parameters. As in other three-phase reactors, changing one parameter can influence others, and these coupled effects ultimately determine the overall hydrodynamic behavior of the system.

A primary determinant of reactor hydrodynamics is reactor design, including the internal configuration, height-to-diameter ratio, liquid inlet distributor, and the configuration of three-phase separators. These structural features control the flow pattern, mixing efficiency, gas-solid phases distribution, biomass retention, and gas–liquid separation efficiency (Hu et al. (2017)).

Among the operational parameters, the superficial upflow velocity is the primary and most important hydraulic design parameter. This parameter is directly related to HRT and dictates the extent of expansion of the sludge bed and the resulting hydrodynamic regime. Increasing the upflow velocity promotes bed expansion and increases bed porosity, thereby reducing dead zones and short-circuiting, enhancing turbulence and mixing, and improving external mass transfer (Aragón-Barroso et al. (2026)). Moreover, sufficient upflow velcocity mitigates gas pocket formation and facilitates effective biomass–biogas separation (Mariraj Mohan and Swathi (2022)). However, excessively high upflow velocities (low HRTs) reduce the contact time between sludge and influent, decreasing the treatment efficiency. In addition, this intensified hydrodynamics increases drag forces acting on the granules, thereby enhancing washout rates, and the associated rise in shear stress might increase the granule's disintegration rate (Wu et al. (2006)).

Overall, improved contact between biomass and wastewater, due to moderate bed expansion, increases the volumetric conversion rate and treatment efficiency (van Lier et al. (2015)). As a result, EGSB and IC reactors can be operated at substantially higher organic loading rates, typically 25–35 kgCOD/m^3·d, which is approximately three to four times higher than those commonly reported for UASB reactors, 4–15 kg COD/m^3·d (Rittmann and McCarty (2001)).

OLR is another key operational parameter that influences the hydrodynamics of AGSRs through coupled biochemical and physical mechanisms. OLR determines substrate availability for the biomass, thereby regulating microbial growth, COD

removal, and biogas production rates. The rising biogas bubbles feed back into the hydrodynamics by intensifying bubble-induced mixing, modifying local flow fields (Gonçalves et al. (2025)). The COD removal and biogas production rates were found to improve with increasing OLR; however, this relationship holds only up to a certain limit, beyond which the performance of the reactor deteriorates due to the accumulation of volatile fatty acids (VFAs). The optimum OLR range varies depending on reactor type and operational conditions (e.g., HRT). Furthermore, parameters such as pH, temperature, substrate type, and the presence of inhibitory compounds or essential compounds at inhibitory concentrations can further regulate microbial activity and biogas production rates (Loganath and Mazumder (2018), Musa et al. (2020)). .

Moreover, physical properties of the multiphase system, including wastewater rheology (viscosity and density), solid volume fraction (biomass concentration), granule size distribution, pressure, and temperature influence three-phase flow dynamics. These parameters, together with the aforementioned parameters, govern interphase interactions among wastewater, biogas bubbles, and granular sludge, thereby affecting gas–liquid–solid slip velocities, phase segregation behavior, turbulence and mixing intensity, shear stress distribution, and mass transfer (Yang et al. (2022), An et al. (2024b)).

Despite the above acknowledged and general consensus on the central role of hydrodynamics in regulating granule properties and reactor performance, the effects of the governinging parameters, particularly the operational parameters, on the local flow dynamics of AGSRs have not been studied (Aragón-Barroso et al. (2026)). This lack of research stems primarily from the inherent lack of optical transparency of gas–liquid–solid three-phase systems, which severely restricts the applicability of most available experimental flow measurement techniques (Poelma (2020)). As a consequence, detailed characterization of local flow features and turbulence dynamics that exist within different AGSR configurations continues to pose a substantial scientific and technical challenge. In Section 1.4 the various approaches to overcome this are discussed.

1.4. Approaches to study the hydrodynamics of AGSRs

Multiple methods and approaches have been utilized to investigate the hydrodynamics of AGSRs. These studies can be categorized into three main groups based on their primary objectives.

The first category comprises studies focused on describing and understanding the hydrodynamics of these three-phase systems, mainly through analyzing the flow patterns, phase distribution, velocity fields, and mixing performance (Ren et al. (2009a), Wang et al. (2009, 2010), Bastiani et al. (2021)). The second category comprises studies aimed at reactor design and process optimization. These investigations focus on analyzing how reactor internal configuration influences flow behavior, particularly in terms of gas–liquid–solid separation efficiency (Hu et al. (2017), Pan et al. (2017), Hao and Shen (2021)). Finally, the third category includes studies aimed at gaining a fundamental mechanistic understanding of transport phenomena at macro-, meso-, and micro-scales within these reactors, and how flow phenomena influence shear stress distribution, mass transfer rates, biogas production, granule properties, and overall pollutant removal performance (Wu et al. (2006), Zhang et al. (2011, 2012), Jiang et al. (2014), Wu et al. (2015), Jiang et al. (2016)). Depending on the objective of the study, both modeling approaches with different degrees of complexity and experimental methods have been adopted (Figure 1.3).

1.4.1. Modeling approaches

The majority of research on the hydrodynamics of AGSRs has been model-based, either focusing on the quantification of specific parameters, such as overall shear stress and shear rate in the reactor, or on simulating the overall gas–liquid–solid three-phase flow within the reactor. Based on their level of complexity and underlying assumptions, these modeling approaches can be categorized into three main types: empirical, phenomenological, and computational fluid dynamics (CFD) models.

Empirical models are the simplest type of modeling approach. They are correlation-based formulations derived from experimental data that can relate operational variables (e.g., upflow velocity) to macroscopic (reactor-scale) hydrodynamic variables (e.g., gas holdup, shear rate) without explicitly resolving the underlying flow physics. These models have been applied to quantify overall shear rate (Pereboom and Vereijken (1994), Wu et al. (2006, 2012a)) and shear force

(Ren et al. (2009b), Kundu et al. (2014a)), which were subsequently correlated with granule properties or overall reactor performance. In this context, hydrodynamics are typically represented through bulk or reactor-averaged indicators. The main advantages of empirical models lie in their simplicity and relatively low data requirements, making them attractive for preliminary design and parametric studies (e.g., assessing the effect of upflow velocity on reactor performance).

Phenomenological models represent another type of models that have been mainly used to describe mixing in AGSR systems. These models sit between fully empirical and mechanistic approaches. They are physics-informed, capturing the dominant transport behavior, bases on experimental observations, using simplified governing equations and a limited set of calibrated parameters (e.g., dispersion coefficients). For example, the tanks-in-series model has been applied to investigate the hydrodynamics of UASB reactors (Ren et al. (2009a), Rodríguez-Gómez et al. (2014)). One-dimensional axial dispersion models have been used to evaluate mixing along the reactor height. Depending on their level of complexity, these models can also assess granular sludge dynamics and predict concentration profiles along the reactor height (Zeng et al. (2005), Kalyuzhnyi et al. (2006), Ren et al. (2008)).

CFD modeling has increasingly been used to study the multiphase flow behavior of these reactors. It involves the use of numerical methods to solve the fundamental governing equations of fluid dynamics (continuity, momentum, and when heat transfer is relevant, energy). The main advantage of CFD over empirical and phenomenological models is its ability to provide time-resolved, three-dimensional predictions of local flow variables (D' Bastiani et al. (2023)). CFD modeling has been applied to analyse flow patterns, velocity fields, phase holdups, and mixing behavior in both UASB reactors (Ren et al. (2009a), Bastiani et al. (2021), Gonçalves et al. (2025)) and EGSB reactors (Wang et al. (2009)). Furthermore, coupled CFD–kinetic models have been developed to predict biogas production and to link local hydrodynamics with biogas production (Wang et al. (2010), Yang et al. (2015)).

The results of the aforementioned models can only be used reliably after proper calibration and rigorous validation. This requires high-quality experimental data, and depending on the model type and the objective of the study, different experimental methods can be employed. In Section 1.4.2 these approaches and related challenges are described.

1.4.2. Experimental approaches

Gas–liquid–solid three-phase systems are recognized as the most challenging systems for experimental flow measurements and hydrodynamic characterization. Their intrinsic opacity, strong phase interactions, and spatiotemporal heterogeneity prevent the application of many conventional measurement techniques, particularly optical and non-intrusive methods. As a result, accurate quantification of flow behavior in such systems remains limited (Yang et al. (2022), An et al. (2024b)). Nevertheless, the choice of experimental approach largely depends on the objective of the study. For instance, investigations focused on global mixing performance may rely on tracer-based and residence time distribution (RTD) methods (Wang et al. (2018), Mullai et al. (2025)), whereas studies targeting local flow fields of the liquid, gas, and solid phases require more advanced and often specialized techniques. Each method offers specific capabilities but also entails inherent limitations in terms of spatial resolution, degree of intrusiveness, applicability at high solid concentrations, and scalability (Poelma (2020)).

The tracer method is a widely applied and robust technique for characterizing the global hydrodynamic behavior of continuous-flow reactors, particularly through the determination of the RTD. By injecting a known quantity of a chemically inert tracer and monitoring its concentration at the reactor outlet using ion-selective electrodes, spectroscopy, or other analytical techniques, the temporal distribution of fluid elements entering and leaving the reactor can be quantified (Li et al. (2022)). RTD analysis provides valuable insights into macroscopic mixing performance, enabling the detection of existence of dead zones and short-circuiting. However, as this method provides reactor-scale mixing information, the spatial distribution of these features within the reactor cannot be resolved. Importantly, because measurements are typically conducted at the inlet and outlet, the tracer method is applicable to laboratory-, pilot-, and full-scale reactors, making it highly scalable and suitable for industrial systems (Mullai et al. (2025)). However, the technique provides only integral (reactor-averaged) information, and the details of local mixing in the reactor are neglected. The tracer method was employed in AGSR systems to investigate mixing behavior and to validate non-ideal hydrodynamic models, such as the tanks-in-series and axial dispersion models (Zeng et al. (2005), Ren et al. (2008, 2009a), Wang et al. (2018), Mullai et al. (2025)).

Particle Image Velocimetry (PIV) and Particle Tracking Velocimetry (PTV) are other methods that have been employed to directly quantify the local flow field inside AGSRs. Both are optical flow measurement techniques that rely on analyzing the motion of micron-scale tracer particles seeded within the fluid (Seyfi et al. (2024)).

In PIV, the displacement of groups of particles between two successive images is determined through cross-correlation analysis, yielding an instantaneous velocity field over a grid. In contrast, PTV identifies and tracks individual tracer particles, reconstructs their trajectories, and provides time-resolved velocity data of each particle (Schröder et al. (2015b)). Compared to PIV, PTV offers higher spatial resolution because it tracks individual particle trajectories rather than providing a spatially averaged velocity field based on groups of tracers. This makes it particularly suitable for resolving sharp velocity gradients and accurately calculating local shear rates (Schröder et al. (2015a)). Additionally, tracking individual particles enables direct quantification of particle-scale transport processes, such as residence times and dispersion coefficients. The main advantage of PIV and PTV over global techniques, such as RTD analysis, is their ability to resolve local hydrodynamics, including flow patterns, phase velocities, shear rates, and turbulence characteristics.

2D-PIV, for example, has been applied at different scales to quantify the shear rate around granules in order to investigate the effect of shear on biogas production and to determine the optimum shear rate for maximum biogas yield (Zhang et al. (2011, 2012), Jiang et al. (2014, 2016)). It has also been used to characterize the hydrodynamics around granular sludge and to assess the contribution of the relative velocity between sludge and liquid, as well as rising gas bubbles, to the shear rate acting on the granules (Wu et al. (2015)). In addition, the combined use of PIV and PTV was employed to analyze the flow pattern and velocity fields of both the fluid and the granules, as well as normal and shear strain rates, in a sequencing batch reactor (SBR) during the formation of aerobic granules (Zima-Kulisiewicz et al. (2008)). Moreover, 2D-PIV has been employed to validate CFD models developed to simulate three-phase flow behavior in UASB and EGSB reactors (Wang et al. (2009, 2010), Bastiani et al. (2021)).

Despite their advantages, PIV and PTV have several limitations in AGSR applications. They require optical access, which necessitates a transparent reactor and working medium, and their application is therefore limited to laboratory-scale reactors.

Moreover, these methods are sensitive to the presence of dispersed phases (solids and gas bubbles) and cannot be reliably applied beyond a certain volume fraction (VOF) of the dispersed phases. Consequently, previous studies based on PIV and PTV have predominantly been performed under low granule concentration conditions, with velocity measurement limited to planar (two-dimensional) flow fields. These limitations underscore the need for new methodologies capable of accurately characterizing flow behavior in gas–liquid–solid reactors, particularly under high solid concentration conditions representative of realistic operational conditions in AGSRs.

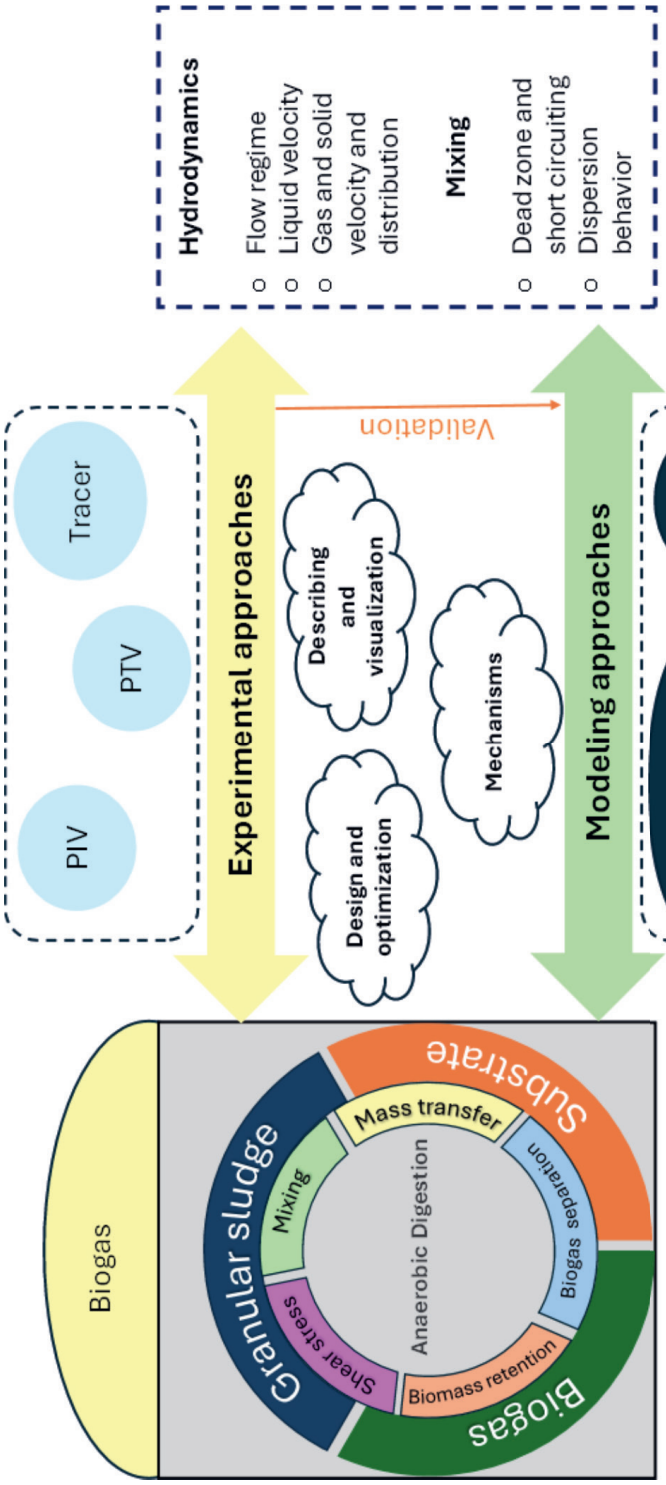


Figure 1.3: Overview of experimental and modeling approaches for hydrodynamic and mixing characterization.

1.5. Calcification of anaerobic granules and role of hydrodynamics

Anaerobic digestion is one of the most effective biological treatment methods for high-calcium industrial wastewaters, including effluents from industries such as paper recycling, dairy processing, and gelatin production (Owodunni and Ismail (2021)). However, granular sludge calcification is frequently observed during the treatment of these calcium-rich wastewaters (ranging from 800 to 2000 mg/L) (Van Langerak et al. (1998, 2000)), meaning that the outer surface of the granules is coated or their interior is transformed into a hard core due to calcium salt deposition. Consequently, this can result in a reduction in pollutant removal efficiency and, in severe cases, reactor failure (Diamantis and Aivasidis (2018)).

In general, calcium plays a fundamental role in anaerobic granular sludge reactors. At moderate concentrations (80–150 mg/L), Ca^{2+} supports granule skeleton formation and cohesion by bridging negatively charged functional groups in EPS, thereby enhancing sludge granulation (Alibhai and Forster (1986), Mahoney et al. (1987), Ma et al. (2020)). Through cationic bridging and stabilization of the EPS matrix, calcium improves the density, structural integrity, and mechanical strength of granules, which are key properties for efficient biomass retention and stable operation in high-rate anaerobic reactors (Wu et al. (2021)). However, excessive calcium concentrations lead to the deposition of calcium salts, predominantly in the form of calcite ($CaCO_3$). This phenomenon is more pronounced in the granule core, where higher local pH favors calcium salt formation, but it can also occur at neutral pH on the outer surface. Other precipitates have also been reported to form via reactions with PO_4^{3-} and S^{2-} (Cunha et al. (2018)). Progressive mineral precipitation modifies both the internal and external structure of the granules by occupying pores and transport channels that play an important role in the transport of substrates, nutrients, and metabolic by-products within the granule matrix. Furthermore, calcium minerals occupy void spaces that would otherwise host active microorganisms, resulting in reduced volatile suspended solids (VSS) in the sludge. The combined effect of reduced VSS and increased mass transfer resistance leads to a decline in methanogenic activity of the granular sludge and, consequently, reduced biogas production (Yu et al. (2019)).

Calcification can also be described as a diffusion–reaction process, involving (i) surface adsorption of Ca^{2+} onto negatively charged functional groups in EPS through

electrostatic interactions and cation bridging, (ii) migration of Ca^{2+} through the granule matrix, which is mostly governed by intragranular diffusivity, and (iii) reaction with available anions (e.g., CO_3^{2-}, PO_4^{3-}, and S^{2-}), leading to the formation of calcium salts (Lian et al. (2023), Peng et al. (2024)). This process is partially controlled by the bio-induced pH gradient within the granule, where microbial activity increases the local pH toward the granule center. As result, this elevated local pH enhances local supersaturation and increases the precipitation rate within the granule matrix, particularly in the core region (Cunha et al. (2018)). Consequently, the transport of substrates, metabolic by-products, and Ca^{2+} plays a crucial role in controlling calcium salt precipitation.

As explained in Section 1.3, flow dynamics in the vicinity of granules directly regulate external mass transfer and indirectly influence intragranular mass transfer by shaping key granule properties, including size, density, internal structure (i.e., porosity and permeability), EPS composition, and surface properties. Moreover, it was reported that biofilm heterogeneous structure together with intensity of surrounding hydrodynamic condition define the transport mechanisms within biofilm. At higher liquid velocities, the contribution of advective transport within pores, voids, and water channels increases, resulting in higher effective intragranular diffusivity which can alter the solutes and pH profile withing biofilm (Guimerà et al. (2016)).

In AGSRs, applied operational conditions, together with other factors explain in section 1.3.3, generate distinct flow regimes and hydrodynamic characteristics. These conditions determine the physical properties of biogas bubbles (i.e., bubble size) as well as their dynamics (i.e., rising velocity and spatial distribution). As a results, this alter the local flow variables in the vicinity of granules, such as liquid mean velocity and turbulent velocity fluctuations are altered. However, how the local hydrodynamics induced by rising gas bubbles influence granule calcification, and the relative contributions of mean flow and velocity fluctuations to this process, remains unclear.

In general, it remains an open research area how a wide range of operational conditions influences hydrodynamics at both the reactor scale and the granule scale. It is important to mention that flow behavior at these two scales can substantially differ, thereby requires a multiscale flow characterization to elucidate mechanistic links between global and local hydrodynamics variables. Moreover, the mechanisms

by which local hydrodynamic characteristics regulate shear stress and mass transfer at the granule surface, particularly the role of turbulence, are not yet fully understood. Furthermore, the mechanism by which shear stress and mass transfer govern the physical, chemical, and biological characteristics of anaerobic granules require systematic investigation.

1.6. Overview of the thesis

In **Chapter 2**, the theoretical background of turbulence and mass and momentum transport mechanisms in turbulent flows is reviewed. The following two chapters address a key research gap in the hydrodynamic characterization of high-rate granular sludge bioreactors—the lack of detailed local flow dynamics information within the sludge bed and sludge blanket regions—by developing experimental methods for flow measurements under conditions characteristic of these multiphase systems. In **Chapter 3**, the feasibility of local hydrodynamic characterization in a two-phase (liquid–solid) system at high solid concentrations was investigated. A combined refractive index matching (RIM) and three-dimensional particle tracking velocimetry (3D-PTV) technique was employed to measure the local flow dynamics in a densely packed fluidized bed, representing the hydrodynamic conditions at solid fractions characteristics of EGSB and IC reactors. Upon validating the feasibility of volumetric flow measurements in such systems, the influence of solid concentration on flow pattern and dynamic was investigated. In **Chapter 4**, the RIM–PTV methodology, developed in **Chapter 3**, was applied to study the flow dynamics in a liquid–gas–solid three-phase system under varying gas flow rates, representing different biogas production rate conditions, and solid VOFs. This approach was motivated by the presence of axial gradients in both solid concentration and gas holdup along the reactor height. The objective was to replicate the range of three-phase flow conditions exist along the height of IC and EGSB reactors for detailed hydrodynamic analysis. -Therefore, the influence of solid concentration and gas flow rate on the bulk liquid velocity (volume-averaged velocity) and the instantaneous velocity components was systematically investigated. The bulk flow velocity provided insight into reactor-scale convective mixing. In addition, local mixing performance induced by turbulent velocity fluctuations was characterized by analyzing the displacement of microscale tracer particles within the measurement volume, and both axial and radial dispersion

coefficients were quantified across the tested operational range. In **Chapter 5**, the objective was to investigate the mechanisms by which local hydrodynamics influence the evolution of granule properties in calcium-rich wastewater. In this study, granule development in two "low-seeded" lab-scale EGSB reactors at distinct hydrodynamic regimes controlled via gas sparging, i.e., high shear (HSR) and low shear (LSR) reactors, were compared to slow-mixing batch continuous reactors (shear-free), all operated under calcium-rich conditions. Inspired by previous studies on biofilm–flow interactions (Wei and Yang (2023)) and the impact of granule calcification on granule properties (Yu et al. (2019)), it was hypothesized that a higher gas flow rate in the HSR would enhance both mean flow and turbulence intensities, thereby increasing shear stress and mass transfer of Ca^{2+}, which should promote the formation of smaller, more highly calcified granules with reduced methanogenic activity. Finally, in **Chapter 6** the results of this thesis are discussed in a broader context, and future research directions are proposed.

Chapter 2

2

Chapter 2

Theoretical background on turbulence and transport in multiphase flows

Abstract

This chapter presents the literature-based theoretical background on turbulence and transport phenomena in multiphase flows. It introduces the statistical description of turbulence and the different scales of turbulent motion. The main sources of turbulent velocity fluctuations in multiphase systems are then discussed, including shear-induced turbulence and bubble- or particle-induced turbulence. This theoretical framework provides a basis for understanding how turbulent velocity fluctuations influence mixing, mass transfer, and shear stress in anaerobic granular sludge reactors.

2.1. Introduction

Mixing and mass transfer are two critical phenomena in anaerobic granular sludge reactors. In these systems, efficient transport of substrates and nutrients toward microbial granules is essential to sustain biological activity and maintain stable wastewater treatment performance.

The flow in anaerobic granular sludge reactors is often turbulent and characterized by velocity fluctuations (Bastiani et al. (2021), Huang et al. (2023)). These fluctuations can strongly influence mixing, mass transfer, and the interaction between the liquid phase and microbial granules. On the one hand, turbulence can enhance cross-stream transport, reduce dead zones, and decrease concentration gradients within the reactor, thereby improving the delivery of substrates and nutrients to microbial cells. On the other hand, excessive turbulence can increase the mechanical forces acting on granule surfaces, leading to erosion, structural damage, or even granule disintegration, which may ultimately impair reactor performance. Therefore, in an ideal case, the desired hydrodynamic conditions should exhibit turbulence characteristics that enhance mass transfer while keeping the imposed mechanical stresses within the tolerance range of the granules.

In the final year of this PhD project, analyzing the experiments on the effect of hydrodynamics on anaerobic granule properties reported in Chapter 5, showed that time-averaged velocity and shear fields in meso-scale were not sufficient to explain the observed changes in granule properties, particularly granule size. After conducting a statistical analysis of the instantaneous velocity fluctuations within the reactors, it became evident that the turbulence characteristics differed between the two reactors. This suggests that velocity fluctuations and their associated timescales may play an important role in determining the mechanical forces experienced by the granules. This motivated a closer examination of turbulence in these reactors beyond time-averaged flow quantities.

The following sections first introduce the statistical description of turbulence and the relevant scales of turbulent motion, then discuss how turbulence is modified in multiphase flows, and finally explain how turbulent fluctuations affect momentum and mass transport, mixing, and shear stress conditions in multiphase flow systems such as anaerobic granular sludge reactors.

2.2. Statistical description of turbulence

Statistics and probability provide the fundamental framework for describing turbulent flows, as turbulence is inherently characterized by irregular and chaotic velocity fluctuations spanning a wide range of scales. Rather than describing the instantaneous flow motion at every point in space and time in full detail, turbulent flows are commonly analyzed using statistical quantities such as variances, correlations, probability density functions (PDFs), and spectra (Pope (2001)).

The transition from laminar to turbulent flow is commonly characterized by the Reynolds number, which expresses the ratio between inertial and viscous forces:

$$Re = \frac{UL}{\nu} \tag{2.1}$$

where U is a characteristic velocity, L is a characteristic length scale, and ν is the kinematic viscosity. At low Reynolds numbers, viscous forces dominate and the flow tends to remain smooth and ordered, i.e., laminar. At high Reynolds numbers, inertial forces become dominant, flow instabilities can develop, and the motion becomes increasingly irregular and fluctuating. In turbulent flows, the instantaneous velocity field can be decomposed into mean and fluctuating components according to Reynolds decomposition:

$$u_i(\mathbf{x}, t) = \langle u_i \rangle (\mathbf{x}) + u_i'(\mathbf{x}, t) \tag{2.2}$$

where $\langle u_i \rangle$ represents the time-averaged velocity field, and u_i' denotes the turbulent velocity fluctuation. By definition, the average of the fluctuating component is zero, i.e., $\left\langle u_i' \right\rangle = 0$. The use of time-averaged velocity is meaningful only when the characteristic timescale of the turbulent fluctuations is much smaller than the time over which the macroscopic velocity changes significantly. In other words, we must assume that there is a clear separation of timescales between the variation of mean velocity and that of velocity fluctuations. This decomposition forms the basis for the statistical description of turbulence and enables quantification of turbulent transport and energy transfer processes.

Turbulence intensity is commonly quantified using the root mean square (RMS) of the velocity fluctuations, which provides a measure of the magnitude of the fluctuating motion:

$$U_{\text{rms}} = \sqrt{\langle u_i'^2 \rangle} \tag{2.3}$$

The turbulent kinetic energy per unit mass is defined as:

$$k = \frac{1}{2}\langle u_i' u_i' \rangle \tag{2.4}$$

For three-dimensional turbulence, this can also be written as:

$$k = \frac{1}{2}\left(\langle u_x'^2 \rangle + \langle u_y'^2 \rangle + \langle u_z'^2 \rangle\right) \tag{2.5}$$

Spectral analysis of velocity is another statistical tool used to characterize turbulent flows. Since turbulence contains fluctuating velocity motions over a wide range of spatial and temporal scales, it is often difficult to describe its structure only from instantaneous velocity fields or time-averaged quantities. Spectral analysis decomposes the velocity fluctuations into contributions from different scales, or equivalently different wavenumbers or frequencies. In this way, it provides information on how turbulent kinetic energy is distributed among large, intermediate, and small-scale motions. This is addressed in more detail in the next section.

2.3. The scales of turbulent motions

Turbulent flows consist of motions spanning a broad range of spatial and temporal scales and are commonly interpreted as a collection of eddies of different sizes. An eddy can be viewed as a swirling fluid motion (whirlpool) with a characteristic length scale ℓ, a velocity $u(\ell)$, and an associated timescale $\tau(\ell) = \ell/u(\ell)$. Although an eddy does not have a strict physical boundary, it represents a turbulent structure that

remains at least moderately coherent over a region of size ℓ.

The largest eddies are typically comparable to the characteristic length scale of the flow, such as the diameter of a reactor, or the size of a large circulation structure. These large-scale motions contain most of the turbulent kinetic energy and are strongly influenced by the geometry of the system, boundary conditions, inlet configuration, and mean flow field.

According to Richardson's cascade concept, large eddies are unstable and progressively break down into smaller eddies, transferring their kinetic energy to smaller scales (Figure 2.1). These smaller eddies undergo a similar break-up process, passing energy to even smaller motions. This scale-to-scale transfer of turbulent kinetic energy is known as the turbulent energy cascade. The cascade continues until the eddies become sufficiently small that viscous forces dominate their motion, causing turbulent kinetic energy to be dissipated into heat.

This above description raises two important questions: what is the size of the smallest eddies at which dissipation occurs, and how do the characteristic velocity and timescale (lifetime) of eddies change as the length scale decreases? These questions are addressed by Kolmogorov's theory. According to this theory, as the eddy size ℓ decreases during the cascade, both the characteristic velocity $u(\ell)$ and the associated timescale $\tau(\ell) = \ell/u(\ell)$ decrease.

Kolmogorov further argued that the largest eddies are generally anisotropic, since they are strongly affected by the mean flow field and boundary conditions (e.g., reactor geometry and internals). However, this directional information is progressively lost as energy is transferred to smaller and smaller scales. Therefore, at sufficiently high Reynolds number, the smallest turbulent motions become approximately locally isotropic, meaning that their statistical properties are nearly independent of direction.

Because these small-scale motions are no longer strongly controlled by the specific geometry of the flow, their statistics can be considered universal. This raises the next question: On what parameters does this statistically universal state depend? In the energy cascade, the two dominant processes controlling the small scales are the transfer of turbulent kinetic energy to successively smaller scales and its eventual dissipation by viscosity. The rate at which energy is transferred through the cascade is ultimately balanced by the rate at which it is dissipated at the smallest scales. Therefore, the statistics of these small-scale motions are governed by the turbulent

kinetic energy dissipation rate, ε, and the kinematic viscosity, ν. This scale where very small and dissipative eddies exist is called Kolmogorov scale.

Having identified the smallest dissipative motions, the full range of turbulent scales can be divided into three main regions: the energy-containing range, the inertial subrange, and the dissipation range. The energy-containing range consists of the largest eddies, which contain the bulk of the turbulent kinetic energy. At the opposite end of the cascade is the dissipation range, where the smallest eddies occur. In this range, viscous effects become significant and are responsible for essentially all of the dissipation of turbulent kinetic energy. Between these two regions lies the inertial subrange, where eddies are much smaller than the energy-containing motions, but still much larger than the dissipative eddies. The main process in this range is the transfer of energy to successively smaller scales.

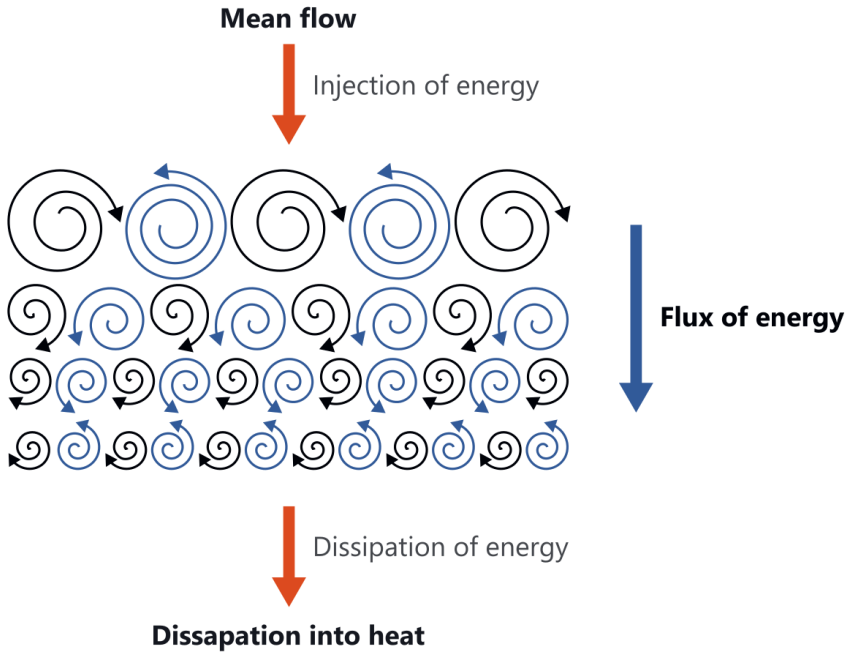


Figure 2.1: Energy Cascade from large to small eddies (Altair Engineering (2025)).

It remains to be determined how energy is distributed among the eddies of different sizes. Energy spectra provide a statistical way to represent how turbulent kinetic energy is distributed across different length scales. Instead of describing the cascade directly in terms of eddies in physical space, spectral analysis expresses the fluid motion in different length scales in terms of wavenumbers. The wavenumber κ is related to the corresponding length scale through $\ell = 2\pi/\kappa$. Therefore, low wavenumbers correspond to large-scale motions, whereas high wavenumbers correspond to small-scale motions. The energy-spectrum function $E(\kappa)$ shows how turbulent kinetic energy is distributed over wavenumber space (Figure 2.2).

In a typical energy spectrum, the energy-containing range appears at low wavenumbers, where most of the turbulent kinetic energy is located. The inertial subrange appears at intermediate wavenumbers and is identified by the well-known Kolmogorov spectrum,

$$E(\kappa) = C\varepsilon^{2/3}\kappa^{-5/3} \tag{2.6}$$

where C is the dimensionless Kolmogorov constant and ε is the turbulent kinetic energy dissipation rate. This $-5/3$ slope on a log–log plot indicates a range in which energy is transferred from larger to smaller scales without significant direct viscous dissipation. At high wavenumbers, the spectrum enters the dissipation range, where viscous effects dominate and the spectral energy decreases rapidly. Therefore, the energy spectrum provides the spectral view of the cascade: energy is concentrated at low wavenumbers, transferred through intermediate wavenumbers, and dissipated at high wavenumbers.

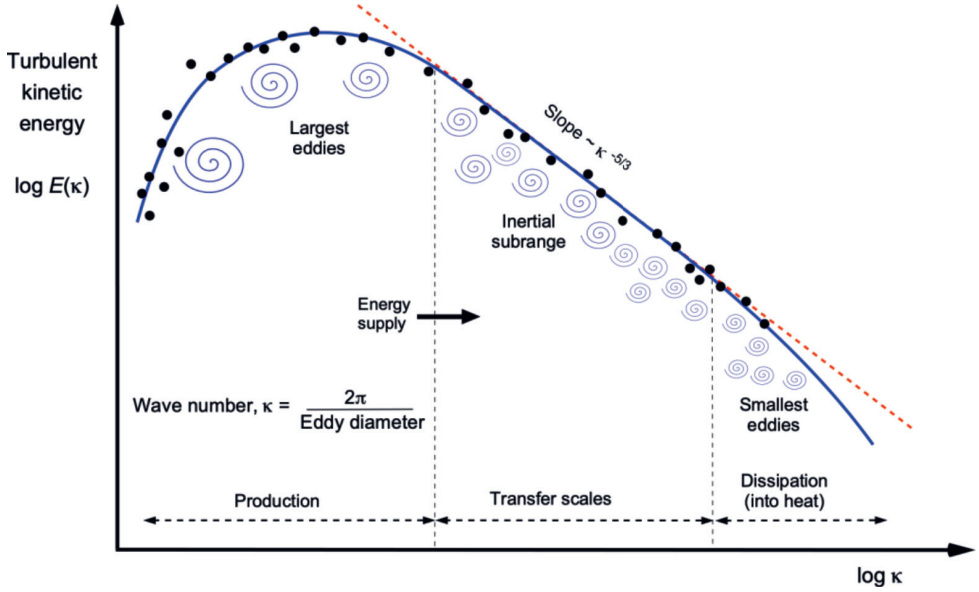


Figure 2.2: The kinetic energy spectra of turbulence span a range of energy and length scales (Leishman (2026)).

2.4. Turbulence in multiphase flows

In multiphase reactors, turbulence is more complex than in single-phase flow because the dispersed phase, such as gas bubbles or granules, can both respond to and modify the turbulent motion of the continuous liquid phase. Even in the absence of a dispersed phase, turbulent fluctuations can be generated by mean shear, i.e., strong gradients in the mean velocity field. In bioreactors, such gradients may arise from reactor-scale circulation, inlet-driven flow, wall effects, or disturbances caused by internal structures such as baffles and three-phase separators. For example, strong velocity gradients can develop at the interface between upward and downward flow regions, promoting flow instabilities and generating shear-induced turbulence (Shi et al. (2019)).

The presence of bubbles or particles introduces an additional mechanism for turbulence modulation. When the dispersed phase is small compared with the relevant turbulent length scales, it tends to follow the liquid motion and may extract energy from the turbulent fluctuations, thereby contributing to turbulence attenuation. In contrast, larger bubbles or particles do not simply follow the liquid

motion. Their relative motion through the continuous phase can generate wakes, local circulation, vortex shedding, and additional velocity disturbances (Brennen (2005)). These fluctuations generated by dispersed phase are often referred to as pseudo-turbulence, particle-induced turbulence, or, in bubbly flows, bubble-induced turbulence. Unlike shear-induced turbulence, where energy is mainly supplied at large flow scales by mean flow and then transferred toward smaller eddies through the energy cascade, pseudo-turbulence is produced locally by the relative motion of the dispersed phase. In this case, energy is introduced directly at the scale of bubbles or particles and is then redistributed to the surrounding liquid motion (Hidman et al. (2023)). This difference in energy injection is also reflected in the spectral behavior of bubbly flows. In bubble-induced turbulence, the motion of rising bubbles disturbs the carrying fluid and induces collective agitation, primarily through wakes, nonlinear wake interactions, and local velocity disturbances around the bubbles. As a result, the spectral behavior deviates from the classical single-phase turbulence scaling. For example, several experimental and numerical studies have reported that the liquid-phase kinetic energy spectrum in bubble-induced turbulence displays a robust scaling close to $E(k) \sim k^{-3}$, rather than the classical Kolmogorov scaling of $E(k) \sim k^{-5/3}$ often associated with single-phase turbulence (Innocenti et al., 2021). Therefore, understanding how bubbles and particles modify turbulence is essential for interpreting mixing and transport phenomena in multiphase reactors.

2.5. Transport phenomena in multiphase turbulent flows

In the previous section, the sources of turbulence and velocity fluctuations in multiphase flows were discussed. These fluctuations are important because they directly influence transport phenomena. In turbulent flow, the instantaneous velocity field is time-dependent and three-dimensional, even when the mean flow appears steady. The main consequence of turbulence is the enhancement of cross-stream transport of momentum, heat, and mass (including dissolved chemicals). Although turbulent velocity fluctuations have a zero mean value, their interaction with other fluctuating quantities (e.g., solute concentrations) can make a non-zero contribution to their transport. Concerning the momentum transport, turbulence also increases the transport of momentum across the flow. Total shear stress in turbulent flow is larger than in laminar flow because it includes both the viscous contribution and the

contribution from velocity fluctuations, commonly referred to as Reynolds stress. This enhanced momentum transfer is associated with larger velocity gradients and greater mechanical energy dissipation in the flow.

In laminar flow, momentum transport occurs primarily through viscous shear stresses between adjacent, non-mixing fluid layers moving at different velocities, and heat and mass transport across streamlines are mainly governed by molecular diffusion. These processes are relatively slow and act at molecular scales. In diffusive transport, fluctuations originate from thermal agitation, i.e., Brownian motion, with typical molecular length scales on the order of $10^{-3}\,\mu$m. In contrast, turbulent fluctuations occur over much larger scales, starting from the Kolmogorov scale, which is typically on the order of $100\,\mu$m or larger, depending on the flow conditions (Mauri (2015)). Physically, this means that turbulent eddies carry fluid parcels with different momentum, temperature, or concentration from one region to another, greatly accelerating (micro-)mixing. Therefore, compared to laminar flows which rely mostly on advection and molecular diffusion, turbulent flow promotes rapid cross-stream exchange through eddies over a wide range of length scales.

Turbulence also affects mass transfer from the bulk liquid to solid surfaces by modifying the liquid film, or liquid boundary layer, surrounding the solid phase. In laminar flow, this film is relatively stable and mass transfer across it is mainly controlled by molecular diffusion. In turbulent flow, velocity fluctuations continuously renew the liquid near the surface and reduce the effective thickness of this boundary layer, thereby increasing the concentration gradient at the interface and enhancing external mass transfer.

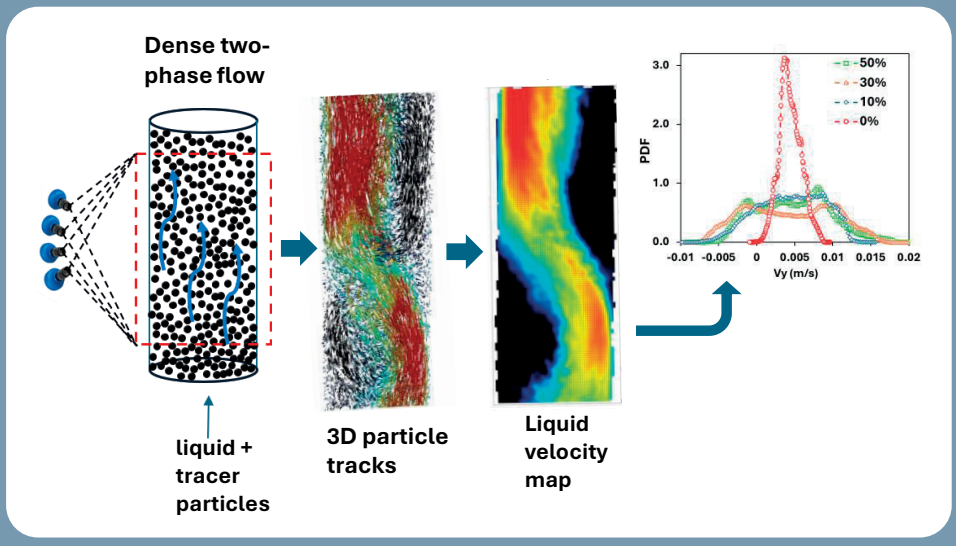
Thus, turbulence is beneficial when enhanced homogenization of dissolved chemicals and mass transfer between phases is desired, but it can be disadvantageous when the associated increase in shear stress or energy dissipation becomes important. Therefore, in a multiphase turbulent flow, improved mixing is often coupled to stronger mechanical forcing at the surfaces of dispersed phases. This coupling is particularly important for anaerobic granular sludge systems, where shear can influence erosion and fine-particle detachment from granule surfaces and, over time, affect granule size, compactness, and intragranular diffusivity.

Chapter 3

3

Chapter 3

3D Hydrodynamic Characterization in Anaerobic Granular Sludge Reactors. Part 1: Application of 3D-PTV in Dense Two-phase Flows



This chapter has been published as:

Eslami, H., Bruning, H., Rijnaarts, H., and Sudmalis, D. (2025). 3D hydrodynamic characterization in anaerobic granular sludge reactors, Part 1: Application of 3D-PTV in dense two-phase flows. Journal of Environmental Chemical Engineering, 118703.

Abstract

The study of hydrodynamics of anaerobic granular sludge reactors (AGSRs) is challenging due to the high concentration of the solid phase and the complex three-dimensional interactions between gas, solid, and liquid phases. This study demonstrates the feasibility of combining refractive index matching (RIM) with particle tracking velocimetry (PTV) techniques to investigate 3D flow dynamics in these reactors. We utilized transparent hydrogel beads as synthetic granules to represent the solid phase and employed the cutting-edge Shake-the-Box (STB) particle tracking algorithm to measure three-dimensional velocity fields in liquid-solid flows with varying solid concentrations, up to 50%. The liquid velocity components were captured across the entire measurement volume, and the effect of increased solid concentration on the flow patterns and liquid velocity distribution was analyzed. This approach provides a robust method and represents a crucial first step toward achieving a comprehensive 3D flow analysis of three-phase flows in AGSRs.

Keywords: Granular sludge bioreactors; Hydrodynamics; 3D particle tracking velocimetry; Refractive index matching

3.1. Introduction

The quest for sustainable and efficient energy sources has led to significant advancements in renewable energy technologies, among which anaerobic digestion stands out for its dual role in wastewater treatment and biogas production (Liu and Tay, 2004). Anaerobic digestion is distinguished by its utilization of anaerobic granule-based bioreactors, such as up-flow anaerobic sludge blanket (UASB), expanded granular sludge blanket (EGSB) and internal circulation (IC) reactors. These technologies are excellently fit for treating high-strength wastewaters with low solids content (van Lier et al., 2015). Arguably, they represent a pivotal advancement in the integration of engineering and biological processes, which place them at the forefront of sustainable wastewater management and energy production solutions (Maximova and Dahl, 2006, van Lier et al., 2015). These reactors have been successfully implemented globally for treating industrial wastewater in various sectors, such as agrochemicals, distilleries, pulp and paper industries (van Lier et al., 2015). The key to the well-functioning of these technologies is formation of dense, strong and active microbial granules (Liu and Tay, 2002).

Granule formation is significantly affected by operational factors such as wastewater composition, organic and volumetric loading rates, and presence of toxic compounds (Gagliano et al., 2020, Yu and Fang, 2001, Tiwari et al., 2006, Batstone and Keller, 2001). Among the complex array of parameters that affect granulation, hydrodynamic conditions have emerged as a critical area of study, underpinning the successful operation of such systems (Tay et al., 2001a). The hydrodynamic conditions within a bioreactor are characterized by mixing dynamics, flow patterns, shear forces, and relative motions between liquid, biogas, and sludge phase. These, in turn, determine the formation, structure, mass transfer, and metabolism of microbial aggregates (Liu and Tay, 2002), thereby influencing the overall efficiency of an anaerobic granular sludge reactor (AGSR) (Arcand et al., 1994).

Traditionally, bioreactor's hydrodynamic conditions have been mainly characterized by superficial liquid and gas velocity (Tay et al., 2001a, Arcand et al., 1994, Feng et al., 2016). Evidently, such metrics do not reliably represent the real conditions exerted on the sludge, due to spatial heterogeneity in the reactors and phenomena like channeling and the presence of dead zones (Zhang et al., 2012). Moreover, factors such as the reactor size, design, inlet configuration, and also the concentration of

sludge can lead to significantly different hydrodynamic conditions in the granular sludge section whilst having similar superficial liquid and gas velocities. This underscores the necessity of local liquid velocity measurements in the bioreactor (Wu et al., 2006, Pereboom and Vereijken, 1994, D' Bastiani et al., 2023).

In attempts to quantify the hydrodynamic conditions in the granule-based bioreactors, empirical models have been employed. For instance, Ren et al. (2009b) used an increasing-sized CSTRs (ISC) model to describe the flow behavior in the UASB reactor. These models are effective tools for studying factors such as hydraulic retention time (HRT), residence time distribution, and dead zones within the reactors. However, they are unable to capture the local flow characteristics (D' Bastiani et al., 2023). Ren et al. (2009b) developed an energy disspation-based model to quantitatively describe the global shear stress in a three-phase granular sludge reactor, which represents the dissipated energy per mean path of circulation and total interfacial areas of gas bubbles and granules. Kundu et al. (2014a) utilized modified Ergun semi-emprical model to estimate the hydrodynamic intensity in a hybrid AGSBR, based on the assumption that the granules create a packed bed in the reactor. While semi-empirical models might prove valuable in specific systems, their application to other systems necessitates validation through experimental fluid dynamics techniques.

Computational fluid dynamics (CFD) modeling is a valuable tool for visualizing and quantifying multiphase flow behavior within reactors. It has been employed to investigate mixing efficiency and flow patterns in UASB reactors (Ren et al., 2009b, Bastiani et al., 2021), as well as to study flow dynamics in EGSB reactors using coupled biokinetic models (Wang et al., 2009, 2010, Yang et al., 2015). Moreover, CFD has been applied in the design and optimization of both UASB and EGSB reactors (Hu et al., 2017, Hao and Shen, 2019, 2021). Most complex interactions among solid, liquid, and gas phases occur in the sludge blanket section, characterized by high solid concentration, significantly influencing granule properties and reactor performance. However, accurately modeling interfacial momentum transfer between phases, in this section, remains challenging (D' Bastiani et al., 2023). Reliable CFD results in this critical section depend on thorough experimental validation, which, to our knowledge, has not yet been addressed.

Various experimental methods in the field of chemical engineering have been employed to characterize flow conditions in high solid-concentration systems, such as fluidized beds and slurry flows, but thorough characterization has historically faced limitations due to the opacity of such multiphase flows. Techniques such as hot-wire anemometry (Stainback and Nagabushana, 1993) and laser doppler anemometry (LDA) (Mudde et al., 1997) have traditionally been used for single-point velocity measurements in single-phase flows. However, these methods are not suitable for multiphase environments (Seyfi et al., 2024). Methods for multiphase imaging include magnetic resonance imaging (MRI) (Penn et al., 2019), electrical capacitance tomography (ECT) (Azzi et al., 2020), and X-ray imaging (Graas et al., 2024). Additionally, radiation-based particle tracking methods—such as radioactive particle tracking (RPT) (Al-Juwaya et al., 2017) and positron emission particle tracking (PEPT) (Cole et al., 2022)—have been used to track the movement of individual particles within the flow. While each method offers specific advantages, they also come with notable limitations. For instance, MRI provides three-dimensional flow information but suffers from limited spatial and temporal resolution and involves high operational costs. X-ray and ECT tomography can resolve the spatial distribution of particles but are unable to measure their velocity. PEPT and RPT enable tracking of particle trajectories, yet they typically allow only one or a few tracer particles to be tracked at a time, which limits statistical reliability in flow characterization (Penn et al., 2019).

These limitations have positioned non-intrusive optical techniques as a suitable alternative for flow studies. Among them, particle image velocimetry (PIV) and particle tracking velocimetry (PTV) are capable of providing high spatiotemporal resolution data on local flow fields by analyzing the motion of microscale tracer particles seeded within the fluid (Seyfi et al., 2024). However, PIV and PTV represent different measurement perspectives: PIV adopts an Eulerian approach by analyzing groups of particles to resolve spatially-averaged velocity fields on a fixed grid, whereas PTV takes a Lagrangian approach by tracking individual particle trajectories over time, offering greater precision in capturing complex, non-uniform flows. Despite these advantages, traditional PTV struggles with high seeding densities due to particle overlap (Schanz et al., 2016). Shake-The-Box (STB), an advanced particle tracking algorithm, overcomes these challenges by enabling accurate 3D particle tracking even in densely seeded flows (Schanz et al., 2013b). For example,

Hofmann et al. (2022) employed this method to analyze the 3D flow behavior of a lab-scale stirred tank reactor (STR) by deriving the time-resolved particle trajectory information in a relatively densely seeded flow. The experimental data were then used to validate a numerical twin of the setup. The main limiting factor in applying these optical measurement techniques to multiphase flow systems, such as anaerobic granular sludge reactors, is the high concentration of solids (i.e., granules) in the flow. (Poelma, 2020). This is because the illumination light becomes increasingly obstructed and scattered by particles as the solid volume fraction increases.

Due to challenges imposed by high solids concentration in the AGSRs, the number of reported studies focusing on the experimental hydrodynamic characterization is relatively limited. 2D-PIV was the most commonly used technique for liquid local velocity measurement in these bioreactors. To address the issues associated with high solids concentrations, researchers employed 2D-PIV in two dimensional reactors with minimal thickness, facilitating optical access to desired flow domain (Wu et al., 2015, Zhang et al., 2011). Alternative strategies included conducting flow measurements at low solids concentrations (Jiang et al., 2016, 2014, Zima-Kulisiewicz et al., 2008) or focusing exclusively on the upper section of the granular sludge blanket, in UASB reactors, where the lower concentration of solid particles enables the feasibility of flow analysis (Bastiani et al., 2021). While these strategies have advanced the measurement of liquid flows within bioreactors, they still result in a partial understanding of flow dynamics. Using a 2D reactor provides an incomplete representation of flow behavior within AGSR systems, as wall interactions have a more pronounced effect on fluid and particle motion. Furthermore, these approaches fail to capture the true flow patterns and velocities that occur in reactors, overlooking the complexities introduced by higher solid volume fractions in full-scale systems. This highlights the necessity of developing methods that can accurately capture three-dimensional local velocities within high solid concentration operational AGSRs (D' Bastiani et al., 2023).

Refractive index matching (RIM) between the bulk liquid and the solid dispersed phase is one of the methods to tackle this problem when optical measurement techniques are applied (Wright et al., 2017). By matching the refractive indices of the model material and the carrier fluid, the entire medium becomes transparent. This transparency enables the detailed analysis of tracer particles behaviour within the

flow (Dijksman et al., 2012). Applying the combination of 2D-PIV or 2D-PTV with RIM has broadened the scope of optical flow measurement techniques to include a range of applications in packed bed and slurry mixture flows (Harshani et al., 2017, Nguyen et al., 2018, Agrawal et al., 2015, Schanz et al., 2016). However, the flow behaviour in real-world packed beds and concentrated slurry flows is inherently more complex and has a three-dimensional nature (Sabbagh et al., 2020).

In the present work, we are taking the first step to develop a method suitable for describing 3D liquid flow fields in expanded granular sludge beds at relevant solid phase fractions. To that end, we use spherical hydrogels to represent synthetic granules. The feasibility of measuring the three-dimensional velocity fields of a liquid-solid flow (in mesoscale) with varying volume fractions of the solid phase (up to 50%) is discussed. The method employs the cutting-edge particle tracking algorithm, Shake-the-Box (STB), developed in 2016 (Schanz et al., 2016), in conjunction with RIM techniques. After obtaining the Lagrangian and Eulerian velocity components across the entire measurement volume, the effects of increased volume fraction of the solid phase on the flow pattern, liquid velocity distribution, and the axial and radial hydrodynamic dispersion coefficients were discussed. To the best of the authors' knowledge, this is the first time that PTV has been successfully applied for 3D velocity field measurement in medium with such high solid concentrations. These findings open the door for further development of multiphase flow measurement techniques to unravel flow dynamics and substrate transport in AGSRs and deepen our understanding of the mechanisms by which reactor hydrodynamics influence granule properties and overall reactor performance. This method also supports the calibration and validation of multiphase computational fluid dynamics (CFD) models for granular-based bioreactors, contributing to improved reactor design and optimization of operational parameters.

3.2. Material and Methods

3.2.1. Flow system and experimental conditions

The experimental facility consisted of flow loop and test section as shown in Figure 3.1. A lab-scale EGSB reactor, constructed from glass, was utilized for the test section. Transparent material was used to build the reactor to facilitate the internal flow visualisation and enable the use of the PTV. The reactor had a diameter of 10 cm

and a height of 1.7 meters, dimensions (diameter to height ratio) typical of lab-scale reactors (Gao et al., 2024a) and suitable for flow measurements at the meso-scale (Jiang et al., 2014). To prevent refraction effects at the curved wall, a rectangular vessel, also made of glass, was built around the test section, covering a height of 90 centimetres along the height of the reactor. The space between the reactor and vessel was filled with demi-water. At the base of the reactor, a liquid distributor section was installed, comprising a 10 cm calming section filled with 1 cm glass beads, followed by a perforate plate with 4 mm diameter holes. This configuration was implemented to achieve uniform liquid distribution across the cross-section of the reactor inlet.

The main elements of the flow loop (Figure 3.1) included a 50-liter cylindrical recirculation tank, a gear pump, manufactured by Tuthill, with an associated variable frequency drive (VFD) and a Coriolis mass flow meter with an integrated PID controller. This setup ensured a flow without pulsations, maintaining accurate liquid flow. In this study, the liquid flow rate was maintained at 2 L/min, corresponding to a superficial velocity of 15 m/h based on the reactor's cross-sectional area. This velocity was selected to meet two operational purposes: first, to ensure complete fluidization of the solid particles, and second, to fall within the typical upflow velocity range of EGSB reactors. The flow rate was monitored by the mass flow meter, and consequently, the pump speed was adjusted by the PID controller to maintain a stable flow rate in response to potential pressure fluctuations in the system. Subsequently, the liquid proceeded to the calming section before entering the reactor's visualization section. It then exited from the reactor's top, returning to the recirculation tank.

Polyacrylamide hydrogel beads (Soil Moist™, JRM Chemical, Inc., Cleveland, Ohio) were used as a solid phase to simulate the anaerobic granules in the reactor. These beads are composed of 80-99% water and have a refractive index nearly identical to water, making them well-suited for optical velocity measurements (Dijksman et al., 2017). The hydrogel beads utilized in this study ranged in size from 1 to 2 mm with a density of approximately 1009 kg/m^3. Different volume fractions of the solid phase were tested, including 0%, 10%, 30%, and 50%, to replicate varying solid loadings observed at different heights in EGSB reactors.

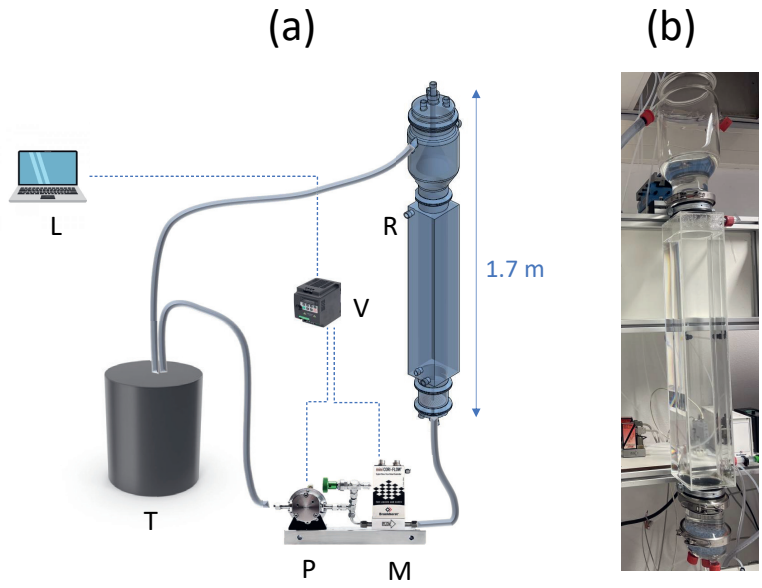


Figure 3.1: (a) Schematic of experimental setup, L: laptop, M: mass flow meter, P: gear pump, R: Reactor (test section), T: Recirculation tank. V: Variable frequency drive. (b) Reactor setup (test section).

3.2.2. Refractive index matching

The index of refraction of hydrogel spheres used in this study was slightly higher than that of water. To perform volumetric liquid velocity measurements within the dense packing of hydrogels, refractive index of the fluid was fine tuned to match with that of hydrogel spheres to image through as many hydrogel layers as possible. For this purpose, polyvinylpyrrolidone (PVP) with the molecular weight of 360,000 was used. It was reported that PVP 360,000 does not permeate the hydrogel network within a timeframe of several weeks (Dijksman et al., 2017).

To achieve refractive index matching (RIM), PVP solutions with varying concentrations, ranging from 0 to 3%, were prepared. An object was placed in the center of the beakers as an imaging reference. For successful RIM, the solid particles should appear invisible, and the image of the object should be clear and undistorted. A refractive index mismatch of up to 0.003 between the liquid and solid is generally considered the maximum tolerable limit to avoid significant optical distortion (Dijksman et al., 2012). This threshold was initially assessed

by observing the clarity of the reference object immersed in the medium, as shown in Figure 3.2, which displays how light refraction varied with different solutions. The medium appeared completely transparent, and the object was fully visible in Fig. 2b, indicating that the 0.5% PVP solution effectively achieved RIM. This solution was used as the working fluid in the experiment. Further assessment of the RIM accuracy was carried out through the efficiency of particle tracking in the medium volume.

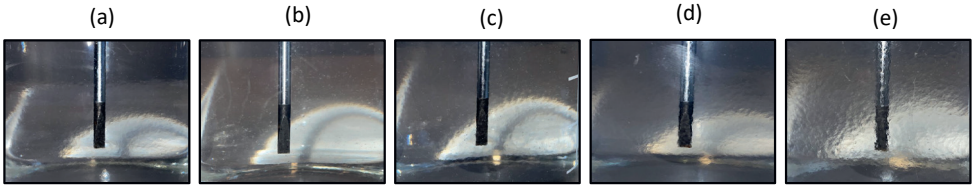


Figure 3.2: The refractive index matching combination of fluid and hydrogel beads (model granular sludge) used in this study. Shown are hydrogel beads in (a) water, (b) 0.5% PVP solution, (c) 1% PVP solution, (d) 1.5% PVP solution, (e) 3% PVP solution. As the refractive index of the glass beads and the fluid are equal in (b), the image of the object in the fluid remains undistorted. The 0.5% PVP solution was used in the experiments.

3.2.3. Experimental setup for 3D-particle tracking velocimetry (3D-PTV)

3.2.3.1. Imaging and illumination setup

The velocity field was captured using 3D-PTV techniques. As illustrated in Figure 3.3, the imaging system comprised a high-intensity blue LED flashlight ($100 \times 300\,mm^2$), and an integrated multi-camera system (MiniShaker, LaVision GmbH) with 4 digital cameras. The four high-speed cameras 1984×1264 pixels with a 10 bit dynamic range, and a maximum acquisition rate of 121 Hz at full resolution were used to record particle images from four different viewing angles in the test section. Each camera was equipped with a Tamron lens with focal length of 12 mm. In front of each lens, a long-pass filter at 540 nm was mounted to selectively capture light from fluorescent seeding particles. These particles emit light when illuminated, making them easy to distinguish from the surrounding medium and enabling the filtering of background noise from the light source, resulting in the acquisition of high-quality images of seeding particle motion.

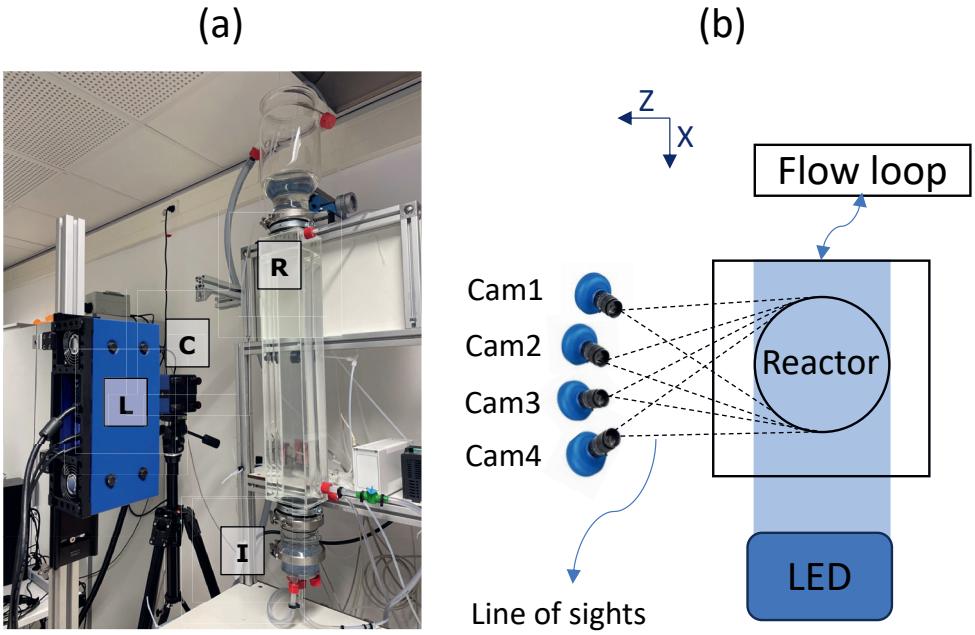


Figure 3.3: (a) Imaging and experimental setup consisting of C: integrated four-camera system (MiniShaker), I: Inlet configuration, L: volumetric LED, R: reactor. (b) Schematic sketch of the experimental setup (the top-view).

3.2.3.2. Calibration

Proper calibration is crucial for ensuring the accuracy of 3D particle tracking velocimetry (PTV) measurements. This step relates pixel positions on the camera sensor to real-world coordinates in the measurement volume (Schanz et al., 2013a). To achieve this, the reactor was filled with 0.5% PVP solution, and a 3D calibration plate ($5 \times 5\,\mathrm{cm}^2$, two-level plate with two patterns on each level) was immersed inside the target volume. Subsequently, the calibration plate was positioned at three predetermined distances from the cameras and its images were recorded. The precise positioning of the calibration plate was done using a custom-made 3D micro traverse system. The captured images were processed in DaVis 10 software (LaVison GmbH). A third-order polynomial function was applied to map the marks on the 3D calibration plate to the 2D camera sensor, with a fitting error of approximately 0.06 pixels (10 μm). The accuracy of mapping model was further improved by conducting the volume-self-calibration using the pre-processed images of tracer particles in the test section, yielding a fitting error of 0.019 pixels (3 μm). Finally, in the last step of

calibration, the optical transfer function (OTF) (Schanz et al., 2013a) was applied to the same image set to define the local particle patterns in different sub-volumes. This is an essential step for STB analysis to optimize the 3D position and intensity of particles.

3.2.3.3. Data acquisition and processing

The measurements were conducted for flows with solid-phase volume fractions ranging from 0% to 50%. For the two-phase flows, between 17,000 and 18,000 fluorescent particles were homogeneously dispersed in the reactor, resulting in a seeding density of approximately 0.02 ppp (particles per pixel). This density was selected to provide sufficient spatial coverage for resolving the flow field while minimizing ghost particle artifacts (Schanz et al., 2016, Hofmann et al., 2022). For the single-phase flow, approximately 14,000 particles were used, which was sufficient given its simpler flow characteristics.

Particle images of each case were recorded from four different views at an imaging rate of 40 Hz and exposure time of 338 μs. This imaging rate was chosen to match the characteristic timescale of the flow, as the time interval between two successive frames should be chosen so that the fastest particles within the measurement volume can be accurately tracked (limiting their displacement to, e.g., 10–20 pixels). (Schanz et al., 2021) In total, 1,000 images of particles, corresponding to 25 seconds of flow time, were captured from each view. All data sets underwent the same image pre-processing to reduce the background signal and improve the particle's shape. The pre-processing steps are as follows: a geometric masking to eliminate noise from outside the measurement volume, a history-minimum-subtraction filter to remove the stationary background noise, and a sliding minimum subtraction filter to eliminate the dynamic background noises by subtracting the local minimum intensity from each pixel. For a step-by-step visual representation, see Figure S.3.1.

In the next step, the pre-processed images were fed to the STB particle tracking algorithm to calculate the trajectory and velocity data of each tracer particle in the measurement volume. Real-time particle tracking statistics for each case are presented in Figure S.3.2. STB, as a novel time-resolved Lagrangian particle tracking approach, was introduced first in 2013 (Schanz et al., 2013b). This method enables a fast and precise tracking within a three dimensional space domain at seeding

densities as high as 0.2 ppp (Schröder and Schanz, 2023). It employs an advanced prediction/correction scheme by combining image matching and triangulation techniques (Wieneke, 2013). The specified STB operating parameters in this study were particle detection intensity threshold of 20 counts and an allowed triangulation error of 2 voxels. (Schanz et al., 2016) reported that, depending on particle image quality and seeding density, a low triangulation error range of 0.5 to 1.5 voxels can be used. A value of 2 voxels was chosen due to the reactor's circular geometry and the slight refractive index mismatch between liquid and solid phase, to balance tracking accuracy and yield. Other STB parameters are listed in Table 3.1.

Table 3.1: STB parameters.

Parameter	**Value**
Reconstructed volume	$574 \times 1619 \times 602$ voxels
Threshold for 2D particle detection	20 counts
Allowed triangulation error	2 voxels
Shaking	
Adding particles (outer loop)	4 iterations
Refine particle position and intensity (inner loop)	4 iterations
Shake particle position by	0.1 voxel
Remove particles if closer than	1 voxel
Remove weak particles if intensity <	0.1 of avg. int
Particle image shape and intensity	
Make OTF smaller	0.8 times
Residuum computation - increase particle intensity	1.5 times
Tracking	
Minimum track length	4 time steps
Max. abs. change in particle shift	5.00 voxel
Max. rel. change in particle shift	20%

Particle track data provide scattered information about the velocity and acceleration of fluid at various points within the measurement volume (Schanz et al., 2021). To obtain the time-averaged 3D velocity vector field, the Lagrangian particle track data were converted to Eulerian grids using binning. The choice of grid size is a trade-off

between achieving higher resolution of sharp gradients and ensuring their statistical reliability (Schröder et al., 2020). Therefore, a grid sensitivity test was performed with four different grid sizes (see Figures S.3.3 and S.3.4). Having evaluated the grid test results, a sub-volume size of 40 voxels with an overlap of 75%, resulting in a resolution of 10 voxels (1.85 mm) in each direction, was chosen for the visualization of the velocity field and further post-processing of the flow data.

3.2.4. Calculation of hydrodynamic dispersion coefficients

For calculating the axial and radial hydrodynamic dispersion coefficients, the displacement variance method (Voronov et al., 2011) was applied to the time-resolved positions of Lagrangian particle tracks. For each particle, the squared displacement over a time interval Δt was calculated in the axial (y) and radial (x–z) directions. The mean squared displacement (MSD) was then obtained by averaging these squared displacements over all particles at each time interval within the measurement volume. The axial mean squared displacement was defined as

$$\mathrm{MSD}_{\mathrm{axial}}(\Delta t) = \frac{1}{N}\sum_{n=1}^{N}[y_n(t+\Delta t) - y_n(t)]^2 \tag{3.1}$$

Similarly, the radial MSD was calculated as

$$\mathrm{MSD}_{\mathrm{radial}}(\Delta t) = \frac{1}{N}\sum_{n=1}^{N}\left([x_n(t+\Delta t) - x_n(t)]^2 + [z_n(t+\Delta t) - z_n(t)]^2\right) \tag{3.2}$$

where N is the total number of displacement pairs contributing at interval Δt; x_n, y_n, z_n denote the spatial coordinates of particle n at time t. The dispersion coefficient was determined from the slope of the MSD versus time using the equation below (Einstein, 1905):

$$D = \frac{\mathrm{MSD}(\Delta t)}{2\Delta t} \tag{3.3}$$

where D is the dispersion coefficient. For each experimental condition, the MSD was calculated over time intervals up to 2 seconds, with a time step of 0.025 seconds (corresponding to the inverse of the imaging frame rate), and the dispersion coefficient was then determined.

3.3. Results and Discussion

3.3.1. Index Matching and 3D Particle Tracking

The flow dynamics within a 30 cm section of the reactor with varying hydrogel concentrations were studied by tracking fluorescent particles, maintaining a seeding density of 0.02 particles per pixel in all two-phase flow experiments. Figure 3.4 displays the 3D particle trajectories over 100 time steps (2 seconds of flow time), color-coded by the vertical velocity component. The number of particles identified and tracked in the measurements was approximately 14,000 for the single-phase flow and between 15,500 and 17,000 for the two-phase flows. The average tracking efficiency was 99.4% in single-phase flow, 97.2% with 10% hydrogel, 95.8% with 30% hydrogel, and 88.8% with 50% hydrogel (see Figure S.3.2). The tracking efficiency is defined as the ratio of tracked particles to the total number of tracer particles in the measurement volume in each time step.

The slight decrease in tracking efficiency with higher hydrogel concentrations can be attributed to minor local mismatches in the refractive index due to the inherent heterogeneity in the refractive index of polydispersed hydrogels (Dijksman et al., 2012). These mismatches cause light scattering, which hinders particle detection as the volume fraction of the solid phase increases.

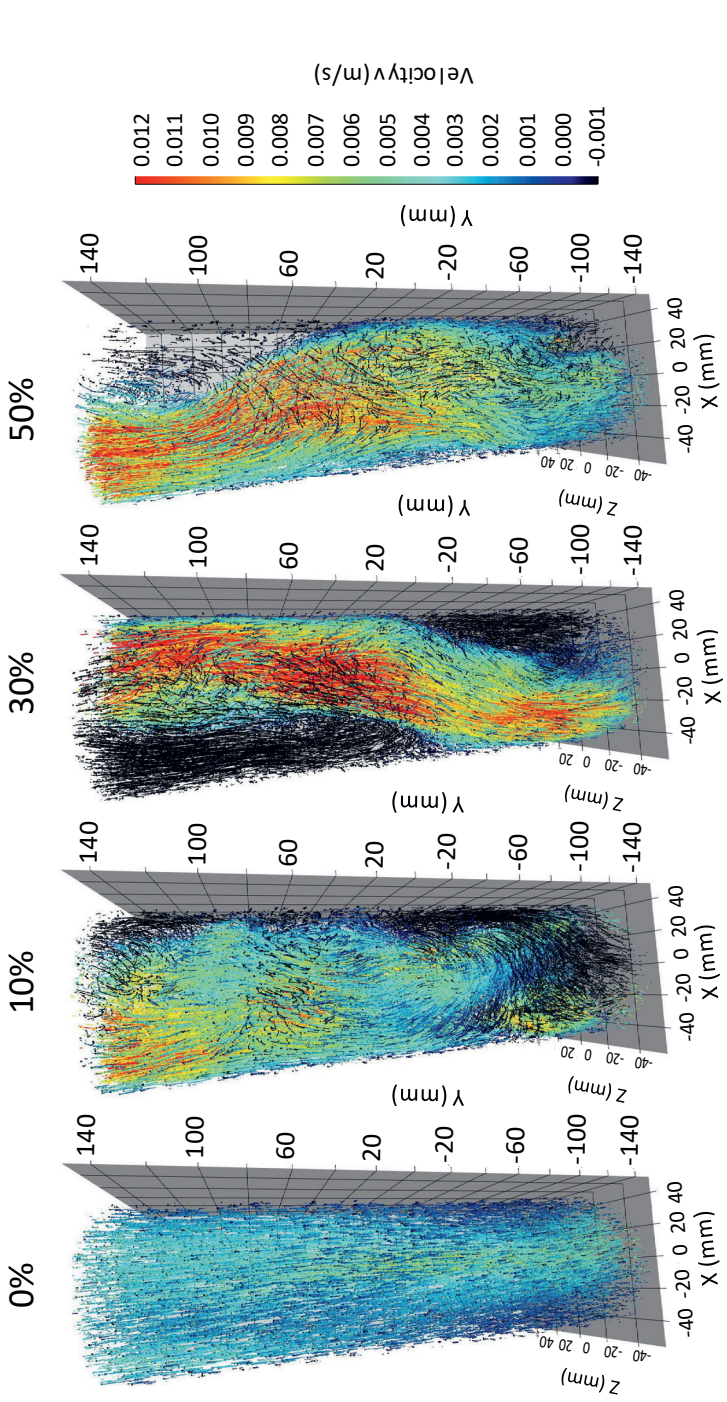


Figure 3.4: Instantaneous snapshot of reconstructed particle tracks visualized with a track length of 100 time-steps across various hydrogel volume fractions.

The 3D distribution of tracked particles is crucial for volumetric flow measurement. High solid concentrations can hinder light from reaching deeper regions of the reactor due to light distortion from multiple interface layers of liquid and hydrogels. Each interface introduces minor refractive index mismatches, that build up across hydorgel layers, depending on the effectiveness of the refractive index matching (RIM) (Wiederseiner et al., 2011). The distribution of tracked particles was analyzed for both hydrogels (synthetic granules) and real anaerobic granules by examining the projection of reconstructed particles on a XZ plane (Figure 3.5). In the cases that anaerobic granules were used, particle tracking was heavily obstructed in the deeper parts of the reactor, even with 2% anaerobic granules (Figure 3.5b). With 10% anaerobic granules, the tracer particles in most regions were not tracked (Figure 3.5c), showing considerable challenges posed by such low solid concentrations.

Due to these difficulties, prior studies primarily focused on flow measurement at very low granule concentrations (Zima-Kulisiewicz et al., 2008, Jiang et al., 2016) or simply within the upper section of the sludge bed (Bastiani et al., 2021). Another approach has been the use of flat, thin reactors, which help minimize light obstruction caused by overlapping particles (Zhang et al., 2011, Jiang et al., 2014). However, this approach oversimplifies the flow dynamics and multiphase interactions. The wall effect dominates the flow pattern, failing to capture the complex 3D behavior of the multiphase flow, which leads to less accurate results for application to full-scale reactors.

Using transparent hydrogels as the solid particles resulted in well-distributed tracking of particles across the reactor's cross-sectional area. Even at high concentrations (50% hydrogel), particles remained detectable, though with some loss in the back of the reactor due to light distortion from multiple layers of hydrogel beads. These observations were quantified by calculating the normalized average number of tracks across different Z planes within the reactor (Figure 3.5g). This analysis allows us to better evaluate the accuracy of RIM as well as the effect of multiple layers of hydrogel beads on the efficiency of particle tracking, especially in regions far from the camera.

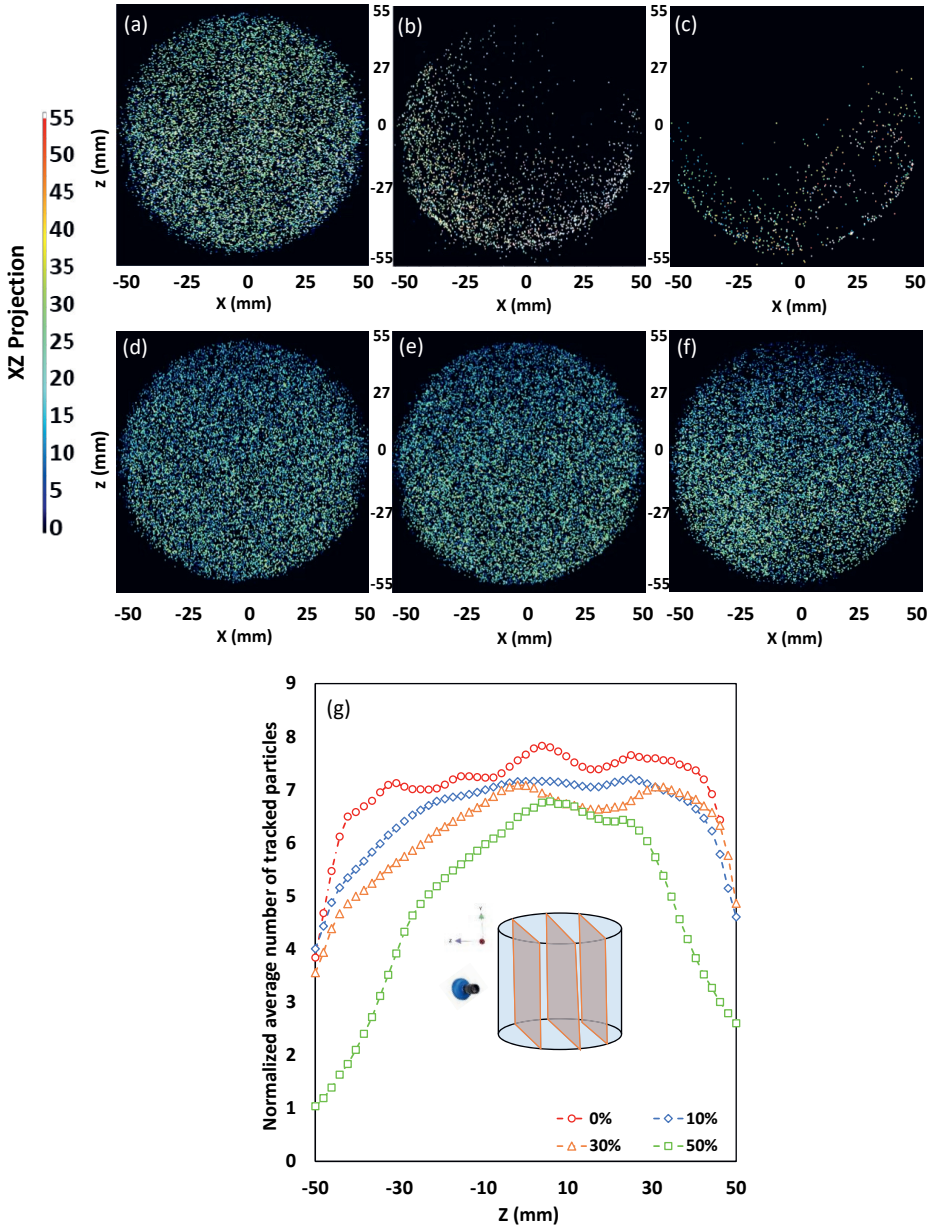


Figure 3.5: Projection of tracked particles at t=5 seconds on XZ plane (top view): (a) 0% solid (single-phase flow), (b) 2% anaerobic granules, (c) 10% anaerobic granules, (d) 10% hydrogels, (e) 30% hydrogels, (f) 50% hydrogels, (g) normalized average number of particle tracks in different z planes.

It was observed that increasing the solid volume fraction (VOF) results in a decrease in particle count in each Z plane, with the most significant drop occurring at 50% hydrogel VOF. Additionally, the parabolic shape of the curves is due to the lower particle count at the sides of the reactor for all cases, which can be attributed to the reactor's cylindrical shape. This shape reduces the volume available for particles at the edges, resulting in fewer particles being present and thus fewer being tracked in these volumes.

The use of transparent hydrogels ensures better light penetration and minimizes obstruction, making it feasible to track particles accurately in dense solid-liquid flows. It is important to note that the hydrogels (1009 kg/m^3) used in this study were at the lower end of the density spectrum reported for real anaerobic granules, which is reported to be in the range of 1000–1050 kg/m^3. The density of granules can vary depending on the type of wastewater and the degree of biogas accumulation within the granules, which can significantly reduce their apparent density before this biogas is released (van Lier et al., 2015). Future work will focus on matching the density of the hydrogels to that of the granules across a broader spectrum and conducting velocity measurements in a three-phase flow by introducing the gas phase. This will ensure more accurate and comprehensive flow dynamics analysis in anaerobic granular sludge reactors (AGSRs). These developments will facilitate better flow measurement methods and support the optimization of anaerobic granule-based bioreactors.

3.3.2. Flow pattern visualization

Successful particle tracking in dense solid volume fractions enables studying the liquid phase behavior across various solid VOFs. The analysis of velocity vector maps and velocity iso-surfaces, as shown in Figure 3.6, demonstrates that variations in the volume fraction of hydrogels significantly influence the flow dynamics within the reactor. At 0% hydrogel, the flow approximately resembles that of a vertical pipe under laminar conditions, with the highest velocity at the center and decreasing toward the reactor wall. However, introduction of 10% hydrogel intensifies the upward flow velocity magnitude and the negative or downward velocity regions appear which indicates the presence of a big vortex in the reactor. As the hydrogel concentration increases to 30%, the velocity profile further diversifies, displaying distinct low- and high-velocity zones. This change in flow pattern indicates that the

upward liquid flow is disrupted by the clusters of solid particles in low-velocity zones. These clusters act as barriers, diverting the liquid into narrower pathways, which causes a localized increase in flow velocity within these channels. At 50% hydrogel, the resistance to flow within the reactor increases by the presence of densely packed beads at certain locations. This leads to heightened velocity gradients in the reactor, particularly within the sharply defined regions of low and high velocities at the top of the reactor.

3.3.3. Quantitative flow analysis

3.3.3.1. Eulerian velocity data analysis

The quantitative analysis of the vertical velocity component distribution demonstrates profound changes in fluid dynamics across varying hydrogel volume fractions (Figure 3.7). Initially, in the absence of hydrogel, the flow is exclusively upward, characterized by a narrow velocity distribution peaking at 0.004 m/s, closely aligned with the superficial velocity in the reactor. This undisturbed flow pattern features a maximum velocity within the core reaching 0.008 m/s. The absence of negative velocity values indicates the lack of vertical recirculation and minimal mixing in the reactor. Upon introducing a 10% solid concentration, the probability distribution function (PDF) expands to include both positive and negative velocities, peaking at 0.008 m/s. This broadening indicates that even a low concentration of solid particles can enhance the flow variability within the reactor, resulting in a circulation pattern marked by the presence of both negative and positive velocities. With 30% solid, the PDF widens even further and develops into a bimodal distribution curve. This bimodal curve was also observed in the PDF of velocity distribution in a packed bed containing spherical particles (Thaker et al., 2019). When these data are compared to the flow visualizations in Figure 3.6, it shows that solid particle clustering leads to the formation of distinct volumes with varying flow resistances. This results in flow channels with high velocity alongside densely clustered volumes with reduced velocities, appearing as two prominent peaks in the velocity distribution curve. At a 50% solid concentration, the velocity distribution significantly shifts toward higher velocities. This indicates denser packing of beads and narrower channels for the liquid, resulting in a significant acceleration of the flow. Increasing the solid concentration causes the PDF curve to broaden, leading to higher velocity gradients and more intense hydrodynamic shear rates within the reactor.

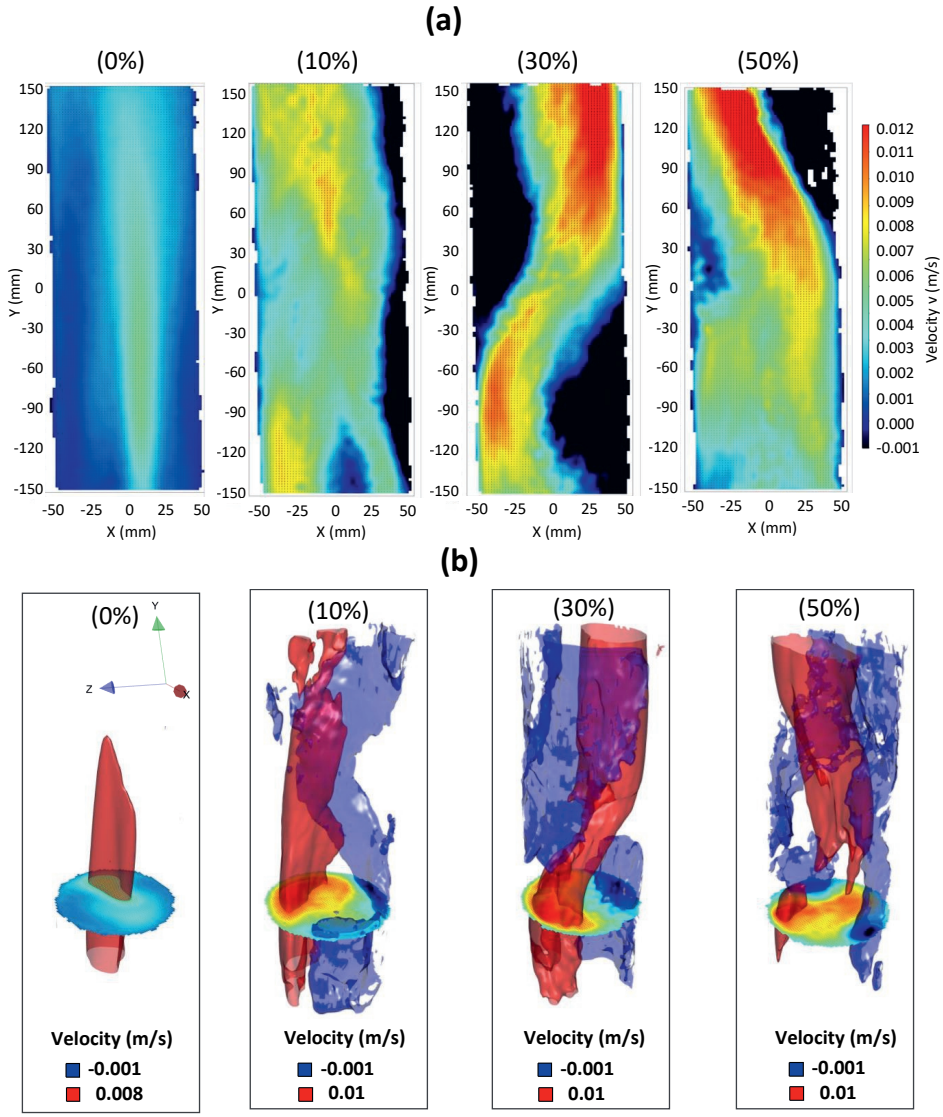


Figure 3.6: (a) 2D representation of time-averaged vertical velocity component of the liquid in different hydrogel volume fractions at the center z-plane. (b) 3D representation of time-averaged liquid vertical velocity at varying hydrogel volume fractions visualized as iso-surfaces.

These findings highlight the significance of flow measurement in AGSRs with high solid concentrations, as the flow dynamics in different regions of these reactors can be drastically affected by the volume fraction of granules, resulting in significantly different shear forces acting on the granules.

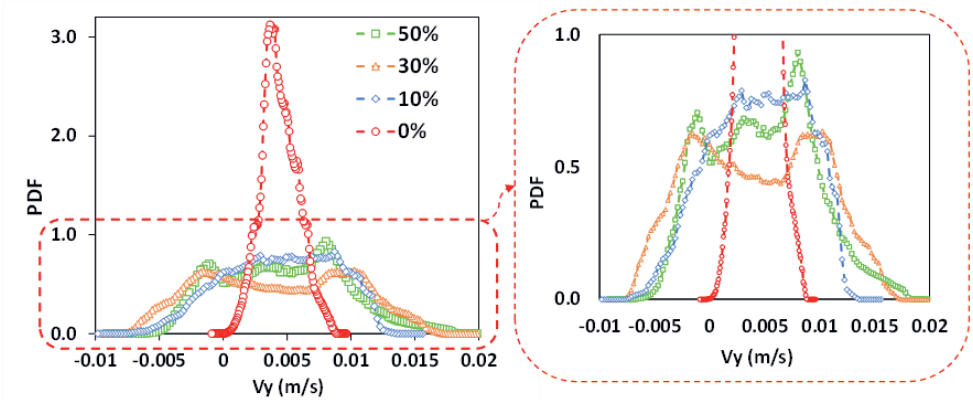


Figure 3.7: Probability density function of vertical component of velocity in the volume of the reactor at different hydrogel volume fractions.

Figure 3.8 displays the velocity profiles of the vertical component of velocity along three reference lines over the height of the reactor in the central z-plane for various cases. It shows that as the solid VOF increases, the velocity gradients become steeper, indicating intensified flow dynamics. The 50% solid case along Line 1 (y=+15 cm) shows the most pronounced velocity variation, where the liquid velocity shifts abruptly from negative values to a peak of approximately 0.018 m/s over a narrow region, exceeding the superficial velocity of 0.004 m/s in single-phase flow by more than four times (see Figure S.3.5 for the single-phase flow velocity profile). The velocity profile for Line 3 (y=-15 cm) in the 50% case shows values similar to those observed in single-phase flow, indicating a lower concentration of solids in that region. It is important to highlight that the the flow under investigation is an unsteady flow, and the velocity values presented are time-averaged. The data are considered a quasi-steady state representation, given that the flow exhibited only slow variations over the measurement time. Due to the unsteady nature of the flow, the VOF and consequently the vertical component of velocity were changing across different regions over time.

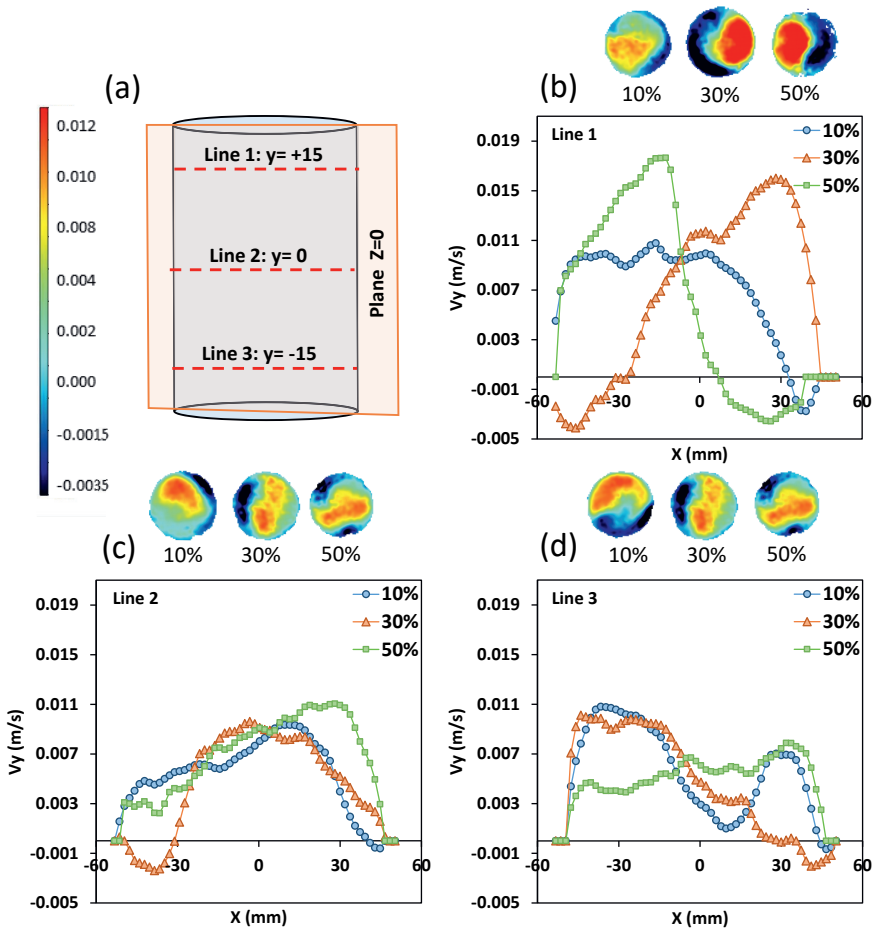


Figure 3.8: Velocity profiles of the vertical velocity component (Vy) along three reference lines in the central z-plane ($z = 0$) for different solid volume fractions, with corresponding velocity maps at xz cross sections at the heights of each reference line. (a) Schematic showing the positions of Line 1 ($y = +15$ mm), Line 2 ($y = 0$ mm), and Line 3 ($y = -15$ mm) within the measurement volume. (b) Vy profiles at Line 1 and xz velocity maps; (c) Vy profiles at Line 2 and xz velocity maps; (d) Vy profiles at Line 3 and xz velocity maps.

3.3.3.2. Hydrodynamic dispersion coefficients

Hydrodynamic dispersion describes the spreading of tracers or substrates within a moving fluid, arising from spatial and temporal variations in the velocity field. The dispersion coefficient quantifies this mixing efficiency by capturing the displacement behaviour of particles caused by velocity heterogeneity, which is particularly important in multiphase flow systems. In Figure 3.9a, b, the axial and radial mean

squared displacement (MSD) of Lagrangian tracer particles are plotted against time. The slope of the linear section of each curve was used to calculate the corresponding dispersion coefficients. Figure 3.9c illustrates how increasing the solid fraction influences both axial and radial dispersion of particles. In single-phase flow (0% solids), the radial dispersion coefficient is nearly zero due to uniform upward velocity and minimal cross-flow motion. As the solid volume fraction increases to 10–30%, the flow field becomes highly heterogeneous with the formation of vortices, recirculation zones, and channeling, which enhance both axial and radial dispersion coefficients and improve overall mixing. At very high solids (50%), these values decrease slightly due to the obstruction of flow by the densely packed solid phase, as well as the formation of stagnant zones and narrower channels, which limit velocity variability and reduce overall mixing potential. This trend is also evident in the axial-to-radial MSD ratios, which show that at relatively low solid volume fractions (10–30%), overall mixing and transport improve in both axial and radial directions, but with further increases, axial flow channeling becomes dominant over radial transport, as the ratio decreases from 69.13 at 0% solids to 5.46 and 6.34 at 10% and 30%, before rising again to 12.36 at 50%. Overall, quantifying the hydrodynamic dispersion coefficient provides critical insight into mixing performance and substrate transport in anaerobic granular sludge reactors, supporting reactor design and operation that maximize contact between wastewater and biomass to improve treatment efficiency.

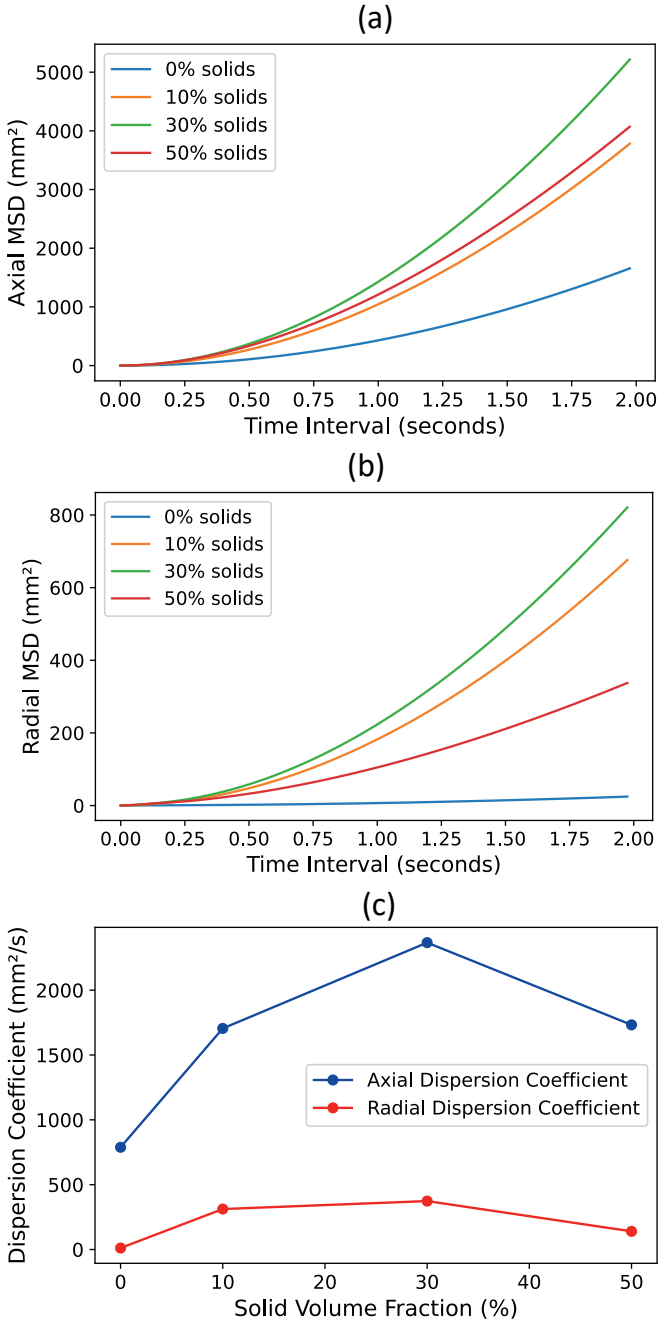


Figure 3.9: (a) Axial MSD and (b) radial MSD of Lagrangian particle tracks as functions of time interval, and (c) axial and radial dispersion coefficients at varying solid volume fractions.

3.4. Conclusions

This study demonstrated the feasibility of combining refractive index matching (RIM) with particle tracking velocimetry (PTV) techniques to investigate 3D flow dynamics in densely packed multiphase flow reactors, such as AGSRs. To our knowledge, it represents the first volumetric flow measurement in fluidized reactors with high solid concentrations using the RIM-PTV method. This approach provides a robust solution for characterizing local hydrodynamic conditions in granule-based reactors, enabling comprehensive flow analysis throughout the entire reactor at varying granule concentrations. It marks a significant advancement over previous methods, which were limited to low solid volume fractions or restricted to the upper sections of the sludge bed. Our upcoming research will aim to match the density of the hydrogels to the granules and perform 3D flow characterization in three-phase flow by incorporating the gas phase. This development paves the way for enhanced methodologies in flow measurement and contributes to the optimization of anaerobic and other granule-based bioreactors.

Supplementary Information

S.3.1. Image preprocessing steps

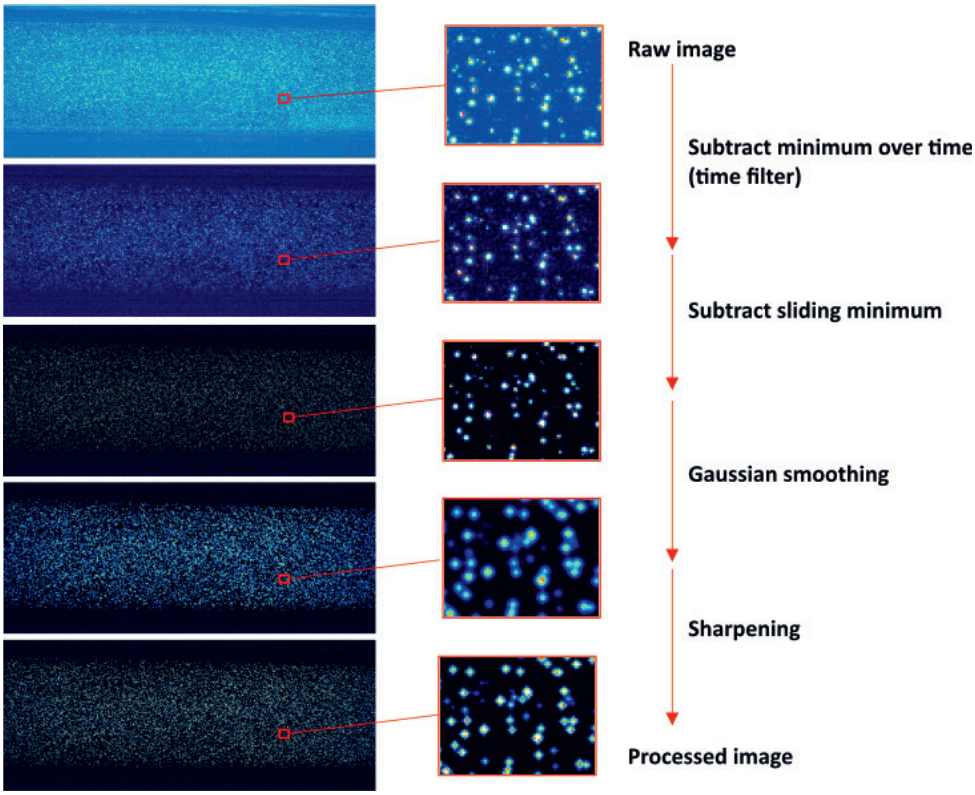


Figure S.3.1: The sequence of the main steps undertaken in the image pre-processing.

S.3.2. Particle tracking statistics

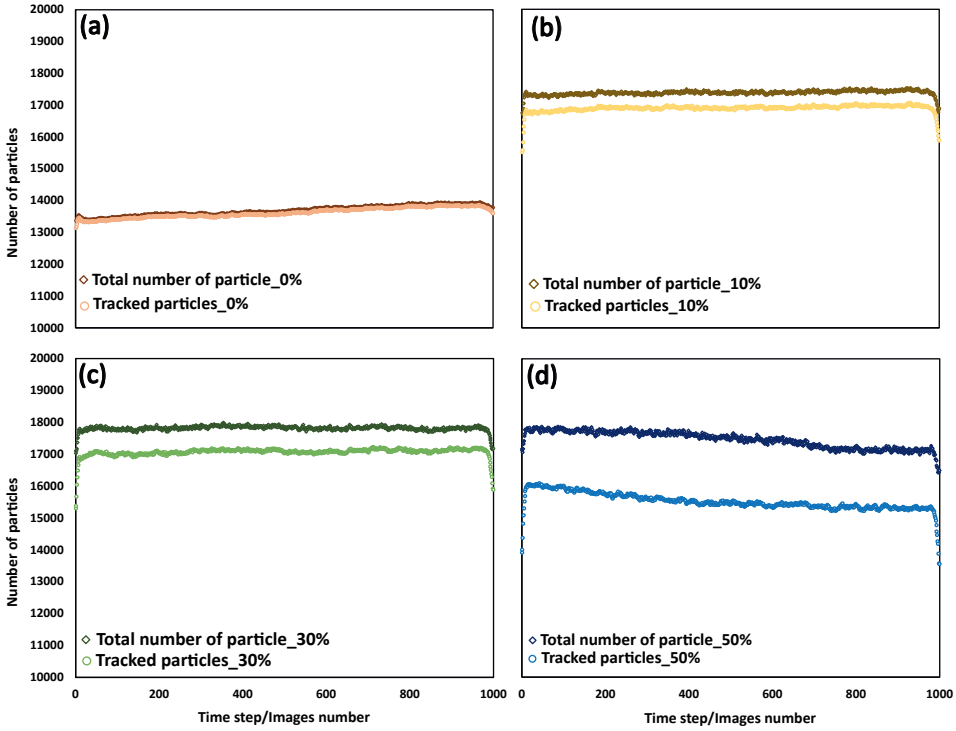


Figure S.3.2: Real-time particle tracking statistics at different solid volume fractions: (a) 0% (single-phase flow), (b) 10%, (c) 30%, and (d) 50%.

S.3.3. Bin size sensitivity analysis

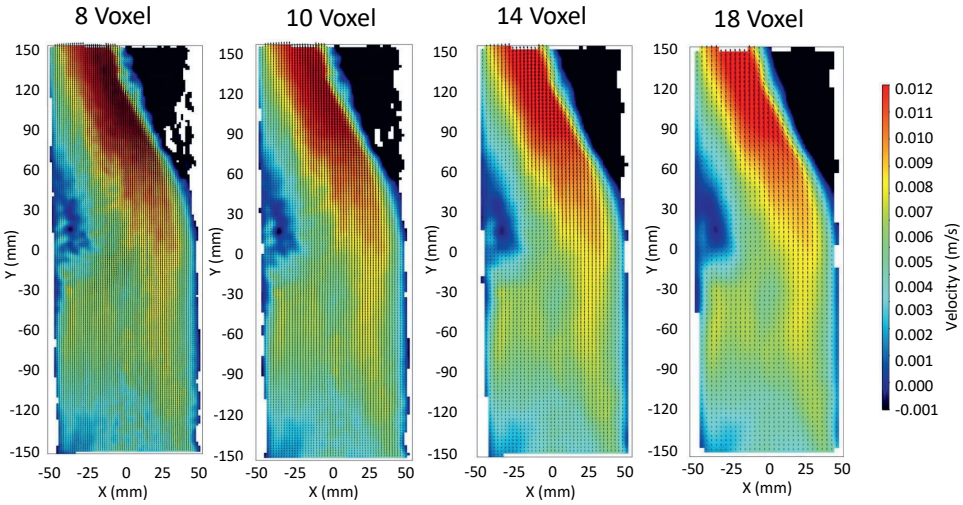


Figure S.3.3: Bin size sensitivity analysis: effect of bin size on the velocity vector map.

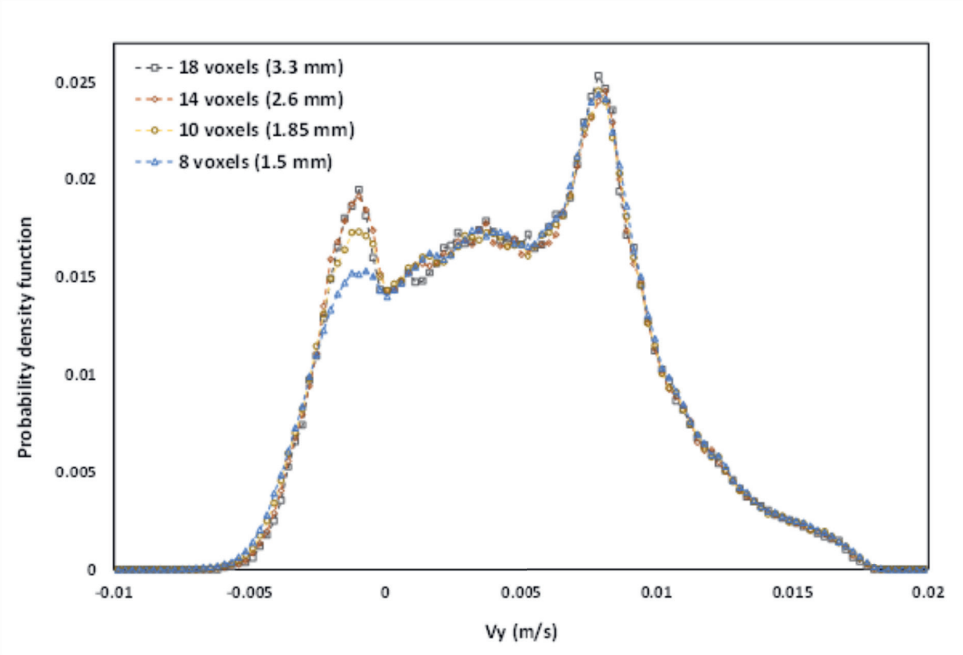


Figure S.3.4: Bin size sensitivity analysis: effect of bin size on the PDF of the liquid vertical component of velocity.

S.3.4. Single-phase flow velocity profile

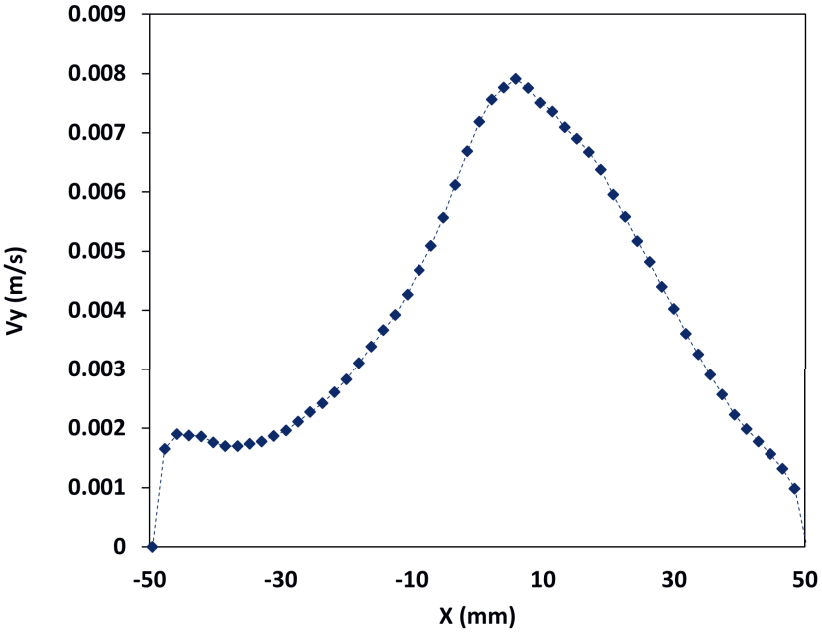


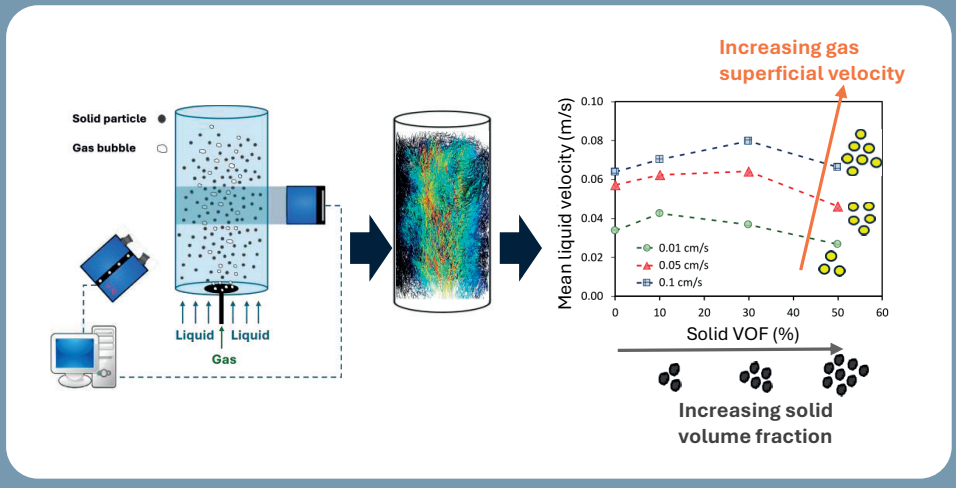
Figure S.3.5: Velocity profile of the vertical component of velocity along the $y = 0$ reference line at the central z-plane for the single-phase flow case.

Chapter 4

4

Chapter 4

3D Hydrodynamic Characterization in Anaerobic Granular Sludge Reactors. Part 2: Effect of Gas Superficial Velocity and Solid Volume Fraction



A modified version of this chapter has been submitted as:

Eslami, H., Bruning, H., Rijnaarts, H.H.M., and Sudmalis, D. 3D Hydrodynamic Characterization in Anaerobic Granular Sludge Reactors. Part 2: Effect of Gas Superficial Velocity and Solid Volume Fraction.

Abstract

Hydrodynamics play a decisive role in the treatment efficiency of anaerobic granular sludge reactors (AGSRs). In these three-phase reactors, the high solids concentration and restricted optical access have limited detailed experimental characterization of local flow behavior. In this study, the hydrodynamics of AGSRs were mimicked using transparent hydrogel beads as synthetic granules, and a combination of refractive index matching (RIM) and three-dimensional particle tracking velocimetry (3D-PTV) was employed to enable volumetric flow measurements. The influence of gas superficial velocity (GSV, 0.01-0.1 cm/s)) and solid volume fraction (VOF, 0-50%) on liquid mean velocity and instantaneous velocity components were systematically investigated. Moreover, mixing performance was characterized by quantifying axial and radial dispersion coefficients. Increasing GSV resulted in a monotonic increase in mean liquid velocity across all solid VOFs, with the most pronounced increase occurring at 30% VOF. Increasing solid VOF exhibited a dual effect on mean liquid velocity: velocity increased up to a critical solid VOF, beyond which it declined. This critical solid VOF shifted toward higher values by increasing GSV. For each tested operating condition, axial dispersion coefficients (4.1×10^{-5} to $2.36 \times 10^{-3}\,m^2/s$) were higher than radial dispersion coefficients (8.1×10^{-6} to $2.28 \times 10^{-4}\,m^2/s$). Increasing GSV enhanced both axial and radial dispersion coefficients for all solid VOFs. At a constant GSV, the effect of increasing solid VOF on the dispersion coefficients varied with the applied GSV and differed between the axial and radial directions. These results provide deeper insight into hydrodynamic mechanisms in AGSRs and establish a basis for quantifying granule-scale shear forces and mass transfer which govern the granule properties. The developed flow measurement approach also enables numerical model validation, supporting improved design, and process optimization of AGSRs.

Keywords: Anaerobic granular sludge; Hydrodynamics; Three-phase flow; 3D particle tracking velocimetry; Refractive index matching

4.1. Introduction

Anaerobic granular sludge reactors (AGSRs) have become pivotal technologies for the treatment of organic-rich industrial and municipal wastewaters. The performance and long-term stability of these reactors depend on the formation and maintenance of dense anaerobic granules that are structurally stable, metabolically active, and mechanically strong (van Lier et al. (2015), Show et al. (2020)). Hydrodynamics play a critical role in AGSR operation by reducing spatial gradients of substrates and nutrients through enhanced mixing and the prevention of stagnant zones (D' Bastiani et al. (2023)). At the granule scale, hydrodynamic conditions simultaneously regulate mass transfer between the bulk liquid and the granule surface and impose continuous mechanical stresses on the granules. These processes directly govern external mass transfer and indirectly modulate intragranular mass transfer by altering granule size, density, morphology, and internal structure, thereby influencing overall reactor performance (Liu and Tay (2002), Baeten et al. (2019)).

Over the past four decades, several high-rate anaerobic granular-based reactor configurations have been developed, among which the upflow anaerobic sludge blanket (UASB), expanded granular sludge bed (EGSB), and internal circulation (IC) reactors are the most widely applied. These reactors operate on the common principle of treating wastewater in an upflow configuration through a dense bed or blanket of anaerobic granular sludge, yet they differ substantially in their operating windows and hydrodynamic regimes (Mariraj Mohan and Swathi (2022)). Owing to intensified hydrodynamics, EGSB and IC reactors can be operated at significantly higher organic loading rates (OLRs) of 25–35 kg $COD/m^3/d$, which are approximately three to four times higher than those typically reported for UASB reactors (10–15 kg $COD/m^3/d$) (van Lier et al. (2015)). This enhanced treatment capacity is mainly attributed to higher superficial liquid and gas velocities, which promote improved mixing and substrate and nutrient mass transfer (Jiang et al. (2014)). This highlights the role of hydrodynamic intensity in governing the performance of anaerobic granular sludge reactors. However, hydrodynamic forces can also damage the granule's structural integrity, leading to increased sludge washout, ultimately resulting in reactor instability or failure if the mixing intensity applied becomes too high (Wu et al. (2012a)).

To quantitatively describe the hydrodynamics in AGSRs, empirical models have been utilized. These models allowed to estimate the shear rate or shear stresses within the reactors (Pereboom and Vereijken (1994), Wu et al. (2006, 2012a), Kundu et al. (2014a)). Although empirical models are useful for correlating bulk shear with reactor operating conditions, they are limited to the operational ranges and cannot be extrapolated to other reactors and flow conditions. For that a more generic approach on spatial flow field variations is needed, and to address this, computational fluid dynamics (CFD) has been increasingly applied to these three-phase systems to evaluate flow patterns, phases (solid and gas) distributions, and mixing efficiency (Ren et al. (2009a), Wang et al. (2009, 2010), Yang et al. (2015), Bastiani et al. (2021)). While CFD modeling is a powerful tool for hydrodynamic analysis, operational optimization, and reactor design, it can only be reliably applied once the model has been accurately calibrated and validated. The calibration and validation of such mathematical models in three-phase flows remain challenging due to limited optical access in these systems and the difficulty of experimental flow measurements to provide accurate data (D' Bastiani et al. (2023)). As a result, mostly tracer experiments have been used to achieve a basic level of validation in a few studies (Ren et al. (2009a), Yang et al. (2015)). To achieve detailed validation of CFD models, particle image velocimetry (PIV), a non-invasive optical technique capable of obtaining both qualitative and quantitative flow-field data (Seyfi et al. (2024)), has been applied (Wang et al. (2009, 2010), Bastiani et al. (2021)). Bastiani et al. (2021) validated their model by measuring liquid velocity above the sludge blanket in a two-phase gas–liquid flow, and Wang et al. (2009, 2010) attempted PIV measurements in a three-phase flow and at high solids volume fraction (35%) to validate the CFD model during biohydrogen production. However, details on the PIV setup, data acquisition, image processing procedures, and resulting flow fields were not reported.

Generally, flow characterization in three-phase systems, such as AGSRs, faces major challenges due to the presence of dispersed phases, in particular, the high concentration of granular sludge. Our recent work showed that already at 2% volume fraction of granules, optical flow measurement techniques (such as particle tracking velocimetry (PTV)) provides very limited data on tracer particles (Eslami et al. (2025)). In fact, the opacity of these systems hinders the application of most available experimental flow measurement techniques (Poelma (2020)). Consequently,

despite the crucial role of hydrodynamics on mixing, mass transfer, and granule properties, only limited number of studies employed experimental techniques to investigate the hydrodynamics of anaerobic granular sludge reactors. Among the available techniques, two-dimensional Particle Image Velocimetry (2D-PIV) has so far been the only method used to quantify local flow dynamics in these reactors. For instance, Zhang et al. (2011), Jiang et al. (2014, 2016) studied the effect of local flow and shear fields for achieving the maximum biogas production rate. Wu et al. (2015) measured the liquid velocity field around individual granules and showed that the shear forces exerted on granule surfaces by rising gas bubbles are significantly higher than those caused by the relative motion between liquid and granular sludge. These studies provided valuable fundamental insight into local flow characteristics and their influence on biogas production rate; however, the experiments were mostly conducted in low concentrations of granular sludge and in two-dimensional reactors with minimal thickness due to limitations of the PIV method. This prevented capturing spatial heterogeneity of flows in AGSRs as predicted in CFD studies of Ren et al. (2009a), and Bastiani et al. (2021).

The above described flow heterogeneity results from variations of both, solids and gas volume fractions (VOFs) along the height of the reactor. This in turn should result in distinct hydrodynamic conditions in different reactor regions (Ren et al. (2009a), Jiang et al. (2014), Bastiani et al. (2021)). Particularly, the presence of solids at varying concentrations can significantly alter liquid velocity, gas bubble spatial distribution and coalescence behavior, bubble rise velocities, and turbulence intensity, thereby directly affecting mixing and mass transfer (An et al. (2024a)). Hence, to study the hydrodynamics in AGSRs experimentally, the complexity introduced by the solid phase should be taken into consideration.

Studies in the field of chemical engineering have investigated the hydrodynamics of three-phase liquid–solid–gas reactors (e.g., slurry bubble columns and air-lift loop reactors) and the effects of operating parameters on reactor hydrodynamics. There is, however, a lack of detailed information on the local hydrodynamics of three-phase flows, particularly at high solid VOF (Yang et al. (2022)), and the mechanisms of particle effects, for instance on local liquid velocity dynamics and shear force exposed onto granules, are rarely discussed. Moreover, the mechanisms that are proposed and discussed often lack in-depth analysis and verification (An et al. (2024b)).

The findings of these studies on multiple hydrodynamic variables (e.g., gas holdup and bubble size distribution) are not directly applicable to granular sludge systems, as they were typically conducted under harsh operating conditions, such as high pressure and high superficial liquid and gas velocities (Mena et al. (2005), Yang et al. (2022)). Particle size is another key parameter influencing reactor flow characteristics. In most three-phase flow studies, micron-scale particles serving as catalysts, reactants, or products are employed, whereas granules in AGSRs can grow to several millimeters in diameter. Therefore, there is a general lack of systematic experimental data on liquid velocity fields at high solid concentrations in three-phase flow systems and over a wide range of solid VOFs and operating conditions representative of AGSR operation. This knowledge gap hinders both the validation of CFD models (D' Bastiani et al. (2023)) and the development of mechanistic links between operational parameters, local hydrodynamics, mass transfer, granule properties, and overall reactor performance.

In the present study, local flow measurements in three-phase systems based on transparent synthetic granules are investigated. We build on a previously developed and published methodology for dense two-phase flows (Eslami et al. (2025)) and apply it to dense three-phase flows representative of anaerobic granular sludge systems. By combining refractive index matching (RIM) with three-dimensional particle tracking velocimetry (3D-PTV), the feasibility of resolving three-dimensional liquid velocity fields at high solid volume fractions of up to 50% in gas–liquid–solid flows is demonstrated. Liquid velocity components and mixing behavior over a range of solid concentrations and gas superficial velocities relevant to practical reactor operation is systematically studied. This approach enables direct experimental investigation of bubble-induced hydrodynamics under realistic conditions and provides high-resolution data that support a deeper understanding of the mechanisms by which hydrodynamics influence treatment efficiency, and contribute to reactor design and optimization of operational parameters in AGSRs.

4.2. Materials and methods

4.2.1. Reactor setup, material properties, and operating conditions

The experiments were conducted in a cylindrical lab-scale EGSB reactor with an internal diameter of 10 cm and a height of 1.7 m (Figure 4.1a). The reactor was constructed from glass with flat outer walls, providing optical access and making it suitable for optical–based flow measurement techniques (Figure 4.1b). A liquid distributor was installed at the bottom of the reactor, consisting of a 10 cm calming section followed by a perforated plate, to ensure uniform liquid distribution at the reactor inlet. Detailed description of reactor design and liquid flow loop components are provided in our previous work (Eslami et al. (2025)). A 3D-printed perforated plate gas sparger was installed on top of the liquid distributor section (Figure 4.1c). The sparger had a diameter of 2 cm and featured eight circular orifices with a diameter of 0.5 mm, distributed along the circumference with an angular spacing of 45° between adjacent orifices. Nitrogen was supplied as the gas phase and the gas flow rate was controlled by a thermal mass flow controller (Bronkhorst, The Netherlands).

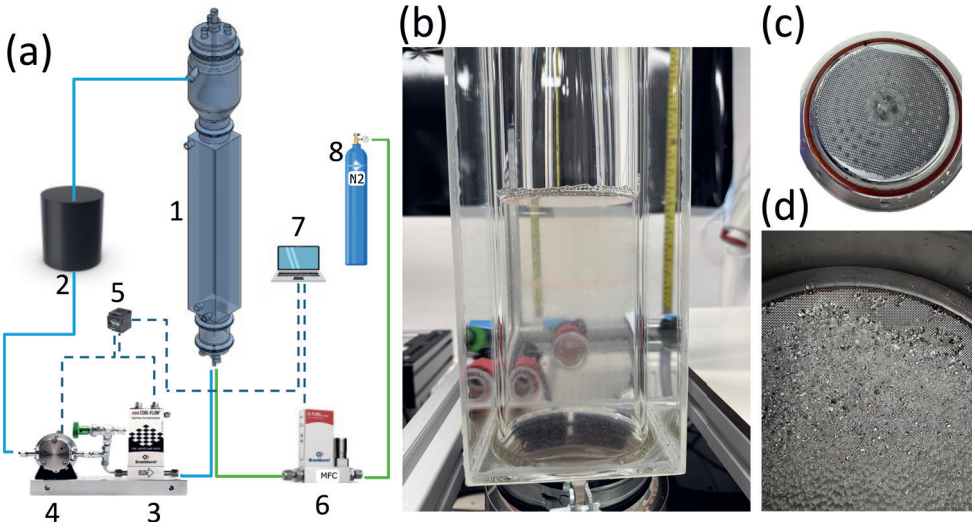


Figure 4.1: (a) schematic of the setup showing (1) reactor, (2) recirculation tank, (3) liquid mass flow meter, (4) pump, (5) variable frequency drive, (6) gas mass flow controller, (7) data acquisition laptop, and (8) nitrogen gas cylinder; (b) reactor with settled hydrogel beads and orange fluorescent tracer particles; (c) gas–liquid distributors, including a perorated plate covered by a hydrogel bead-retaining mesh and a gas sparger in the center; (d) hydrogel beads.

Polyacrylamide hydrogel beads (Soil Moist™, JRM Chemical, Inc., Cleveland, OH, USA) were used as the transparent solid phase to mimic anaerobic granules (Figure 4.1d). The refractive index (RI) of hydrogels was nearly identical to water (Dijksman et al. (2017)), making them suitable for optical flow measurement techniques. The beads used in this study had diameters in the range of 1–2 mm and a density of approximately 1009 kg/m^3, which falls well within the range of densities (1000-1050 kg/m^3) reported for anaerobic granules (van Lier et al. (2015)).

To achieve refractive index matching between water and hydrogel beads, polyvinylpyrrolidone (PVP) with a molecular weight of 360,000 was dissolved in tap water. As demonstrated in our previous work, optimal refractive index matching was achieved using a 0.5 % (w/w) PVP solution, enabled successful volumetric particle tracking at a solid VOFs as high as 50% (Eslami et al. (2025)). This solution was therefore used as the working fluid in the present experiments.

To investigate both effects of varying solid VOF and GSV on reactor hydrodynamics, experiments were conducted at four solid VOFs (0, 10, 30, and 50%). For each solid

VOF case, the reactor was operated at three gas flow rates (Q_G = 0.05, 0.25, and 0.5 L/min). In all cases, the liquid flow rate was kept constant at Q_L = 2.0 L/min, corresponding to an upflow liquid velocity of approximately 15 m/h, which lies within the typical operating window of EGSB and IC reactors. The experimental operating conditions are summarized in Table 4.1.

Table 4.1: Experimental operating conditions

Case	Solid VOF (%)	Q_L (L/min)	Q_G (L/min)	GSV (cm/s)
1			0.05	0.01
2	0	2	0.25	0.05
3			0.50	0.10
4			0.05	0.01
5	10	2	0.25	0.05
6			0.50	0.10
7			0.05	0.01
8	30	2	0.25	0.05
9			0.50	0.10
10			0.05	0.01
11	50	2	0.25	0.05
12			0.50	0.10

4.2.2. Imaging system

The imaging system consisted of a high-power LED light source (100 × 300 mm^2) and four high-speed cameras (1984 × 1264 pixels, 10-bit dynamic range) integrated into a single camera housing (MiniShaker, LaVision GmbH) (Figure 4.2). All cameras were equipped with 12 mm Tamron lenses, and a 540 nm long-pass optical filter was mounted on each lens. Fluorescent tracer particles (100–150 μm, LaVision GmbH) were used as seeding particles.

4.2.3. Experimental procedure, data acquisition and processing

All image acquisition and processing were performed using DaVis 10.2 (LaVision GmbH). The calibration procedure consisted of three steps: planar calibration,

volume self-calibration using pre-processed images of tracer particles, and optical transfer function (OTF) calculation. Details of the image pre-processing and calibration procedures are described in our previous work (Eslami et al. (2025)).

For each experiment, fluorescent tracer particles were uniformly mixed in the recirculation tank and pumped into the reactor, yielding a mean seeding density of approximately 0.02 particles per pixel (ppp). This density provided adequate spatial coverage while minimizing occurrence of ghost particles (Schanz et al. (2016), Hofmann et al. (2022)). For each case, a 25 cm axial section of the reactor, corresponding to a measurement volume of 0.625 L, was imaged. Images were acquired at 198.4 Hz with an exposure time of 338 μs (see raw images of tracer particles in Figure S.4.1). This frame rate ensured that the maximum particle displacement between successive frames remained within the recommended range of 10–20 pixels for accurate particle tracking (Schanz et al. (2021)). In the next step, Shake-the-Box (STB) method was employed to reconstruct time-resolved 3D trajectories of individual tracer particles. STB is a Lagrangian particle tracking technique for volumetric flow measurements that determines particle positions using an iterative prediction–correction scheme combining image matching and triangulation techniques (Wieneke (2013), Novara et al. (2023)). Compared to conventional 3D-PTV, STB provides higher spatial resolution by permitting increased seeding densities of up to 0.2 ppp, while maintaining accurate particle reconstruction at moderate computational cost (Schröder and Schanz (2023)). In this study, a minimum intensity of 15 counts and an allowed triangulation error of 2.5 voxel were used for particle detection. The STB processing parameters are summarized in Table S.4.1.

4.2.4. Post-processing

Particle track data, consisting of time-resolved 3D particle positions within the measurement volume, were extracted over 500 images (images 500 to 1000 for all cases). This range was chosen to ensure the inclusion of the longest particle track in statistical analysis. Instantaneous velocity components of particles along each trajectory were computed from the particle position time series using a central difference scheme. Moreover, mixing performance was quantified by calculating axial and radial hydrodynamic dispersion coefficients using the displacement variance method (Voronov et al. (2011), Xia et al. (2013)). Mean-squared

displacement (MSD) curves were obtained by ensemble-averaging the squared particle displacements over all tracked particles for different lag times (τ), where the lag time represents the time interval between two positions along the same particle trajectory. The MSD was evaluated separately for the axial direction (y) and for the radial direction, defined as the combined displacement in the x–z plane. Axial and radial dispersion coefficients were determined from the segment of the MSD–time curve exhibiting a linear scaling (slope of 1.0 ± 0.1 on a log–log scale) (Xia et al. (2013), Huang et al. (2025)). Further details are provided in our previous work (Eslami et al. (2025)). All post-processing was performed in `Python` 3.11, and particle field data were imported using the `lvpyio` 1.3.0 package (LaVision Python add-on).

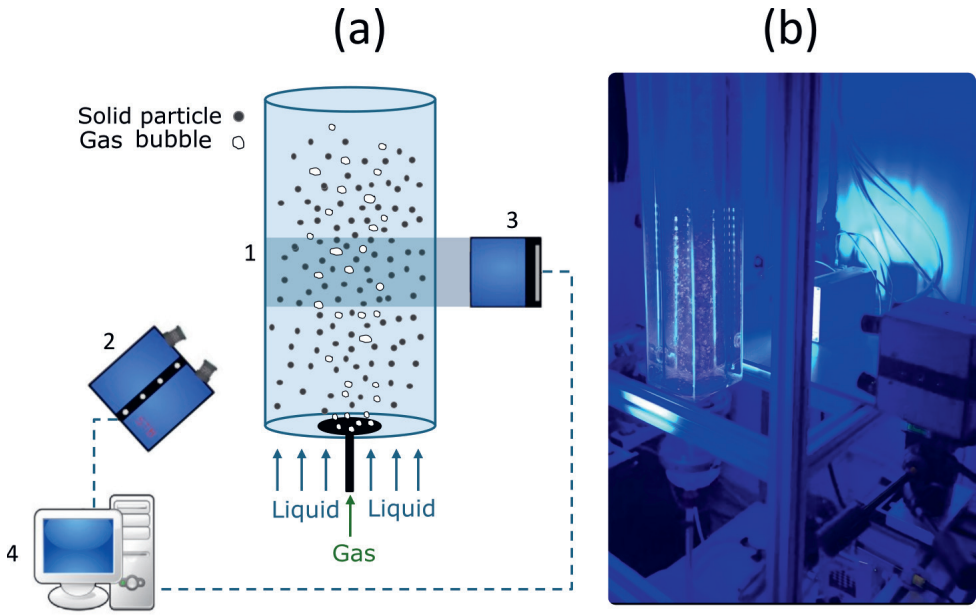


Figure 4.2: (a) Schematic sketch of imaging setup, including (1) reactor, (2) multi-camera housing, (3) LED, (4) computer. (b) photograph of the imaging setup, showing the cameras and the reactor illuminated by blue LED light.

4.3. Results and discussion

4.3.1. Particle tracking results and flow visualization

Instantaneous location of reconstructed particles over 60 consecutive time-steps for all investigated cases are shown in Figure 4.3. Depending on the applied gas superficial velocity (GSV) and solid volume fraction (VOF), approximately 20,000–30,000 particles were detected and tracked within the measurement volume. Detailed tracking statistics are provided in Supplementary Information (Section S.4.2). The overall flow structure can be determined from the ensemble of particle trajectories. In all cases, a high-velocity, bubble-induced upflow region was observed in the reactor core, and a downward flow in the vicinity of the reactor walls. The relative spatial extent of the upward and downward flow regions varied with GSV and solid VOF.

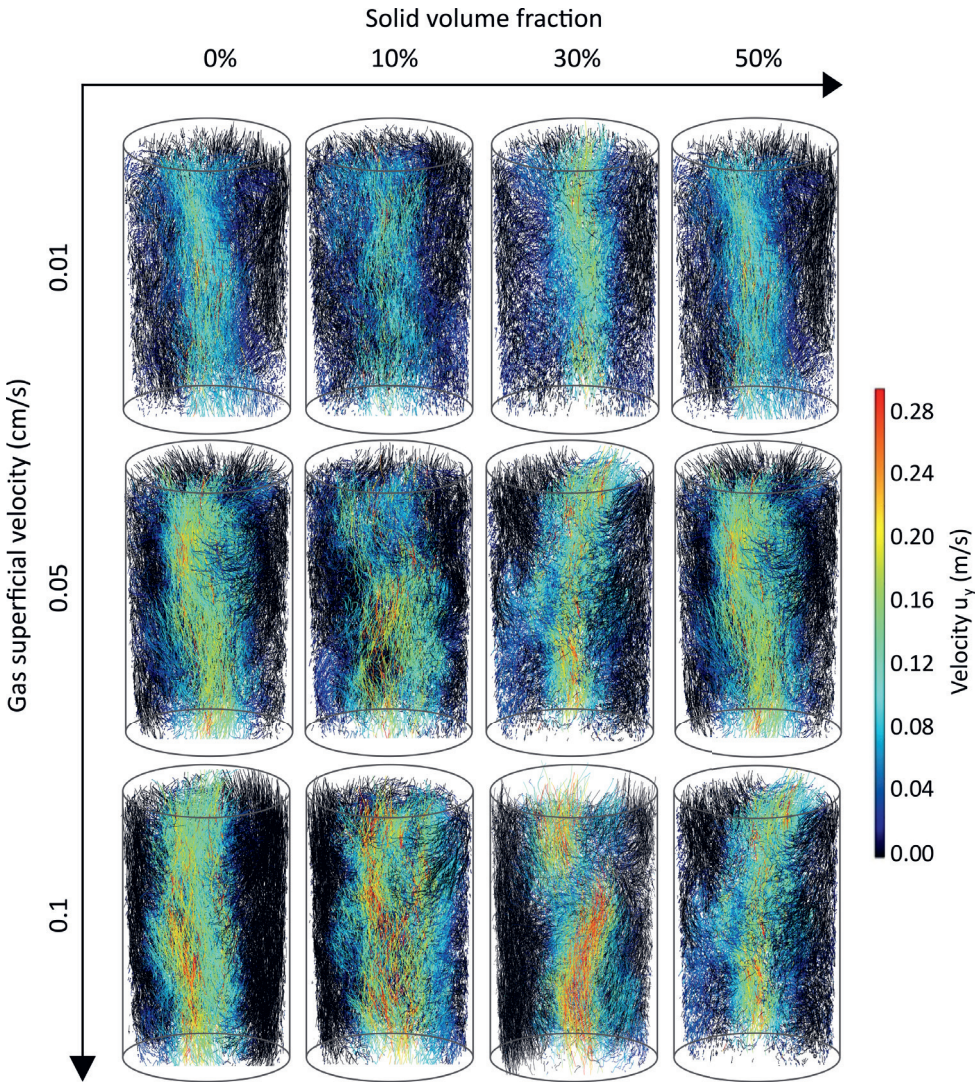


Figure 4.3: Instantaneous snapshots of reconstructed Lagrangian particle tracks with tracking lengths of 60 time-steps across different solid VOFs and GSVs. The particles and particle tracks are colored by the axial velocity component.

4.3.2. Effect of increasing gas superficial velocity and solid VOF on liquid mean velocity

The mean liquid velocity, commonly referred to as the upflow velocity, is a key operational parameter in anaerobic granular sludge reactors (AGSRs). It governs the sludge bed expansion, mixing intensity, hydrodynamic shear stress, mass transfer

efficiency, and the residence time of granules within the reactor (D' Bastiani et al. (2023), Gonçalves et al. (2025)). The combined effect of these physical factors strongly influences overall process stability. In three-phase gas–liquid–solid systems, the upflow liquid velocity is not an independent variable but emerges from the complex coupling between GSV, gas holdup, bubble size and distribution, and solid VOF. As a result, the mean liquid velocity can vary significantly along the reactor height and across operating conditions. To capture these effects, the mean liquid velocity was determined for each combination of gas flow rate and solid VOF, as shown in Figure 4.4.

Figure 4.4a illustrates the effect of GSV on the mean liquid velocity at constant solid VOFs. For all solid VOFs, increasing the gas flow rate led to a monotonic increase in mean liquid velocity, which can be attributed to the corresponding rise in overall gas holdup. At higher GSVs, enhanced bubble generation and coalescence resulted in the formation of larger, faster-rising bubbles, thereby intensifying liquid circulation and increasing the mean liquid velocity. When the GSV was increased from 0.01 to 0.05 cm/s, the mean liquid velocity increased with a comparable slope across all solid VOFs; however, upon a further increase from 0.05 to 0.1 cm/s, two distinct slopes were observed. At higher solid VOFs (30–50%), the mean liquid velocity increased more steeply with GSV than at low solid VOFs (0-10%). A similar behavior was observed in the work of Milivojevic and Bugarski (2012), and can be attributed to regime transition from homogeneous to heterogeneous flow, characterized by wider bubble size distribution. At elevated solid VOFs, the apparent viscosity of the liquid–solid suspension (slurry) increases, which promotes bubble coalescence and the formation of larger bubbles. These larger bubbles experience higher buoyant forces, enhancing liquid circulation and thereby intensifying the mean liquid velocity.

Increasing solid VOF, at constant GSVs, had a dual effect on mean liquid velocity as presented in Figure 4.4b. For each GSV, increasing the solid VOF initially led to an increase in mean liquid velocity up to a critical solid concentration, beyond which further increases in solid VOF caused a reduction in velocity. This agrees with the findings of previous studies in three-phase fluidized and slurry reactors where the mean liquid velocity was reported to decrease above solid VOFs of 5% (Mena et al. (2005)) and 2.5% (Milivojevic and Bugarski (2012)).

In the present study, we observed that the critical solid VOF beyond which the

mean liquid velocity decreases depends on the GSV. As shown in Figure 4.4b, higher gas flow rates shifted the critical solid VOF toward larger values. At low GSV, the maximum mean velocity occurred at relatively low solid concentrations, whereas at higher GSV, the peak velocity was attained at higher solid VOFs. This behavior can be interpreted in terms of the balance between energy input and energy dissipation in the gas–liquid–solid flows. Increasing the solid VOF raises the apparent viscosity of the slurry due to higher particle-induced friction, thereby increasing energy dissipation. At the same time, added solids promote bubble coalescence and the formation of larger bubbles, which rise faster and, up to a point, intensify liquid circulation by transferring more momentum to the surrounding fluid. However, at higher solid VOFs, hindered bubble rise and enhanced energy dissipation outweigh the energy input, resulting in a reduction of the mean liquid velocity.

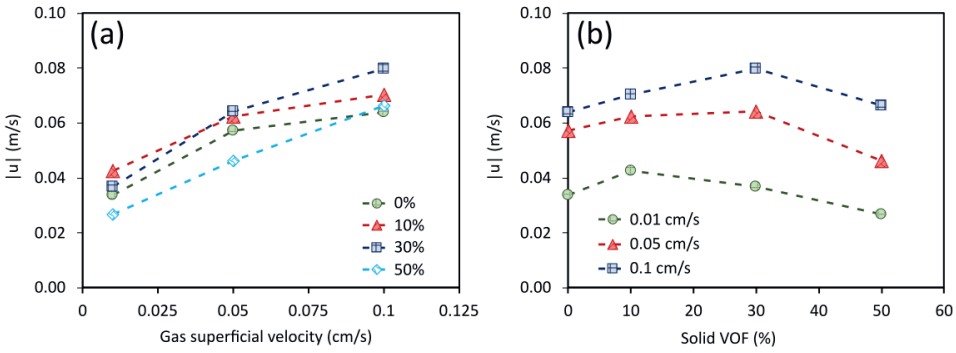


Figure 4.4: (a) Effect of gas superficial velocity (GSV) on liquid mean velocity magnitude at constant solid volume fractions (VOFs), (b) effect of solid VOF on liquid mean velocity magnitude at constant GSVs

4.3.3. Effect of gas superficial velocity at different solid VOFs on axial and lateral liquid velocity components

A detailed statistical evaluation of the velocity components of all Lagrangian particles within the measurement volume is presented in Figure 4.5, illustrating the effect of GSV on the frequency distribution of the axial (Figure 4.5a) and lateral (Figure 4.5b) liquid velocity components at constant solid VOFs.

As a first observation, across all operating conditions, the probability density functions (PDFs) of the axial liquid velocity are right-skewed with a long tail

(Figure 4.5a), whereas the PDFs of the lateral velocity exhibit a relatively symmetric distribution centered around zero (Figure 4.5b). Moreover, for each case, the width of distribution curve of the axial velocity is consistently greater than that of the lateral velocity component. This anisotropy in the flow arises from the dominant upward liquid motion induced by rising bubble swarms and upflow velocity (Martínez-Mercado et al. (2007)).

Increasing GSV broadened the PDFs of both axial and lateral velocity components for all solid VOFs, reflecting intensified liquid circulation. However, the magnitude of this effect depended on the solid concentration, with the most pronounced PDF broadening observed at solid VOF of 30%, suggesting that higher GSV is most effective in enhancing circulation at intermediate solid VOFs. In addition, higher GSV increased the magnitude of negative axial velocities, indicating stronger downward liquid motions. This effect became progressively more pronounced with increasing solid VOF, as evidenced by the growing separation between the curves on the negative side of the axial velocity PDFs (Figure 4.5a). Additional statistical analyses of particle tracks, including PDFs of the velocity magnitude ($|u|$), axial particle acceleration (a_y), and out-of-plane lateral velocity component (u_z), are provided in Supplementary Information (Section S.4.3).

The PDF of u_z velocity component (Figure S.4.4) showed a slightly broader distribution than u_x, which is attributable to the experimental imaging geometry and optical distortions. Curved reactor walls and multiple refractive interfaces (air–glass–water–glass–PVP solution and hydrogels) introduce systematic uncertainty in the reconstruction of particle positions in the z direction, and because particle positions in this direction are obtained via triangulation between multiple camera views, the out-of-plane velocity component (u_z) is inherently more sensitive to optical distortions than the in-plane velocity components.

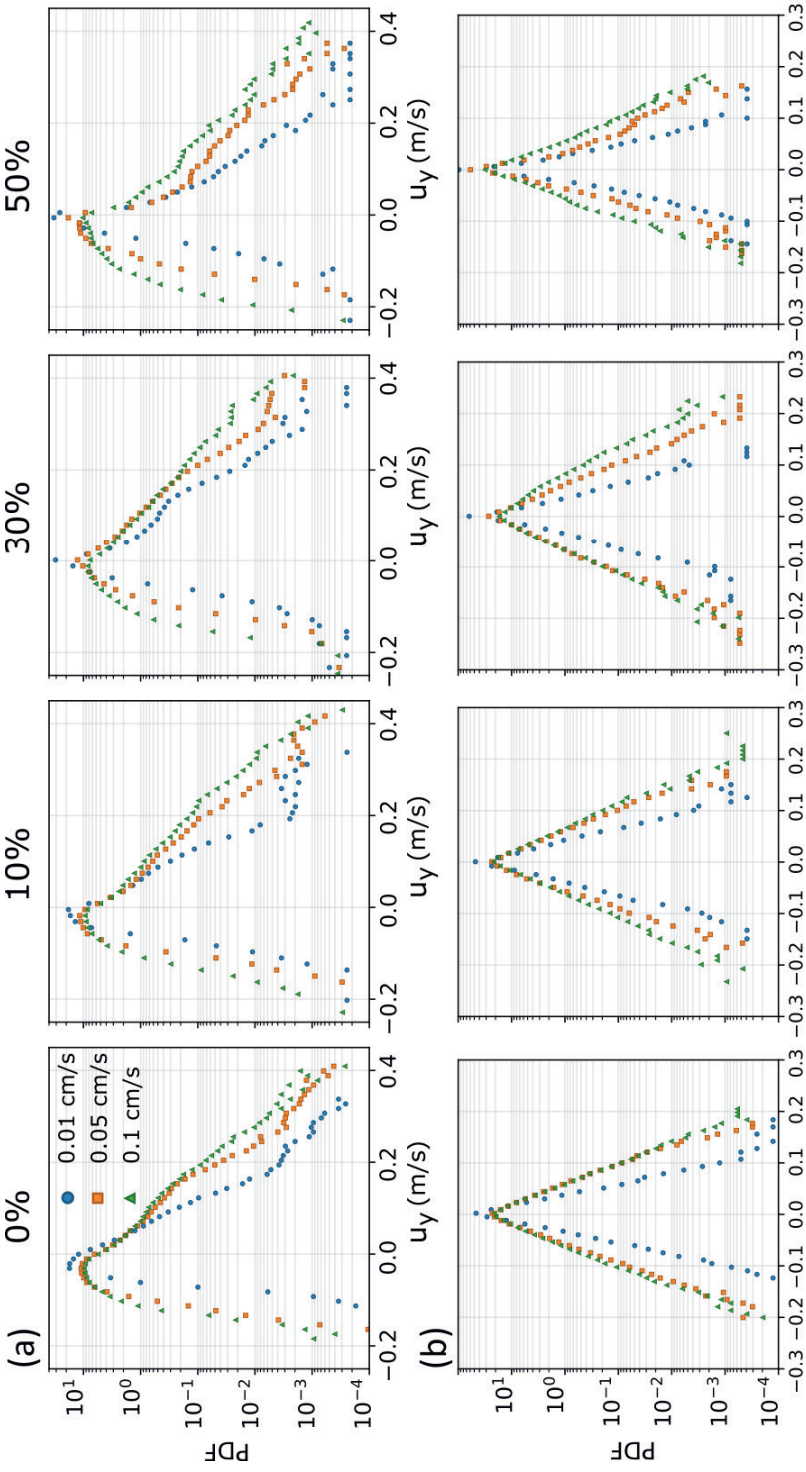


Figure 4.5: Effect of gas superficial velocity (GSV) on the frequency distribution of the (a) axial (u_y) and (b) lateral (u_x) liquid velocity components at constant solid volume fractions (VOFs).

4.3.4. *Effect of solid VOF at different gas superficial velocity on liquid axial and lateral velocity components*

Figure 4.6 shows the effect of solid VOF on the PDF of instantaneous axial and lateral liquid velocities at constant GSV. Overall, increasing the solid VOF had a dual influence on the velocity distributions, and an approximately similar pattern was observed for all cases with constant GSV. As shown in Figure 4.6a, increasing the solid VOF from 0% to 30% broadened the positive tail, indicating higher upward liquid velocities and an increased probability of occurrence of extreme liquid velocity events. With a further increase to 50% solid VOF, the distribution narrowed, reflecting reduced upward liquid motion. At high GSV (0.1 cm/s), this effect was slightly weaker for the upward velocity distribution but more pronounced for downward liquid motion, as evidenced by the reduced separation between the curves at positive velocities and the increased separation at negative velocities. At intermediate (0.05 cm/s) and high (0.1 cm/s) GSVs, lateral velocity PDFs followed trends comparable to those of the axial component (Figure 4.6b). At low GSV (0.01 cm/s), the width of the lateral velocity distributions remained nearly unchanged up to 30% solid VOF and decreased at 50%. PDFs of $|u|$, a_y, and u_z are provided in Supplementary Information (Section S.4.4).

In general, the likelihood of occurrence of extreme upward velocity events increased with increasing solid VOF up to 30% and decreased at 50%. Moreover, increasing the solid concentration enhanced the extent of stagnant and near-zero velocity zones, as reflected in the PDF curves by a progressive shift of the axial velocity distribution peak toward zero (see the linear-scale axial velocity PDFs in Figure S.4.5).

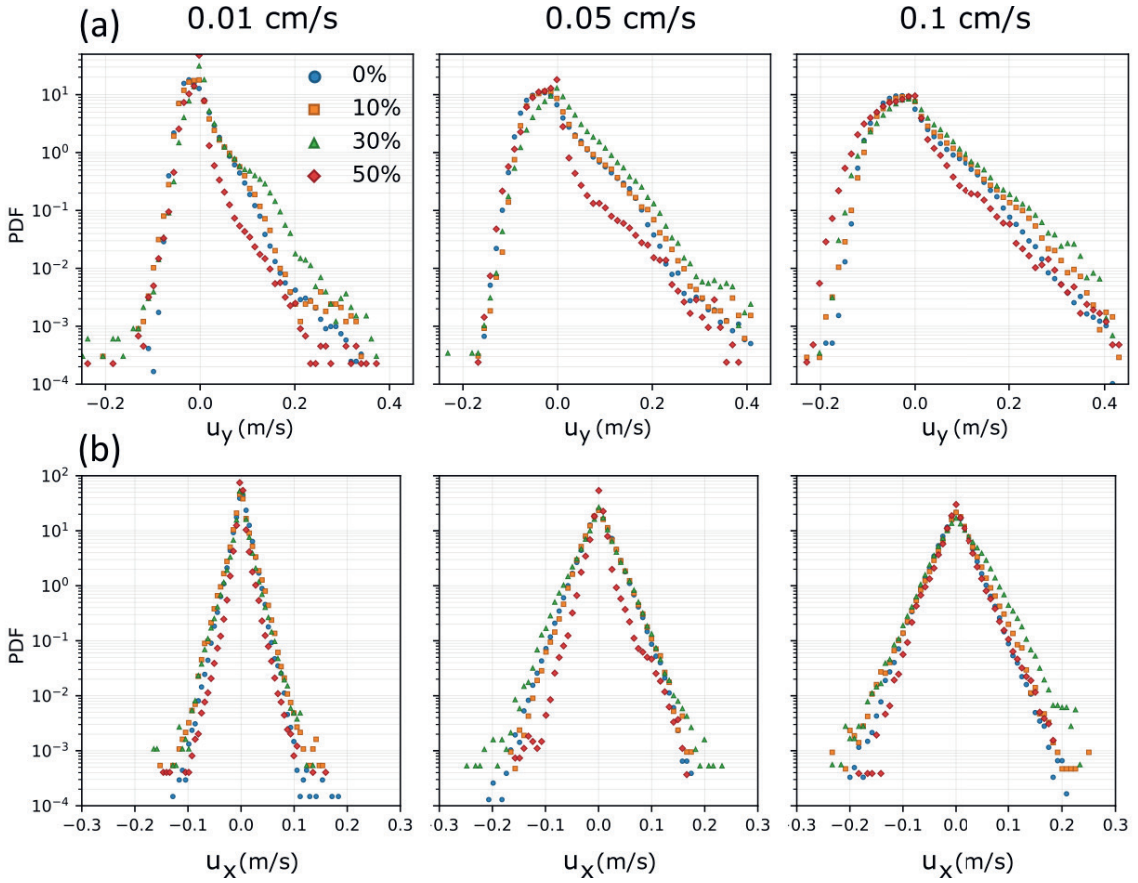


Figure 4.6: Effect of solid volume fraction (VOF) on the frequency distribution of the (a) axial (u_y) and (b) lateral (u_x) liquid velocity components at constant gas superficial velocities (GSVs).

4.3.5. Effect of varying gas superficial velocity and solid VOF on mixing performance

Mixing is a critical design and operating parameter in anaerobic granular sludge reactors because it governs the contact efficiency between wastewater and anaerobic granules and thereby influences treatment performance. The hydrodynamic behavior in such systems is commonly described using two idealized flow regimes, plug flow and completely mixed flow, or combinations of the two patterns (Hmissi et al. (2020)). In practice, AGSRs operate between these extremes, as mixing results from the combined effects of convection and dispersion (Mullai et al. (2025)): convection driven by the bulk liquid velocity, and dispersion arising from velocity fluctuations generated by bubble-induced turbulence (BIT) and shear-induced turbulence (SIT) in the gas–liquid–solid three-phase flows (Risso (2018), An et al. (2024b)). The relative strength of convective transport versus dispersion determine where the reactor's mixing behaviour lies along the spectrum from plug-flow (convection-dominated) and ideally mixed (dispersion-dominated) regimes. This is a key determinant in hydrodynamic modelling and in predicting overall treatment performance (Ren et al. (2008), Mullai et al. (2025)).

In this study, dispersion coefficients in both axial and radial directions under different operating conditions were evaluated by analyzing the displacement of tracer particles over time. The mean squired displacement (MSD) method quantifies the average squared distance traveled by particles over a different time lags, As shown in Figure 4.7, the ensemble-averaged MSD curves for all cases exhibit two distinct regimes: an initial ballistic growth at short time lags, followed by a linear increase at longer times. The ballistic regime potentially reflects the advection-dominated motion, where particles predominantly follow coherent flow structures with relatively constant velocities. At sufficiently long times, however, the MSD transitions to a diffusive regime with linear growth in time, indicating that particle motion becomes dominated by random, turbulent velocity fluctuations, similar to previous observations (Xia et al. (2013), Hofmann et al. (2022), Huang et al. (2025)). The dispersion coefficients (also known as eddy diffusivity), which quantifies the efficiency of particle spreading within the reactor, was determined from the slope of the linear MSD curves for all operating conditions.

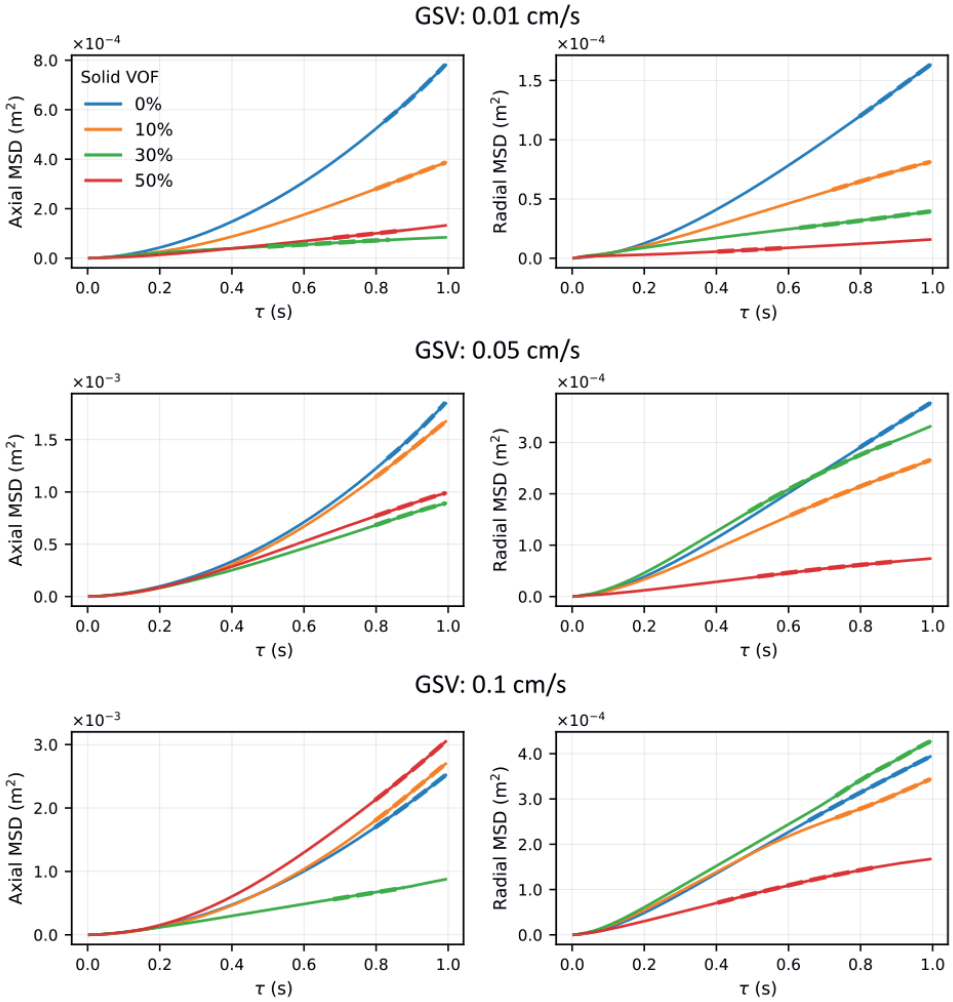


Figure 4.7: Ensemble-averaged mean-squared displacement (MSD) of tracer particles as a function of lag time under different solid volume fractions (VOF) and gas superficial velocities (GSV), shown for the axial (left) and radial (right) directions. Dashed lines highlight the lag-time range over which the MSD scales linearly with lag time; this range was used for straight-line fitting and dispersion coefficient (D) calculation (MSD $\sim 2D\tau$).

The influence of solid VOF on the axial and radial dispersion coefficients showed a distinct dependence on the GSV (Figure 4.8a-b) At low (0.01 cm/s) and intermediate (0.05 cm/s) GSV, increasing the solid VOF resulted in a monotonic decrease in axial dispersion up to 30%, and no changes was observed with further increasing the solids to 50% (Figure 4.8a). This can be attributed to the combined effects

of several mechanisms. Higher solid VOFs hinder bubble rise, reducing the slip velocity between the gas bubbles and slurry phase. Simultaneously, the increase in solid VOF raises the apparent viscosity of the slurry, which suppresses velocity fluctuations. At the highest GSV (0.1 cm/s), the axial dispersion coefficient first increased as the solid VOF increased from 0 to 10%. This can be due to the higher gas holdup at low solid VOFs, as reported by Mena et al. (2005), which enhances bubble-induced turbulence (BIT) and promotes axial mixing. Further increasing the solid VOF to 30 % led to a sharp decrease in the axial dispersion coefficient. This reduction may be attributed to the development of a stronger reactor-scale circulation pattern, characterized by higher overall mean velocity (Figure 4.4b), in which the majority of bubbles rise within a high-velocity upflow core. While this intensified circulation enhances shear-induced turbulence (SIT), it reduces the relative velocity between the bubble and slurry phases, thereby reducing the contribution of BIT to velocity fluctuations and dispersion of tracer particles (Gvozdić et al. (2019)). At a solid VOF of 50 %, the axial dispersion coefficient increased again, which may be associated with a more homogeneous spatial distribution of gas bubbles (see the raw images of rising gas bubbles shown in Figure S.4.1). The radial dispersion coefficient showed an overall decreasing trend with increasing solid VOF for all GSVs (Figure 4.8b). However, at intermediate and high GSV (0.05 cm/s), a slight increase in radial dispersion was observed at 30% solid VOF. This may be due to the strong circulation rate (see Figure 4.4b)

Figure 4.8c–d shows the effect of increasing GSV on the axial and radial dispersion coefficients. Overall, higher GSV leads to larger dispersion coefficients in both directions. Increasing the gas flow rate introduces more bubbles, enhances bubble coalescence and the formation of larger, faster-rising bubbles, and supplies additional energy to the slurry phase. This results in stronger bubble-induced agitation, larger velocity fluctuations, and consequently enhanced mixing. The underlying physical mechanisms of bubble-induced mixing are complex, and the presence of a solid phase adds an additional layer of complexity. To fully interpret the observed trends with increasing GSV and solid volume fraction, detailed information on bubble size, spatial distribution, and relative rise velocities would be required.

The results of this study, as the first direct experimental evidence on flow dynamics in dense fluidizing three-phase flows similar to multiphase flow conditions in the sludge

blanket of AGSRs, show that spatial variations in granular sludge concentration and gas holdup generates different hydrodynamic and mixing conditions. Rising gas bubbles influence the local hydrodynamics and mixing and can alter mass transfer and shear stress at the granule scale. However, their impact depends on the gas holdup and bubble characteristics (i.e., size and spatial distribution) and dynamics (i.e., relative velocity to the bulk flow). In these reactors, the granule-scale hydrodynamics, intensified by both bulk flow and rising gas bubbles, can in turn influence biogas detachment and bubble size. Therefore, a higher upflow velocity may not guarantee enhanced mixing, as smaller gas bubbles and reduced slip velocity decrease the contribution of rising biogas bubbles to local hydrodynamics and mixing.

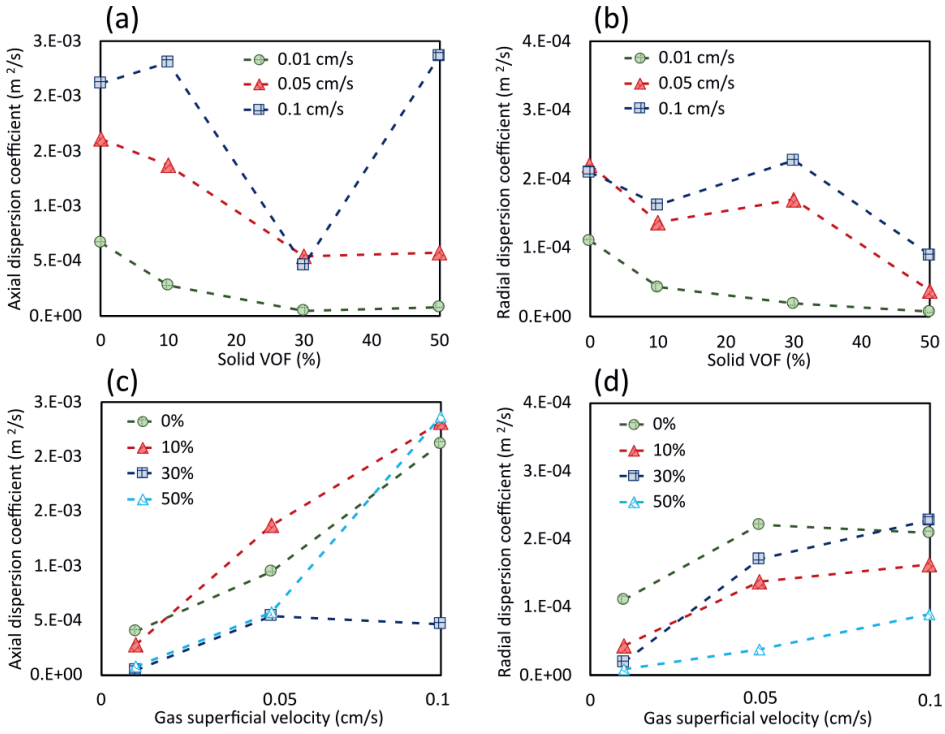


Figure 4.8: (a-b) effect of increasing solid volume fraction (VOF) at constant gas superficial velocity (GSV) on axial and lateral dispersion coefficients. (c-d) effect of increasing gas superficial velocity at constant solid VOF on axial and lateral dispersion coefficients.

4.4. Conclusion

This study demonstrates the feasibility of combining refractive index matching (RIM) with particle tracking velocimetry (PTV) to investigate hydrodynamics and mixing behavior in three-phase (liquid–solid–gas) representative of anaerobic granular sludge reactors (AGSRs) at high solid volume fractions (VOFs). The effects of increasing solid VOF and gas superficial velocity (GSV) on both mean liquid velocity and instantaneous velocity components were systematically analyzed, and mixing performance was quantified using axial and radial dispersion coefficients. Increasing gas superficial velocity led to a monotonic increase in mean liquid upflow velocity and a broadening of axial and lateral velocity probability density functions (PDFs), indicating enhanced circulation. This effect was most pronounced at an intermediate solid VOF of 30%, demonstrating that gas-driven enhancement of circulation is most effective at moderate solid loadings.

Increasing solid VOF showed a dual effect on the mean liquid velocity, which increased up to a critical VOF and subsequently decreased. This critical solid VOF was dependent on the GSV, with higher GSVs shifting the critical point toward higher solid volume fractions. In addition, increasing solid VOF enhanced the extent of stagnant and near-zero velocity zones. However, the likelihood of extreme axial and lateral velocity events increased with solid VOF up to 30% and decreased at 50%.

For all operating conditions, the axial dispersion coefficient was larger than the radial dispersion coefficient. Increasing GSV generally increased both axial and radial dispersion coefficients. However, the effect of solid VOF on dispersion coefficients depended on GSV and the resulting strength of reactor-scale circulation, relative velocity between gas bubbles and bulk flow, and spatial distribution of gas bubbles.

This study advances understanding of three-phase flow in AGSRs and supports the development of strategies to control hydrodynamics and mixing in these reactor. The developed methodology also offers a framework for the calibration and validation of multiphase CFD models.

Supplementary Information

S.4.1. Raw images

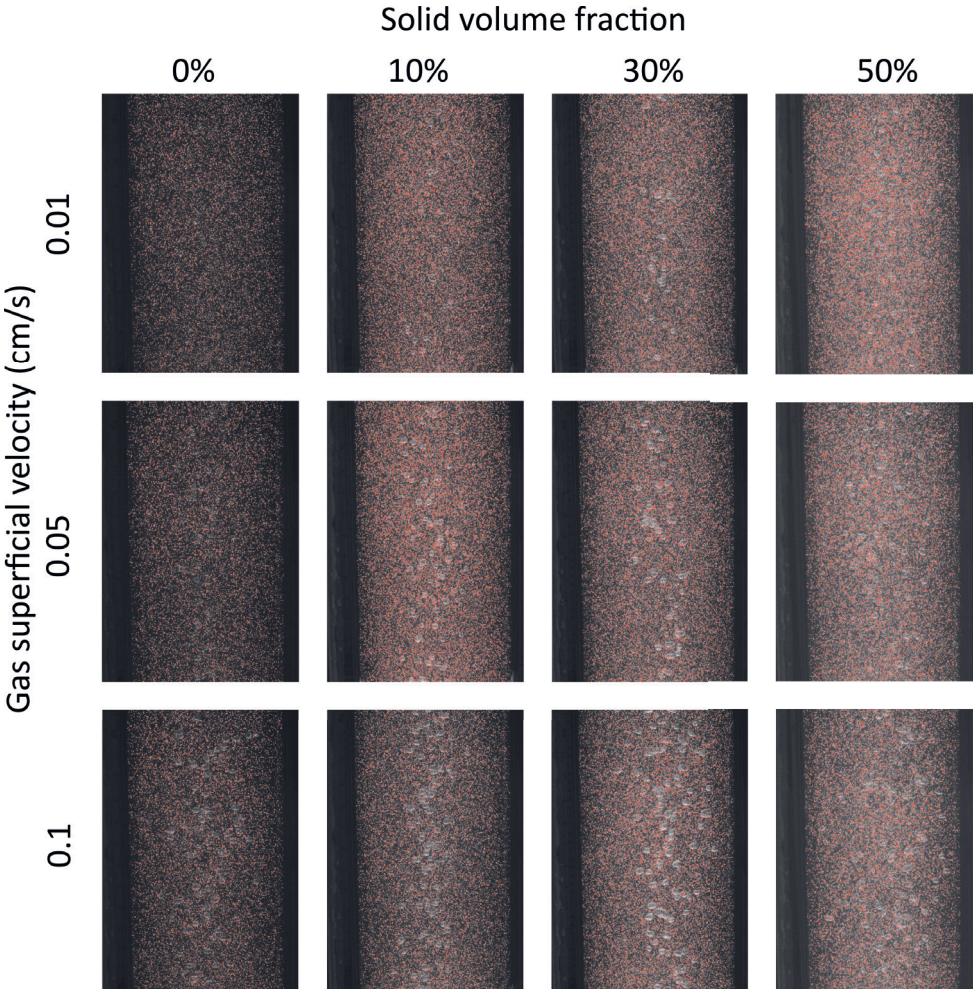


Figure S.4.1: Snapshots of tracer particles and rising gas bubbles at varying gas superficial velocity (GSV) and solid volume fraction (VOF).

S.4.2. STB settings and statistics

In two-phase flows with low gas flow rates, nearly all tracer particles (close to 100%) were successfully tracked. Increasing the gas flow rate reduced the ratio of tracked to available particles. In three-phase flows, both higher gas flow rates and higher solid

VOFs further decreased the tracking ratio. To compensate, a slightly higher seeding density was used at high solid VOFs and GSVs. Across all cases, the number of tracked particles within the measurement volume was between 20,000 and 30,000.

Table S.4.1: STB parameters.

Parameter	**Value**
Reconstructed volume	$660 \times 1457 \times 642$ voxels
Threshold for 2D particle detection	15 counts
Allowed triangulation error	2.5 voxels
Shaking	
Adding particles (outer loop)	4 iterations
Refine particle position and intensity (inner loop)	4 iterations
Shake particle position by	0.1 voxel
Remove particles if closer than	1 voxel
Remove weak particles if intensity <	0.1 of avg. int.
Particle image shape and intensity	
Make OTF smaller	0.8 times
Residuum computation - increase particle intensity	1.5 times
Tracking	
Minimum track length	4 time steps
Max. abs. change in particle shift	5.00 voxel
Max. rel. change in particle shift	20%

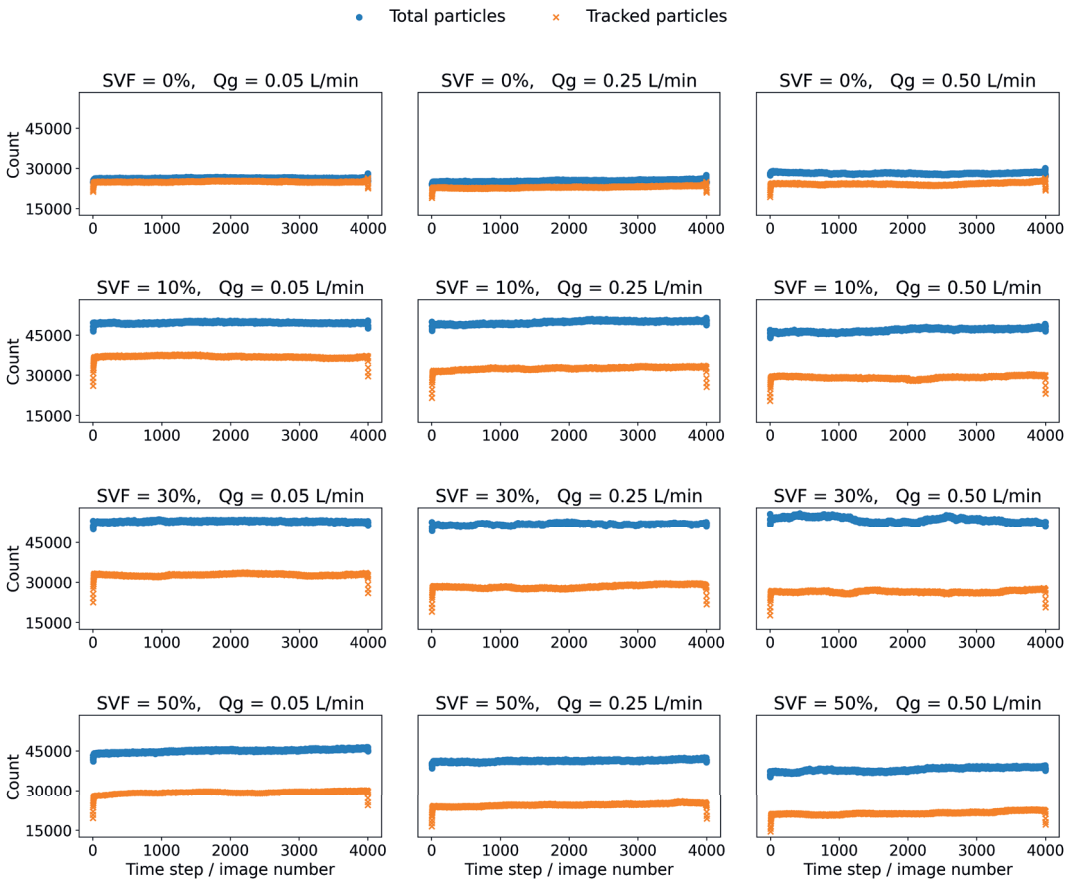


Figure S.4.2: Particle tracking statistics across cases with varying solid volume fraction (SVF) and GSV.

S.4.3. Effect of gas flow rate on liquid velocity and acceleration

Figure S.4.4 shows the effect of increasing GSV on the PDF of u_z. The broader distribution, as discussed, is most likely attributable to the experimental imaging geometry and optical distortions, including multiple refractive index transitions and the curved reactor walls. In addition, calibration plate size and selected particle-tracking settings may have contributed to increased particle reconstruction uncertainty in the z direction. For example, the use of a relatively small calibration plate (5×5 cm), which covered about 20% of the measurement volume height, may not have fully captured optical distortions near the top and bottom regions of the measurement volume. Furthermore, the calibration procedure relied on three planar calibration planes with 2.5 cm spacing; although a subsequent volumetric self-calibration using tracer particles was performed, a larger calibration target and a greater number of planar calibration planes could have improved the capture of optical distortions and increased the accuracy of depth-wise interpolation of the calibration parameters. Finally, the selected triangulation threshold of 2.5 voxels (scale factor: 5.84 voxels/mm) provided an optimal compromise between reconstruction accuracy and maintaining a sufficiently large number of detected particles for statistical analysis, but may have introduced additional uncertainty in the u_z velocity component.

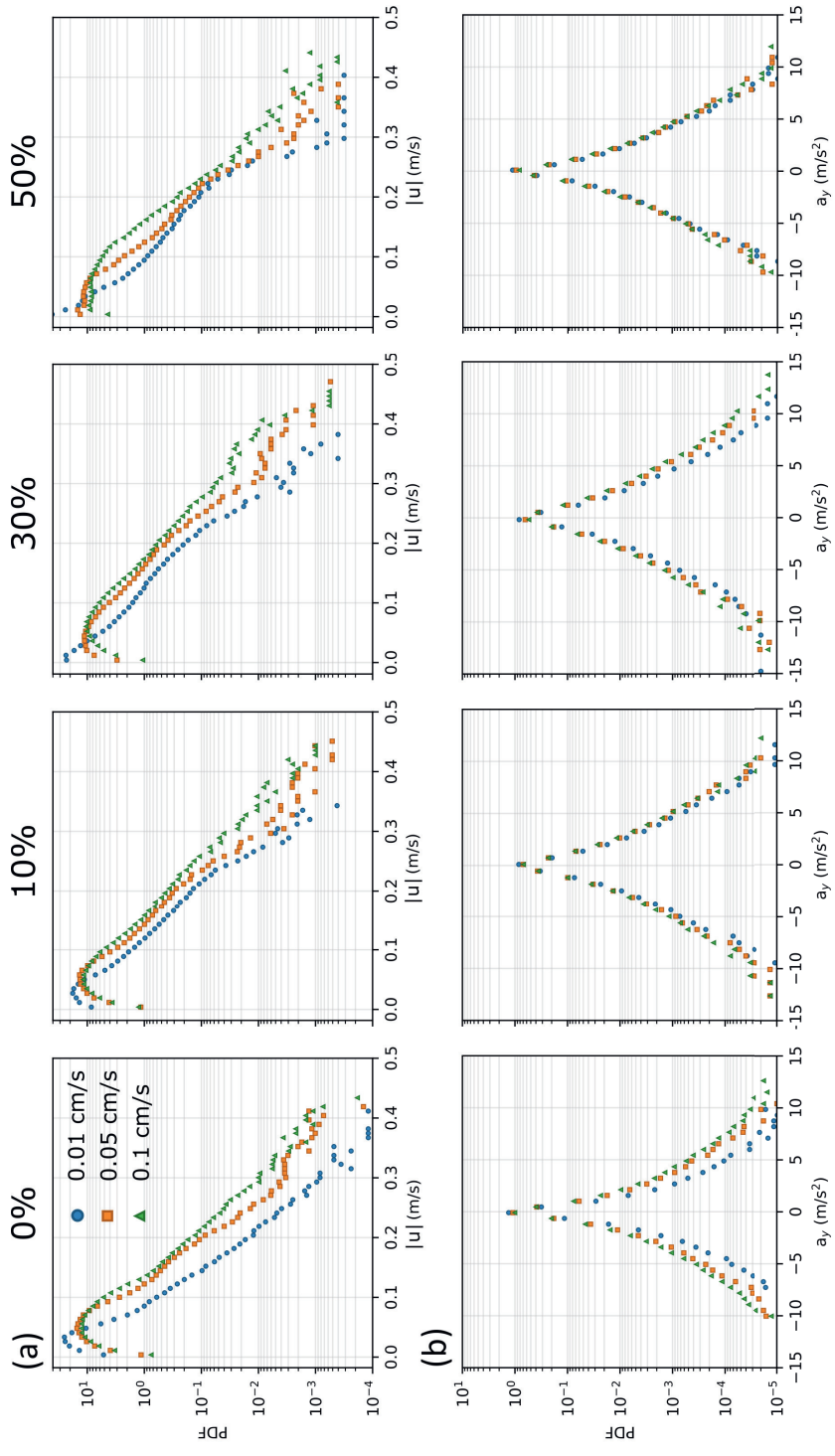


Figure S.4.3: Effect of GSV on the frequency distribution of the (a) liquid velocity magnitude ($|u|$) and (b) axial acceleration (a_y) at constant solid VOFs.

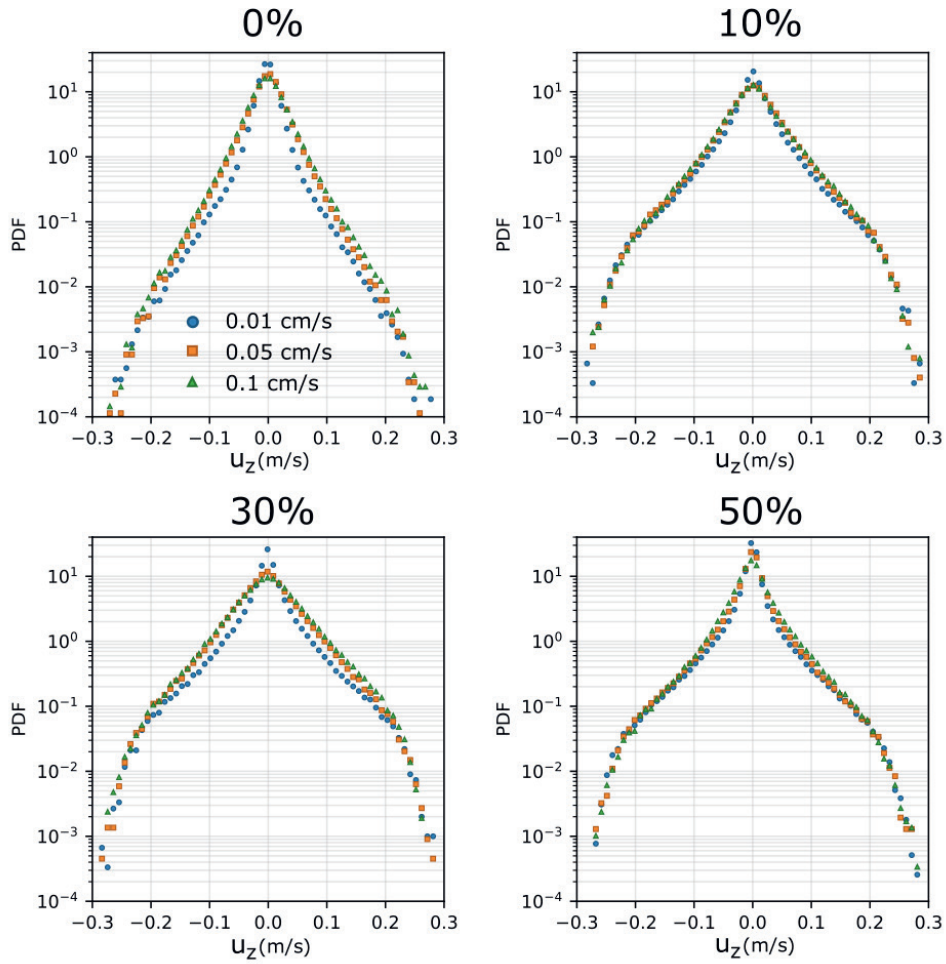


Figure S.4.4: Effect of GSV on the frequency distribution of the lateral liquid velocity (u_z) at constant solid VOFs.

S.4.4. Effect of solid VOF on liquid velocity and acceleration

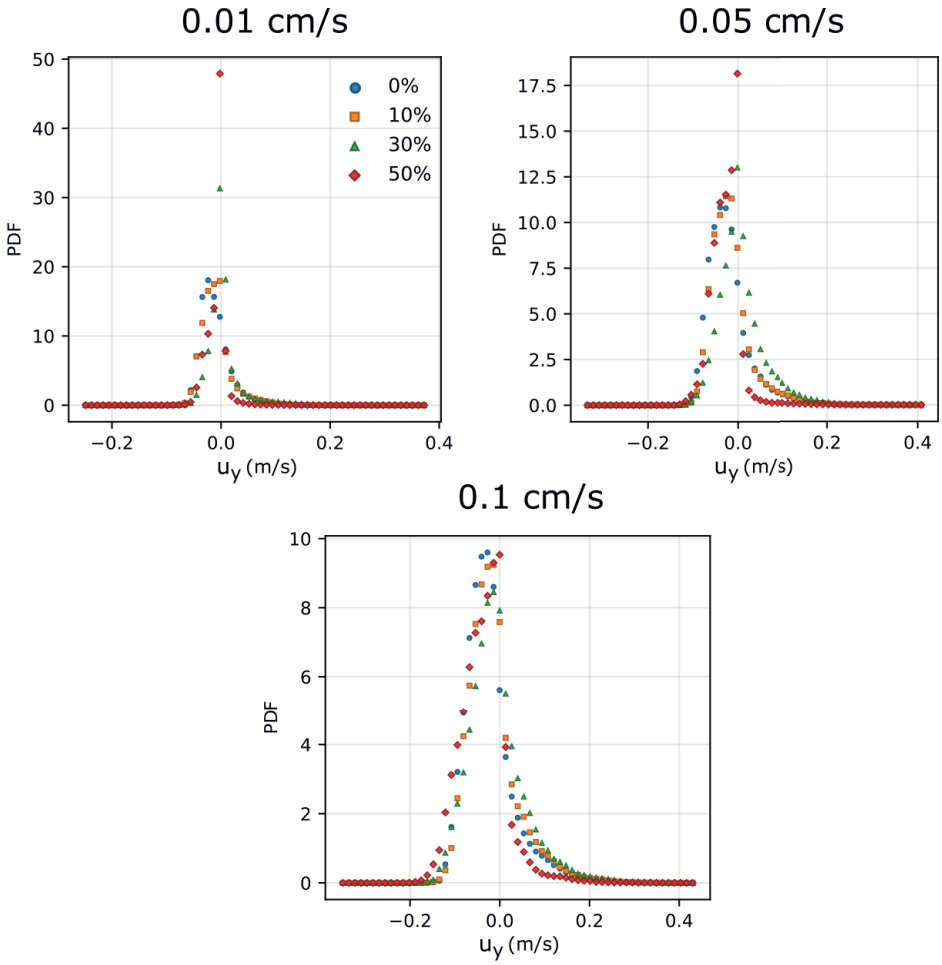


Figure S.4.5: Effect of solid VOF on the frequency distribution of the liquid axial velocity (u_y) at constant GSVs.

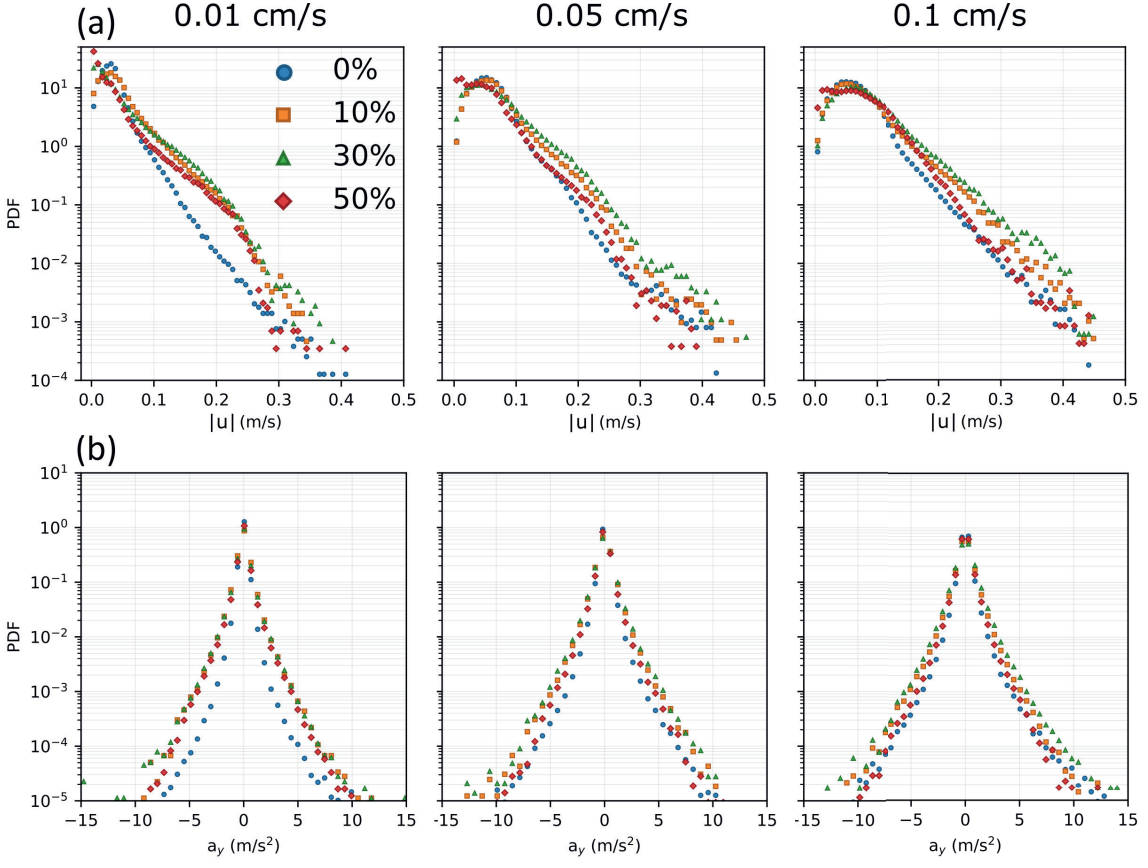


Figure S.4.6: Effect of solid VOF on the frequency distribution of the (a) liquid velocity magnitude ($|u|$) and (b) axial acceleration (a_y) at constant GSVs.

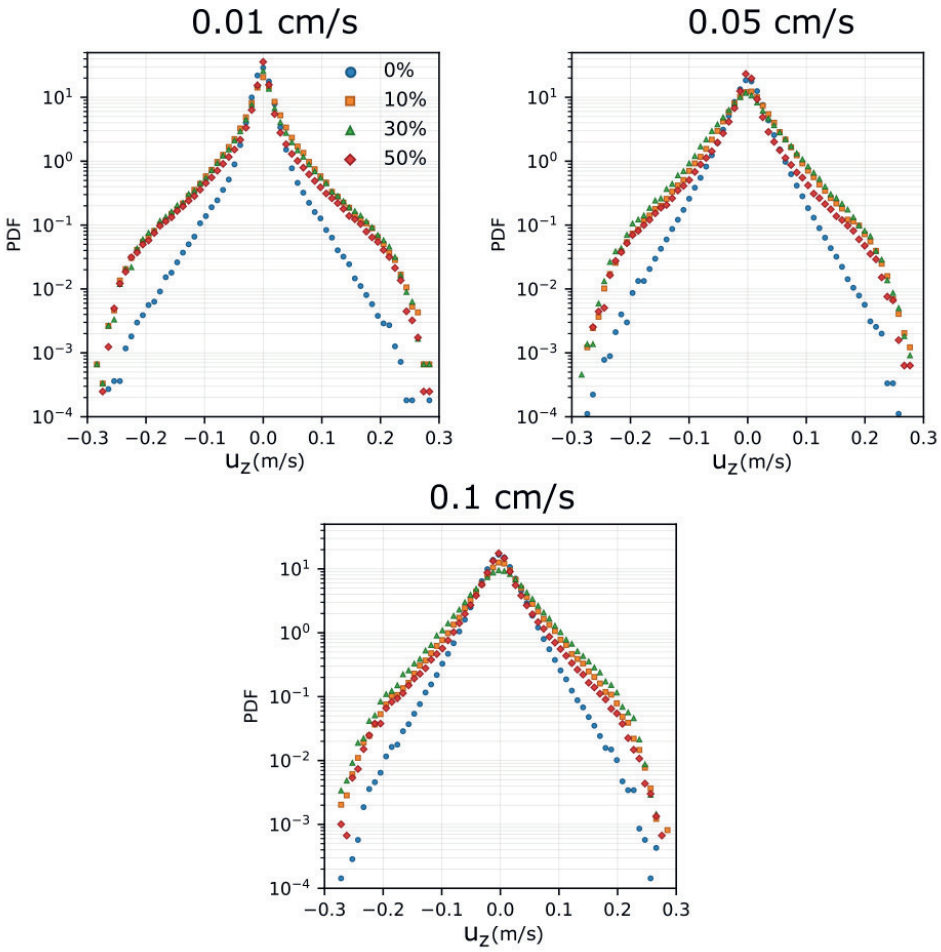


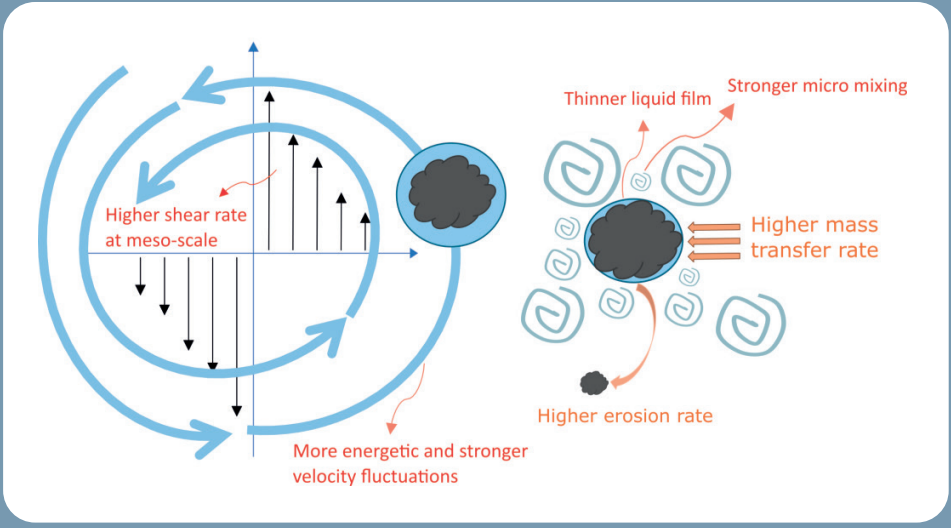
Figure S.4.7: Effect of solid VOF on the frequency distribution of the lateral liquid velocity (u_z) at constant GSVs.

Chapter 5

5

Chapter 5

Mechanistic Effects of Hydrodynamic Shear and Turbulence on Anaerobic Granule Properties in Calcium-Rich Wastewater



To be submitted as:

Eslami, H., Bruning, H., Krug, J., van de Wetering, A., Rijnaarts, H.H.M., and Sudmalis, D. Mechanistic Effects of Hydrodynamic Shear and Turbulence on Anaerobic Granule Properties in Calcium-Rich Wastewater.

Abstract

Calcification of granules in anaerobic granular sludge reactors can influence granule's structure, activity, and reactor performance. However, the role of hydrodynamics in calcification is poorly understood. In this study, granule development in two "low-seeded" lab-scale expanded granular sludge bed (EGSB) reactors at distinct hydrodynamic conditions controlled via gas sparging i.e., high shear (HSR) and low shear (LSR) reactors, were compared to slow-mixing continuous reactors (shear-free), all operated under calcium-rich conditions. The liquid velocity fields in EGSBs were quantified using three-dimensional particle tracking velocimetry (3D-PTV). The average liquid velocity was 0.075 and 0.043 m/s in HSR and LSR, respectively with average shear rates of 0.125 1/s in LSR and 0.25 1/s in HSR. Average methanogenic activity of developed granules was 0.65, 0.38 and 0.1 g CH_4-COD/gVSS/day in HSR, LSR and shear-free reactors, respectively. This difference is likely due to reduced mass transfer efficiency in shear-free reactors during granule development. Surprisingly, granules developed in the LSR were smaller (1–1.5 mm) compared to HSR (1.5–2 mm) and were more extensively calcified (~ 83 versus 185 gCa/kgdry-weight). SEM-EDS analysis showed that the calcium in HSR granules had a gradient with increasing calcium content towards granule's center leaving the granule's surface porous, whereas in LSR granules such gradient was either absent or opposite, i.e., with highly calcified outer surface thereby decreasing it's porosity. Statistical analysis of the turbulence characteristics showed that the HSR exhibited stronger velocity fluctuations and higher overall kinetic energy. However, the dominant turbulent eddy size at granule scale in the LSR was smaller. These small-scale flow structures likely generated higher frequency velocity fluctuations, resulting in increased mechanical stress at the granule surface and enhanced mass transfer of Ca^{2+} into the granule structure. Based on these findings, limiting small-scale flow structures in reactors, by e.g., controlling gas-liquid relative velocity may mitigate excessive granule calcification.

Keywords: Anaerobic granular sludge; Hydrodynamics; 3D particle tracking velocimetry; Turbulent fluctuation; Saline wastewater

5.1. Introduction

Anaerobic digestion (AD) is a well-established biological process for the treatment of organic-rich wastewater due to low sludge production, and the generation of biogas as a renewable energy source (Liu and Tay (2004)). Within AD technologies, anaerobic granular sludge reactors (AGSRs) have emerged as a robust and efficient approach due to high biomass retention, compact design, and efficient treatment capabilities (van Lier et al. (2015)). The performance of AGSRs largely depends on the formation, activity and stability of anaerobic granules, which are dense, self-immobilized spherical biofilms. These granules are primarily composed of microbial consortia embedded within a matrix of extracellular polymeric substances (EPS), which facilitate the retention of biomass and thereby effective degradation of organics (Liu and Tay (2002)).

Many industries relying on AGSRs generate calcium-rich effluents. These include paper recycling, dairy, and gelatin plants (Owodunni and Ismail (2021)). While Ca^{2+} supports granular structure, by bridging negatively charged functional groups of EPS, excessive accumulation leads to precipitation of $CaCO_3$ or precipitates associated with e.g., PO_4^{3-} and S^{2-} (Cunha et al. (2018)). This is particularly evident in the core with elevated local pH, but can also take place at neutral pH on the outer surface, provided that the Ca^{2+} content of wastewater is high. This progressive mineral precipitation alters the internal and external structure of granules by blocking pores and channels, reducing space for microbial cells and substrate mass transfer, deactivating microbial activity, and ultimately impairing reactor performance (Yu et al. (2019)).

So far, several strategies have been proposed to mitigate granule calcification, including the use of quorum-sensing signal molecules to stimulate microbial activity (Fu et al. (2022)), pH adjustment to protonate EPS and weaken Ca^{2+} binding association (Lian et al. (2023), Peng et al. (2024)). However, application of these approaches in full-scale reactors remains challenging due to near-neutral pH requirements for methanogenesis and the high costs associated with continuous chemical dosing. Other factors also expected to significantly affect calcification are the mass transfer from liquid and mechanical stresses on granule's surface, neither of which have been explored in detail.

Based the above, hydrodynamics in AGSRs must play a crucial role, because it determines bulk mixing at the reactor scale and also creates distinct flow conditions in the vicinity of individual granules. These local flow fields are known to profoundly influence the physical, chemical, and bio-logical properties of biofilms by imposing mechanical stresses and regulating the advection–diffusion of substrates and ions like Ca^{2+} (Tsagkari et al. (2022)). For example, Tsagkari et al. (2022) and Pizzi et al. (2025) demonstrated that in single phase flows when biofilms are grown on solid substrates local shear stress and turbulence characteristics shape their density, porosity, size and thickness.

Since granules are essentially spherical biofilms, the above should also apply. Gao et al. (2024b) recently showed that the viscoelasticity of granular EPS, and therefore the mechanical strength of granules, may vary when treating the same wastewater in reactor configurations differing in their mixing intensity. Consistently, low shear has been associated with the formation of larger, fluffy granules (with non-smooth surfaces) of low density, whereas high shear favors the development of smaller, denser, and more compact granules (Liu and Tay (2002)).

Local flow characteristics and hence mechanical shear stress experienced by microbial granules arises from multiple hydrodynamic interactions, such as relative motion between granules and the surrounding fluid (drag force), local velocity gradients (shear rates) in the liquid phase, and turbulent velocity fluctuations. Turbulence in multiphase flows involving rising gas bubbles, such as those in AGSRs, is mainly generated through two mechanisms: shear-induced turbulence (SIT) and bubble-induced turbulence (BIT) (Risso (2018)). Additionally, granule-to-granule interactions contribute to mechanical stress by exerting both normal and tangential forces on granule surfaces (Ren et al. (2009b)). The relative dominance of these mechanisms depends on operational parameters such as liquid upflow velocity, bubble size distribution and generation frequency, granule concentration, and the rheological properties of the wastewater. These parameters are interdependent and can mutually alter each other's characteristics, thereby modulating both the magnitude and type of mechanical stress acted on granules and the mass transport across different spatial scales (An et al. (2024b)).

Although, there is a general consensus on the significance of hydrodynamics in shaping granules, the understanding of local shear and turbulence effects is still

lacking. This is because most hydrodynamic characterization of flow in AGSRs focused on empirical models and correlations to estimate hydrodynamic shear rates within reactors, thereby reporting global or macroscale shear rates (Pereboom and Vereijken (1994), Wu et al. (2006), Ren et al. (2009c), Kundu et al. (2014b), Wu et al. (2012b)). Detailed and systematic experimental investigation to capture the local flow characteristics are needed.

The latter is partially addressed in recent investigations employing advanced experimental fluid dynamics tool i.e., particle image velocimetry (PIV) in specifically designed (often flat and thin) AGSRs. Here, most work has focused on linking hydrodynamic shear from velocity fields to biogas production and bubble characteristics (Zhang et al. (2012), Jiang et al. (2016)). For example, enhanced biogas production was reported within specific shear-rate ranges, including 24–48 1/s Jiang et al. (2014), 24–37 1/s at the microscale, and 32–63 1/s at the mesoscale (Zhang et al. (2011)). (Wu et al. (2012b)) investigated the effect of rising bubbles on shear conditions in the vicinity of granules, and showed that bubble-induced shear rates are substantially higher than those generated by the bulk liquid flow. There is no study in AGSRs to date studying the turbulence effects on properties of anaerobic granules. Hence, to date such effects have only been studied on aerobic biofilms in single phase flows (Tsagkari et al. (2022), Pizzi et al. (2025)).

In this study, we aim to advance the understanding of the interplay between bulk shear and turbulence on the properties of anaerobic granules in a calcium-rich wastewater. Two different configurations were considered: (i) shear-dominated system, where reactors hydrodynamics were controlled by nitrogen gas sparging at varying gas superficial velocities (GSV), and (ii) shear-free system, where granules were subjected to mild mixing. Hence, the effects of the wastewater composition and hydrodynamics on granule properties were isolated. Hydrodynamic characterization was carried out using three-dimensional particle tracking velocimetry (3D-PTV). Flow characteristics were analyzed from both Eulerian and Lagrangian perspectives. To the best of our knowledge, this is the first study investigating the effects of turbulence induced by gas bubbles on microbial granules, particularly in Ca^{2+} rich streams. The findings provide new insights into the dominant mechanisms governing granule property changes and calcification in AGSRs, thereby supporting improved reactor design and operation strategies.

5.2. Materials and methods

5.2.1. Reactor setup

The experimental setup consisted of four continuous-flow reactors: two shear-dominated and two shear-free reactors, all connected to a shared 50 L cylindrical recirculation tank (Figure 5.1). The use of a shared tank ensured that all reactors were subjected to identical substrate concentration, pH, and nutrient composition. The two shear-free reactors consisted of 2 L Schott bottles and were operated as control units to decouple the medium's effect from hydrodynamics on the evolution of granule properties. The shear-dominated reactors were identical cylindrical columns with an internal diameter of 10 cm, height of 2 m and an active volume of 7 L. Each reactor consisted of three main sections: a gas and liquid distribution section at the base, a reacting section (active volume), and a three-phase separator at the top (Figure 5.2). The liquid distributor comprised a 10 cm calming section filled with 1 cm glass beads, followed by a perforated plate with 4 mm diameter holes and a 500 μm mesh to prevent granules from entering the calming zone. Gas distributor was a spider-type sparger with six arms, each fitted with a porous metal diffuser (20 μm average pore size), to generate fine bubbles.

5.2.2. Operating condition and flow control

The shear-dominated reactors were operated in a separate flow loop connected to the shared recirculation tank. The main components of each loop included a gear pump (Gather Industrie GmbH, Germany) equipped with a variable frequency drive (VFD), and a Coriolis mass flow meter (Bronkhorst, The Netherlands) with an integrated PID controller for flow adjustments. This reactor setup configuration enabled steady, pulsation-free pumping, precise flow control and stable operating conditions throughout the experiment, while compensating for potential pressure variations.

In the shear-dominated reactors, the liquid flow rate was maintained at 2 L/min, corresponding to a superficial velocity of 15 m/h. This velocity was chosen to ensure fluidization of granules and to remain within the typical operational range of the expanded granular sludge bed (EGSB) reactors. To generate two different hydrodynamic conditions in the reactors, nitrogen gas was sparged into the reactors at two different flow rates: 0.6 L/min in one reactor, referred to as the high-shear

reactor (HSR), and 0.2 L/min in the other, referred to as the low-shear reactor (LSR) (Table 5.1). Based on visual observations (video link), the higher gas flow in the HSR promoted more intense fluidization of the granules, while the lower flow in the LSR provided comparatively milder conditions.

In parallel, the shear-free reactors were operated under minimal hydrodynamic stress. These reactors were placed on a low-speed shaker to introduce only mild mixing, and their medium was continuously renewed with the effluent of LSR and HSR at 0.5 L/h using a peristaltic pump. Shear-free reactor 1 received the effluent from the HSR, and shear-free reactor 2 from the LSR. The effluent from both reactors was returned to the common recirculation tank (see Figure S.5.1 for the tank design), ensuring that all reactors remained connected to the same substrate pool.

The substrate and nutrients were continuously supplied to the shear-dominated reactors using two peristaltic pumps. Based on a diffusion–reaction model in a spherical coordinate system COD concentration of 65 mg/L was calculated as the minimum bulk COD concentration required to prevent substrate diffusion limitations within the granule core (further details are provided in section S.5.2). Hence, the flow rate of these pumps was conservatively adjusted to maintain the bulk COD concentration above this value. The experiments were conducted in a temperature-controlled room, with the temperature maintained at 30 °C.

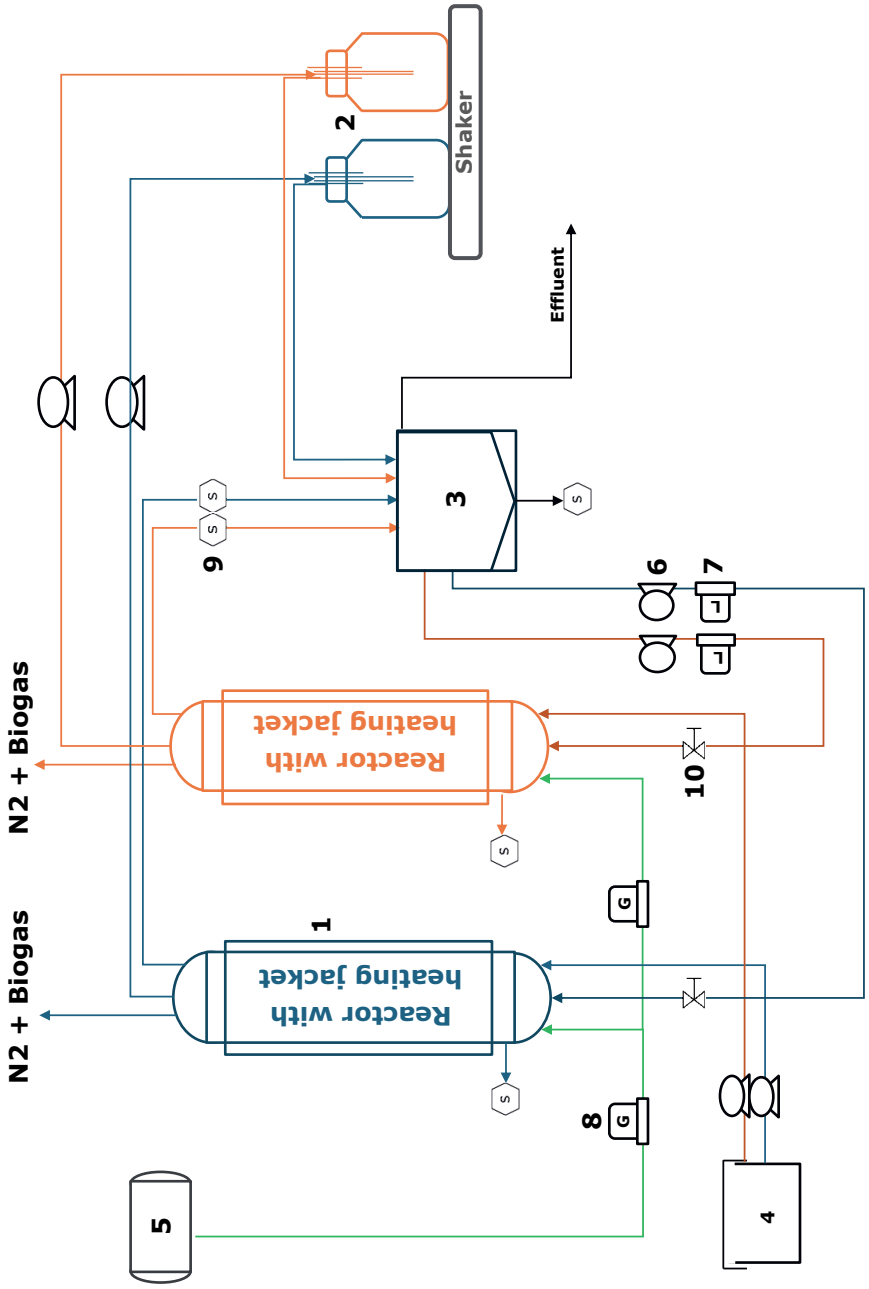


Figure 5.1: Schematics of the experimental setup. (1) Shear-dominated reactor, (2) shear-free reactor, (3) recirculation tank, (4) influent tank maintained at 4 °C, (5) nitrogen tank, (6) pump, (7) liquid mass flow controller, (8) gas mass flow controller, (9) sampling point, and (10) valve.

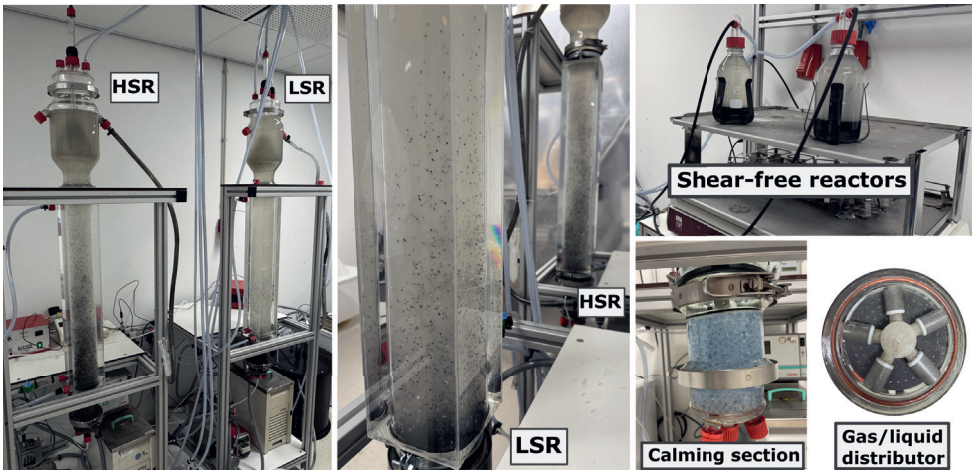


Figure 5.2: Photograph of experimental setup. Shear-dominated reactors, refered to as high shear reactor (HSR) and low shear reactor (LSR), were operated with varying gas flow rates. Shear-free reactors served as controls to isolate the medium effect from hydrodynamic influence. The calming section and the gas/liquid distributor ensured uniform phase distribution at the reactor inlet.

5.2.2.1. Medium and inoculum

The nutrient medium composition was based on Vallero et al. (2003), with the following final concentrations in the feed in (mg/L): $CoCl_2 \cdot 6H_2O$ (1.2), $FeCl_2 \cdot 4H_2O$ (1.2), $MnCl_2 \cdot 4H_2O$ (0.3), $ZnCl_2$ (0.03), H_3BO_3 (0.03), $(NH_4)_6Mo_7O_{24} \cdot 4H_2O$ (0.054), $CuCl_2 \cdot 2H_2O$ (0.018), $Na_2SeO_3 \cdot 5H_2O$ (0.06), $NiCl_2 \cdot 6H_2O$ (0.03), EDTA (0.6), Na-Resazurin (0.3), and HCl 36% (0.216 mL/L). The Macronutrient concentrations (in g/L) were: NH_4Cl (1.02), $MgSO_4 \cdot 7H_2O$ (0.05), $CaCl_2 \cdot 2H_2O$ (1.47), KH_2PO_4 (0.22), and $NaHCO_3$ (0.30). The concentration of $CaCl_2 \cdot 2H_2O$ was adjusted to obtain a Ca^{2+} concentration of 400 mg/L in the medium. The influent COD was composed of acetic acid, propionic acid, sodium glutamate, and tryptone in COD proportions of 50:25:15:10, respectively.

$NaHCO_3$ was added during reactor start-up to neutralize the pH. Further, the pH was maintained at 7.5 to increase the rate of calcification. This was done by 0.5 L/min CO_2 injection into the recirculation tank thereby also offsetting continuous pH increase by N_2 sparging. COD and pH monitoring data of all reactors are shown in Figure S.5.2.

The inoculum was anaerobic granular sludge sampled from a full-scale EGSB reactor

treating paper mill wastewater (Eerbeek, The Netherlands). A total of 200 g (wet weight) of granules with a size range of 1–2 mm were inoculated into each reactor. This corresponds to a concentration of 4.13 gVSS/L in the working volume of the shear-dominated reactors and 14.4 gVSS/L in the shear-free reactors.

Table 5.1: Operating conditions.

Reactor	Liquid flow rate ($L\,min^{-1}$)	Gas flow rate ($L\,min^{-1}$)	GSV ($cm\,s^{-1}$)
LSR	2	0.2	0.042
HSR	2	0.6	0.127
Shear-free 1	0.0083	0	0
Shear-free 2	0.0083	0	0

5.2.3. Experimental setup for 3D-particle tracking velocimetry (3D-PTV)

5.2.3.1. Preparation and conduct of measurement

The velocity field was obtained using three-dimensional particle tracking velocimetry (3D-PTV). The imaging setup consisted of a high-power blue LED light source ($100 \times 300\,mm^2$), and an integrated multi-camera system (MiniShaker, LaVision GmbH) equipped with 4 high-speed cameras with a fixed relative orientation (Figure 5.3). Each camera was equipped with a Tamron lens (focal length of 12 mm) and a full HD resolution (1984×1264 px) with a frame rate (f_{fps}) of up to 121 Hz at maximum resolution. To selectively capture signals from tracer particles, improve signal-to-noise ratio and minimize interference from bubbles, fluorescent particles were used as tracers, and a 540 nm long-pass filter was mounted in front of each lens.

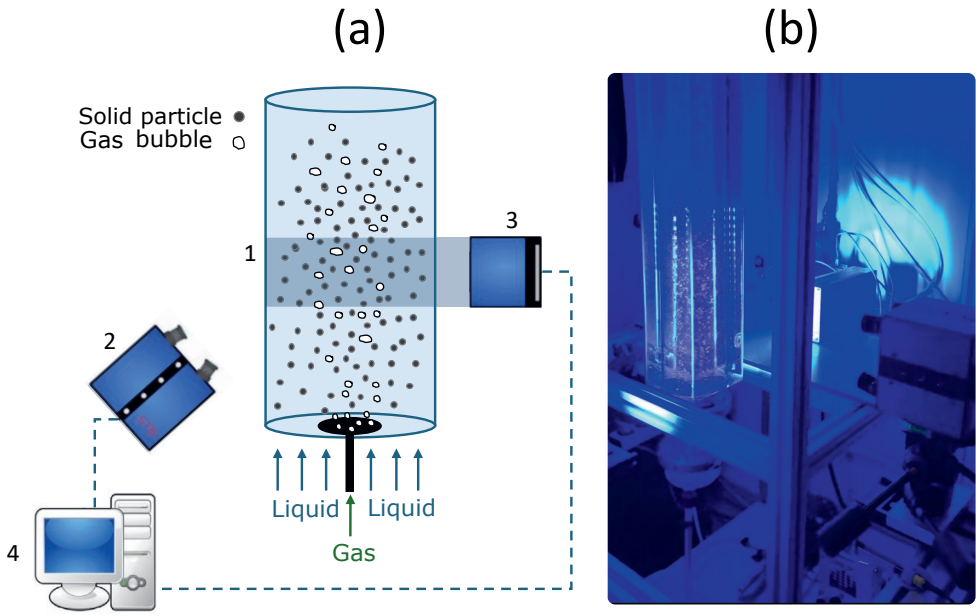


Figure 5.3: (a) Photograph of the PTV experimental setup showing the four cameras and the LED light source pointing at the measurement volume; (b) instantaneous tracer particles image; (c) visualization of detected particle tracks, displayed with a track length of 50 time steps and color-coded by the stream-wise velocity component (along Y-axis).

Hydrodynamic characterizations were carried out in a dedicated imaging reactor (Figure 5.3), which had the same geometry as the shear-dominated reactors. Flow measurements were performed both before and after the biological experiments to assess potential changes in hydrodynamic conditions during the course of experiments (Figure S.5.8). The inlet sections of each reactor, including the liquid and gas distributors, were installed on the imaging reactor, thereby ensuring that the flow conditions in each reactor were accurately replicated.

The imaging setup was mounted on a custom-built vertical traverse system, allowing calibrations (see section S.5.4) and measurements to be performed along the reactor axis. For each experiment, fluorescent tracer particles were dispersed in the recirculation tank and pumped into the reactor to achieve homogeneous distribution, resulting in an approximate seeding density of 0.02 ppp. This density provided sufficient spatial coverage to resolve the flow fields while minimizing the occurrence of ghost particle artifacts (Schanz et al. (2016), Hofmann et al. (2022)).

For each measurement, particle images were recorded from four camera views at a

frame rate of 208.5 Hz with an exposure time of 200 μs. This frame rate was selected to ensure that the displacement of the fastest particles remained within 10–20 pixels between successive frames (Schanz et al. (2021)). Imaging was conducted over three 25-cm sections along the vertical axis, covering a total height of 75 cm of the reacting section. In each section, 4,000 images were recorded, corresponding to 19.2 s of flow time, yielding a total raw data volume of 336 GB. All images were subjected to pre-processing following the procedure described in Eslami et al. (2025).

A Lagrangian particle tracking (LPT) technique, Shake-the-Box (STB) (Novara et al. (2023)), was employed to conduct time-resolved three-dimensional particle tracking. STB was chosen because it significantly improved conventional 3D-PTV by delivering flow data with high spatial resolution, achieved through increased particle seeding densities (up to 0.2 ppp (Schröder and Schanz (2023)), while maintaining accurate 3D particle reconstruction at an affordable computational cost. Detailed STB operating parameters used in this study are shown in Table S.5.2.

5.2.3.2. Lagrangian particle track data processing

Lagrangian particle trajectories were analyzed to determine the turbulence characteristics. The instantaneous particle velocities along each trajectory were computed from the real-time particle positions using a central difference scheme. Velocity fluctuations for each component were defined as:

$$u_i'(t) = u_i(t) - \bar{u}_i, \tag{5.1}$$

where $i \in \{x, y, z\}$ and $\bar{u}_i = \langle u_i(t) \rangle$ is the mean velocity along the trajectory. The root-mean-square (RMS) velocity fluctuation was then calculated as:

$$u_{i,\mathrm{RMS}}' = \sqrt{\langle (\, u_i(t) - \bar{u}_i \,)^2 \rangle}. \tag{5.2}$$

The local turbulent kinetic energy (TKE) was calculated from the three velocity components as:

$$TKE = \frac{1}{2}\left(u'_x(t)^2 + u'_y(t)^2 + u'_z(t)^2\right). \tag{5.3}$$

The temporal correlation of velocity magnitude fluctuations was quantified using the velocity autocorrelation function (ACF). It was defined as (Xia et al. (2013)):

$$\rho_{|u|}(\tau) = \frac{\langle |u|'(t+\tau)\,|u|'(t)\rangle}{\left\langle (|u|'(t))^2\right\rangle}, \tag{5.4}$$

where $\tau = n\Delta t$ is the time lag. Δt corresponds to the sampling time interval of the measurement, given by the inverse of the acquisition frame rate ($\Delta t = 1/f_{\mathrm{fps}}$), and n is the number of frames between the two data points being compared.

The energy spectra of the liquid-velocity fluctuations were calculated using the Welch method (Welch (1967)). In short, firstly, each velocity signal from individual particle trajectories was divided into overlapping segments, and the energy spectrum of each segment was determined using the Fast Fourier Transform (FFT). The spectrum of the signal was then obtained by averaging the spectra calculated for each segment, and the overall energy spectrum of the flow was computed by ensemble-averaging over approximately 2000 trajectories.

5.2.3.3. Eulerian field reconstruction and 3D shear-rate calculation

The Eulerian velocity field was obtained by converting the Lagrangian STB measurements of particle velocities to the three-dimensional Eulerian grid, which was used for calculating the local time-averaged velocity gradients. A voxel size of 24 pixels with an overlap of 75% was applied, resulting in a vector grid spacing of 6 pixels (corresponding to 1.03 mm). Velocity values were calculated only for voxels containing at least five particle samples, and a second-order spatial polynomial fit was employed for velocity interpolation.

Local velocity gradients were obtained from the reconstructed velocity field. The symmetric strain-rate tensor was then calculated as:

$$S_{ij} = \frac{1}{2}\left(\frac{\partial u_i}{\partial x_j} + \frac{\partial u_j}{\partial x_i}\right), \tag{5.5}$$

Where $i, j \in \{x, y, z\}$. The eigenvalues of this tensor represent the principal strain rates. The maximum shear is obtained as half the difference between the largest and smallest principal values. Accordingly, the 3D shear rate was defined as:

$$\dot{\gamma}_{3D} = \frac{\lambda_{\max} - \lambda_{\min}}{2}, \tag{5.6}$$

where $\lambda_{\max}$ and $\lambda_{\min}$ are the maximum and minimum eigenvalues of S_{ij}. This provides the maximum shear rate at a given location and is independent of coordinate orientation.

The time-averaged velocity field and the associated shear rate sensitivity to the chosen averaging time interval is shown in section S.5.6. FFT spectra from three representative points in each reactor suggested that a characteristic fluctuation timescale of 4.7 s can be used as a averaging interval for both reactors to capture dominant reactor-scale flow fluctuating period (see section S.5.7). Accordingly, velocity fields were averaged over this timescale, providing a representative description of the flow features, and the mean shear rate was subsequently calculated from these velocity fields.

5.2.4. Analytical methods

5.2.4.1. Particle Size distribution (PSD) and strength of granules

The size of the granules was determined using a macroscope (Nikon SMZ800, Japan). For each sample, 200 granules were randomly selected for measurement. The major and minor axes of each granule were measured using Image Focus Alpha software (Euromex, The Netherlands), and the equivalent diameter was calculated. The PSD is reported as the percentage of granules within a given size range relative to the total number of granules.

5.2.4.2. Methanogenic activity with the reactor influent

Methanogenic activity of the granules was assessed in duplicate 120 mL serum bottles. Each bottle was inoculated with 0.7–0.8 g wet sludge and fed with 50 mL of medium containing the same macro- and micronutrients and substrate composition described for reactor influent (section 5.2.2.1). Incubations were performed at 35 °C and 44 rpm, and biogas production was monitored over 5 days by recording headspace pressure twice per day. Biogas composition was determined by gas chromatography (GC; Shimadzu GC-2010, Kyoto, Japan), and volatile fatty acids were quantified with a GC system (Agilent 7890B, Santa Clara, CA, USA) Gagliano et al. (2020). The procedure and methanogenic activity calculation approach were adapted from Holliger et al. (2016). The initial COD concentration corresponded to the reactor influent COD during reactor operation (10944 and 16772 mgCOD/l).

5.2.4.3. Calcification and internal structure characterization of granules

Powder X-ray diffraction (XRD): to identify the crystalline form of calcium precipitates, XRD measurements were performed using a Bruker D8 Advance diffractometer (Bruker AXS) with Cu-Kα radiation operated at 40 kV and 40 mA. Scans were recorded in the angular range of 10°–70° (2θ) with scanning speed of 0.24° 1/min. The X-ray diffractograms were evaluated by the software DIFFRAC.EVA V5 (Bruker AXS).

Inductively coupled plasma optical emission spectrometry (ICP-OES): calcium concentration in granules was determined by ICP-OES (PerkinElmer Avio® 500) in digested granules according to (Sudmalis et al. (2020)). In short, 0.1 g of dried granules were mixed with 4 ml of nitric acid (HNO_3), 1 ml of perchloric acid ($HClO_4$), 1 ml of hydrogen peroxide (H_2O_2), and 1 ml of ultrapure water. The biomass was then completely digested in a microwave oven (Milestone S.r.l., ETHOS 1).

Scanning electron microscopy (SEM) and energy-dispersive X-ray spectroscopy (EDX): SEM and SEM-EDX were used to characterize the granule's surface morphology and elemental composition of their cross-sections. For SEM-EDX analysis granules were fixated for 24 h at 4 °C in the reactor medium at 2.5% glutaraldehyde concentration. Subsequently granules were rinsed with the nutrient medium and dehydrated in graded series (10%, 30%, 50%, 70%, 80%, 90%, 96%,

100%) of ethanol for 10 min in each concentration and by repeating the last step for additional 20 min. Next, the samples were critical point dried (CPD) with carbon dioxide (CPD300, Leica, Vienna, Austria). Finally, the granules were sliced with a thin blade under a microscope and glued with a carbon glue (Leit-C, EMS, Hatfield, PA, USA) to the sample stubs for sputter coating with approximately 12 nm of tungsten. The coating was done by tilting the sample stubs (45°) in two different directions to better cover their irregular shapes (SCD 500, Leica, Vienna, Austria). Imaging was done at room temperature in a field emission scanning electron microscope (Magellan 400, FEI Company, Oregon, USA) equipped with an energy dispersive X-ray detector. For back scattered electron imaging the acceleration voltage and beam current were 2 kV and 13 pA, respectively. Energy dispersive X-ray spectroscopy was performed at an acceleration voltage of 10 kV and a beam current of 0.4 nA. The images were processed using AZtec software (OXFORD Instruments).

Magnetic resonance imaging (MRI): MRI was used to study the internal structure of granules. For this, one set of granules was randomly sampled from each reactor (HSR, LSR, Shear-free 1, Shear-free 2). A second set was selected for their visual appearance as calcified (Figure S.5.16).

All samples were inserted into a 5 mm NMR tube (Hilgenberg). A 14.1 T standard-bore magnet equipped with an Avance III console and a Micro5 probe base with a maximal gradient of 3 T/m, a 10 mm-^{1}H saddle coil and ParaVision 6.0.1 was used (Bruker, Ettlingen, Germany). T_1-weighted images with several slices were used to construct so called virtual slices through various intact granules. Slice locations were chosen to coincide with the center of various granules. For the T_1-weighted images the following parameters were used: 2D spin echo sequence (MSME), repetition time 550 ms, echo time 2.9 ms, number of averages 12, experiment time 10 min 34 s, field-of-view (4.5 x 4.5) mm^2, matrix 96 x 96, spatial resolution 47 x 47 μm, receiver bandwidth 100 kHz, pulse excitation and refocusing bandwidth 4.2 kHz, 3–6 slices with a slice thickness of 0.5 mm. For visualization, the image intensities were scaled uniformly to the maximum image intensity across slices, excluding slices with hyperintense signal due to so-called susceptibility artefacts (as seen in Figure S.5.16B) and magnified by a factor of 2 without interpolation (nearest neighbour), using FIJI/ImageJ (Schindelin et al. (2012)).

5.3. Results

5.3.1. Flow characteristics in shear-dominated reactors

The velocity measurements were conducted in three 25 cm sections along the reactor axis, covering a total height of 75 cm from the bottom (section 1) to the top (section 3). Figure 5.4 shows the time-averaged axial liquid velocity in multiple XZ cutting planes together with an iso-surface representation,highlighting persistent upward (red) and downward (blue) flow zones. These zones appeared consistently across all three sections, indicating the presence of a large-scale recirculation pattern (reactor-scale eddy) that governs mixing in the reactors. This large eddy, mainly, originated from the rising gas bubbles released by the spider-type sparger. Because the bubble generation was not completely uniform across the sparger arms, regions with higher gas holdup developed above the more active arms, where buoyant bubbles intensified the upward liquid velocity. The liquid subsequently returned downward through areas of lower gas holdup, such as above the less active arms and along the reactor walls. Hence, albeit the overall average liquid velocity differed (0.075 m/s in high shear reactor (HSR) and 0.043 m/s in low shear reactor (LSR)), both reactors contained reactor-scale eddies as would be expected in the reactor configurations applied.

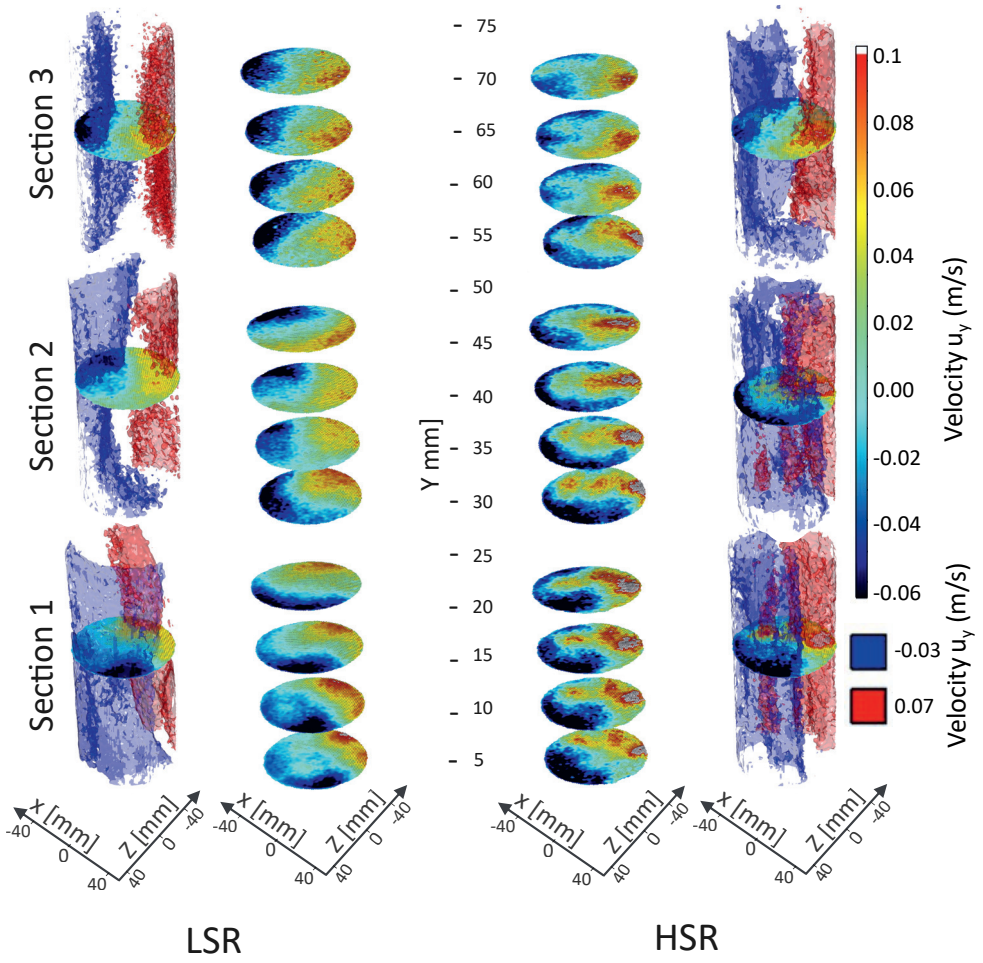


Figure 5.4: Time-averaged liquid axial velocity component (u_y) distribution at different cross-sections along the axis of the reactors, and iso-surfaces of u_y showing strong upward (red) and downward (blue) velocity regions. The average liquid velocity magnitude was 0.075 m/s in HSR, and 0.043 m/s in LSR.

5.3.1.1. Time-averaged velocity and shear rate distribution

The probability density functions (PDFs) of the time-averaged axial velocity component (u_y) and the shear rate over three sections in both reactors are presented in Figure 5.5. These statistics were extracted from the time-averaged Eulerian velocity fields reconstructed from particle track data. The most pronounced influence of the rising bubbles was observed in the axial velocity component. As illustrated in Figure 5.5a–c, the reactor with higher gas superficial velocity displayed broader u_y

distributions with longer tails on both sides, consistent with earlier observations by Martínez-Mercado et al. (2007). This indicates stronger recirculation and a higher degree of fluidization in the HSR compared to the LSR. With increasing height, the peaks of the distributions in both reactors shifted toward zero, likely due to a relatively more uniform gas distribution in the upper sections of the column and a reduced influence of the liquid inlet at the bottom, both of which contribute to stronger recirculation in regions closer to the inlet. The shear-rate PDFs (Figure 5.5d-f) showed that, at all heights, the HSR consistently exhibited distributions with longer tails, suggesting a greater probability of high shear-rate events (Mean and maximum shear-rate profiles along the reactor diameter are provided in section S.5.8). This trend directly corresponds to the u_y PDFs: broader velocity distributions imply larger velocity differences and, consequently, stronger velocity gradients in the HSR. No appreciable variations in shear-rate distributions were observed with reactor height. Thus, at the meso-scale, the granules were exposed to a similarly distributed shear field across the height of each reactor.

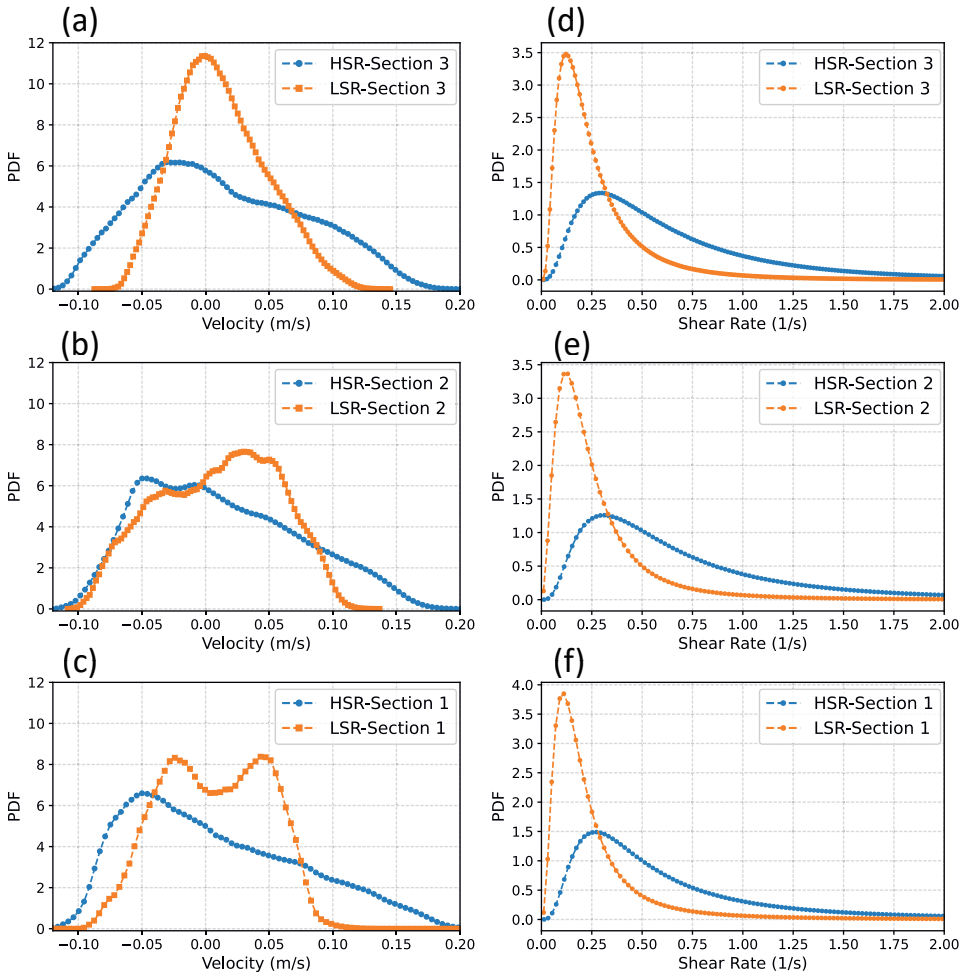


Figure 5.5: Probability density functions (PDFs) of time-averaged (a–c) axial velocity component (u_y) and (d–f) 3D shear rate in each section.

5.3.2. Pseudo-turbulence characterization

The Eulerian time-averaged velocity fields presented in the previous section resolved the flow features at the meso- and macro-scales, as the averaging process filtered out the velocity fluctuations. However, the agitation induced by rising bubbles generates a multiscale flow motion (Pope (2001)). Therefore, for the statistical analysis of instantaneous velocity fluctuations, the Lagrangian particle track data were used.

The frequency distribution of velocity magnitude fluctuations in both reactors are shown in Figure 5.6a. In both cases, the PDFs are right-skewed, and this feature

was more pronounced in the HSR, indicating a higher probability of extreme events (stronger fluctuations) in this reactor. The three-dimensional fluctuations of the flow can be further characterized by the turbulent kinetic energy. Figure 5.6b shows the 3D turbulent kinetic energy (3D-TKE) field in multiple planes of the lower section for both reactors. Since the primary source of velocity fluctuations is the rising gas bubbles, regions above the more active sparger arms exhibited higher TKE. The extent of high-TKE regions in the HSR was notably greater than in the LSR, confirming that the higher gas superficial velocity (GSV) induced more intense fluctuations and higher overall turbulence intensity.

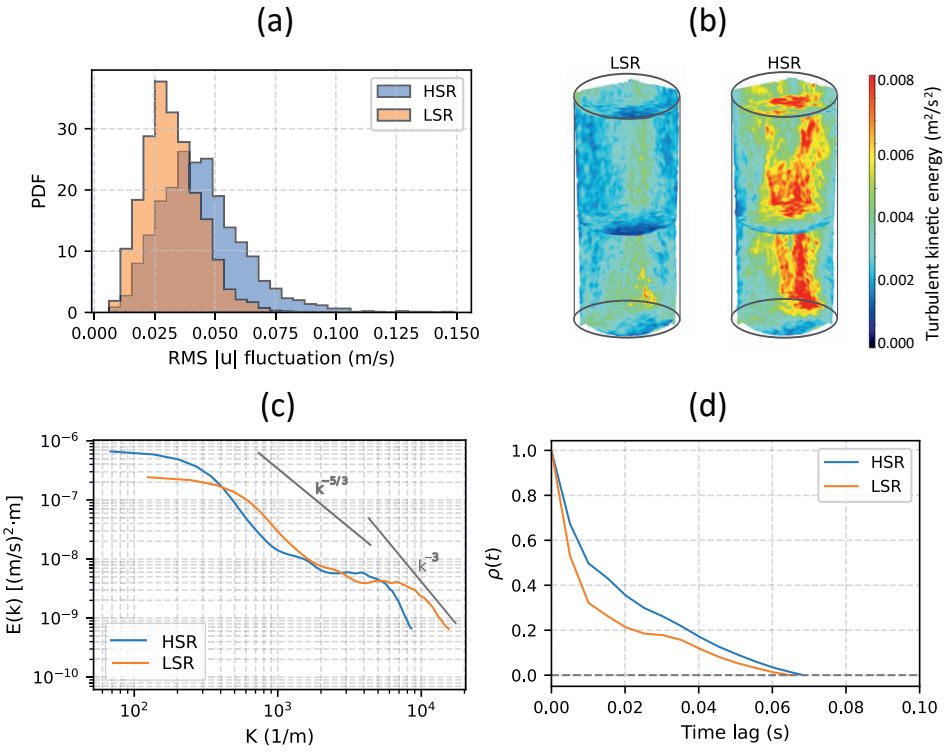


Figure 5.6: (a) Probability density function of root mean square (RMS) of velocity magnitude fluctuations, (b) time-averaged 3D turbulent kinetic energy field visualized in the X-Y, Z-Y, and three X-Z cross-sections, (c) Ensemble-averaged kinetic-energy spectra plotted as a function of the wavenumber k, where $k = 2\pi/\lambda$ represents the spatial wavenumber associated with eddies of characteristic size λ (Hidman et al. (2023)), (d) ensemble-averaged Lagrangian autocorrelation of velocity magnitude fluctuations.

Turbulence in fluids is primarily characterized by nonlinear energy cascade phenomena, typically expressed as the flux of kinetic energy across a range of scales. An energy spectrum makes these transfers observable by showing how energy is distributed over spatial scales (Alexakis and Biferale (2018)).

Figure 5.6c presents the ensemble-averaged energy spectra ($E(k)$) of velocity-magnitude fluctuations in both high-shear and low-shear reactors. The characteristic k^{-3} spectral slope commonly observed in bubbly flows (Riboux et al., 2010, Roghair et al., 2011, Risso, 2018, Innocenti et al., 2021, Rockstroh, 2022) was found in the spectra of both cases. This scaling originates from the mechanism of bubble-induced turbulence, where energy is injected directly at spatial scales on the order of the bubble diameter. Unlike classical turbulence, where large-scale motions supply energy that cascades through the inertial range, bubble wakes act as localized sources of small-scale energy input, leading to a balance between production and dissipation within that wavenumber range (Martnez Mercado et al., 2010).

At low wavenumbers ($k < 300$), the spectra indicate that the HSR contains more kinetic energy than the LSR. This agrees with the higher gas flow rate and larger bubbles in the HSR, which promote stronger recirculation (higher time-averaged liquid velocity) and consequently more large-scale fluctuation energy. At high wavenumbers, the spectra reflect wake-dominated agitation. Smaller bubbles in the LSR inject energy at higher wavenumbers, corresponding to smaller spatial scales. Moreover, the lower recirculation or upward liquid velocity in the LSR, potentially, increases the relative velocity between the gas bubbles and the surrounding liquid, thereby enhancing wake formation and, consequently, the small-scale energy input.

The Lagrangian velocity autocorrelation function provides valuable insight into the temporal structure of turbulent flows by quantifying how quickly a fluid particle loses memory of its past velocity along its trajectory (Xia et al. (2013)). This measure reflects the degree of coherence in the flow structures encountered by the tracer, and its decay characterizes the timescales over which velocity fluctuations remain correlated. Larger eddies tend to transport tracers for longer periods before they transition into another eddy, resulting in a slower decay of autocorrelation. Conversely, small-scale eddies produce frequent directional changes and higher-frequency velocity fluctuations, leading to a more rapid loss of correlation.

Similar to energy spectra analysis, the autocorrelation function (ACF) was calculated for each particle trajectory and subsequently ensemble-averaged to obtain the final curve. Figure 5.6d compares the Lagrangian autocorrelation of velocity magnitude fluctuations in both reactors. In the LSR, the correlation decays more rapidly to zero, indicating that velocity fluctuations lose coherence faster than in the HSR. This behavior suggests the dominance of smaller eddies with shorter characteristic timescales in the LSR. Hence, this is consistent with the kinetic energy spectra shown in Figure 5.6c.

5.3.3. Granule properties characterization

5.3.3.1. Size distribution of granules

At the start of the experiment, the majority of granules were within the size range of 1.5 to 2.5 mm (Figure 5.7). Over time, in the LSR, the granule size progressively decreased with 1.0–1.5 mm granules becoming dominant and granules larger than 2 mm disappearing completely. In contrast, in the HSR granules larger than 2 mm were retained until the end of the experiment with dominant granule size ranging between 1.5 and 2.0 mm. This was despite the higher fluidization intensity and bulk shear in HSR compared to LSR.

No appreciable size trend was observed in the shear-free reactors (Figure 5.7). Notably, the smallest size fractions detected in this reactor originated from the effluent of the shear-dominated reactors, reflecting the generation of fines from erosion of granules under different shear conditions. Having a shared recirculation tank and high fine particle washout, it was not possible to directly attribute fine particle production to each shear-dominated reactor. Instead, the accumulation of fines in the shear-free reactors provided an indicator of granule abrasion and fine generation in the shear-dominated systems. A good indication of the origin of these fines is the reduction of fractions of larger granules in LSR and HSR (Figure 5.7) suggesting that most abrasion of larger particles occurred in LSR.

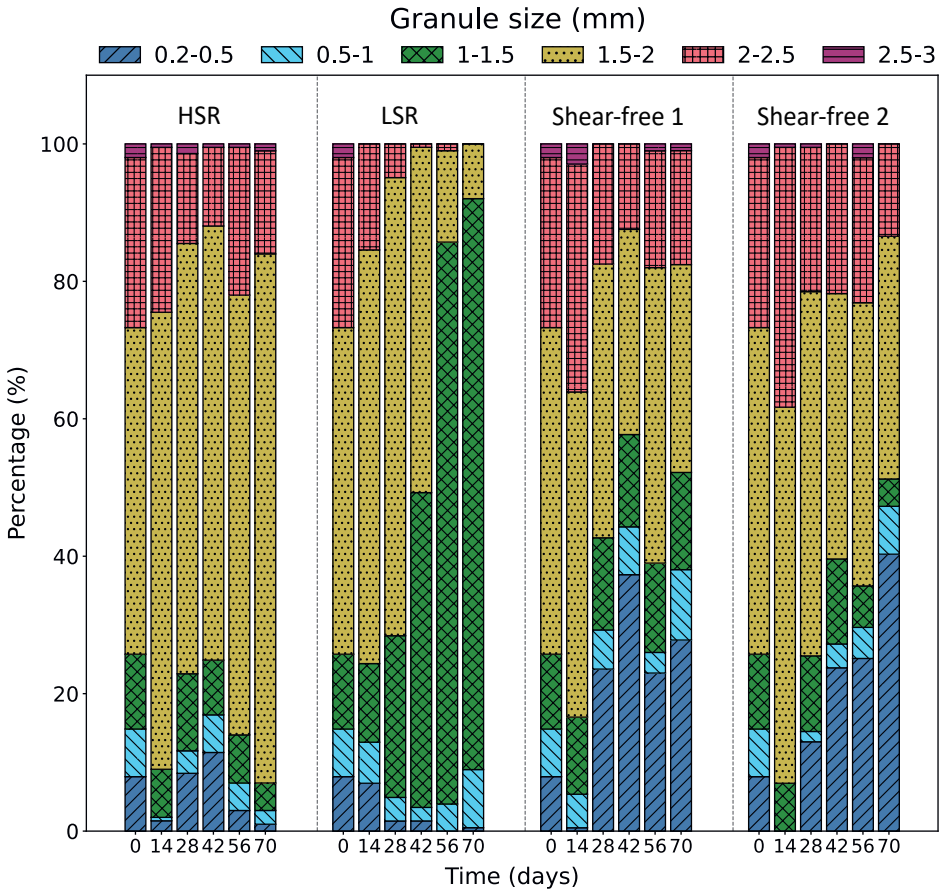


Figure 5.7: Evolution of the size distribution of granules over time in all reactors. Shear-free Reactor 1 received medium from the effluent of the high-shear reactor (HSR), and Shear-free Reactor 2 received medium from the low-shear reactor (LSR). The accumulation of fine particles in the shear-free reactors was used as an indirect measure of granule's abrasion intensity in the shear-dominated reactors.

5.3.3.2. Accumulation of calcium in granules under various flow regimes

Calcium (Ca) accumulation in the granules of various reactors proceeded differently. In the LSR, the Ca concentration steadily increased from 70.5 g/kg of granule's dry weight to 185 g/kg, thereby more than doubling from the initial value (Figure 5.8a). In contrast, Ca in granules from the HSR and shear-free reactors increased only slightly reaching calcium content of 83.8 g/kg of granule's dry weight (Figure

5.8a). X-ray diffraction (XRD) analysis of the calcified granules showed that the dominant crystalline precipitate was calcite ($CaCO_3$, JCPDS No.05-0586) with its characteristic peaks clearly visible in the diffractogram (Figure 5.8b).

The Scanning electron microscopy (SEM) and energy-dispersive X-ray spectroscopy (EDX) results in Figure 5.8c,d aligned well with Ca quantification in Figure 5.8a. Interestingly, the calcification profiles, measured as calcium to nitrogen weight percent ratios (Ca/N) were very different in HSR compared to LSR. In granules from HSR, the Ca/N ratios ranged from 0.4 to 1.8 across granule's cross-sections with Ca content typically increasing towards the centre of the granule (Figure 5.8c). In LSR, the calcification was much more pronounced with Ca/N ratios reaching ~60 and without clear trends in calcium content throughout the granule's depth (Figure 5.8d).

Surface analysis of the granules with SEM revealed a "rough", seemingly porous surface wherein microbial cells could be clearly seen in HSR (Figure 5.8e). This was different from LSR, where granules looked "smoother", less porous and with microbial cells embedded in an amorphous precipitate (Figure 5.8f), most probably calcium containing compounds (See Figure 5.8d and Ca quantification in Figure 5.8a). Higher magnification images of the LSR granules revealed clear nucleation sites of precipitates on the surfaces of microbial cells (Figure S.5.11). When considering elements other than Ca that can potentially form precipitates, the weight percentage of e.g., sulphur (S) ranged between 5.5–16.7% in HSR and between 5–12% in LSR (Figure S.5.12, Figure S.5.13). Iron content ranged between 1.6–15.5% in HSR and between non-quantifiable to 25% in LSR (Figure S.5.12, Figure S.5.13).

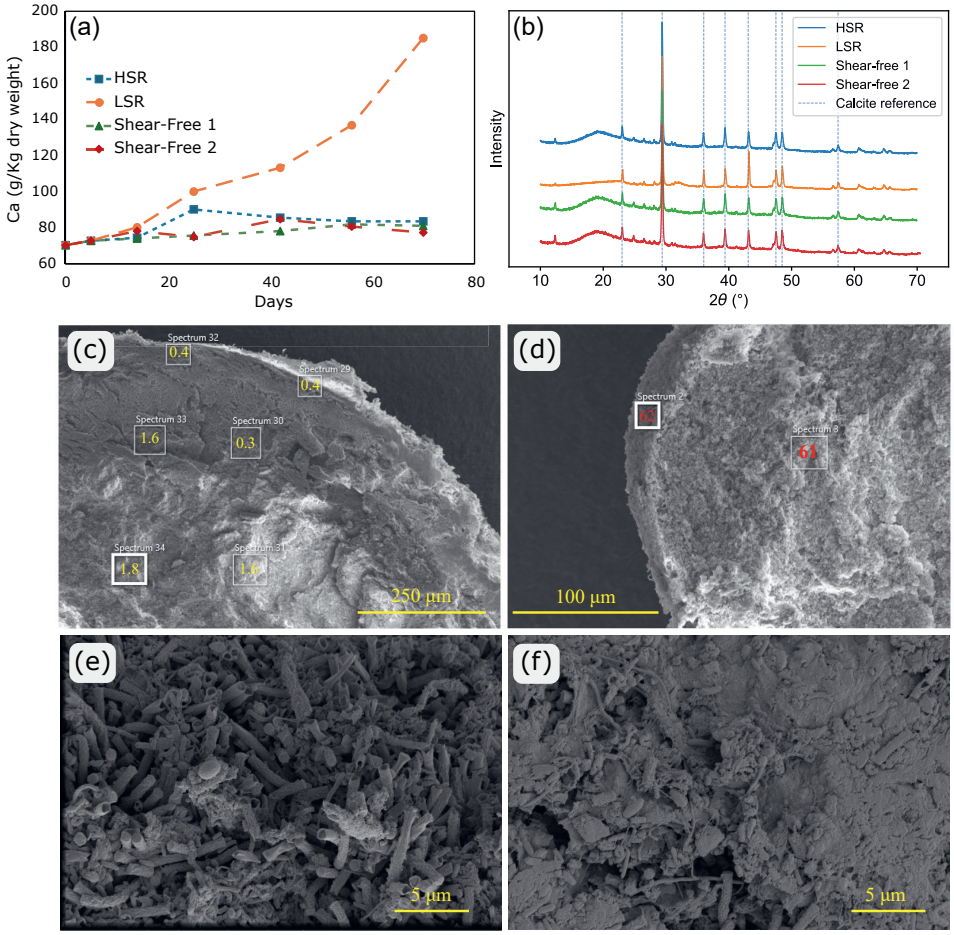


Figure 5.8: (a) Calcium concentration in granules sampled at different time points. (b) XRD diffractograms of granule samples collected from reactors on Day 70 (offset for clarity). (c-f) SEM images of granules sampled on Day 70. (c-d) electron images of sliced granules with EDS spectra areas from HSR in (c) and from LSR in (d). (e)-(f) electron images of surfaces of non-sliced granules in HSR (e) and LSR (f) show a "rough" and porous surface in HSR (e) and a "smooth" surface filled with precipitates in LSR (f). Numbers in the squared boxes of (c), (d) show the ratio of wt.% between Ca/N from EDS spectra. Red numbers indicate that N w% could not be detected and the denominator for the ratio was set to 1. EDS – energy dispersive X – ray spectroscopy.

5.3.3.3. Internal structure of granules

Magnetic resonance imaging (MRI) was used to evaluate the internal structure of granules from the different reactors at different time points, by imaging several

cross-sections through granules stacked in a 5 mm tube and submerged in water (Figure 5.9a). Overall, granules from all reactors show a layered structure and either spherical or slightly elongated cross sections (Figure 5.9, Figure S.5.15). Slices coincide with the center of various granules, however, some granules are only partially located in the slice and hence have a less defined boundary, due to partial volume effects. Granules from the inoculum are heterogeneous in their internal structure, i.e. dark and light intensity layers with visible broken outer layers (Figure 5.9b). Granule internal structure in the HSR reactor stays overall similar between the Day 28 and Day 70 consisting of distinct thin outer layers, and a relatively large apparent homogeneous core (Figure 5.9c). In the LSR reactor, an overall larger heterogeneity is present in the signal intensities between different granules (Figure 5.9d). In the shear-free reactors, a heterogeneous internal structure seems to be present in granules (Figure S.5.15). Additionally, a selection of visually-calcified granules was made. Here, parts with lower image intensities inside the granules were visible, specially in granules from shear-free reactor, suggesting a larger heterogeneity within the granules (Figure S.5.16).

Using a T_1-weighted spin echo sequence, a high MRI image intensity can correlate to shorter T_1 relaxation times of water protons inside the biofilm, but especially in complex biofilms the MRI signal intensity depends on a combination of proton density, T_1 and $T_{2,\text{eff}}$ relaxation times (Van As and Lens (2001)). A lower image intensity can either originate from water with a longer T_1 relaxation time or indicate the absence of protons, due to solids or the presence of a very short $T_{2,\text{eff}}$. T_2-weighted MRI images show lower contrast inside the granules (Figure S.5.17), due to the overall shorter $T_{2,\text{eff}}$-values, as previously studied by Hoskins et al. (1999). In biofilm model systems short T_1 relaxation times could be correlated to the presence of cells (Willett et al. (2024)), however, the granules in this current study are a more complex biofilm system, and differences in signal intensity are only interpreted qualitatively. The very low image intensities observed in visually calcified granule layers may indicate the presence of solids or a very short $T_{2,\text{eff}}$. However, to potentially correlate with the degree of calcification will require the co-registration of the exact same granule with MRI and SEM-EDX.

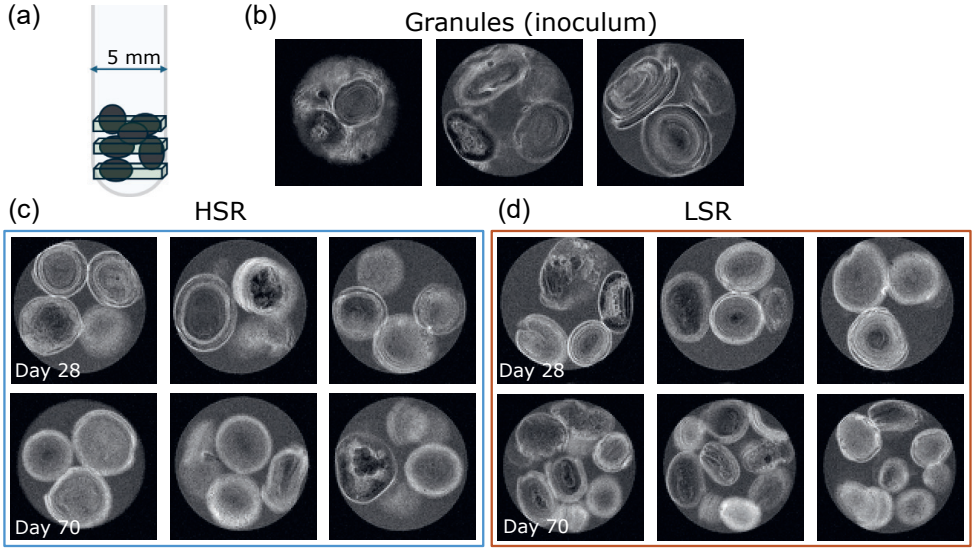


Figure 5.9: (a) scheme of the MRI tube filled with several granules indicating the virtual cross-sections of the MRI images. T_1-weighted 2D MRI-images of (b) granules taken from the inoculum before insertion into the reactors. The left slice is located at the bottom of a round-bottom tube. (c) Granules from the HSR reactor at Day 28 and 70 and (d) granules from the LSR reactor at Day 28 and 70. Water surrounding the granules is visible and has a homogeneous image intensity. The field-of-view of all images is 4.5 mm × 4.5 mm.

5.3.3.4. Methanogenic activity

Methanogenic activity (SMA) of granules on the synthetic influent from all reactors over time is shown in Figure 5.10. The SMA of granules developed in the shear-free reactors declined steadily throughout the experiment (Figure 5.10c-d). In contrast, granules developed in HSR and LSR exhibited significantly higher activity at all sampling points (Figure 5.10a-b). The initial SMA was 331 mg CH_4-COD/g VSS/day. By the end of the experiment, SMA reached 656 and 388 mg CH_4-COD/g VSS/day in HSR and LSR, respectively, and decreasing to 100 and 117 mg CH_4-COD/g VSS/day in shear-free 1 and 2. On average, SMA in the HSR was 80% higher than in shear-free 1, and the LSR was 67% greater than in shear-free 2. Moreover, the average SMA of granules in the HSR was 32% higher than that of the LSR.

The residual volatile fatty acid (VFA) concentrations in batch bottles containing granules from the shear-free reactors showed a substantial accumulation of acetate, whereas granules from the shear-dominated reactors degraded nearly all available acetate during the batch tests especially after a short acclimation period of five

days (Figure 5.10). This observation suggests that granules developed under shear-dominated conditions likely possessed a more active acetoclastic methanogenic community and/or had lower intergranular mass-transfer resistance compared with granules cultivated in shear-free environments.

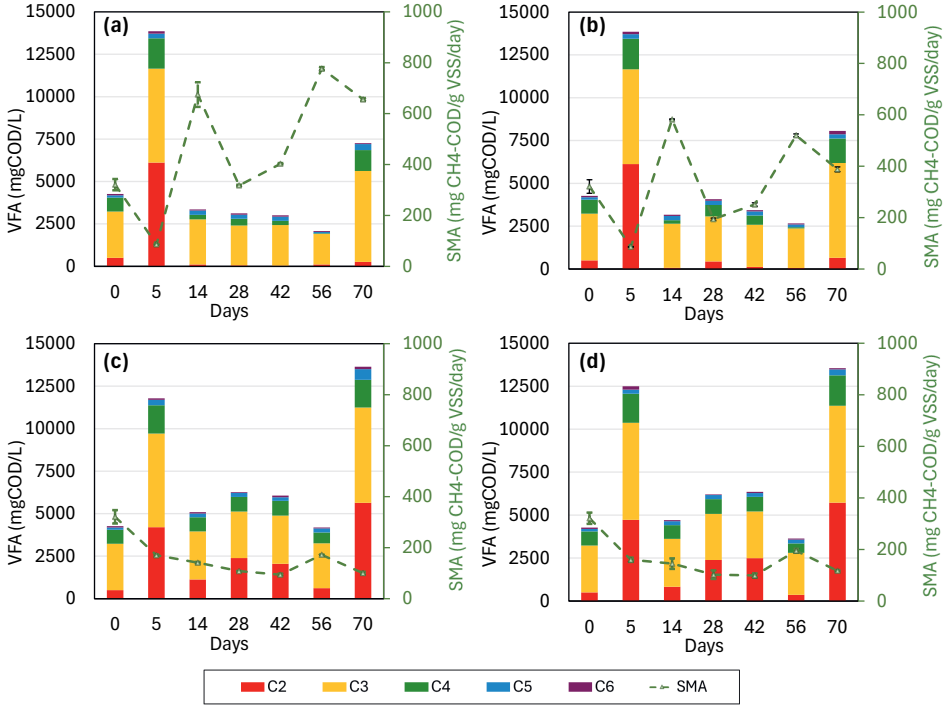


Figure 5.10: Methanogenic activity (SMA) of granule samples obtained at different time points and incubated with influent substrate under batch conditions for (a) the high-shear reactor (HSR), (b) the low-shear reactor (LSR), (c) shear-free reactor 1, and (d) shear-free reactor 2. Residual VFAs (C_2–C_6) concentrations measured at the end of batch tests and expressed as COD-equivalent values on the primary y-axis. The SMA values are plotted on the secondary y-axis with standard deviation error bars. The initial medium COD concentration was 16,772 mgCOD/L for samples from Days 5 and 70 and 10,944 mgCOD/L for other time points. Abbreviations of VFAs: C_2 – acetic acid, C_3 – propionic acid, C_4 – butyric acid, C_5 – valeric acid, C_6 – caproic acid.

5.4. Discussion

5.4.1. Effects of gas bubbles on the hydrodynamics and mass transfer

Buoyancy is one of the main driving forces governing the hydrodynamics of multiphase flows involving rising gas bubbles. This upward motion disturbs the surrounding fluid, generating both mean and velocity fluctuations in the liquid phase (Innocenti et al. (2021)). As bubbles ascend, they shed unsteady wakes that act as localized sources of agitation, normally referred to as bubble induced turbulence (BIT). Each wake consists of vortical structures with characteristic scales on the order of the bubble diameter, which disturbs the surrounding fluid. In a swarm of bubbles, these wakes interact with each other, producing complex velocity fluctuations. The interaction of wakes generates a broad spectrum of eddy sizes, producing a turbulent-like feature in the liquid (Risso (2018)).

In an ideal homogeneous bubbly flow, with uniformly distributed gas bubbles, the mean liquid velocity remains close to zero (bulk Re=0) (Risso (2018)). In the present study, however, the bubble spatial distribution was non-uniform, and together with the concurrent liquid flow, this led to the development of bulk liquid recirculation in both reactors. This reactor-scale coherent flow structure was observed in the u_y iso-surfaces of both reactors (Figure 5.4). Moreover, PDFs of u_y distributions (Figure 5.5) demonstrated that the HSR exhibited stronger recirculation than the LSR. Previous studies (Gvozdić et al. (2019)) have shown that increasing the gas superficial velocity (GSV), under inhomogeneous bubble injection, promotes the formation of reactor-scale (macro-scale) circulation in bubble columns, leading to shear layers between the bubble-injected region and the opposite side of the reactor. The strength of this circulation directly influences the time-averaged shear rate in the reactor. In the present work, the effects of both GSV and liquid superficial velocity (LSV) on the time-averaged shear rate were also examined (see section S.5.10). The results showed that increasing the GSV or decreasing the LSV led to higher shear rates, which can be attributed to the enhanced relative velocity between rising gas bubbles and the surrounding liquid, increasing the frequency of high-velocity events in the liquid phase. Notably, overall the measured shear rate represents the sum of two mechanisms: local shear produced by buoyancy-driven bubbles and shear generated at the interfaces of liquid layers, particularly, the upward and downward flows due to large-scale circulation.

Apart from the relative bubble rising velocity, the characteristics of velocity fluctuations caused by rising bubbles (BIT) depend on the gas bubble diameter, population, and presence of solid phase. Bubbles inject energy and vorticity at scales comparable to their diameter, which are then redistributed across different length scales. In this study, the bubbles in the HSR were relatively larger than those in the LSR (data not shown), potentially generating larger local eddies. On top of that, the stronger reactor-scale circulation and enhanced fluidization of granules in the HSR may have contributed to damping the BIT-related or the smaller-scale flow structures, while increasing the shear induced turbulence (SIT) (Gvozdić et al. (2019), An et al. (2024b)). This trend is consistent with the findings of Cui and Fan (2004), who showed that the presence of solid particles reduces turbulence intensity under low gas superficial velocity (aligned with the GSV conditions of this study).

Based on the statistical analysis of velocity and velocity fluctuations in both reactors (Figure 5.6), we postulated that, at the granule-scale, the flow in HSR was dominated by large, energy-containing eddies, whereas, the LSR was dominated by comparatively smaller eddies. The root mean squared (RMS) of velocity magnitude fluctuations was greater in the HSR (Figure 5.6a). Although RMS values do not provide a direct measure of eddy length scale, they are a reliable indicator of the kinetic energy accumulated in turbulent motions (Xia et al. (2013)). Larger, more energetic eddies generate stronger velocity fluctuations (with lower frequency), which increase the RMS of the velocity fluctuations, whereas smaller, less energetic eddies appear as weaker fluctuations (with higher frequency) in the tracer particle velocity signals (Figure 5.6a,c). The ACF analysis in Figure 5.6d further supports this interpretation: eddies with longer characteristic length and time scales transport tracer particles over longer durations, thereby increasing the velocity memory of particles in the HSR compared to the LSR.

5.4.2. Interdependent effect of hydrodynamics and Ca^{2+} on the properties of granules

In this section we discuss how hydrodynamics and calcification alter the granules properties separately and in synergy with an emphasis on mechanisms utilizing the results of this study and other studies in the literature.

In shear-dominated reactors, because a low solids volume fraction was applied, granule–granule interactions were minimal. Hence, granule properties were primarily

governed by the surrounding fluid dynamics. The statistical analysis of tracer particle velocity time series showed that the turbulence characteristics in LSR and HSR reactors were different (Figure 5.6c,d). The results suggest that coherent flow structures may have developed at smaller scales in the LSR reactor compared to HSR. A visual representation of the dominant eddies is shown in Figure 5.11. The force exerted on granules is strongly dependent on the characteristics of the nearby turbulent eddy, influencing granule development. In interaction with turbulent eddies, depending on their size and energy, granules may either be entrained within the flow of larger eddies or directly hit by smaller ones. As postulated, the HSR reactor was mainly dominated by high-energy, large-scale eddies, which caused a higher fluidization degree. Under these conditions, the granules may have experienced stronger drag forces. However, comparison of the granule-size evolution in the HSR and LSR (Figure 5.7) suggests that these forces imposed a relatively smooth shear stress on the granule surfaces. In contrast, the LSR was dominated by small-scale eddies that continuously acted on the granules surface. This persistent high-frequency stress led to the disintegration of most granules in LSR by the end of the experiment, with the remaining granules reduced to sizes of 1.0–1.5 mm, considerably smaller than in HSR (Figure 5.7). A similar result was observed by Wei and Yang (2023) in biofilm systems, where low-frequency fluctuations promoted biofilm growth, whereas high-frequency fluctuations reduced its thickness.

The other parameter considered highly influential on granule properties is the mass transport of substrates and nutrients, particularly Ca^{2+} ions in this study due to their relation to calcification. In general, in inhomogeneous bubbly flows, three main mechanisms contribute to mixing: (i) advective transport, (ii) bubble-induced turbulence, and (iii) shear-induced turbulence. The overall mixing results from the superimposed effects of these mechanisms, and their interplay and relative contributions vary across different flow regimes (Gvozdić et al. (2019)). At the reactor scale, advection driven by large eddies distributes substrates and nutrients throughout the bulk liquid, maintaining a relatively uniform concentration around the granules. In the vicinity of individual granules, however, mass transfer is governed by the presence of a thin boundary layer at the liquid–granule interface as well as by internal diffusional limitations within the granule matrix (Baeten et al. (2019)). Granules in the LSR exhibited more extensive calcification compared to HSR (Figure 5.8), indicating that higher amounts of Ca^{2+} were transported from the bulk liquid and

accumulated within the granules, as well as increased nucleation sites on the surface of granules (Figure S.5.11). This can be attributed to the dominance of BIT and micro-scale eddies, which continuously refreshed the fluid near the granule surface (micro-mixing) and thinned the boundary layer, thereby enhancing the external mass transfer of Ca^{2+}. By contrast, in the HSR, reduced micro-mixing was likely to result in a comparatively thicker boundary layer at the granule surface, reducing the diffusion of Ca^{2+} into the granules. In addition to the higher mass transfer, the higher calcification in the LSR may also reflect a selection effect, where weaker and less calcified granules were disintegrated, leaving behind stronger and more calcified granules. Therefore, both enhanced Ca^{2+} mass transfer and selection for mechanically stronger, calcified granules may have contributed to the higher calcium content measured in the LSR granules.

Despite the higher disintegration rate observed in the LSR, the granules had greater mechanical strength at all time points compared with those developed in the HSR (see section S.5.16). This is likely attributable to the higher degree of calcification in the LSR. The SEM images (Figure 5.8) demonstrated that differences in local hydrodynamics and calcification altered the granule's surface morphology. More Calcium precipitation on LSR granules filled surface pores and valleys, producing a smoother outer layer that likely reduced the detachment of fine particles during strength measurements. A similar observation was reported by Chen et al. (2021).

Calcium precipitation may be a key factor contributing to the lower SMA of granules from the LSR. This process reduces activity through two primary mechanisms (Yu et al. (2019)): space occupation and pore blockage. First, the formation of a calcium-rich core occupies volume that would otherwise be available for active biomass, thereby reducing the effective local cell density in the center of the granules. Second, calcium precipitates within the EPS matrix (mostly outer layers) can clog micropores and transport channels, increasing mass transfer resistance.

A comparison of the SMA of granules from shear-dominated and shear-free reactors clearly shows the role of hydrodynamics in granule activity. Both the heavily calcified granules from the LSR and the HSR granules, exhibited substantially higher SMA than those from shear-free reactors. This suggests that hydrodynamic forces restructure the internal architecture of granules, reducing intragranular mass transfer limitations and sustaining higher activity.

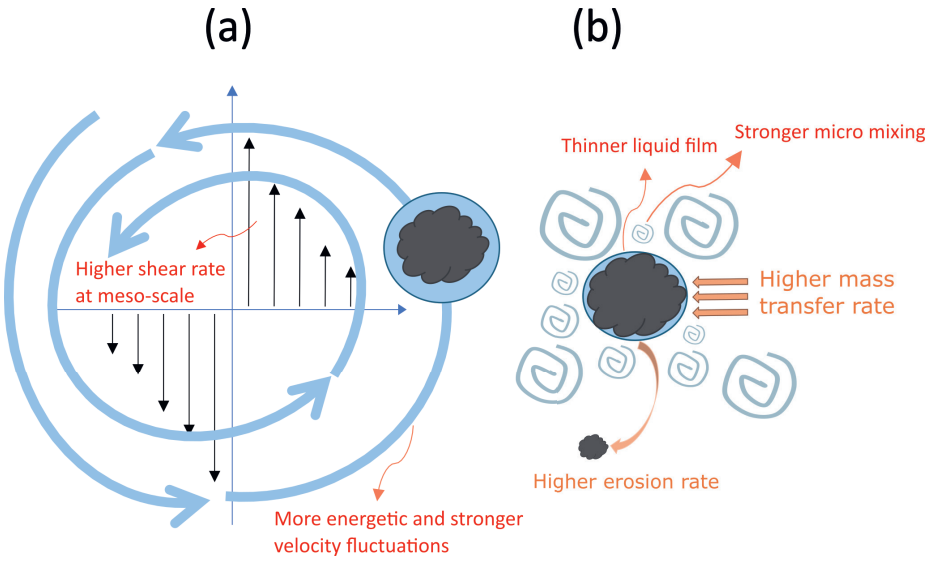


Figure 5.11: Schematic diagram of local hydrodynamics around the granules: (a) large eddies and bulk shear rate, (b) eddies with the same size or smaller than granules.

5.5. Limitations and future work

SMA tests were performed in batch bottles under identical hydrodynamic conditions for all samples; therefore, the measured methanogenic activities reflect the combined effects of intrinsic microbial activity and intragranular mass-transfer resistance. In these experiments, the influence of the reactor's hydrodynamics on mass transfer was absent. Direct measurement of substrate conversion rates in individual reactors during operation was not feasible as all reactors shared a common substrate reservoir.

Flow measurements were conducted before and after the biological experiments. However, over the 70-day operation period, changes in gas-sparger surface properties could have changed the bubble size and spatial distribution. Additionally, continuous granule sampling, which reduced the solid volume fraction, may have altered turbulence characteristics within the reactors.

The imaging frame rate used for turbulence analysis was lower than typically required to fully resolve micro-scale, high-frequency flow motions. In future studies, a higher acquisition rate at the expense of a lower imaging window could be achieved to characterize the feature of the flow at smaller scales.

Mechanical stress and mass transport in both reactors resulted from the combined effects of advection, shear-induced turbulence (SIT), and bubble-induced turbulence (BIT). Future studies should aim to decouple these mechanisms and systematically investigate the governing parameters of each phenomenon.

The degree of calcification of granules can be characterized using MRI analysis, however, this would require the test of the exact same granule with MRI and SEM-EDX, which will be investigated further in the future.

5.6. Conclusions

This study demonstrates that hydrodynamics in calcium rich medium plays a key role in controlling not only granule size and morphology but also biological activity. Granules developed under shear-dominated conditions had 80% (high shear reactor (HSR)) and 67% (low shear reactor (LSR)) higher methanogenic activities than those developed in shear-free reactors, indicating that hydrodynamic agitation alters the internal granule architecture by maintaining pores and channels and reducing mass-transfer resistance, likely due to continuous agitation-driven biogas release.

Despite higher mean liquid velocities and stronger fluidization in the HSR, this reactor produced larger, less calcified, and more active granules, demonstrating that turbulence characteristics rather than mean flow governed mass transfer and mechanical loading. In both reactors, turbulent velocity fluctuations resulted from the combined effects of bubble-induced turbulence (BIT) and shear-induced turbulence (SIT), with BIT potentially dominating in the LSR and SIT in the HSR.

The dominant turbulence source determined the microscale hydrodynamic environment surrounding the granules. BIT-dominated conditions, characterized by lower-magnitude and higher-frequency velocity fluctuations, imposed higher mechanical stress on the surface of granules, enhanced Ca^{2+} transport into the granules, and promoted granule calcification, resulting in smaller and more strongly calcified granules in the LSR.

The findings of this study are also relevant to aerobic granular sludge systems, demonstrating that higher mixing and mass transfer rate can be achieved at lower gas flow rates, thus improving reactor efficiency while reducing energy demand.

Supplementary Information

S.5.1. Recirculation tank design

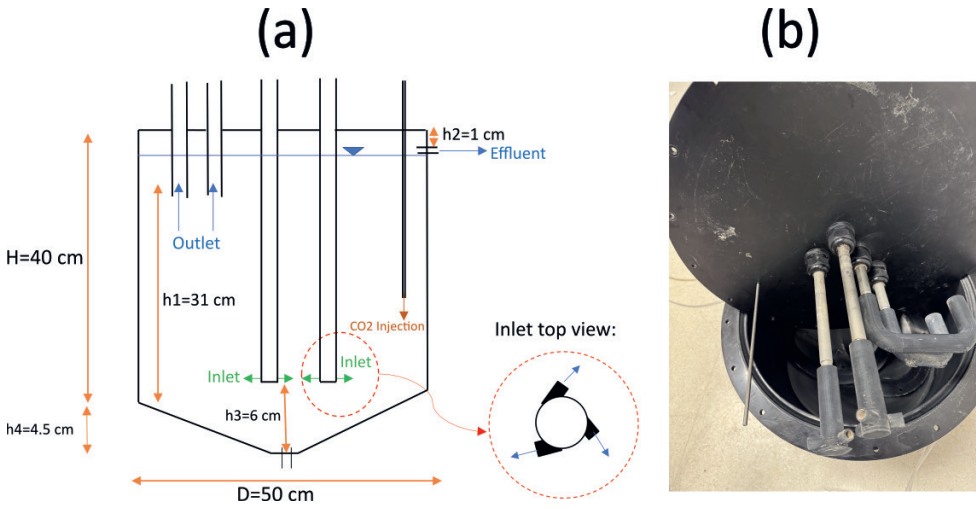


Figure S.5.1: Recirculation tank

S.5.2. Biofilm diffusion–reaction model for spherical granules

Insufficient concentration of the rate-limiting reactant in the fluid surrounding the granules prevents complete penetration into the centre. As a result, only the outer layer exposed to the fluid remains active, while the inner region becomes inactive. A biofilm model based on Fick's law in spherical coordinates was applied to a single granule to determine the minimum substrate concentration in the bulk liquid. The following assumptions were made:

1. The cells have such a low Monod constant that uptake can be assumed to follow zero-order kinetics.
2. The aggregate has a uniform concentration of active biomass (X_{VSS}) and a constant effective diffusivity (D_s).
3. The system is in steady state with respect to substrate diffusion and reaction.
4. Granule expansion or decay does not affect substrate diffusion.
5. External liquid-film resistance is negligible due to high hydrodynamic intensity in the reactor.

Table S.5.1: Parameters used for the uptake-rate calculation.

Symbol	Parameter	Value	Unit
f_{VSS}	VSS mass fraction in wet granule	0.15	g VSS g^{-1} wet
ρ_{wet}	Wet granule density	1,050,000	g wet m^{-3}
X_{VSS}	VSS concentration in granule	157,500	g VSS m^{-3}
SMA	Specific methanogenic activity	0.4	g COD g_{VSS}^{-1} d^{-1}
R_{SP}	Volumetric uptake rate	63,000	g COD m^{-3} d^{-1}
R	Granule radius	1.0×10^{-3}	m
D_s	Effective diffusivity of acetate (Gonzalez-Gil et al., 2001)	0.00013	m^2 d^{-1}

Note: $R_{SP} = \text{SMA} \times X_{VSS} = 63{,}000$ g COD m^{-3} d^{-1}.

The steady-state diffusion–reaction equation in spherical coordinates is

$$D_s\left[\frac{1}{r^2}\frac{d}{dr}\left(r^2\frac{dC}{dr}\right)\right] - R_{SP} = 0. \tag{S.5.1}$$

Boundary conditions: (i) $\frac{dC}{dr} = 0$ at $r = 0$, and (ii) $C(R) = C_{bulk}$. After double integration and applying these conditions, the concentration at the centre is

$$C(0) = C_{bulk} - \frac{R_{SP}R^2}{6D_s}. \tag{S.5.2}$$

For complete substrate penetration ($C(0) = 0$), the bulk concentration must satisfy

$$C_{bulk} = \frac{R_{SP}R^2}{6D_s}. \tag{S.5.3}$$

Using the parameter values listed above, the minimum bulk substrate concentration required to avoid diffusion limitation in the granule core was calculated as 64.8 mg COD L^{-1}. It is worth noting that this value was approximately three times higher when calculated using a one-dimensional (1D) model for a stratified biofilm.

S.5.3. Reactor process performance

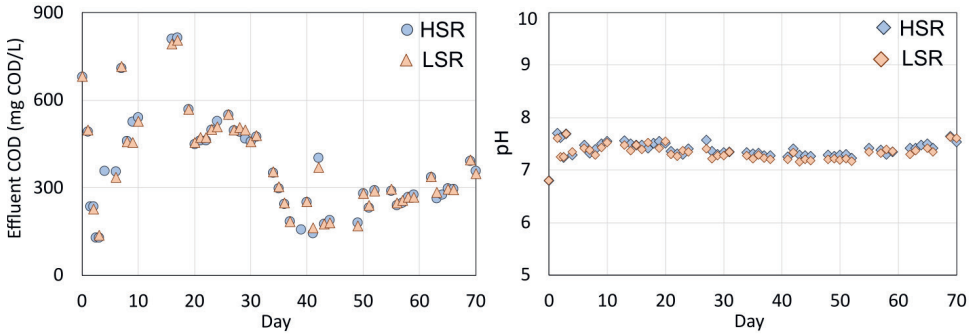


Figure S.5.2: Effluent COD concentration and pH during the operation of reactors

S.5.4. Camera calibrations and image prepossessing

Accurate calibration is critical for reliable 3D particle tracking. A two-level calibration plate ($5\times5\,cm^2$) and the polynomial fitting approach were used to calibrate the cameras. The calibration plate was imaged at three equidistant positions from the cameras to achieve a volume mapping of the field of view onto the camera sensors. The accurate positioning of the calibration target was done using a custom-made 3D micro traverse device. Image processing was performed in DaVis 10 software (LaVison GmbH), resulting in an average fitting error of approximately 0.06 pixels (10 μm) for all cameras. This error was further reduced to 0.013 pixels (2 μm) using tracer particle images within the measurement volume through an iterative volumetric self-calibration procedure (Wieneke (2008)). In the final calibration step, the optical transfer function (OTF) (Schanz et al. (2013a)) was applied to the recorded image set to identify local particle image patterns within measurement sub-volumes.

S.5.5. Particle tracking settings

Table S.5.2: STB parameters.

Parameter	Value
Reconstructed volume	647 × 1457 × 642 voxels
Threshold for 2D particle detection	18 counts
Allowed triangulation error	2 voxels
Shaking	
Adding particles (outer loop)	4 iterations
Refine particle position and intensity (inner loop)	4 iterations
Shake particle position by	0.1 voxel
Remove particles if closer than	1 voxel
Remove weak particles if intensity <	0.1 of avg. int.
Particle image shape and intensity	
Make OTF smaller	0.8 times
Residuum computation - increase particle intensity	1.5 times
Tracking	
Minimum track length	4 time steps
Max. abs. change in particle shift	5.00 voxel
Max. rel. change in particle shift	20%

S.5.6. Effect of averaging time interval on PDF of velocity and shear rate in shear-dominated reactors

Increasing the averaging time interval attenuated transient velocity fluctuations. As the averaging time increased, the shear-rate PDFs in both reactors shifted toward lower values with a reduced high-shear tail (Figure S.5.3a–b). This resulted in a narrowing of the axial liquid-velocity distributions (Figure S.5.3c–d).

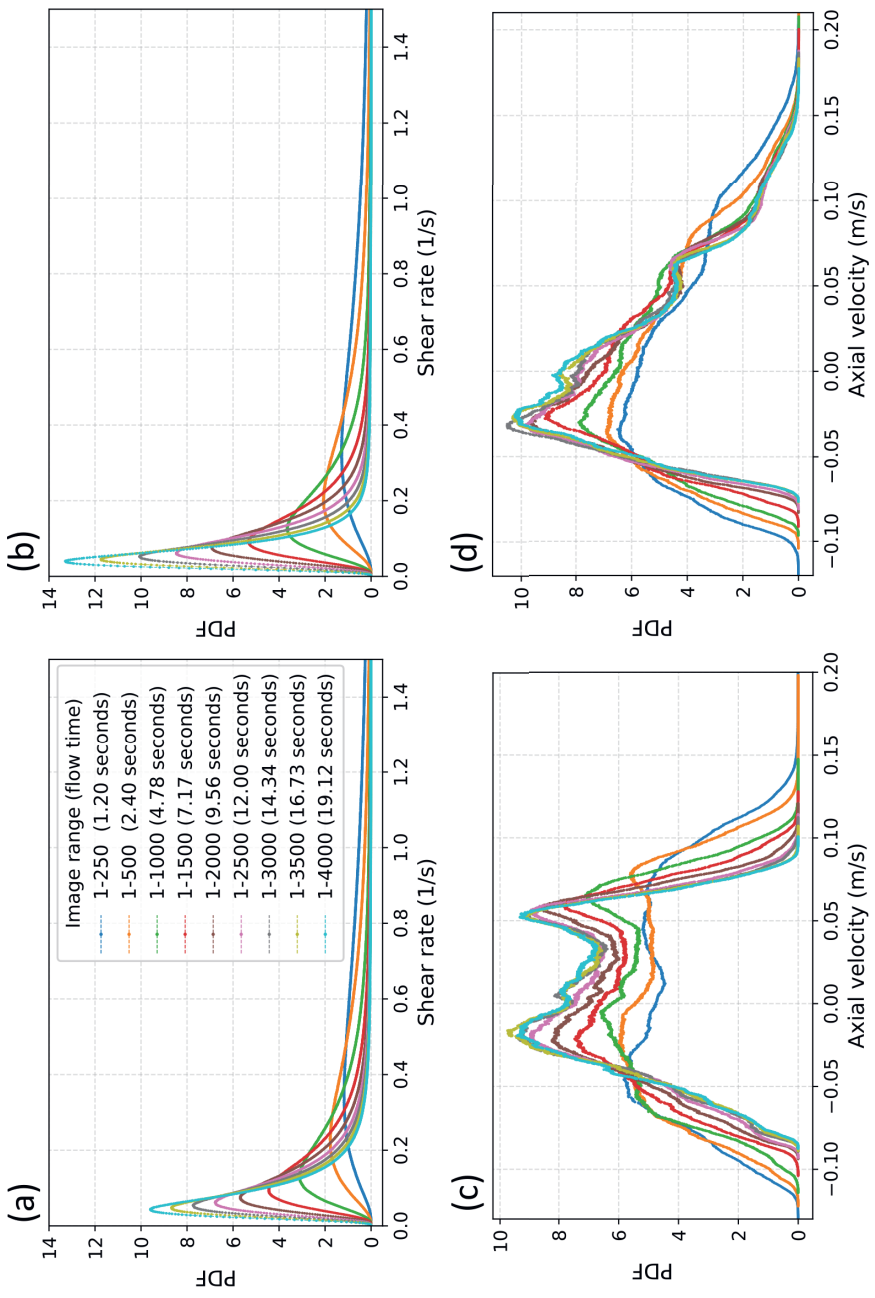


Figure S.5.3: PDF of Vy in reactors averaging over varying time intervals

S.5.7. Real-time axial velocity at three different points in the reactors and flow time-scale calculation using FFT.

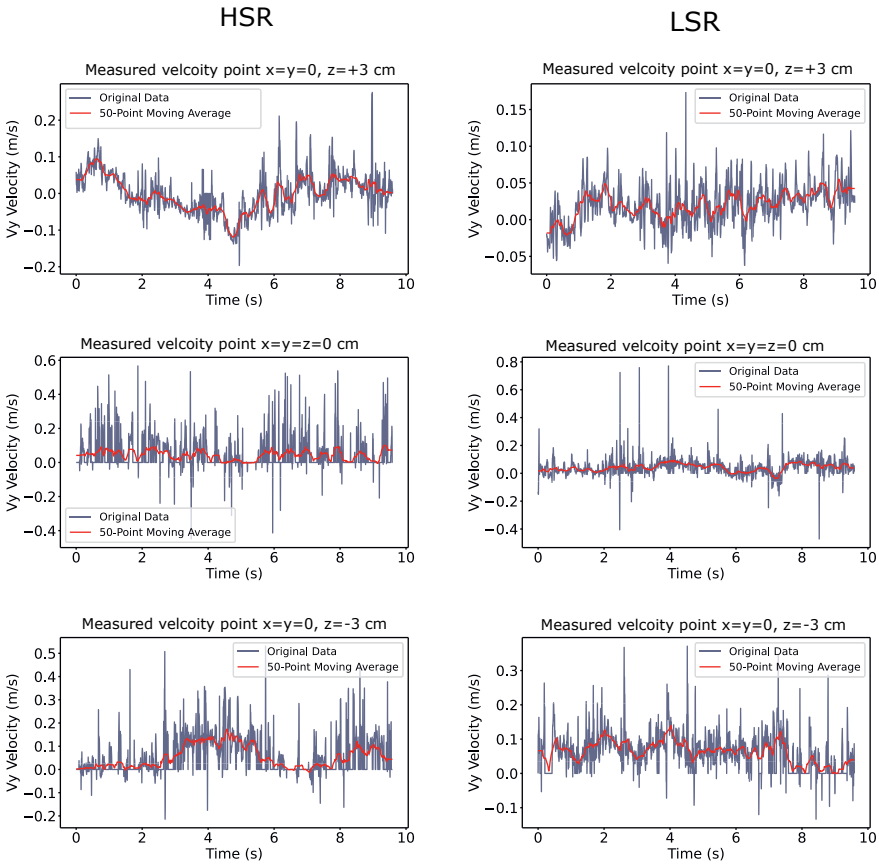


Figure S.5.4: Real-time Vy velocity signals measured at three locations in HSR (left) and LSR (right)

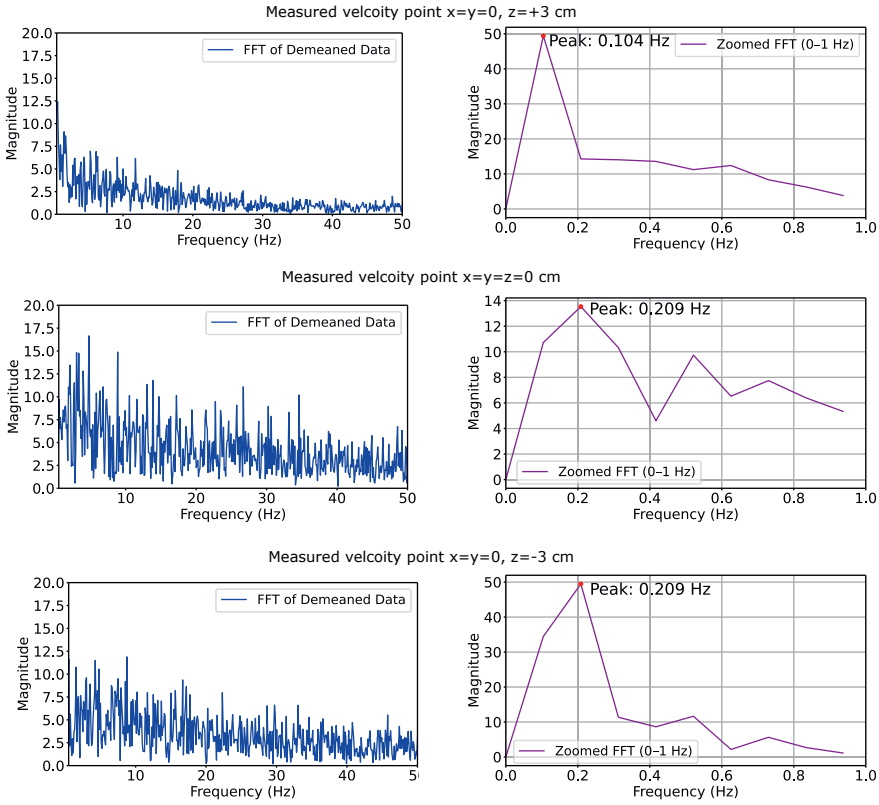


Figure S.5.5: FFT of demeaned Vy velocity signals measured at three points in HSR. Left: spectra in frequency range (0–50 Hz); right: zoomed low-frequency spectra (0–1 Hz) for peak identification and estimation of reactor-scale flow timescales. Peak frequencies (f) are converted to characteristic flow time scales as $T = 1/f$.

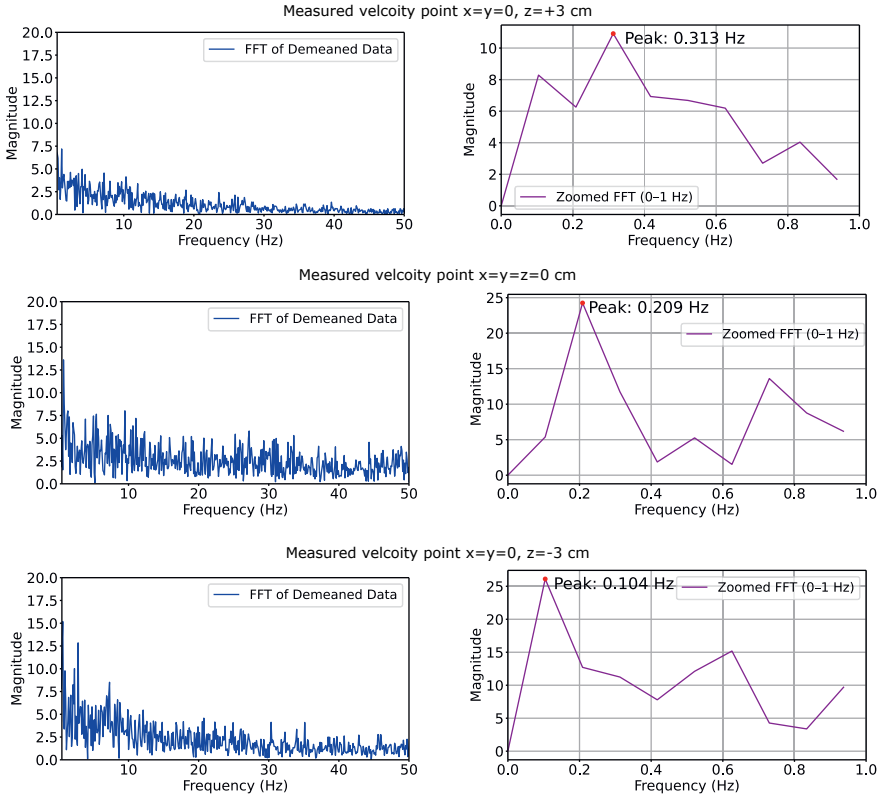


Figure S.5.6: FFT of demeaned Vy velocity signals measured at three points in LSR. Left: spectra in frequency range (0–50 Hz); right: zoomed low-frequency spectra (0–1 Hz) for peak identification and estimation of reactor-scale flow timescales. Peak frequencies (f) are converted to characteristic flow time scales as $T = 1/f$.

S.5.8. Shear rate distribution across the reactor's diameter

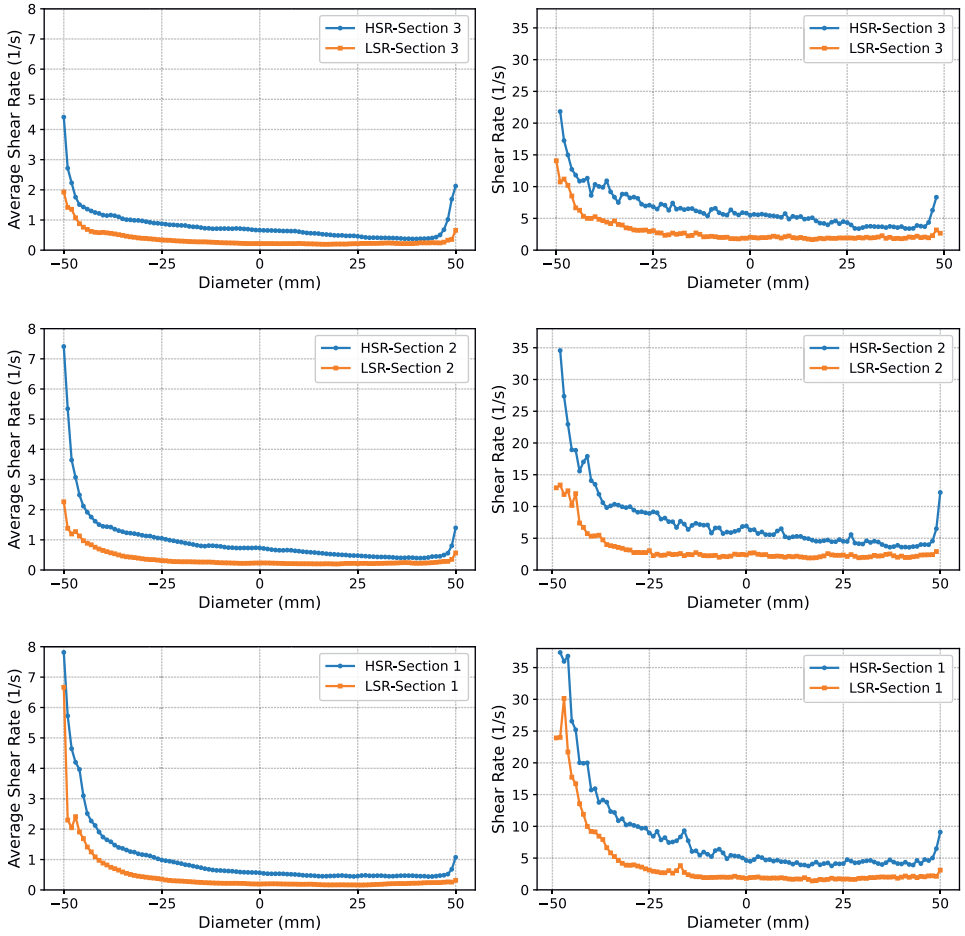


Figure S.5.7: Mean and maximum shear rate comparison along the reactor's diameter in HSR and LSR at different sections.

S.5.9. Post-experiment flow measurement

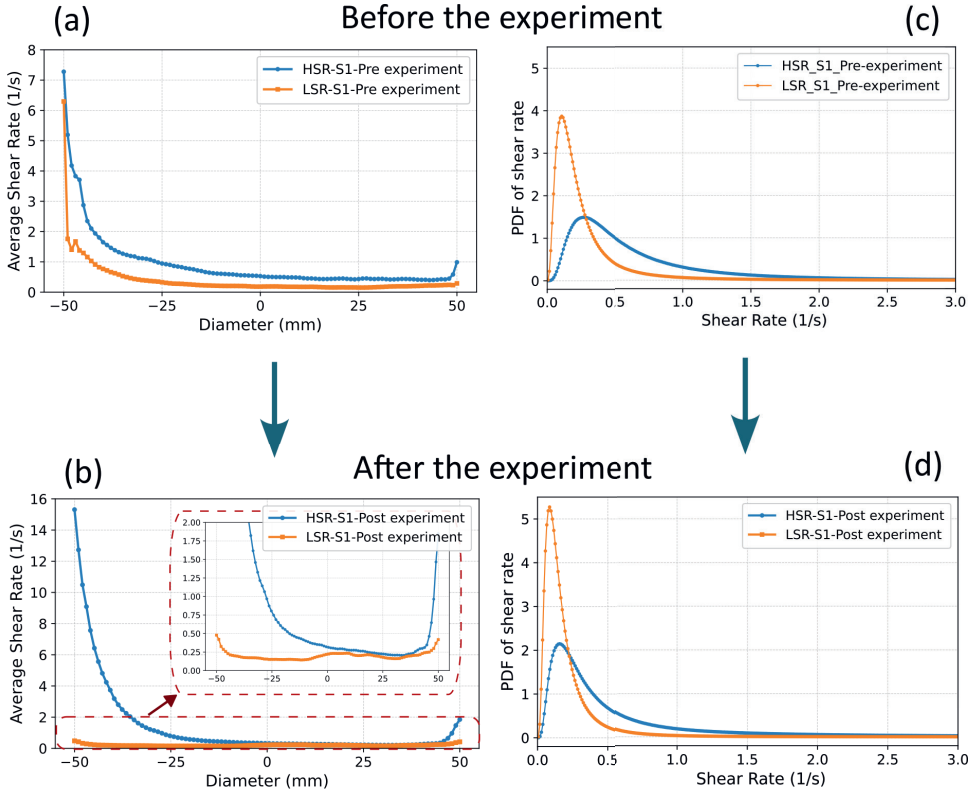


Figure S.5.8: Comparing the shear rate intensities in HSR and LSR, before and after the anaerobic experiments. (a)-(b) time-averaged shear rate distribution over the reactor's diameter, and (c)-(d) frequency distribution of time-averaged shear rate in the reactor's volume

S.5.10. Effect of gas and liquid on shear intensities

Increasing the gas superficial velocity increased the mean shear rate, primarily due to the higher relative (slip) velocity between rising gas bubbles and the bulk liquid. In contrast, increasing the superficial liquid velocity enhanced the liquid upflow velocity, thereby reducing the gas–liquid relative velocity. This decrease in slip velocity weakened the shear generated by rising bubbles, resulting in a lower mean shear rate in the reactor.

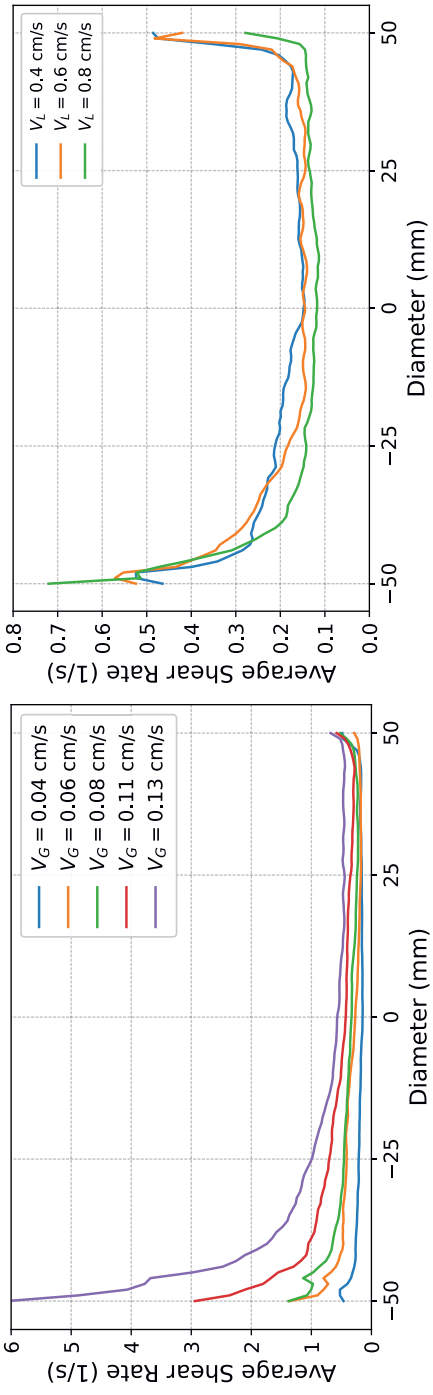


Figure S.5.9: Effect of increasing gas (left) and liquid (right) superficial velocities on mean shear rate in the reactor.

S.5.11. Macroscopic images of surface and cross-section of granules

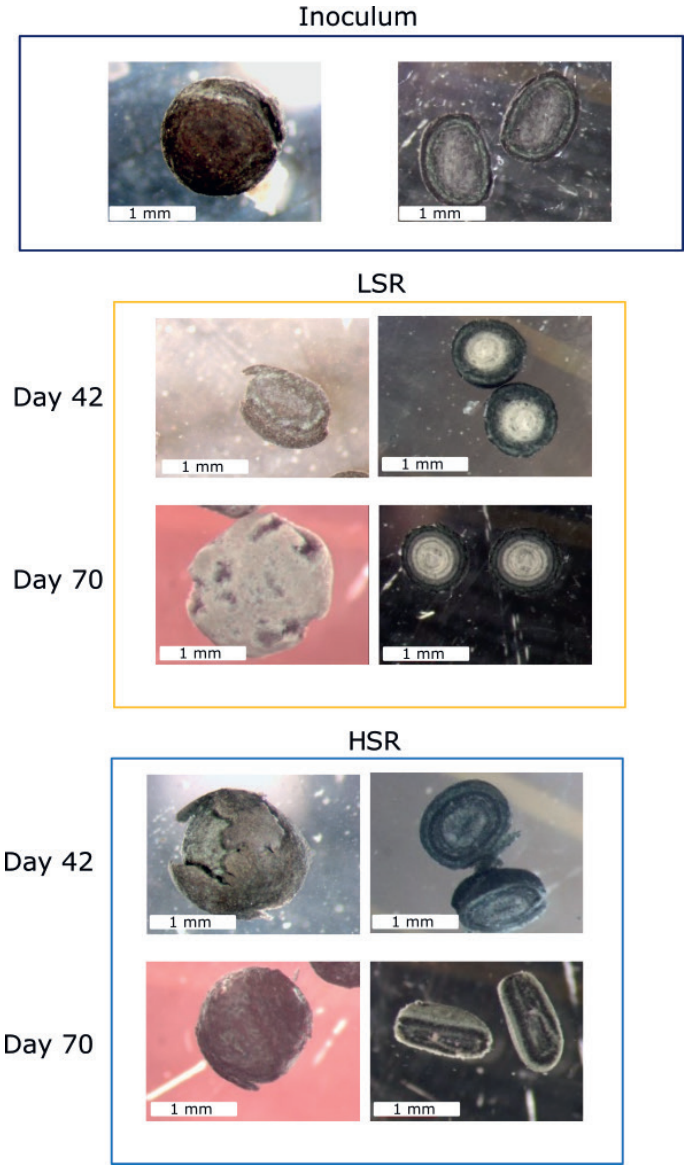


Figure S.5.10: Macroscopic images of granule's surfaces and cross-sections at Days 0 (inoculum), 42, and 70. In each box, the left image shows the granule surface, and the right image shows the cross-section. The granules used for cross-section imaging were not the same as those used for surface imaging. The scale bar represents 1 mm for all images."

S.5.12. Precipitation on surfaces of cells in LSR

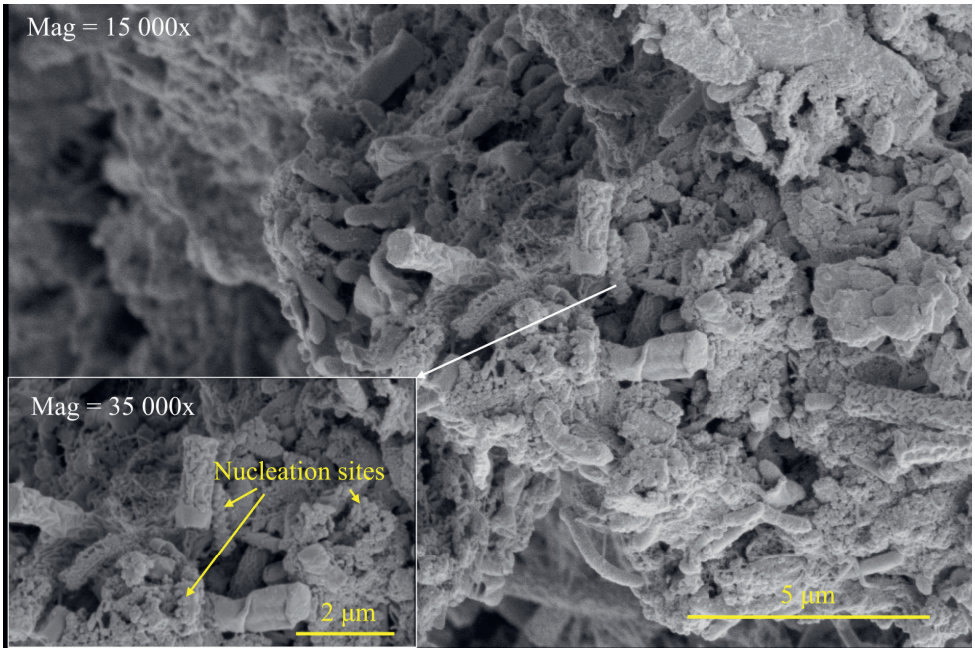


Figure S.5.11: High magnification SEM images of granule's surface in LSR.

S.5.13. EDS spectra of sliced HSR and LSR granules

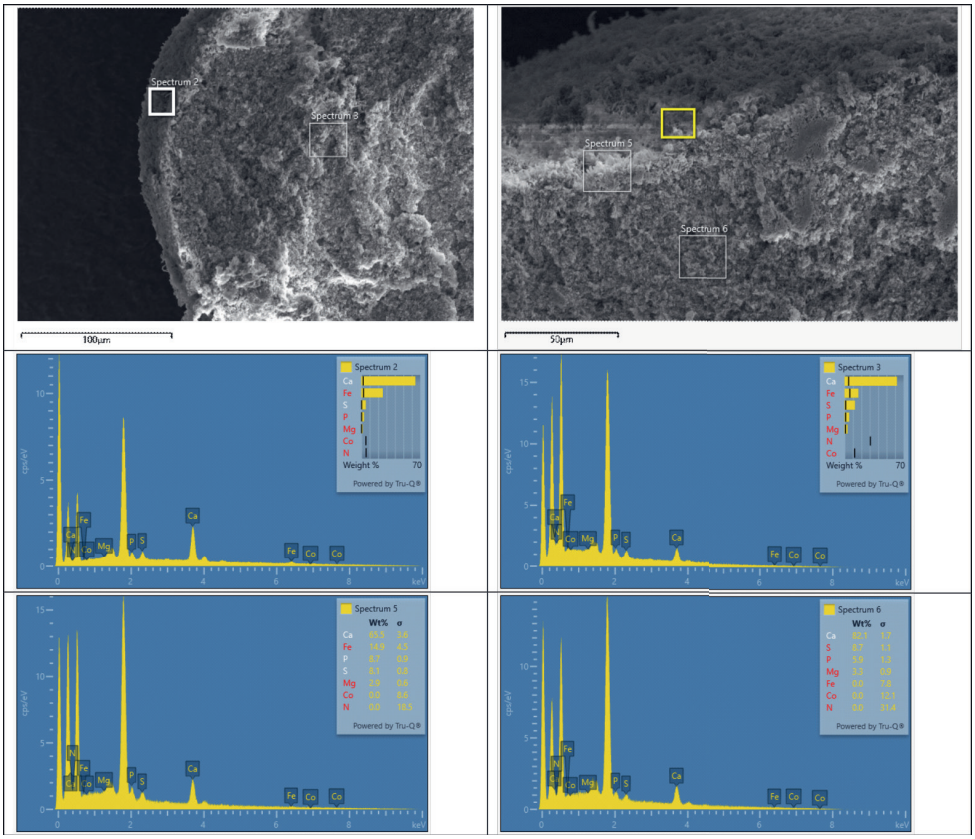


Figure S.5.12: EDS spectral data HSR granule shown in Fig. 8. To increase Ca/N sensitivity Tungsten, Carbon and Oxygen were excluded from the analysis, therefore their peaks are not labelled. The X - axis in the spectra represent the X-ray energy (keV) and the Y axis corresponds to the X – ray counts (cps/eV).

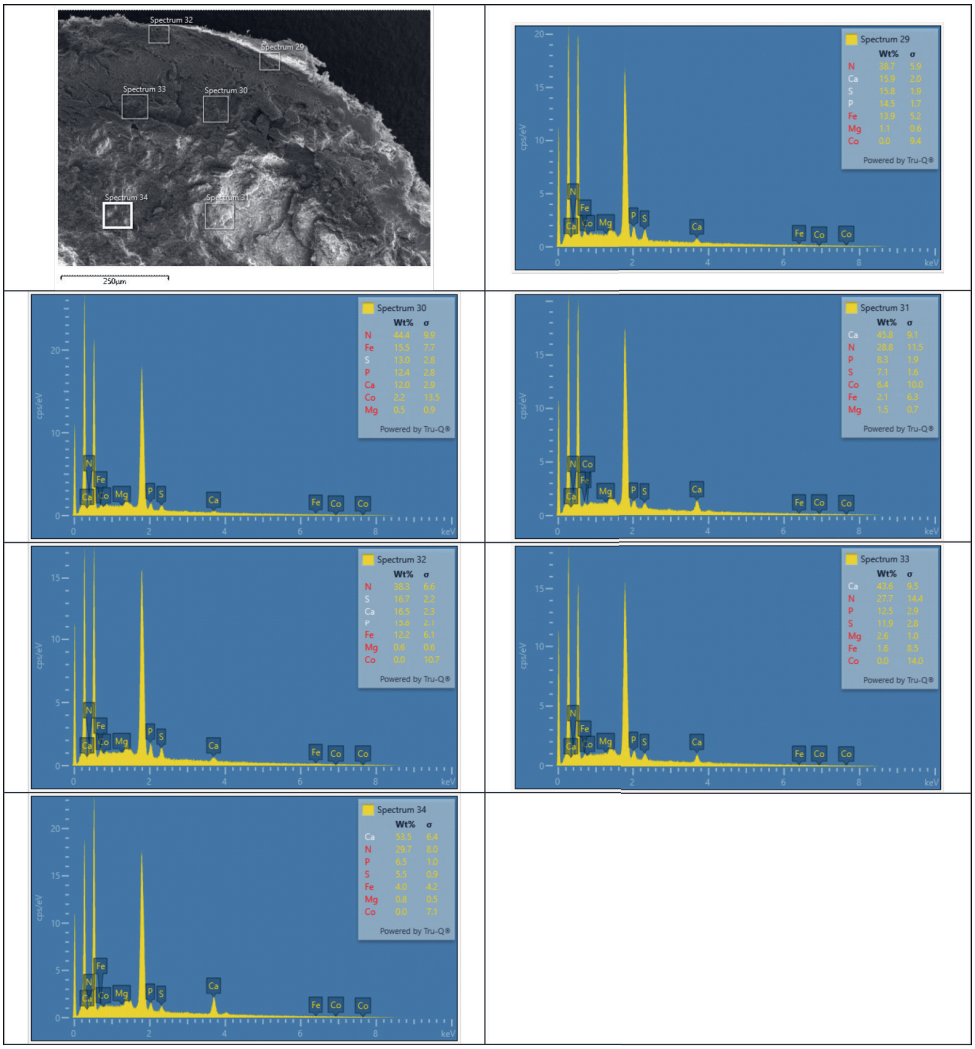


Figure S.5.13: EDS spectral data from LSR granule shown in Fig. X (left) and additional sample to demonstrate reproducibility (right). To increase Ca/N sensitivity Tungsten, Carbon and Oxygen were excluded from the analysis, therefore their peaks are not labelled. The X - axis in the spectra represent the X-ray energy (keV) and the Y axis corresponds to the X – ray counts (cps/eV).

S.5.14. SEM and SEM-EDS of granules analysed with MRI as "calcified"

Figure S.5.14A-B show the EDS spectra of sliced granules, which were visually identified as calcified for MRI analysis. The spectra confirm, that indeed these granules contained high levels of calcium. For HSR (high shear reactor) the Ca

content of these pre-selected granules was larger than that of those selected randomly (See Figure 5.8c in the manuscript). For LSR (low shear reactor) the content of Ca on the outer edge was as high as for randomly selected granules shown in Figure 5.8d of the manuscript, but decreased towards the centre. These results agree with the ionic composition measurements of the granules (See Figure 5.8a in the manuscript) showing that the bulk of the granules was more calcified in LSR compared to HSR. Also, the surfaces of these MRI pre-selected granules indicate precipitation on the surfaces of both, HSR and LSR, albeit still the granules from HSR seemed to have a "rougher" and more porous surface (Figure S.5.14C) compared to those of LSR (Figure S.5.14D).

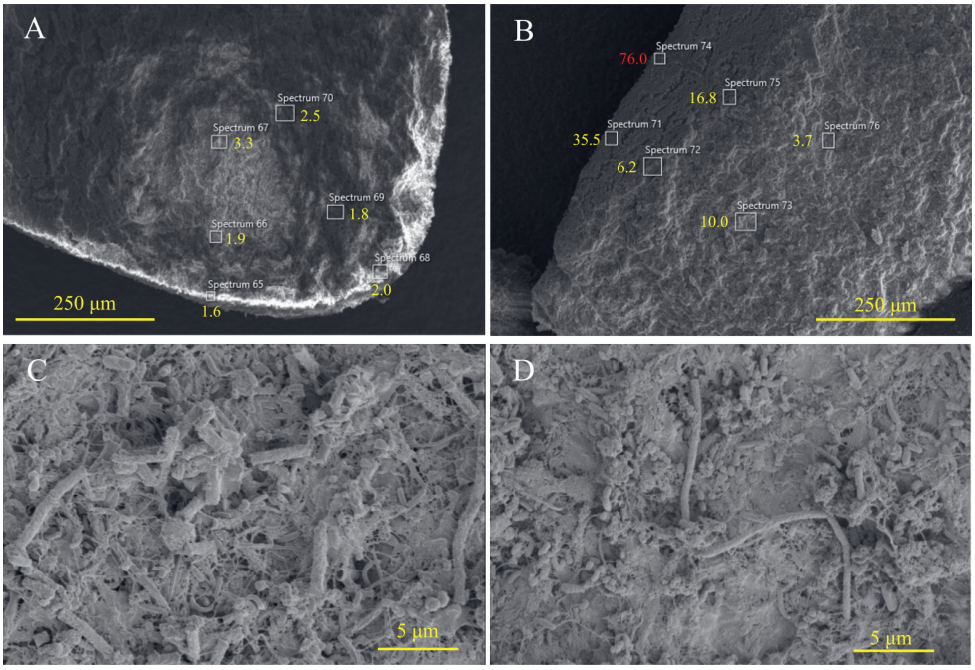


Figure S.5.14: SEM images of "calcified" granules studied with MRI at T70. In the top row electron images of sliced granules with EDS spectra areas from HSR in A and from LSR in B. In the bottom row electron images of surfaces of non-sliced granules in HSR (C) and LSR (D) show some precipitation, but a "rough" and porous surface in HSR (C) and a "smooth" surface filled with precipitates in LSR (D). Numbers next to the squared boxes of A, B show the ratio of wt.% between Ca/N from EDS spectra. Red numbers indicate that N wt% could not be detected and the denominator for the ratio was set to 1. EDS – energy dispersive X – ray spectroscopy.

S.5.15. Internal structure of granules

T1-weighted images – MRI method: The same MRI acquisition parameters were used as for imaging the HSR and LSR granules.

T1-weighted images – Results: Granules from both batch reactors show distinct layers in the internal structure and a large variability in size, heterogeneity, and shape. In contrast to the LSR, granules in the batch 2 reactor do not decrease in size.

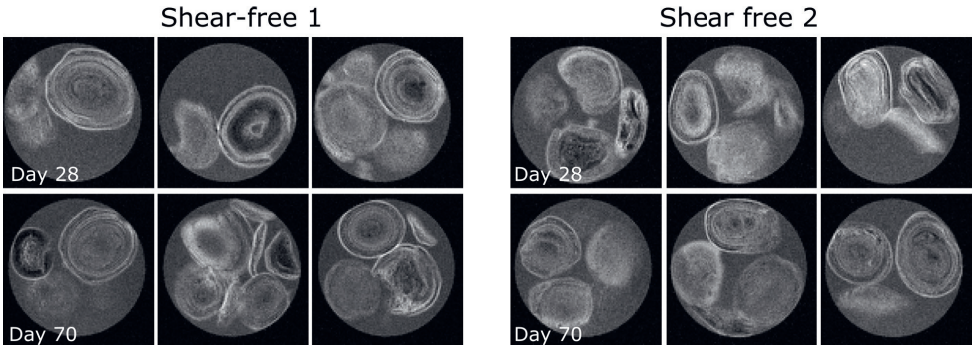


Figure S.5.15: T1-weighted image of shear-free 1 and shear-free 2 reactors at Day 28 and Day 70.

T1-weighted images – MRI method: Granules were specifically selected based on their visually apparent calcification. The MRI acquisition parameters were the same as those used for the T1-weighted MRI experiments described in the main paper. For LSR at day 70, the image intensity was manually scaled due to the presence of an imaging artefact.

T1-weighted images – Results: A high degree of heterogeneity is observed in the selected granules, with darker regions indicating the potential presence of solids or short $T_{2,\text{eff}}$ values.

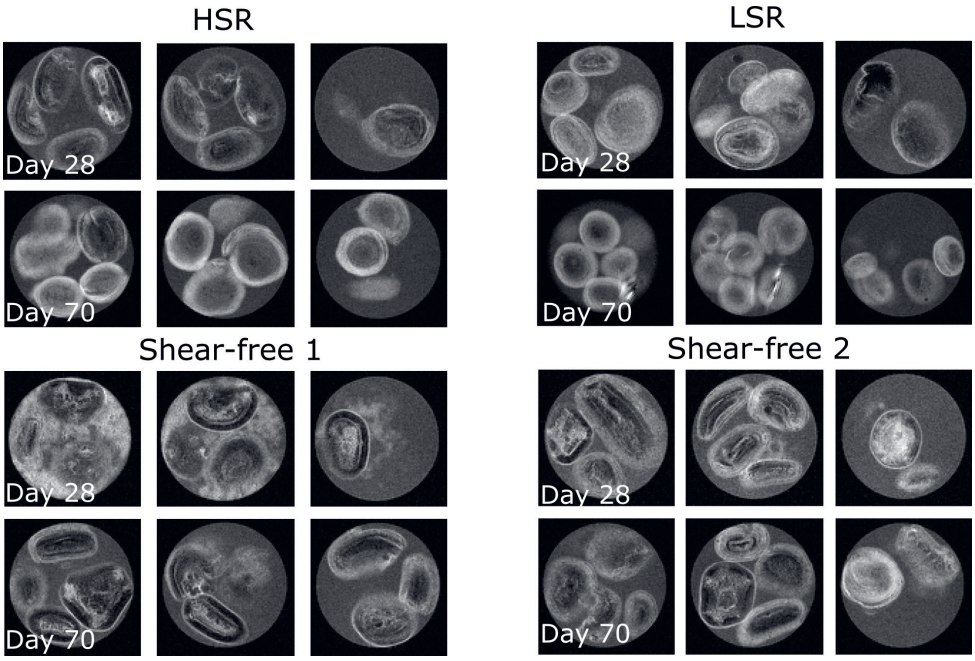


Figure S.5.16: MRI images of granules with visually apparent surface calcified layers

T2-weighted images – MRI method: A 2D spin echo sequence (MSME) was used on the granules from the HSR reactor at day 28 using the following parameters: repetition time 5000 ms, echo time 2.91 ms, number of echoes 32, number of averages 2, experiment time 16 min, field-of-view (4.5 × 4.5) mm^2, matrix 96 × 96, spatial resolution 47 × 47 μm, receiver bandwidth 100 kHz, pulse excitation and refocusing bandwidth 4.2 kHz, slice thickness 0.5 mm.

T2-weighted images – Results: The MRI images at different echo times show that the signal intensity in the biofilm is lower compared to bulk water and also that at the 4th echo (echo time (TE)= 11.7 ms) most signal in the biofilm has decayed.

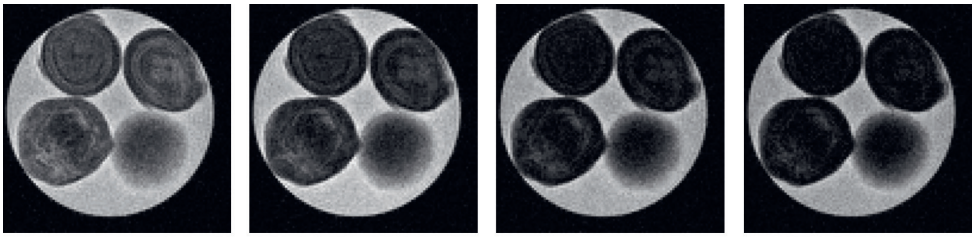


Figure S.5.17: T2-weighted images of HSR-granules at Day 28.

S.5.16. Mechanical strength of the granules

Methods:

The strength of the granules was measured by exposing them to high-turbulence conditions in a bubble column. Granules (2 g, with a known dry weight X_0) were introduced into a cylindrical bubble column (diameter 46 mm, height 305 mm) filled with tap water. The column was sparged with nitrogen gas at a superficial velocity of 1.7 cm/s. During the experiment, abraded fines were collected every 30 min for a total of 2 h, and their dry weight (X_F) was determined according to Standard Methods (2540). The cumulative fines production was then used to estimate the shear strength of the granules, expressed as strength (s), following de Graaff et al. (2020):

$$\frac{dX_F}{dt} = K(X_0 - X_F) \tag{S.5.4}$$

$$X_F = X_0\left(1 - e^{-Kt}\right) \tag{S.5.5}$$

$$Strength = \frac{1}{K} \tag{S.5.6}$$

where X_F is the cumulative production of fines (gTS) at time t (s), X_0 is the dry weight of granules at $t = 0$ (gTS), K is the abrasion coefficient (s^{-1}), and S_{granule} is the shear strength of the granules (s). A detailed description of the protocol is

provided by Gao et al. (2024b).

Results:

Figure S.5.18 presents the evolution of the granule's strength over time. During the initial five-day acclimation period, granule strength declined most likely due to the influence of the new medium, as a similar trend was observed in all reactors. This decreasing trend persisted for approximately two weeks after the experiment began, after which granules in the shear-free reactors showed a recovery in strength. The strength of granules in the HSR and LSR followed different trends, with those in the LSR developing stronger granules, while the granules in the LSR became weaker over time.

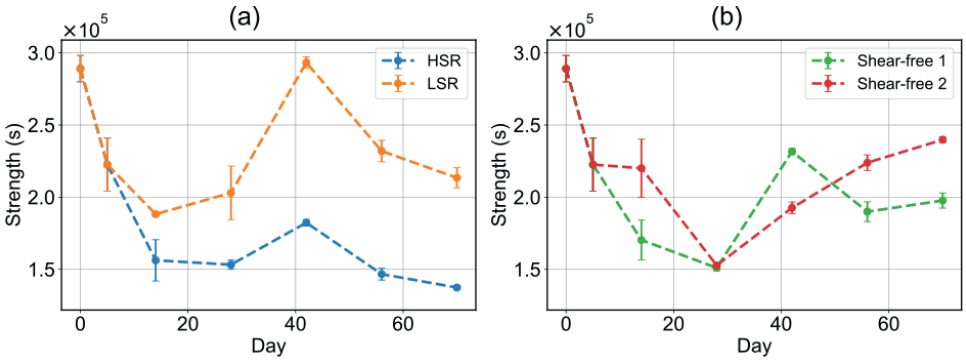


Figure S.5.18: Strength of the granules in shear-dominated reactors (a) and shear-free reactors (b).

Chapter 6

6

Chapter 6

General Discussion

6.1. Introduction

Anaerobic granular sludge technology has become the cornerstone of high-rate anaerobic wastewater treatment. This technology has been successfully implemented to treat different types of industrial effluents across a wide range of sectors, such as breweries, dairies, distilleries, slaughterhouses, and pulp and paper mills (Mainardis et al. (2020)). Anaerobic granular sludge reactors (AGSRs) are characterized by a small footprint and the ability to operate at high volumetric organic loading rates. Maximum performances are obtained when the reactor contains a high concentration of active, well-settling granular biomass (van Lier et al. (2015)). This is achieved through the formation and development of anaerobic granules, which provide rich microbial diversity within a robust structure with good settling ability and tolerance to environmental stresses (e.g., inhibitory compounds) (Wilén et al. (2018)).

Hydrodynamics play a central role in the operation of AGSRs. It is well known that, beyond mixing, hydrodynamic conditions control the hydraulic selection pressure, through which poorly structured flocs are continuously washed out while dense, well-settling aggregates are retained (Aragón-Barroso et al. (2026)). These aggregates can subsequently undergo granulation and further development through concurrent mechanisms influenced by multiple parameters. One of these key parameters is the local hydrodynamics in the vicinity of granules. Local flow dynamics, not only during granulation but also throughout granule maturation, influence the physical, chemical, and biological properties of granules, which directly impact reactor performance (Liu and Tay (2002), Wilén et al. (2018)). However, hydrodynamics in AGSRs are not an independent variable but, as further explained in this chapter, emerge from complex gas–liquid–solid interactions. They are governed by a number of interrelated parameters, including physical and chemical characteristics of wastewater (i.e., viscosity, density, organic composition, macro- and micro-nutrients, inhibitory compounds), operational conditions (e.g., pH, temperature, upflow velocity, and organic loading rate (OLR)), and reactor design (i.e., height-to-diameter ratio, liquid distributor and three-phase separator design, and internal configuration). Collectively, these parameters determine the hydrodynamic conditions in these reactors, either directly or indirectly through different mechanistic pathways.

Previous studies have suggested that biogas generation from anaerobic granules may be maximized within specific ranges of hydrodynamic intensity. For example,

reported optimal shear-rate windows include 24–48 1/s (Jiang et al. (2014)), as well as 24–37 1/s at the microscale and 32–63 1/s at the mesoscale (Zhang et al. (2011)). This indicates the existence of an optimal hydraulic operational window for enhanced mass transfer and biological conversion and these reactors require operational optimization to enhance microbial activity and biogas yield (Meng et al. (2021)). However, the diversity of wastewater types introduces uncertainty regarding the existence of a single optimal operational window, as substrate conversion kinetics and metabolic routes strongly depend on wastewater characteristics. Instead, operating conditions may need to be tailored to specific wastewater compositions to achieve optimal performance (Aragón-Barroso et al. (2026)). Such optimization requires a mechanistic understanding of how local hydrodynamics influence granule properties and microbial activity through their effects on shear stress and mass transfer. Currently, limited knowledge exists on how aforementioned parameters (i.e., Wastewater characteristics, operational condition and reactor design) affect reactor-scale hydrodynamics, how these translate to granule-scale flow dynamics, and how the flow behavior at granules surface governs mass transfer and shear stress. Consequently, the links between operational parameters, hydrodynamics, granule properties, and reactor performance remain insufficiently understood. Addressing this gap requires detailed characterization of multiphase flow behavior at both reactor and granule scales. However, such efforts have been constrained by the lack of experimental techniques capable of resolving local flow dynamics in dense three-phase systems.

In this chapter, we endeavored to integrate the findings of this thesis with state-of-the-art advances in multiphase flows, and the recent findings on how biofilm-flow interactions influence biofilm properties to identify the key hydrodynamic variables in three-phase AGSRs and propose potential mechanisms by which they govern granule properties.

6.2. Overview of the thesis findings: from black box reactor to resolved local hydrodynamics

In Chapter 3, the feasibility of investigating local hydrodynamics in the sludge bed section of AGSRs at high granular sludge concentrations was evaluated using transparent hydrogel beads as synthetic granules. A combined approach

of refractive index matching (RIM) with three-dimensional particle tracking velocimetry (3D-PTV), a non-intrusive, image-based flow measurement technique, was successfully applied. The method demonstrated robust capability in resolving the liquid-phase three-dimensional velocity fields within the reactor volume under dense two-phase flow conditions, with solid volume fractions reaching up to 50%. This represents the first experimental study in the field of anaerobic granular sludge systems attempting to quantify 3D flow dynamics at such high solid concentrations. This enables us to investigate the effect of key influential parameters (e.g., granular sludge concentration and biogas production rate) on the liquid velocity field and mixing performance in the reactor. Therefore, in Chapter 4, the method was extended to three-phase flow conditions, which are characteristic of AGSRs. At constant upflow velocity (superficial liquid velocity), the contribution of biogas production rate and solid volume fraction to the changes in hydrodynamics and mixing behavior of the reactor was systematically investigated over a gas superficial velocity range of 0.01–0.1 cm/s and a solid volume fraction range of 0–50%. It was shown that the biogas production rate exhibits a positive correlation with the mean liquid velocity and with the occurrence of extreme instantaneous velocity components in both axial and lateral directions. In contrast, increasing the solid volume fraction was found to have a dual effect on these variables with both the mean liquid velocity and the likelihood of high-velocity events initially increase up to a peak value and subsequently decrease. Notably, this critical solid volume fraction and the peak mean velocity value was found to depend on the gas superficial velocity. Finally, in chapter 5, the effect of local hydrodynamics on granule property evolution in calcium rich conditions, typical of cardboard industry, was investigated under shear-dominated (including meso-scale high- and low-shear) and shear-free conditions. The results indicate that turbulence characteristics within the reactor play a more decisive role than the mean (bulk) flow in determining granule properties. It was proposed that turbulent fluctuations govern mass transfer and shear stress at the granule surface, thereby influencing granule size, morphology, mechanical strength, and internal structure. Under calcium-rich conditions, these effects further promote calcification by enhancing the transport of Ca^{2+} into the granule interior. Moreover, beyond the intensity of turbulent fluctuations, their temporal frequency was identified as a critical parameter governing both shear stress and mass transfer at the granule scale.

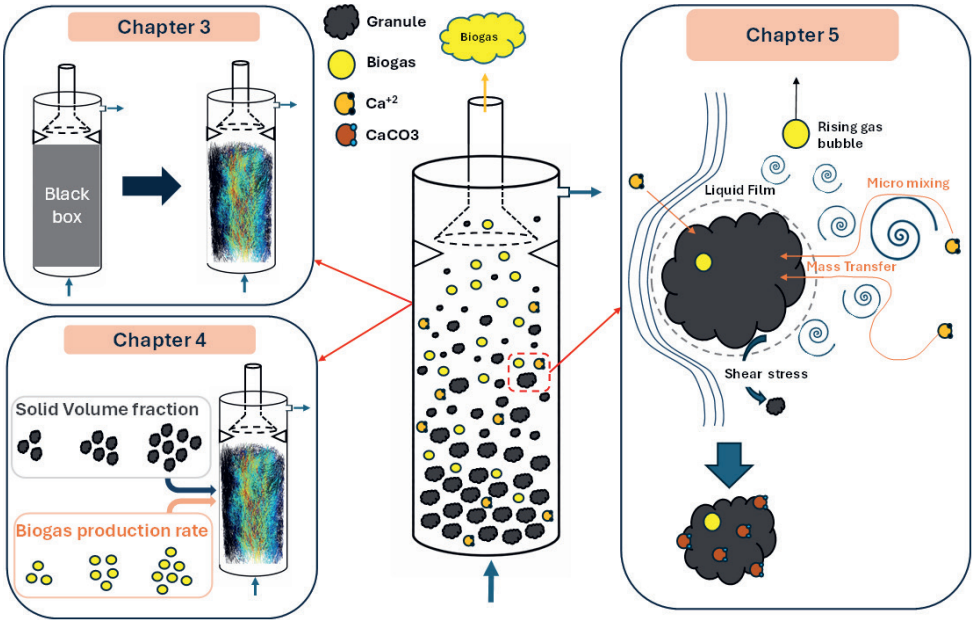


Figure 6.1: Schematic outline of this thesis.

6.3. Scientific insights practical implications and research limitations

6.3.1. Parameters affecting key hydrodynamic variables and the transport phenomena in AGSRs

AGSRs exhibit highly heterogeneous hydrodynamics arising from the complex and dynamic interactions among the wastewater, granules, and biogas, synthesized within the granules themselves. In these three-phase systems, operated either as packed or fluidized beds, both the solids concentration and gas production rate and holdup vary along the reactor height, resulting in distinct hydrodynamic conditions across different regions of the reactor. The highest sludge concentration is typically found near the reactor bottom, where small biogas bubbles are generated through nucleation, growth, and detachment from the granule surface. In this region, hydrodynamic and mixing intensities are relatively low, as small bubbles are transported by the bulk liquid flow (Jiang et al. (2014)). Along the reactor height, continuous bubble generation increases the likelihood of bubble coalescence, leading to the formation of larger bubbles that rise faster This alters the on-way momentum coupling between gas bubbles and liquid to two-way coupling, in which the gas bubbles no longer

passively follow the bulk liquid flow, but they can attain a significant rise velocity that can modify the surrounding velocity fields. As a result, local hydrodynamics are intensified and local mixing is enhanced. Through the collective motion of bubble swarms, these local effects can propagate to the reactor-scale bulk flow, thereby improving overall mixing in the reactor.

In previous studies on AGSR hydrodynamics, upflow velocity and OLR are typically considered the primary parameters governing reactor behavior, and shear rate is commonly used as a variable to quantify hydrodynamic intensity and mixing. However, shear rate inferred from spatially averaged velocity fields, typically measured using particle image velocimetry (PIV) or particle tracking velocimetry (PTV), represents an apparent velocity-gradient quantity whose value depends on the spatial scale over which it is evaluated. Consequently, shear rates estimated at the reactor or meso scale cannot necessarily be translated directly into the shear stress and mass-transfer conditions experienced at the granule surface.

In Chapter 5, the time-averaged liquid velocity field was measured at the meso-scale, and the corresponding shear rate was calculated. However, no physically meaningful correlation was observed between the measured mean-flow quantities, i.e., liquid velocity and velocity gradients (shear rate) (Fig. 5) and the evolution of granule size in the reactor (Fig. 7). This indicates that the shear stress experienced at the granule surface differed significantly from the time-averaged hydrodynamic intensity quantified at the meso-scale and reactor-scale. Therefore, a multiscale approach would be required to measure shear rate at the granule scale. However, velocity measurement at the surface of suspended and moving granules is technically challenging due to constant motion of granules. Recent findings in biofilm research show that biofilm properties can change significantly even in the absence of mean flow, driven solely by velocity fluctuations. This observation motivated us to look for additional hydrodynamic variables, whose effects on local flow dynamics may not be fully captured by mean-flow characterization, yet may strongly influence local shear stress and mass transfer within these three-phase systems.

The hydrodynamic variables typically used to assess three-phase reactor systems include (i) liquid velocity, (ii) gas holdup, (iii) bubble characteristics and dynamics (e.g., size distribution, spatial distribution, and rise (slip) velocity), (iv) turbulence, and (v) pressure drop (Yang et al. (2022), Ahmed et al. (2026)). These variables

are inherently interdependent, with changes in one variable influencing the others through complex phase interactions. Moreover, they are governed by multiple parameters, such as reactor structural design, phases properties, and operating parameters (e.g., upflow velocity and OLR). To investigate how hydrodynamics affects granular properties and reactor performance, and to gain deeper insight into the mass and momentum transport processes governed by these variables, it is essential to have a deeper understanding on how different parameters influence these variables as well as the interplay between them.

In the following sections, the effects of the main parameters on the hydrodynamic variables relevant to operation of AGSRs are discussed. This is done based on the findings of this thesis and based on insights from studies on relatively similar three-phase systems such as slurry bubble columns and slurry airlift reactors in the chemical engineering field.

6.3.1.1. Wastewater characteristics

Chemical characteristics

The type of wastewater strongly influences the microbial community, structure, and function of anaerobic granules (Batstone et al. (2004)). The chemical characteristics of wastewater, such as organics composition, nutrient balance, and the presence of inhibitory compounds can indirectly modify reactor hydrodynamics by regulating microbial activity and biogas production.

Biogas production is tightly coupled to hydrodynamics through feedback mechanisms (Figure 6.3, mechanisms B1-H2). An increase in gas production rate alters gas holdup and bubble dynamics, which intensify the local hydrodynamics. This might increase the mass transfer of substrates, nutrients, and inhibitory compounds toward and within the granules and alter the shear stress at the granules surface. In the short term, enhanced external mass transfer (i.e., transport of solutes across the liquid boundary layer surrounding the granule) can modify substrate diffusion rates, which directly influences microbial activity and biogas production (Figure 6.3, mechanisms H3-T1-G4). The changes in the mass transfer rates of substrates and metabolic byproducts within the granule create different chemical concentration profiles, leading to the formation of new ecological niches along the altered chemical gradients. This can affect microbial community composition and structural organization within

the granules, based on the growth kinetics of different populations (Picioreanu et al. (2000)). Together with increased shear forces at the granule surface, these effects, in the long term, reshape granule properties, including size, density, and internal structure, thereby influencing external and intragranular transport processes that regulate the biogas production rate (Figure 6.3, mechanism G2).

The higher mass transfer rate also includes the transport of inhibitory compounds or essential compounds present at inhibitory concentrations. As shown in Chapter 5, in calcium-rich wastewater, enhanced granule-scale hydrodynamics (formation of turbulent eddies with length-scale comparable or smaller than granule size) can increase the transport of Ca^{2+} into the granule. This led to a decrease in methanogenic activity of granules due to formation of calcium (e.g., carbonate) precipitates, thereby increasing resistance to mass transfer. This further emphasizes that, depending on the chemical characteristics of the wastewater, hydrodynamic conditions need to be optimized to maximize reactor performance.

Physical characteristics

The extent to which biogas motion can intensify local hydrodynamics depends on multiple parameters, in particular the physical characteristics of the wastewater. The chemicals present in the influent wastewater (e.g., surfactants, proteins, fats, and polymeric electrolytes), together with extracellular polymeric substances (EPS) produced by the biomass can modify key wastewater physical properties such as viscosity, density, and interphase properties such as interfacial surface tension. These properties play an important role in regulating the flow dynamics at both reactor and granule scales. In particular, increased viscosity dampens turbulence and thickens the diffusion boundary layer surrounding the granules (You et al. (2020)), thereby limiting the exchange of substrates and metabolic products between the bulk liquid and the granule interior.

Viscosity and surface tension also directly influence biogas bubble formation, interactions, and transport, which is a critical mechanism linking microbial activity to local hydrodynamics. Surface tension controls bubble nucleation, growth, detachment, and subsequent transport and coalescence. It is widely accepted that lower surface tension, associated with the presence of surface-active compounds, promotes the formation of smaller bubbles and earlier detachment. This results in smaller average bubble size and lower bubble rising velocity, which decreases

the contribution of gas bubbles to hydrodynamics (Yang et al. (2022)). From an operational perspective, this can potentially reduce gas–liquid separation efficiency and increase the likelihood of gas carryover in the effluent. This can lead to to considerable energy loss and contribute to greenhouse gas emission (Stazi and Tomei (2021)).

In Chapter 5, the working fluid was tap water (with added substrates and nutrients), whereas in Chapters 3 and 4, polyvinylpyrrolidone (PVP) was added at concentration of 0.5% w/w to achieve refractive index matching between the liquid and solid phases. This altered the physical properties of the liquid. However, due to the limited availability of data on the physical properties of different wastewaters, it is difficult to determine whether these conditions fall outside the typical range. Given the wide variability in wastewater composition, as well as the presence of micron-scale suspended solids (e.g., biomass and influent solids), the rheological properties of wastewater can vary significantly.

6.3.1.2. Operational parameters

Upflow velocity

The upflow velocity, often defined as the superficial liquid velocity based on the imposed reactor inlet flow rate divided by the reactor cross-sectional area, is a key parameter in the hydraulic design of AGSRs. This parameter is important in governing the flow regime, e.g., packed or fluidized bed, and strongly influencing liquid–solid–gas interactions. Notably, in three-phase flows, the upflow velocity does not necessarily directly translate to the measured mean liquid velocity in the reactor. As demonstrated in Chapters 3 and 4, variations in solid volume fraction and gas flow rate (biogas production rate) can significantly influence the mean liquid velocity even at the same upflow velocity (Figure 6.3, mechanisms G1-B1). This, in turn, creates a feedback mechanism by altering the solid volume fraction through changes in solids retention time (SRT) and biomass washout (Figure 6.3, mechanism H1). A higher mean liquid velocity can also increase the velocity gradient (shear rate), creating turbulent velocity fluctuations. Increased hydrodynamic intensity, particularly at the granule scale, can affect biogas detachment from granule surfaces, bubble size, and relative bubble rising velocity, thereby regulating the effect of biogas on mean liquid velocity and turbulence (Figure 6.3, mechanism H2).

Organic loading rate, temperature, and pH

Temperature, pH, and OLR influence hydrodynamics through their control of microbial activity and biogas production rates. An increase in OLR, for example, enhances granules activity and gas production, which along the reactor axis leads to higher gas holdup and bubble population. This, in turn, increases the coalescence rate, resulting in larger bubbles that can intensify local liquid flow and cumulatively increase the overall mean flow (Figure 6.3, mechanisms OB1-G4-B1).

In Chapter 4, the hydrodynamics of the reactor were intensified by varying the gas flow rate to mimic different biogas production rates and gas holdup along the reactor height, resulting from continuous biogas generation from different sludge layers. Different solid volume fractions were also tested to represent the decreasing granular sludge concentration profile along the height of AGSRs. The results showed that increasing the gas superficial velocity (GSV) increased the mean liquid velocity and, across all tested solid volume fractions, enhanced both the magnitude of the mean velocity and the probability of extreme liquid velocities in both axial and lateral directions.

It should be noted that bubble size is also a critical parameter determining the extent to which bubbles influence the surrounding and overall flow. In the experiments (chapter 4), bubble size was not experimentally measured; however, qualitative observations (Figure 6.2) indicated the presence of a wide range of bubble sizes, including bubbles of several millimeters, which are less likely to form in the bottom of the full-scale AGSRs. Moreover, varying solid volume fraction affected both the size of bubbles generated from the gas sparger and their spatial distribution. In future experiments, different sparger designs could be tested (e.g., capillary tube spargers) to provide better control over bubble size and improved coverage of the reactor cross-section, thereby achieving more uniform bubble generation and more closely replicating three-phase flow conditions in AGSRs. In Chapter 5, the critical role of gas dynamics and bubble characteristics on shear stress and mass transfer at the granule surface was also demonstrated. This will be further discussed in section 6.3.2.

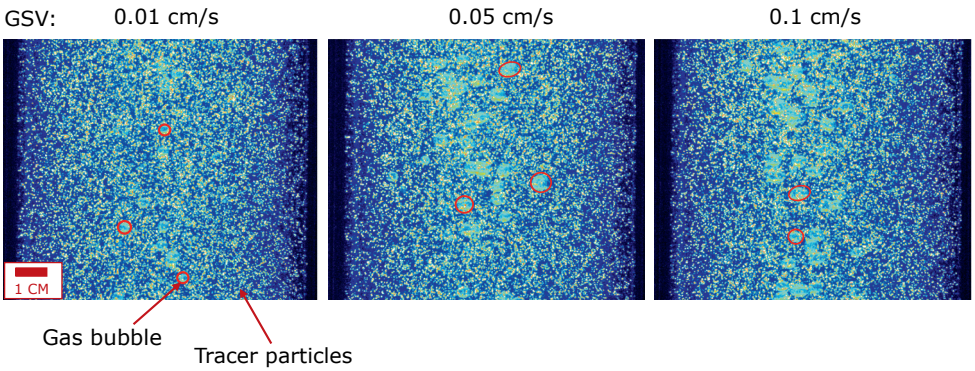


Figure 6.2: Snapshots of fluorescent tracer particles and rising gas bubbles at different gas superficial velocities (GSVs) and at 30% solids volume fraction using transparent hydrogels (chapter 4). Larger bubbles were observed with increasing GSV. The images were captured with long-pass filters mounted on the camera lenses.

6.3.1.3. Reactor design

Structural parameters such as the height-to-diameter (H/D) ratio, internal configurations, inlet design, and gas–liquid–solid (GLS) separator design influence phase distribution (gas–solid), flow patterns, mixing behavior, and local flow dynamics. These parameters are tailored to the intended operating conditions (i.e., upflow velocity) and also play an important role in controlling granular sludge concentration through hydraulic selection pressure, enabling retention of dense, well-settling granules, and washout of dispersed flocculent biomass (Figure 6.3, mechanisms OB1-H1-O1). The reactor used in the experiments in this thesis had a diameter of 10 cm, ensuring minimized effect of the wall on the local hydrodynamics. The GLS separator design was based on (Hu et al. (2017)) to ensure effective three-phase separation under the high upflow velocities applied in this study.

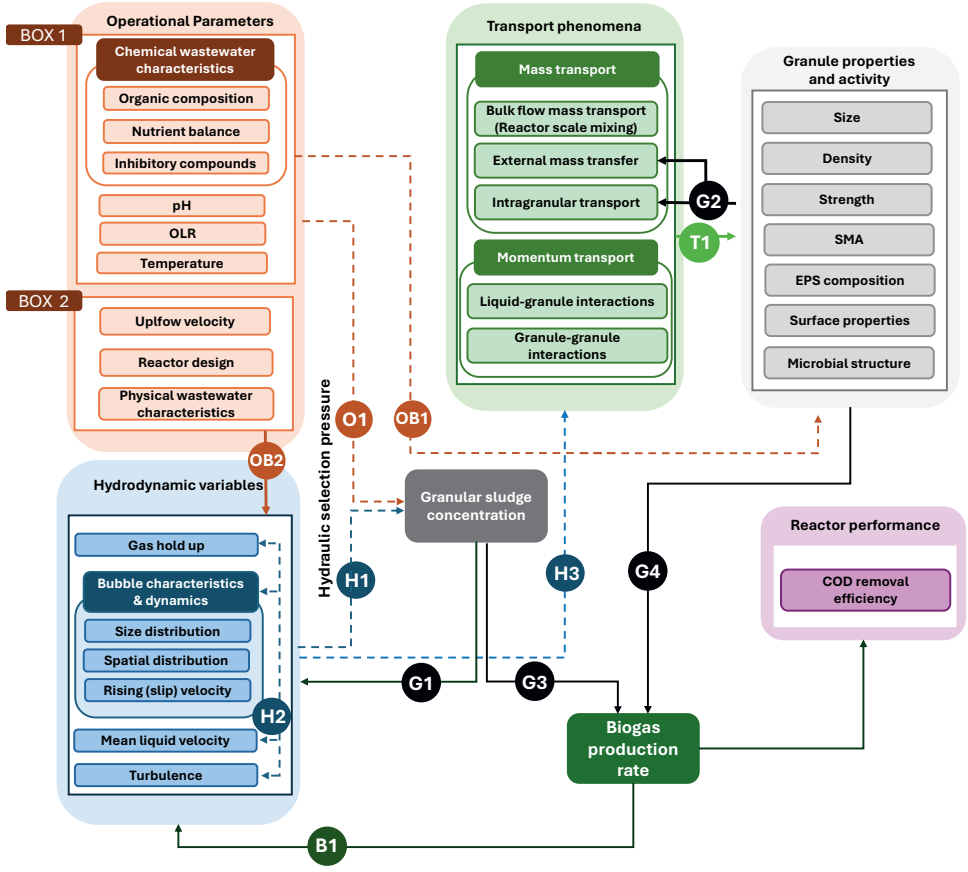


Figure 6.3: Conceptual diagram illustrating factors affecting treatment performance in AGSRs. Operational parameters, hydrodynamic variables, and reactor design (e.g., GLS separator) govern granular sludge concentration via hydraulic selection pressure (granulation, retention of dense granules, and washout of flocculent biomass) (O1-H1). Hydrodynamics are influenced by operational conditions (box 2), sludge concentration, and biogas production (OB2–G1–B1). The outcome of three phase interactions (H2-G1-B1) effect the mean liquid velocity and turbulence which determines mass and momentum transport (H3). These transport phenomena influencing mixing, mass transfer, shear stress, and together with operational parameters (box 1) affect granule properties and activity (OB1-T1), which in turn affect the external and intragranular transports (G2). Granule properties, particularly their activity, and sludge concentration determine biogas production rate (G3–G4), ultimately governing COD removal and overall reactor performance.

6.3.2. Turbulence characteristics as the missing puzzle piece in hydrodynamics studies of AGSRs

6.3.2.1. Role of turbulence characteristics in granular sludge development

Hydrodynamic forces have been recognized as a critical factor in shaping the properties of anaerobic granules (Liu and Tay (2002)). In particular, granule size is generally assumed to be governed by mechanical forces arising from liquid–granule and granule–granule interactions (Ren et al. (2009b)). In Chapter 5, the low-seeded experiments enabled the isolation of liquid–granule interactions by minimizing granule-granule interactions, thereby allowing investigation of the mechanisms by which flow dynamics influence granule development. It was hypothesized that increasing the gas flow rate would increase the shear rate and intensify the hydrodynamics, consequently leading to smaller and more compact granules due to an increased abrasion rate at the granules surface. Surprisingly, the above hypothesis was not supported by the experimental observations. The experiments were repeated twice (with only the final results reported), and consistently, the reactor operated at lower gas flow rates resulted in the preservation/development of smaller granules, while larger granules disintegrated, as evidenced by the increased amount of washed-out fine particles (Chapter 5, Figure 5.7). This suggests that the hydrodynamic conditions at the granule scale were more severe in the reactor intended to operate under lower shear conditions (LSR). This outcome was surprising given that all measured hydrodynamic indicators at the meso- and reactor-scale, including overall mean liquid velocity (Chapter 5, Figure 5.4) , shear rate (Chapter 5, Figure 5.5), the likelihood of high-velocity events (Chapter 5, Figure 5.6a), and visual observations of granule fluidization intensity, indicated a lower hydrodynamic intensity in that reactor.

These results suggest that the flow variables often reported as indicators of reactor hydrodynamic intensity (i.e., upflow velocity, fluidization intensity, and average shear rate) (Arcand et al. (1994), Kundu et al. (2014a)) do not necessarily reflect the hydrodynamics and shear stress, particularly at granule scale. Instead, additional mechanisms might be at play, which determine the effective mechanical stress at the granule surface and, consequently, control granule size through surface erosion.

Moreover, these results challenge the long-established idea that as fluid velocity increases, so does the probability that pieces of granules are eroded and entrained into the flow. (Tsagkari et al. (2022)).

The statistical analysis on the temporal liquid velocity dynamics showed that turbulence is the missing piece of the puzzle in explaining the observed variations in granule size between the reactors. Turbulence is inherently characterized by a hierarchical cascade of eddies spanning a wide range of length scales, each inducing liquid motion at its corresponding scale. This multiscale nature is reflected in the liquid velocity time series (Pope (2001)). Two complementary statistical analysis were used to characterize turbulence: the autocorrelation function (ACF) of the velocity time series and the kinetic energy spectra from velocity fluctuations. The former provided insights on the coherent flow structures (dominant eddy scales), and the latter estimated the distribution of kinetic energy across spatial scales, enabling turbulence characteristics comparison between reactors. The results suggested differences between reactors in both dominant eddy size and kinetic energy distribution at the granule scale. It is worth mentioning additional parameters, such as the energy dissipation rate and the Kolmogorov scale, are commonly extracted for turbulence characterization (Prakash et al. (2016)). However, in these experiments, we were limited by the image acquisition rate (approximately 200 Hz) and therefore the velocity sampling rate. In turbulence studies, sampling rates are typically above 1 kHz to capture high-frequency velocity fluctuations associated with the smallest turbulent scales, the Kolmogorov scale, which can be on the order of 100 μm or larger depending on the flow conditions (Mauri (2015)). This can be achieved with the setup developed during this PhD project by reducing the imaging window in future studies.

The relevance of these turbulence characteristics might lie in the way eddies of different sizes impose mechanical forcing on the granule surface. Larger eddies generally contain more kinetic energy but occur less frequently, appearing as strong velocity fluctuations in the measured velocity time series. Granules can be entrained by these eddies and experience shear stress from the bulk flow due to their relative velocity with the surrounding liquid. In contrast, smaller eddies are more numerous and contain less energy individually, appearing as weaker but higher-frequency fluctuations in the liquid velocity signal. These eddies can create steeper local

velocity gradients, meaning that they can impose higher local shear stress on particle surfaces (Morshed et al., 2014). The distribution of eddy sizes, the transfer of kinetic energy between scales, and the smallest turbulent length scale, i.e., the Kolmogorov scale, vary depending on flow conditions. In three-phase systems, these turbulence characteristics are governed by multiple interacting parameters, including gas–liquid–solid interactions, phase properties, and relative phase velocities, and remain largely unexplored (An et al., 2024b).

Assuming a flow dominated by fine-scale structures and eddies comparable to or smaller than the granule size (e.g., low shear reactor (LSR) in Chapter 5), as granules move within the reactor, there is a higher likelihood of interaction with these eddies. The results suggest that the flow in the LSR reactor may have higher kinetic energy at scales smaller than approximately 1.6 mm, corresponding to wavenumber of $k \approx 4{\times}10^3\ 1/m$ (Chapter 5, Figure 5.6). Due to their high abundance and small length scales, these small-scale eddies may impose frequent localized velocity gradients at the granule surface, thereby contributing to persistent mechanical stress which can control granule size through surface erosion. In contrast, the larger eddies which determine the mean flow may have a lesser impact on surface erosion. These results support findings from biofilm studies under fluctuating flows, which show that shear dynamics and fluctuation frequency strongly influence biofilm thickness: low-frequency fluctuations tend to support biofilm growth, whereas high-frequency fluctuations enhance erosion (Wei and Yang (2023), Pizzi et al. (2025)). Notably, a distinction should be made between erosion, which refers to the detachment of small particles, and sloughing, which refers to the detachment of larger fragments or splitting of granules. It is likely that erosion was the dominant mechanism acting at the granule surface, leading to smaller granule size in LSR. In contrast, in the other reactor, all hydrodynamic variables, including both time-averaged liquid velocity and velocity gradient and time resolved probability of occurrence of strong velocity fluctuations (Chapter 5, Figures 5.5 and 5.6a), indicated a higher probability of stronger (but less frequent) shear forces, which could promote the sloughing of a chunk of the granule. However, the preservation of large granules at the end of the experiment suggests that they were able to tolerate these high shear forces at frequencies encountered.

In conclusion, erosion appears to be the predominant mechanism controlling granule size, yet it is not captured by conventional hydrodynamic variables typically reported in literature, such as the overall magnitude of upflow velocity or average shear rate in the reactor, and require flow measurements at the granule surface or detailed turbulence characterization. These conclusions are supported by the recent work of Wei and Yang (2023), who reported that under low-frequency flow fluctuation conditions ($f < 2 \times 10^{-5}$ Hz), the biofilm growth rate and mean biofilm thickness were higher than under steady-state conditions without flow fluctuations ($f = 0$ Hz). At higher fluctuation frequencies ($f > 1 \times 10^{-3}$ Hz), biofilm thickness decreased with increasing fluctuation frequency. They proposed a theory that the inhibition of biofilm growth by high-frequency fluctuations occurs because biofilms require an adjustment time to grow after shear stress switches from high to low; thus, the time available for growth during low shear stress is limited. They stated that biofilms experience a dynamic equilibrium between detachment and regrowth, which determines the mean biofilm thickness.

Based on the findings of this thesis, this theory can be extended to anaerobic granular sludge reactors (AGSRs). However, translating these findings to full-scale AGSRs introduces an additional layer of complexity because these systems are characterized by strong spatial heterogeneity. This heterogeneity arises from spatial variations in solids and gas holdup, bubble size distribution, bubble rise velocity, and liquid velocity (Ren et al. (2009a), Wang et al. (2009)). These factors can generate distinct turbulence structures across different regions of the reactor. Due to this high heterogeneity, a single dominant eddy size cannot be identified, and in each region the turbulence characteristics may differ, with regions characterized by high- and low-frequency velocity fluctuations that interact differently with granules and exert mechanical forces of varying magnitude and frequencies at the granule surface. As granules circulate through the reactor, they are exposed to time-varying shear stress, and the exposure time and the time interval between two successive high-shear exposures may become a critical parameter according to shear dynamic theory proposed by Wei and Yang (2023). These time intervals can potentially determine the balance between growth and erosion, which ultimately governs the granule size in the reactor. Therefore, it can be argued that average granule size depends on the turbulence characteristics in different reactor regions, the frequency distribution of high granule-scale shear regions, and granules motion. These findings and proposed

mechanisms can be further studied for granule properties engineering through new reactor design and operational strategies, with better control over turbulence characteristics and granule shear exposure dynamics, tailored to the operational goals (e.g., COD removal, nutrient recovery) and wastewater characteristics (e.g., presence of inhibitory compounds). For example, different reactor internals could be used to generate turbulence with different characteristics. In addition, upflow velocity could be adjusted according to gas production to regulate the relative motion between bubbles and the liquid flow, thereby influencing bubble-induced turbulence. CFD modelling would be useful to evaluate such design and operational scenarios before experimental implementation.

6.3.2.2. Origin dependency of turbulent fluctuations

In multiphase flows with rising gas bubbles, liquid velocity fluctuations originate from the coexistence of fundamentally different mechanisms (see Figure 6.5). The first mechanism relates to shear-induced turbulence (SIT) which arises from velocity gradients associated with the mean flow and large-scale circulation. The kinetic energy in this type of turbulence follows the classical energy cascade from large to small scales (Risso (2018)), while the presence of solids can affect this energy transfer between scales. An et al. (2024b), in their review on the effect of particles on turbulence field modulation, indicated that the presence of particles can lead to both augmentation and attenuation effects, with the former mainly affecting small-scale eddies and the latter large-scale eddies. Regarding augmentation, particles can shed vortices in their wake as they move, generating unsteady pulsations in the flow. In contrast, at larger scales, the presence of solids tends to attenuate turbulence by reducing liquid velocity fluctuations. This attenuation is attributed to the increased inertia of the slurry (liquid–solid mixture), the enhanced dissipation rate of turbulent kinetic energy caused by drag of particles, and increased viscous dissipation due to the distortion and stretching of eddies at the no-slip boundaries of solid particles. Consequently, the apparent effect of particles on turbulence is determined by the counteraction between attenuation and augmentation mechanisms. In different regions of AGSRs, the granule size and concentration are different; however, there is still very limited understanding of how particle size and concentration affect the local turbulence characteristics.

The second mechanism relates to bubble-induced turbulence (BIT) which originates from the rise of gas bubbles. Here the wake-induced instabilities inject energy directly at smaller scales, making it more likely to directly exert shear stress at the granule surface. Wu et al. (2015) reported that the contribution of rising gas bubbles on shear rate on the granules was significantly higher than that driven by the bulk liquid flow.

In the above context, the findings of Chapter 5, suggested that the dynamics and characteristics of bubbles play a critical role in determining the extent to which rising bubbles contribute to granule-scale shear forces through turbulence modulation. In particular, bubble size and slip velocity are likely key parameters governing BIT. In the reactor operated at higher gas flow rates (HSR), larger bubbles were observed (Figure 6.4), along with higher measured mean liquid velocities (Chapter 5, Figure 5.4). Since rising bubbles generate eddies with length scales comparable to their size, and lower relative velocity between the gas phase and the bulk liquid reduces the intensity of BIT, these mechanisms could potentially explain the lower kinetic energy observed at the granule scale in this reactor (Chapter 5, Figure 5.6c). However, because the bubble size distribution and the relative gas–liquid velocity was not measured in these experiments, it is not possible to explain which factor was more influential in the lower kinetic energy in the flow at granule scale in that reactor. Future studies should fill this gap.

These findings provide important insight into how reactor-scale hydrodynamics and granule-scale hydrodynamics are linked through the modulation of turbulence characteristics. In three-phase AGSRs, hydrodynamic conditions at the reactor scale directly influence bubble generation at the granule surface. It has been reported that higher shear conditions promote the detachment of smaller biogas bubbles (Zhang et al. (2011)), which are more likely to be transported with the bulk liquid with minimum impact on turbulence modulation. A higher biogas production rate and local solid VOF can increase the bubble coalescence rate (Xu et al. (2025)) and lead to the formation of larger bubbles. These bubbles can rise faster and cause changes in distribution of kinetic energy across spatial scales, known as turbulence modulation through bubble induced agitation or pivoting effect on the turbulence energy spectrum (Risso (2018)).

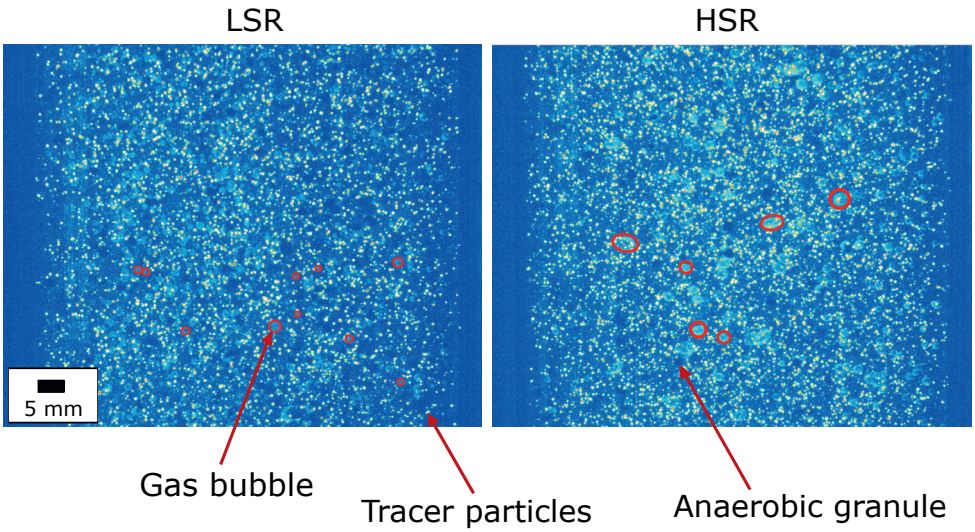


Figure 6.4: Images of three-phase gas–liquid–solid flow in low-shear reactor (LSR) and high-shear reactor (HSR) (chapter 5), showing fluorescent tracer particles, anaerobic granules, and rising gas bubbles. Relatively larger gas bubbles were observed in HSR compared with the LSR. The images were captured with long-pass filters mounted on the camera lenses.

6.3.2.3. Connecting practitioners' experience to findings of this thesis

As explained in chapter 1, in full-scale operation, UASB reactors are generally characterized by lower upflow velocities and longer hydraulic retention times (HRT), which are often interpreted as indicators of lower overall hydrodynamic intensity in these reactors reactors. EGSB reactors, by contrast, are fluidized systems operated at higher upflow velocities and are therefore commonly associated with stronger mixing and higher hydrodynamic intensity. However, practitioners have observed that granules in UASB reactors can be smaller than those in EGSB reactors.

A potential explanation for why granule size in UASB reactors can be smaller than in EGSB reactors, despite the lower apparent hydrodynamic intensity, may lie in differences in turbulence characteristics. Translating reactor-scale flow features directly to the granule scale is not straightforward; however, the mean (bulk) flow can influence several hydrodynamic variables that are critical in determining flow dynamics at granule scale, including bubble population, bubble size, and bubble slip velocity, as illustrated by mechanism L2 in Figure 6.5. These differences in biogas bubble behavior can generate distinct turbulence characteristics around the granules (mechanisms B3 and T1 in Figure 6.5). Based on the findings of this thesis and

the shear dynamics theory proposed in biofilm studies Wei and Yang (2023), local turbulence characteristics and the frequency of shear stress exposure may play an important role in controlling granule surface erosion and growth.

In UASB reactors, the lower upflow velocity can lead to a higher local solids concentration in the sludge bed and, consequently, a higher bubble population. Both factors may promote bubble coalescence and the formation of larger bubbles. At the same time, the lower liquid velocity can increase bubble slip velocity, thereby enhancing bubble-induced turbulence and generating more energetic small-scale flow structures at the granule scale. Due to the frequent passage of bubbles through the sludge bed, granules may experience repeated shear stress exposure, which can contribute to increased surface erosion.

In contrast, EGSB reactors, which operate at higher upflow velocities and generally have lower local solids concentrations due to greater bed expansion, are likely to generate smaller bubbles, lower bubble coalescence rates, and lower relative velocity between gas bubbles and the bulk liquid flow. These conditions may reduce the contribution of bubble-induced turbulence (BIT) to the overall turbulence characteristics. Therefore, shear-induced turbulence (SIT) may be the dominant source of turbulence in EGSB reactors, while turbulence modulation may be governed primarily by the solid phase, i.e., granular sludge, rather than the gas phase. Nevertheless, further experimental and modelling studies are required to improve our understanding of turbulence characteristics in these reactors.

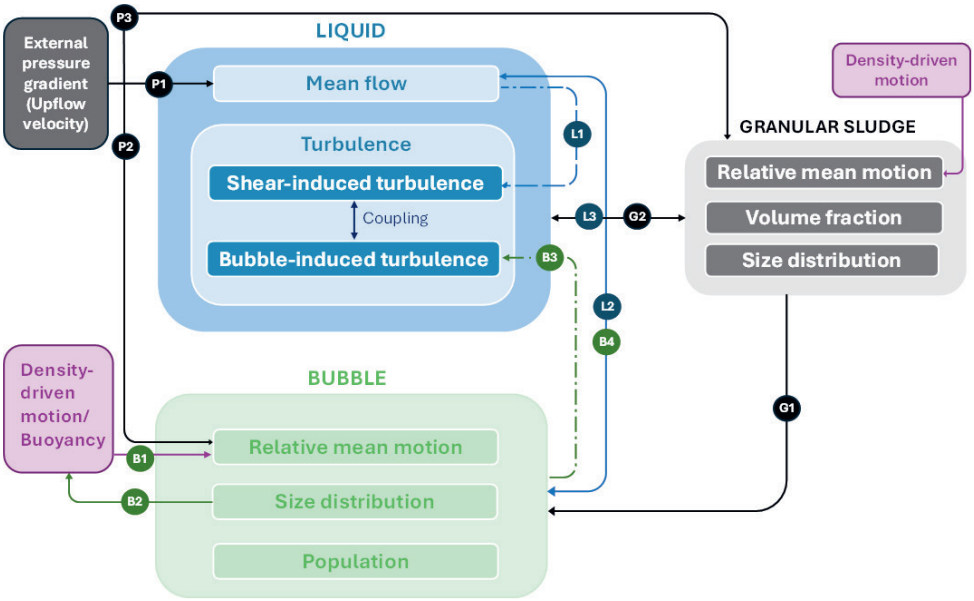


Figure 6.5: Potential physical mechanisms involved in three-phase flow in anaerobic granular sludge reactors. There are two main causes of motion: external pressure gradient, mainly driven by upflow velocity (black), and density-driven motion (pink). The pressure gradient causes a mean flow (P1) in the liquid (blue). Concurrently, the pressure gradient induces a mean motion in the dispersed phases, bubbles (P2) and granular sludge, and determines the degree of bed expansion and local solid volume fraction (P3). Buoyancy causes the bubbles to rise (B1), and depending on their size, bubbles experience different buoyant forces (B2). The size and population (number of bubbles per unit volume) of bubbles are controlled by the solid volume fraction, average size, and relative (to the bulk flow) mean motion of granular sludge, which in turn control the bubble detachment size and rate of coalescence (G1). The disturbance generated by bubble rising motion induces velocity fluctuations in the surrounding liquid (B3). Buoyancy may also generate a mean liquid flow (B4). The mean flow generates strong velocity gradients that eventually produce turbulence (L1). The liquid mean flow determines the sludge retention time (SRT), and therefore the overall sludge concentration in the reactor and local solid volume fraction through controlling the bed expansion. Together with turbulence, it determines the average size of granules (L3). In return, these granular sludge parameters affect the mean flow and modulate the turbulence (G2). Adapted from (Risso (2018)) and modified for three-phase flow in AGSRs.

6.4. Future perspectives

6.4.1. Hydrodynamic characterization approaches for three-phase flow in AGSRs

Based on the findings of this thesis and existing knowledge within the domain of multiphase flows, a number of hydrodynamic variables were identified that play a

critical role in determining flow dynamics in three-phase AGSRs. These variables are interdependent and influence hydrodynamics across different scales; however, the interactions between these variables and their relative contributions to both global and local flow characteristics, particularly the flow dynamics around the granule, which govern shear stress and mass transfer, remain unclear and not well understood.

In Chapter 4, increasing the solids concentration altered the size, rising velocity, and spatial distribution of gas bubbles, which in turn affected the liquid mean velocity and velocity fluctuations (dispersion behavior). However, definitive conclusions could not be drawn, as these bubble-related parameters were not directly characterized. In Chapter 5, the characteristics and dynamics of both gas bubbles (e.g., population, size, and slip velocity) and granules (e.g., volume fraction) likely influenced the turbulence field; however, this requires accurate measurement of these phase-specific variables. In general, advancing the understanding of the interactions between these variables, and their effect on transport phenomena critical to granule property development, requires detailed information on all three phases. Future research on hydrodynamics in three-phase AGSRs should therefore move toward integrating multiphase characterization methods to resolve gas, liquid, and solid motion and distribution simultaneously across different scales. For example, at the reactor scale (macro-scale), this includes the spatial distribution of granular sludge concentration and gas holdup gradients, particularly along the reactor height, as well as overall flow patterns, mean liquid velocity, and turbulence intensity. At the meso-scale, this includes bubble size distribution, rise velocity, bubble coalescence, and granular sludge motion. At the granule scale and smaller scales, this includes relative phase velocities and turbulence characteristics. Depending on the objective of the study, the relevant spatio-temporal scales and appropriate hydrodynamic variables should be selected. For instance, when the objective is to analyze reacor-scale mixing or bed expansion, variables describing reactor-scale hydrodynamics should be prioritized, including the time-averaged liquid velocity field. However, when the objective is to investigate the effect of mass transfer rate on granule properties, near granule surface flow dynamics become more important.

In multiphase opaque systems such as AGSRs, achieving such comprehensive characterization requires the simultaneous use of multiple experimental techniques. However, these methods are limited in spatial and temporal resolution, often costly,

and in most cases restricted to laboratory-scale reactors (see Table 6.1). Moreover, key phenomena relevant at the granule scale, such as mechanical stress, interfacial mass transfer, and granule–granule interaction forces, are extremely difficult or even impossible to quantify directly through experiments alone. Therefore, future efforts should also be directed toward developing computational fluid dynamics (CFD) models that can accurately describe the motion of all three phases, with a focus on phase interactions in the sludge bed region, so that they can be used in a complementary way with experiments. Once these models are properly verified and validated, they can be extended beyond laboratory conditions and applied to pilot- and full-scale reactors for multiphase flow studies. In this context, experimental techniques should be selected strategically for model validation, ensuring that the selected methods and targeted hydrodynamic variables are aligned with the objective study, as described above.

Table 6.1: Experimental techniques for hydrodynamic characterization in three-phase gas–liquid–solid systems.. Adapted from (Ahmed et al., 2026).

Parameter	Measurement technique	Spatial/temporal resolution	Phase measured	Cost	Advantages	Limitations
Global/Macroscopic Techniques						
Mixing time	Tracer response	Global, transient	Liquid	Low	Practical, simple setup	Assumes well-mixed conditions; cannot resolve local heterogeneities
Global gas hold-up	Liquid height change	Global estimate, low resolution	Gas	Very low	Non-intrusive; easy to implement	Assumes uniform dispersion; insensitive to local variations
Local/Point-wise Techniques						
Local velocity	LDA	Point-wise, high temporal	Liquid	High	Non-intrusive; good temporal resolution	Only point-wise; limited spatial coverage; alignment difficulties in multiphase flows
Local velocity	Hot-wire anemometry	Point-wise, very high temporal	Liquid	Moderate	High temporal resolution for turbulence statistics	Intrusive; requires calibration; fragile sensor; difficult to apply in opaque multiphase flows
Velocity field	PIV/PTV	High spatial, low–moderate temporal	Liquid	High	High-resolution 2D/3D velocity maps	Requires optical access; challenging in opaque or multiphase systems
Velocity in opaque flows	Ultrasound velocimetry	Moderate spatial and temporal	Liquid	Moderate–high	Works in opaque media	Strong signal distortion by gas bubbles
Bubble size	Conductivity probes	Point-wise, high temporal	Gas	Moderate–high	Direct bubble diameter measurement	Probe intrusion may disturb flow; calibration errors; limited spatial coverage
Bubble size	Shadowgraphy	Planar, low–moderate temporal	Gas	Moderate	Non-intrusive; direct visualization of bubble size, shape, and distribution	Requires optical access; affected by overlapping bubbles and high solids concentration

Table 6.1: Experimental techniques for hydrodynamic characterization in three-phase gas–liquid–solid systems. (continued).

Parameter	Measurement technique	Spatial/temporal resolution	Phase measured	Cost	Advantages	Limitations
Tomographic and Advanced Imaging Techniques						
Phase concentration	Tomography ERT, ECT, X-ray CT	Cross-sectional, moderate temporal	Gas, solids	Moderate	Non-intrusive; visualizes phase distribution	Lower temporal resolution; calibration needed; limited to certain fluids or conductivities
Phase separation gas vs. solids	ERT + pressure transducers	Cross-sectional, moderate–high temporal	Gas + solids	Moderate–high	Distinguishes phases when coupled	Complex setup; calibration required
Flow visualization	MRI/XCT	High spatial, low–moderate temporal, 3D	All phases	Low–moderate	Non-invasive; detailed imaging of internal flow and phase distribution	Costly; usually limited to small-scale systems; radiation safety issues for XCT
Solid particle motion	PEPT	High temporal, 3D trajectories	Solids	Very high	Provides full 3D trajectories of tracer particles in opaque systems	Requires radioisotopes and specialized facilities; usually tracks only one or a few particles

Abbreviations: LDA, laser Doppler anemometry; PIV, particle image velocimetry; PTV, particle tracking velocimetry; ERT, electrical resistance tomography; ECT, electrical capacitance tomography; X-ray CT, X-ray computed tomography; MRI, magnetic resonance imaging; XCT, X-ray computed tomography; PEPT, positron emission particle tracking.

Resolution ranges: Low spatial resolution refers to global or reactor-scale measurements with no local spatial information. Moderate spatial resolution refers to measurements resolved at approximately millimetre to centimetre scale. High spatial resolution refers to measurements resolved at sub-millimetre to millimetre scale. Low temporal resolution refers to sampling frequencies below approximately 1 Hz or time-averaged measurements. Moderate temporal resolution refers to approximately 1–100 Hz. High temporal resolution refers to approximately 100 Hz–1 kHz, and very high temporal resolution refers to sampling frequencies above approximately 1 kHz.

6.4.2. Turbulence characteristics in AGSRs

As discussed in this chapter, turbulence characteristics appear to play a critical role in determining the effect of fluid flow on granule properties. Despite their importance, turbulence in AGSRs remains largely unexplored. In Figure 6.5, potential mechanisms were proposed through which mean liquid flow and bubble motion generate turbulence, which can subsequently be attenuated or enhanced by the presence of granular sludge. Each of these mechanisms requires further investigation, particularly the influence of granule size, volume fraction, and relative motion on bubble formation, coalescence, and rise dynamics. In addition, turbulence generated by rising bubbles (BIT) requires more systematic study. Gaining deeper insight into how bubble size, population, and relative velocity contribute to turbulence generation, and quantifying these parameters ranges in which they have more contribution in influencing granule-scale flow dynamics, can provide valuable guidance for the operation and design of AGSRs, particularly in controlling granule size and stability.

The experimental results in Chapter 5 on the evolution of granules in the shear-dominated reactors was influenced by the combined effects of mean flow (i.e., relative motion of granules) and turbulent velocity fluctuations. Future studies should aim to disentangle these two mechanisms by isolating their contributions through controlled experimental designs, for example by using oscillating grids to produce nearly homogeneous turbulence with minimal mean flow. Such separation is essential to understand the distinct roles of mean flow and turbulence in determining shear stress and mass transfer at the granule surface, and to quantify their influence on granule properties, such as surface properties, intergranular transport, and microbial structure.

Turbulence may also provide a potential solution to the long start-up period of AGSRs. The effect of turbulence characteristics on granulation requires further investigation. The use of different inlet designs and internal configurations (e.g., zig-zag vertical baffles) to engineer turbulence characteristics, by enhancing microscale flow structures, may promote bacterial interactions, facilitate initial microbial attachment, and accelerate granule nucleation.

Monitoring and controlling turbulence in full-scale AGSRs is also essential. Low turbulence at the granule scale may promote formation of large granules, leading to diffusion limitations, as often reported in EGSB reactors (Aragón-Barroso et al.

(2026)). In contrast, high turbulence at the granule scale may increase granule disintegration and a decline in reactor performance. Given that most experimental flow measurement techniques cannot be applied at full scale, future efforts should focus on extracting information on local velocity fluctuations through indirect measurements, such as real-time pressure fluctuation signals. This may be achieved using both wall-mounted and floating pressure sensors, which are applicable at both laboratory and industrial scales.

Finally, to improve the reproducibility and comparability of future hydrodynamic studies, efforts should be directed toward developing and reporting relevant dimensionless groups that capture the key parameters governing hydrodynamics and transport phenomena in AGSRs. In biological wastewater treatment, ratios such as COD/N and COD/P are routinely reported to support comparison and standardization across systems. A similar approach can be extended to hydrodynamic studies, where multiple parameters are strongly coupled, making direct comparison between studies challenging. For gas–liquid–solid systems, An et al. (2024b) proposed five key dimensionless groups: the Stokes number ($St_1 = \tau_s/\tau_l$, where τ_s is the particle response time and τ_l is the characteristic flow time), the solid-to-liquid density ratio (ρ_s/ρ_l), the particle-to-Kolmogorov length-scale ratio (d_p/η), the normalized contact angle ($\theta/90°$), and the solid volume fraction (C_s). In bubble-dominated systems, an additional Stokes number can be defined as ($St_2 = \tau_s/\tau_b$), where $\tau_b = d_b/u_b$ is the bubble characteristic time, d_b is the bubble diameter, and u_b is the bubble rise velocity. In future endeavors these dimensionless parameters should be further tailored and adapted anaerobic granular sludge systems.

References

Agrawal, Y.K., Shokri, R., Sanders, R.S., Nobes, D.S., 2015. Turbulence statistics in solid-liquid flow using a refractive index matching and particle image velocimetry technique. 10th Pacific Symposium on Flow Visualization and Image Processing , 15–18.

Ahmed, R., Kazemzadeh, A., Ein-Mozaffari, F., Lohi, A., 2026. Critical Review of CFD and Key Hydrodynamic Aspects in Three-Phase Mechanically Agitated Reactors: Challenges and Future Directions. Processes 14. doi:10.3390/pr14030523.

Al-Juwaya, T., Ali, N., Al-Dahhan, M., 2017. Investigation of cross-sectional gas-solid distributions in spouted beds using advanced non-invasive gamma-ray computed tomography (CT). Experimental Thermal and Fluid Science 86, 37–53. URL: http://dx.doi.org/10.1016/j.expthermflusci.2017.03.029, doi:10.1016/j.expthermflusci.2017.03.029.

Alexakis, A., Biferale, L., 2018. Cascades and transitions in turbulent flows. Physics Reports 767-769, 1–101. URL: https://doi.org/10.1016/j.physrep.2018.08.001, doi:10.1016/j.physrep.2018.08.001.

Alibhai, K.R.K., Forster, C.F., 1986. An examination of the granulation process in UASB reactors. Environmental Technology 7, 193–200.

Altair Engineering, 2025. Turbulence Scales and Energy Cascade. URL: https://help.altair.com/hwcfdsolvers/acusolve/topics/acusolve/training_manual/turb_scales_energy_cascasde_r.htm.

An, M., Gao, J., Wang, T., Li, X., 2024a. Particle effects on the hydrodynamics in slurry bubble column reactors: A review from multiscale mechanisms. Particuology 91, 176–189. URL: https://doi.org/10.1016/j.partic.2024.02.009, doi:10.1016/j.partic.2024.02.009.

An, M., Gao, J., Wang, T., Li, X., 2024b. Particuology Particle effects on the hydrodynamics in slurry bubble column reactors : A review from multiscale mechanisms. Particuology 91, 176–189. URL: https://doi.org/10.1016/j.partic.2024.02.009, doi:10.1016/j.partic.2024.02.009.

Aragón-Barroso, A.J., González-Martínez, A., González-López, J., Osorio, F., 2026. Impact of operational conditions and microbial dynamics on expanded granular sludge bed reactor performance: A comprehensive review. Bioresource Technology , 134118.

Arcand, Y., Guiot, S.R., Desrochers, M., Chavarie, C., 1994. Impact of the reactor hydrodynamics and organic loading on the size and activity of anaerobic granules. The Chemical Engineering Journal and the Biochemical Engineering Journal 56, B23–B35. URL: https://www.sciencedirect.com/science/article/pii/0923046794870284, doi:https://doi.org/10.1016/0923-0467(94)87028-4.

Atmakuri, A., Yadav, B., Tiwari, B., Drogui, P., Tyagi, R.D., Wong, J.W.C., 2024. Nature's architects: A comprehensive review of extracellular polymeric substances and their diverse applications. Waste Disposal & Sustainable Energy 6, 529–551.

Azzi, A., Bouyahiaoui, H., Berrouk, A.S., Hunt, A., Lowndes, I.S., 2020. Investigation of fluidized bed behaviour using electrical capacitance tomography. Canadian Journal of Chemical Engineering 98, 1835–1848. doi:10.1002/cjce.23748.

Baeten, J.E., Batstone, D.J., Schraa, O.J., van Loosdrecht, M.C., Volcke, E.I., 2019. Modelling anaerobic, aerobic and partial nitritation-anammox granular sludge reactors - A review. Water Research 149, 322–341. URL: https://doi.org/10.1016/j.watres.2018.11.026, doi:10.1016/j.watres.2018.11.026.

Bastiani, C.D., Alba, J.L., Mazzarotto, G.T., de Farias Neto, S.R., Reynolds, A., Kennedy, D., Beal, L.L., 2021. Three-phase hydrodynamic simulation and experimental validation of an upflow anaerobic sludge blanket reactor. Computers and Mathematics with Applications 83, 95–110. doi:10.1016/j.camwa.2020.02.017.

Batstone, D.J., Keller, J., 2001. Variation of bulk properties of anaerobic granules with wastewater type. Water Research 35, 1723–1729. doi:10.1016/S0043-1354(00)00446-2.

Batstone, D.J., Keller, J., Blackall, L.L., 2004. The influence of substrate kinetics on the microbial community structure in granular

anaerobic biomass. Water Research 38, 1390–1404. URL: https://www.sciencedirect.com/science/article/pii/S0043135403006717, doi:https://doi.org/10.1016/j.watres.2003.12.003.

van den Berg, L., 2022. Diffusion in Aerobic Granular sludge, Dissertation (TU Delft). Delf University of Technology. https://doi. org/10 ....

van den Berg, L., van Loosdrecht, M.C.M., de Kreuk, M.K., 2021. How to measure diffusion coefficients in biofilms: A critical analysis. Biotechnology and bioengineering 118, 1273–1285.

Brennen, C.E., 2005. Fundamentals of multiphase flow. Cambridge university press.

Chen, L., Ji, Y., Yu, Z., Wang, C., Alvarez, P.J., Xu, X., Zhu, L., 2021. Uncover the secret of granule calcification and deactivation in up-flow anaerobic sludge bed (UASB) reactor with long-term exposure to high calcium. Water Research 189, 116586. URL: https://doi.org/10.1016/j.watres.2020.116586, doi:10.1016/j.watres.2020.116586.

Cole, K., Brito-Parada, P.R., Hadler, K., Mesa, D., Neethling, S.J., Norori-McCormac, A.M., Cilliers, J.J., 2022. Characterisation of solid hydrodynamics in a three-phase stirred tank reactor with positron emission particle tracking (PEPT). Chemical Engineering Journal 433, 133819. URL: https://doi.org/10.1016/j.cej.2021.133819, doi:10.1016/j.cej.2021.133819.

Cui, Z., Fan, L.S., 2004. Turbulence energy distributions in bubbling gas – liquid and gas – liquid – solid ow systems 59, 1755–1766. doi:10.1016/j.ces.2004.01.031.

Cunha, J.R., Tervahauta, T., van der Weijden, R.D., Temmink, H., Hernández Leal, L., Zeeman, G., Buisman, C.J.N., 2018. The effect of bioinduced increased pH on the enrichment of calcium phosphate in granules during anaerobic treatment of black water. Environmental science & technology 52, 13144–13154.

D' Bastiani, C., Kennedy, D., Reynolds, A., 2023. CFD simulation of anaerobic granular sludge reactors: A review. Water Research 242, 120220. URL: https://doi.org/10.1016/j.watres.2023.120220, doi:10.1016/j.watres.2023.120220.

Diamantis, V., Aivasidis, A., 2018. Performance of an ECSB reactor for high-rate anaerobic treatment of cheese industry wastewater: effect of pre-acidification on process efficiency and calcium precipitation. Water Science and Technology 78, 1893–1900.

Dijksman, J.A., Brodu, N., Behringer, R.P., 2017. Refractive index matched scanning and detection of soft particles. The Review of scientific instruments 88, 051807. doi:10.1063/1.4983047.

Dijksman, J.A., Rietz, F., Lőrincz, K.A., van Hecke, M., Losert, W., 2012. Invited Article: Refractive index matched scanning of dense granular materials. Review of Scientific Instruments 83, 11301. URL: https://doi.org/10.1063/1.3674173, doi:10.1063/1.3674173.

Duan, Y., Wang, Z., Ganeshan, P., Sar, T., Xu, S., Rajendran, K., Sindhu, R., Binod, P., Pandey, A., Zhang, Z., 2025. Anaerobic digestion in global bio-energy production for sustainable bioeconomy: Potential and research challenges. Renewable and Sustainable Energy Reviews 208, 114985.

Einstein, A., 1905. On the movement of small particles suspended in a stationary liquid demanded by the molecular-kinetic theory of heart. Annalen der physik 17, 549–560.

Eslami, H., Bruning, H., Rijnaarts, H., Sudmalis, D., 2025. 3D hydrodynamic characterization in anaerobic granular sludge reactors, Part 1: Application of 3D-PTV in dense two-phase flows. Journal of Environmental Chemical Engineering , 118703.

Feng, Q., Tai, X., Sun, Y., Li, M., 2019. Influence of turbulent mixing on the composition of extracellular polymeric substances (EPS) and aggregate size of aerated activated sludge. Chemical Engineering Journal 378, 122123. URL: https://doi.org/10.1016/j.cej.2019.122123, doi:10.1016/j.cej.2019.122123.

Feng, Q., Xiao, Y., Wang, X., Li, J., Wu, Y., Xue, Z., Cao, J., Oleyiblo, J.O., 2016. The influences of shear stress on Extracellular Polymeric Substances of activated sludge. Desalination and Water Treatment 57, 15835–15842. doi:10.1080/19443994.2015.1079254.

Flemming, H.C., Neu, T.R., Wozniak, D.J., 2007. The EPS matrix: the "house of biofilm cells". Journal of bacteriology 189, 7945–7947.

Flemming, H.C., Wingender, J., Szewzyk, U., Steinberg, P., Rice, S.A., Kjelleberg, S., 2016. Biofilms: an emergent form of bacterial life. Nature Reviews Microbiology 14, 563–575.

Fu, W., Li, M., Dang, W., Zhu, K., Chen, G., Zhang, J., Wang, S., Guo, Y., Wang, Z., 2022. Study on the mechanism of inhibiting the calcification of anaerobic granular sludge induced by the addition of trace signal molecule (3O-C6-HSL). Bioresource Technology 344, 126232.

Gagliano, M.C., Sudmalis, D., Temmink, H., Plugge, C.M., 2020. Calcium effect on microbial activity and biomass aggregation during anaerobic digestion at high salinity. New Biotechnology 56, 114–122. URL: https://www.sciencedirect.com/science/article/pii/S1871678419301189, doi:https://doi.org/10.1016/j.nbt.2020.01.001.

Gao, C., Doloman, A., Alaux, E., Rijnaarts, H.H., Sousa, D.Z., Hendrickx, T.L., Temmink, H., Sudmalis, D., 2024a. De novo anaerobic granulation with varying organic substrates: granule growth and microbial community responses. Science of the Total Environment 951, 175570. URL: https://doi.org/10.1016/j.scitotenv.2024.175570, doi:10.1016/j.scitotenv.2024.175570.

Gao, C., Habibi, M., Hendrickx, T.L.G., Rijnaarts, H.H.M., Temmink, H., Sudmalis, D., 2024b. Variation of viscoelastic properties of extracellular polymeric substances and their relation to anaerobic granule's mechanical strength in full-scale treatment plants. Bioresource Technology 411, 131233.

Gonçalves, A.B.D., Freitas, L.N.d., Brito, M.G.d.S.L., Nunes, F.C.B., Silva, J.P.d., Mendonça, L.A.R., Silva, F.J.A.d., Lima, A.G.B.d., 2025. Three-dimensional numerical modeling and analysis of multiphase distribution in a UASB reactor with experimental validation of biogas volumetric flow rate. Revista Brasileira de Ciências Ambientais 60, 1–10. doi:10.5327/z2176-94782300.

Gonzalez-Gil, G., Seghezzo, L., Lettinga, G., Kleerebezem, R., 2001. Kinetics and mass-transfer phenomena in anaerobic granular sludge. Biotechnology and Bioengineering 73, 125–134.

de Graaff, D.R., van Dijk, E.J.H., van Loosdrecht, M.C.M., Pronk, M., 2020. Strength characterization of full-scale aerobic granular sludge. Environmental Technology .

Graas, A.B., Wagner, E.C., van Leeuwen, T., van Ommen, J.R., Batenburg, K.J., Lucka, F., Portela, L.M., 2024. X-ray tomography for fully-3D time-resolved reconstruction of bubbling fluidized beds. Powder Technology 434, 119269. URL: https://doi.org/10.1016/j.powtec.2023.119269, doi:10.1016/j.powtec.2023.119269.

Guimerà, X., Dorado, A.D., Bonsfills, A., Gabriel, G., Gabriel, D., Gamisans, X., 2016. Dynamic characterization of external and internal mass transport in heterotrophic biofilms from microsensors measurements. Water Research 102, 551–560. doi:10.1016/j.watres.2016.07.009.

Gvozdić, B., Dung, O.Y., Alméras, E., van Gils, D.P.M., Lohse, D., Huisman, S.G., Sun, C., 2019. Experimental investigation of heat transport in inhomogeneous bubbly flow. Chemical engineering science 198, 260–267.

Hao, F., Shen, M., 2019. Simulation investigation of the baffle overlapping rate on three-phase separation efficiency in a typical UASB reactor. IOP Conference Series: Earth and Environmental Science 227. doi:10.1088/1755-1315/227/5/052032.

Hao, F.L., Shen, M.W., 2021. Development, simulation, and laboratory test of novel gas-solid-liquid separator for UASB/EGSB reactor of wastewater treatment. Journal of Environmental Chemical Engineering 9, 105217. URL: https://doi.org/10.1016/j.jece.2021.105217, doi:10.1016/j.jece.2021.105217.

Harshani, H.M., Galindo-Torres, S.A., Scheuermann, A., Muhlhaus, H.B., 2017. Experimental study of porous media flow using hydro-gel beads and LED based PIV. Measurement Science and Technology 28, 15902. URL: http://dx.doi.org/10.1088/1361-6501/28/1/015902, doi:10.1088/1361-6501/28/1/015902.

Hidman, N., Ström, H., Sasic, S., Sardina, G., 2023. Assessing passive scalar dynamics in bubble-induced turbulence using direct numerical simulations. Journal of Fluid Mechanics 962, A32.

Hmissi, M., Harmand, J., Shayeb, H., Hmissi, M., Harmand, J., Shayeb, H., 2020. Hydrodynamic model of an anaerobic reactor To cite this version : HAL Id : hal-01602892 Hydrodynamic Model of an Anaerobic Reactor 9, 213–221.

Hofmann, S., Weiland, C., Fitschen, J., von Kameke, A., Hoffmann, M., Schlüter, M., 2022. Lagrangian sensors in a stirred tank reactor: Comparing trajectories from 4D-Particle Tracking Velocimetry and Lattice-Boltzmann simulations. Chemical engineering journal 449, 137549.

Holliger, C., Alves, M., Andrade, D., Angelidaki, I., Astals, S., Baier, U., Bougrier, C., Buffière, P., Carballa, M., De Wilde, V., 2016. Towards a standardization of biomethane potential tests. Water Science and Technology 74, 2515–2522.

Hoskins, B.C., Fevang, L., Majors, P.D., Sharma, M.M., Georgiou, G., 1999. Selective imaging of biofilms in porous media by NMR relaxation. Journal of Magnetic Resonance 139, 67–73.

Hu, Y.F., Dan, J.F., Pu, W.H., Yang, C.Z., Yang, J.K., 2017. CFD optimization of the baffle angle of an expanded granular sludge bed reactor. Journal of Environmental Chemical Engineering 5, 4531–4538. URL: http://dx.doi.org/10.1016/j.jece.2017.07.050, doi:10.1016/j.jece.2017.07.050.

Huang, G., Hessenkemper, H., Tan, S., Ni, R., Sommer, A., Bragg, A.D., 2025. Taylor dispersion of bubble swarms rising in quiescent liquid , 1–12doi:10.1017/jfm.2025.10316.

Huang, H., Zeng, S., Luo, C., Long, T., 2023. Separate effect of turbulent pulsation on internal mass transfer in porous biofilms. Environmental Research 217, 114972. URL: https://doi.org/10.1016/j.envres.2022.114972, doi:10.1016/j.envres.2022.114972.

Innocenti, A., Jaccod, A., Popinet, S., Chibbaro, S., 2021. Direct numerical simulation of bubble-induced turbulence. Journal of Fluid Mechanics 918. doi:10.1017/jfm.2021.288.

Jiang, J., Wu, J., Poncin, S., Li, H.Z., 2016. Effect of hydrodynamic shear on biogas production and granule characteristics in a continuous stirred tank reactor. Process

Biochemistry 51, 345–351. URL: http://dx.doi.org/10.1016/j.procbio.2015.12.014, doi:10.1016/j.procbio.2015.12.014.

Jiang, J., Wu, J., Zhang, J., Poncin, S., Li, H.Z., 2014. Multiscale hydrodynamic investigation to intensify the biogas production in upflow anaerobic reactors. Bioresource Technology 155, 1–7. URL: http://dx.doi.org/10.1016/j.biortech.2013.12.079, doi:10.1016/j.biortech.2013.12.079.

Kalyuzhnyi, S.V., Fedorovich, V.V., Lens, P., 2006. Dispersed plug flow model for upflow anaerobic sludge bed reactors with focus on granular sludge dynamics. Journal of Industrial Microbiology and Biotechnology 33, 221–237. doi:10.1007/s10295-005-0217-2.

Kehrein, P., Van Loosdrecht, M., Osseweijer, P., Garfí, M., Dewulf, J., Posada, J., 2020. A critical review of resource recovery from municipal wastewater treatment plants–market supply potentials, technologies and bottlenecks. Environmental Science: Water Research & Technology 6, 877–910.

Kundu, K., Bergmann, I., Klocke, M., Sharma, S., Sreekrishnan, T.R., 2014a. Influence of hydrodynamic shear on performance and microbial community structure of a hybrid anaerobic reactor. Journal of Chemical Technology and Biotechnology 89, 462–470. doi:10.1002/jctb.4194.

Kundu, K., Bergmann, I., Klocke, M., Sharma, S., Sreekrishnan, T.R., 2014b. Influence of hydrodynamic shear on performance and microbial community structure of a hybrid anaerobic reactor. Journal of Chemical Technology and Biotechnology 89, 462–470. doi:10.1002/jctb.4194.

Leishman, J.G., 2026. Turbulent Flows. URL: https://eaglepubs.erau.edu/introductiontoaerospaceflightvehicles/chapter/turbulent-flows/.

Lettinga, G., Van Velsen, A.F.M., Hobma, S.W.d., De Zeeuw, W., Klapwijk, A., 1980. Use of the upflow sludge blanket (USB) reactor concept for biological wastewater treatment, especially for anaerobic treatment. Biotechnology and bioengineering 22, 699–734.

Li, L., Wang, K., Zhao, Q., Gao, Q., Zhou, H., Jiang, J., Mei, W., 2022. A critical review of experimental and CFD techniques to characterize the mixing performance of anaerobic digesters for biogas production. Reviews in Environmental Science and Biotechnology 21, 665–689. URL: https://doi.org/10.1007/s11157-022-09626-z, doi:10.1007/s11157-022-09626-z.

Lian, H., Liu, S., Liu, Z.X., Liu, X., Song, H.N., Qin, C.R., Wang, Z.W., Wang, S.F., Zhang, J., 2023. Retardation of sludge calcification by blocking the transportation of Ca2+ into anaerobic granular sludge. Colloids and Surfaces A: Physicochemical and Engineering Aspects 663, 131112. URL: https://doi.org/10.1016/j.colsurfa.2023.131112, doi:10.1016/j.colsurfa.2023.131112.

van Lier, J.B., van der Zee, F.P., Frijters, C.T., Ersahin, M.E., 2015. Celebrating 40 years anaerobic sludge bed reactors for industrial wastewater treatment. Reviews in Environmental Science and Biotechnology 14, 681–702. doi:10.1007/s11157-015-9375-5.

Liu, Y., Tay, J.H., 2002. The essential role of hydrodynamic shear force in the formation of biofilm and granular sludge. Water Research 36, 1653–1665. doi:10.1016/S0043-1354(01)00379-7.

Liu, Y., Tay, J.H., 2004. State of the art of biogranulation technology for wastewater treatment. Biotechnology Advances 22, 533–563. doi:10.1016/j.biotechadv.2004.05.001.

Loganath, R., Mazumder, D., 2018. Performance study on organic carbon, total nitrogen, suspended solids removal and biogas production in hybrid UASB reactor treating real slaughterhouse wastewater. Journal of Environmental Chemical Engineering 6, 3474–3484.

Luo, C., Guo, L., Zeng, S., Long, T., 2021. Effects of turbulence fluctuation intensity in bioreactor of sewage treatment on physical and chemical properties of biofilms. Bioprocess and Biosystems Engineering 44, 1865–1874. URL: https://doi.org/10.1007/s00449-021-02566-y, doi:10.1007/s00449-021-02566-y.

Ma, H., Guo, C., Yao, M., Wu, M., Wang, Z., Wang, S., 2020. Calcium ions affect sludge digestion performance via changing extracellular polymeric substances

in anaerobic bioreactor. Biomass and Bioenergy 137, 105548. URL: https://doi.org/10.1016/j.biombioe.2020.105548, doi:10.1016/j.biombioe.2020.105548.

Mahoney, E.M., Varangu, L.K., Cairns, W.L., Kosaric, N., Murray, R.G.E., 1987. The effect of calcium on microbial aggregation during UASB reactor start-up. Water Science and Technology 19, 249–260.

Mainardis, M., Buttazzoni, M., Goi, D., 2020. Up-flow anaerobic sludge blanket (UASB) technology for energy recovery: a review on state-of-the-art and recent technological advances. Bioengineering 7, 43.

Mariraj Mohan, S., Swathi, T., 2022. A review on upflow anaerobic sludge blanket reactor: Factors affecting performance, modification of configuration and its derivatives. Water Environment Research 94, 1–27. doi:10.1002/wer.1665.

Martínez-Mercado, J., Palacios-Morales, C.A., Zenit, R., 2007. Measurement of pseudoturbulence intensity in monodispersed bubbly liquids for 10<Re8lt;500. Physics of Fluids 19, 1–14. doi:10.1063/1.2772256.

Martnez Mercado, J., Chehata Gmez, D., Van Gils, D., Sun, C., Lohse, D., 2010. On bubble clustering and energy spectra in pseudo-turbulence. Journal of Fluid Mechanics 650, 287–306. doi:10.1017/S0022112009993570.

Mauri, R., 2015. Transport phenomena in multiphase flows. volume 112. Springer.

Maximova, N., Dahl, O., 2006. Environmental implications of aggregation phenomena: Current understanding. Current Opinion in Colloid and Interface Science 11, 246–266. doi:10.1016/j.cocis.2006.06.001.

Mena, P.C., Ruzicka, M.C., Rocha, F.A., Teixeira, J.A., Drahoš, J., 2005. Effect of solids on homogeneous – heterogeneous flow regime transition in bubble columns 60, 6013–6026. doi:10.1016/j.ces.2005.04.020.

Meng, L., Wang, J., Li, X., Yu, Y., Zhu, Y., 2021. Microbial community and molecular ecological network in the EGSB reactor treating antibiotic wastewater: Response to environmental factors. Ecotoxicology and Environmental Safety 208, 111669. URL: https://www.sciencedirect.com/science/article/

pii/S0147651320315062, doi:https://doi.org/10.1016/j.ecoenv.2020.111669.

Milivojevic, M., Bugarski, B., 2012. Liquid velocity in a high-solids-loading three-phase external-loop airlift reactor , 1529–1540doi:10.1002/jctb.3783.

Morshed, K.N., Bark Jr, D., Forleo, M., Dasi, L.P., 2014. Theory to predict shear stress on cells in turbulent blood flow. PloS one 9, e105357.

Mudde, R.F., Groen, J.S., Van Den Akker, H.E., 1997. Liquid velocity field in a bubble column: LDA experiments. Chemical Engineering Science 52, 4217–4224. doi:10.1016/S0009-2509(97)88935-X.

Mullai, P., Vishali, S., Dharmalingam, K., 2025. Residence time distribution experiments in a hybrid anaerobic blanket reactor treating real pharmaceutical wastewater. Journal of the Taiwan Institute of Chemical Engineers 166, 105381. URL: https://doi.org/10.1016/j.jtice.2024.105381, doi:10.1016/j.jtice.2024.105381.

Musa, M.A., Idrus, S., Harun, M.R., Tuan Mohd Marzuki, T.F., Abdul Wahab, A.M., 2020. A comparative study of biogas production from cattle slaughterhouse wastewater using conventional and modified upflow anaerobic sludge blanket (UASB) reactors. International journal of environmental research and public health 17, 283.

Nguyen, H., Ybarra, A., Başağaoğlu, H., Shindell, O., 2021. Biofilm viscoelasticity and nutrient source location control biofilm growth rate, migration rate, and morphology in shear flow. Scientific Reports 11, 16118.

Nguyen, T., Kappes, E., King, S., Hassan, Y., Ugaz, V., 2018. Time-resolved PIV measurements in a low-aspect ratio facility of randomly packed spheres and flow analysis using modal decomposition. Experiments in Fluids 59, 1–29. URL: http://dx.doi.org/10.1007/s00348-018-2583-3, doi:10.1007/s00348-018-2583-3.

Novara, M., Schanz, D., Schröder, A., 2023. Two-Pulse 3D particle tracking with Shake-The-Box. Experiments in Fluids 64, 1–21. URL: https://doi.org/10.1007/s00348-023-03634-7, doi:10.1007/s00348-023-03634-7.

Owodunni, A.A., Ismail, S., 2021. Revolutionary technique for sustainable plant-based green coagulants in industrial wastewater treatment—A review. Journal of Water Process Engineering 42, 102096.

Pan, H., fan Hu, Y., hong Pu, W., fen Dan, J., kuan Yang, J., 2017. CFD optimization of the baffle angle of an expanded granular sludge bed reactor. Journal of environmental chemical engineering 5, 4531–4538.

Pan, K., Su, K., Zhang, S., Sun, Z., Xu, D., Liu, S., 2016. Hydrodynamics and permeability of aerobic granular sludge: The effect of intragranular characteristics and hydraulic conditions. Biochemical Engineering Journal 113, 133–140. doi:10.1016/j.bej.2016.06.012.

Pechaud, Y., Peyre Lavigne, M., Bessiere, Y., Ochoa, J.C., Queinnec, I., Paul, E., 2022. Influence of shear stress, organic loading rate and hydraulic retention time on the biofilm structure and on the competition between different biological aggregate morphotypes. Journal of Environmental Chemical Engineering 10, 107597. URL: https://doi.org/10.1016/j.jece.2022.107597, doi:10.1016/j.jece.2022.107597.

Peng, L., Zhang, J., Chen, Y., Xie, C.M., Su, L., Wang, S.F., 2024. Strategy to prevent calcification by restricting surface adhesion of Ca2+: Reduced affinity of extracellular polymeric substances for Ca2+ by mild acidic conditions. Bioresource Technology 406, 131032.

Penn, A., Boyce, C.M., Conzelmann, N., Bezinge, G., Pruessmann, K.P., Müller, C.R., 2019. Real-time magnetic resonance imaging of fluidized beds with internals. Chemical Engineering Science 198, 117–123. URL: https://doi.org/10.1016/j.ces.2018.12.041, doi:10.1016/j.ces.2018.12.041.

Pereboom, J.H.F., Vereijken, T., 1994. Methanogenic granule development in full scale internal circulation reactors. Water Science and Technology 30, 9.

Picioreanu, C., Van Loosdrecht, M.C.M., Heijnen, J.J., 2000. Effect of diffusive and convective substrate transport on biofilm structure formation: A two-dimensional modeling study. Biotechnology and bioengineering 69, 504–515.

Pizzi, F., Peters, F., Sorribes, E., Marín-Beltrán, I., Romera-Castillo, C., Grau, J., Rahmani, M., Jofre, L., Capuano, F., 2025. Modulation of biofilm growth by shear and fluctuations in turbulent environments. Scientific Reports 15, 1–21. doi:10.1038/s41598-025-95822-0.

Poelma, C., 2020. Measurement in opaque flows: a review of measurement techniques for dispersed multiphase flows. Acta Mechanica 231, 2089–2111. URL: https://doi.org/10.1007/s00707-020-02683-x, doi:10.1007/s00707-020-02683-x.

Pope, S., 2001. SB Pope, Turbulent Flows, Cambridge University Press, Cambridge, UK, 2000, 771 pp.

Prakash, V.N., Martínez Mercado, J., Van Wijngaarden, L., Mancilla, E., Tagawa, Y., Lohse, D., Sun, C., 2016. Energy spectra in turbulent bubbly flows. Journal of Fluid Mechanics 791, 174–190. doi:10.1017/jfm.2016.49.

Ren, T., Mu, Y., Ni, B., Yu, H., 2009a. Hydrodynamics of upflow anaerobic sludge blanket reactors. AIChE Journal 55, 516–528.

Ren, T.T., Mu, Y., Liu, L., Li, X.Y., Yu, H.Q., 2009b. Quantification of the shear stresses in a microbial granular sludge reactor. Water Research 43, 4643–4651. doi:10.1016/j.watres.2009.07.019.

Ren, T.T., Mu, Y., Liu, L., Li, X.Y., Yu, H.Q., 2009c. Quantification of the shear stresses in a microbial granular sludge reactor. Water Research 43, 4643–4651. doi:10.1016/j.watres.2009.07.019.

Ren, T.T., Mu, Y., Yu, H.Q., Harada, H., Li, Y.Y., 2008. Dispersion analysis of an acidogenic UASB reactor. Chemical Engineering Journal 142, 182–189. doi:10.1016/j.cej.2007.11.028.

Riboux, G., Risso, F., Legendre, D., 2010. Experimental characterization of the agitation generated by bubbles rising at high Reynolds number. Journal of Fluid Mechanics 643, 509–539. doi:10.1017/S0022112009992084.

Risso, F., 2018. Agitation, Mixing, and Transfers Induced by Bubbles. Annual Review of Fluid Mechanics 50, 25–48. doi:10.1146/annurev-fluid-122316-045003.

Rittmann, B.E., McCarty, P.L., 2001. Environmental biotechnology: principles and applications. (No Title) .

Rockstroh, T., 2022. Benchmarking of different Multi-pass Shake-the-Box strategies. Proceedings of the International Symposium on the Application of Laser and Imaging Techniques to Fluid Mechanics 20, 1–11. doi:10.55037/lxlaser.20th.15.

Rodi, W., 2017. Turbulence modeling and simulation in hydraulics: A historical review. Journal of Hydraulic Engineering 143, 3117001.

Rodríguez-Gómez, R., Renman, G., Moreno, L., Liu, L., 2014. A model to describe the performance of the UASB reactor. Biodegradation 25, 239–251. doi:10.1007/s10532-013-9656-z.

Roghair, I., Mercado, J.M., Sint Annaland, M.V., Kuipers, H., Sun, C., Lohse, D., 2011. Energy spectra and bubble velocity distributions in pseudo-turbulence: Numerical simulations vs. experiments. International Journal of Multiphase Flow 37, 1093–1098. doi:10.1016/j.ijmultiphaseflow.2011.07.004.

Sabbagh, R., Kazemi, M.A., Soltani, H., Nobes, D.S., 2020. Micro- and Macro-Scale Measurement of Flow Velocity in Porous Media: A Shadow Imaging Approach for 2D and 3D. Optics 1, 71–87. doi:10.3390/opt1010006.

Schanz, D., Gesemann, S., Schröder, A., 2016. Shake-The-Box: Lagrangian particle tracking at high particle image densities. Experiments in fluids 57, 1–27.

Schanz, D., Gesemann, S., Schröder, A., Wieneke, B., Novara, M., 2013a. Non-uniform optical transfer functions in particle imaging: Calibration and application to tomographic reconstruction. Measurement Science and Technology 24. doi:10.1088/0957-0233/24/2/024009.

Schanz, D., Novara, M., Schröder, A., 2021. Shake-The-Box particle tracking with variable time-steps in flows with high velocity range (VT-STB). 14th International Symposium on Particle Image Velocimetry 1. doi:10.18409/ispiv.v1i1.65.

Schanz, D., Schröder, A., Gesemann, S., Michaelis, D., Wieneke, B., 2013b. ‘ Shake The Box ’: A highly efficient and accurate Tomographic Particle Tracking

Velocimetry (TOMO-PTV) method using prediction of particle positions. 10th International Symposium on Particle Image Velocimetry - PIV13. Delft, The Netherlands, July 1-3. , 1–13.

Schindelin, J., Arganda-Carreras, I., Frise, E., Kaynig, V., Longair, M., Pietzsch, T., Preibisch, S., Rueden, C., Saalfeld, S., Schmid, B., 2012. Fiji: an open-source platform for biological-image analysis. Nature methods 9, 676–682.

Schröder, A., Schanz, D., 2023. 3D Lagrangian Particle Tracking in Fluid Mechanics. Annual Review of Fluid Mechanics 55, 511–540. doi:10.1146/annurev-fluid-031822-041721.

Schröder, A., Schanz, D., Geisler, R., Gesemann, S., Willert, C.E., 2015a. Near-wall turbulence characterization using 4D-PTV Shake-The-Box. 11th International Symposium on Particle Image Velocimetry , 1–14.

Schröder, A., Schanz, D., Michaelis, D., Cierpka, C., Scharnowski, S., Kähler, C.J., 2015b. Advances of PIV and 4D-PTV "shake-The-Box" for Turbulent Flow Analysis -the Flow over Periodic Hills. Flow, Turbulence and Combustion 95, 193–209. doi:10.1007/s10494-015-9616-2.

Schröder, A., Willert, C., Schanz, D., Geisler, R., Jahn, T., Gallas, Q., Leclaire, B., 2020. The flow around a surface mounted cube: a characterization by time-resolved PIV, 3D Shake-The-Box and LBM simulation. Experiments in Fluids 61, 1–22. URL: https://doi.org/10.1007/s00348-020-03014-5, doi:10.1007/s00348-020-03014-5.

Seyfi, S., Karimpour, S., Balachandar, R., 2024. Simultaneous flow and particle measurements for multiphase flows in hydraulic engineering: A review and synthesis of current state. Flow Measurement and Instrumentation 99, 102666. URL: https://doi.org/10.1016/j.flowmeasinst.2024.102666, doi:10.1016/j.flowmeasinst.2024.102666.

Shi, W., Yang, X., Sommerfeld, M., Yang, J., Cai, X., Li, G., Zong, Y., 2019. Modelling of mass transfer for gas-liquid two-phase flow in bubble column reactor with a bubble breakage model considering bubble-induced turbulence. Chemical Engineering Journal 371, 470–485. URL: https://doi.org/10.1016/j.cej.2019.04.047, doi:10.1016/j.cej.2019.04.047.

Show, K.Y., Yan, Y., Yao, H., Guo, H., Li, T., Show, D.Y., Chang, J.S., Lee, D.J., 2020. Anaerobic granulation: A review of granulation hypotheses, bioreactor designs and emerging green applications. Bioresource Technology 300, 122751. URL: https://doi.org/10.1016/j.biortech.2020.122751, doi:10.1016/j.biortech.2020.122751.

Stainback, P.C., Nagabushana, K.A., 1993. Review of hot-wire anemometry techniques and the range of their applicability. American Society of Mechanical Engineers, Fluids Engineering Division (Publication) FED 167, 93–133.

Stazi, V., Tomei, M.C., 2021. Dissolved methane in anaerobic effluents: A review on sustainable strategies for optimization of energy recovery or internal process reuse. Journal of Cleaner Production 317, 128359.

Sudmalis, D., Mubita, T.M., Gagliano, M.C., Dinis, E., Zeeman, G., Rijnaarts, H.H.M., Temmink, H., 2020. Cation exchange membrane behaviour of extracellular polymeric substances (EPS) in salt adapted granular sludge. Water Research 178, 115855. URL: https://www.sciencedirect.com/science/article/pii/S0043135420303924, doi:https://doi.org/10.1016/j.watres.2020.115855.

Tay, J.H., Liu, Q.S., Liu, Y., 2001a. The effects of shear force on the formation, structure and metabolism of aerobic granules. Applied Microbiology and Biotechnology 57, 227–233. doi:10.1007/s002530100766.

Tay, J.H., Liu, Q.S., Liu, Y., 2001b. The role of cellular polysaccharides in the formation and stability of aerobic granules. Letters in Applied Microbiology 33, 222–226. doi:10.1046/j.1472-765X.2001.00986.x.

Thaker, A.H., Karthik, G.M., Buwa, V.V., 2019. PIV measurements and CFD simulations of the particle-scale flow distribution in a packed bed. Chemical Engineering Journal 374, 189–200. URL: https://doi.org/10.1016/j.cej.2019.05.053, doi:10.1016/j.cej.2019.05.053.

Tiwari, M.K., Guha, S., Harendranath, C.S., Tripathi, S., 2006. Influence of extrinsic factors on granulation in UASB reactor. Applied Microbiology and Biotechnology 71, 145–154. doi:10.1007/s00253-006-0397-3.

Tsagkari, E., Connelly, S., Liu, Z., McBride, A., Sloan, W.T., 2022. The role of shear dynamics in biofilm formation. npj Biofilms and Microbiomes 8. doi:10.1038/s41522-022-00300-4.

Uemura, S., Harada, H., 2000. Treatment of sewage by a UASB reactor under moderate to low temperature conditions. Bioresource Technology 72, 275–282.

Vallero, M.V.G., Pol, L.W.H., Lettinga, G., Lens, P.N.L., 2003. Effect of NaCl on thermophilic (55 C) methanol degradation in sulfate reducing granular sludge reactors. Water Research 37, 2269–2280.

Van As, H., Lens, P., 2001. Use of 1H NMR to study transport processes in porous biosystems. Journal of Industrial Microbiology and Biotechnology 26, 43–52.

Van Langerak, E.P.A., Gonzalez-Gil, G., Van Aelst, A., Van Lier, J.B., Hamelers, H.V.M., Lettinga, G., 1998. Effects of high calcium concentrations on the development of methanogenic sludge in upflow anaerobic sludge bed (UASB) reactors. Water Research 32, 1255–1263.

Van Langerak, E.P.A., Ramaekers, H., Wiechers, J., Veeken, A.H.M., Hamelers, H.V.M., Lettinga, G., 2000. Impact of location of CaCO3 precipitation on the development of intact anaerobic sludge. Water Research 34, 437–446.

Van Lier, J.B., 2008. High-rate anaerobic wastewater treatment: diversifying from end-of-the-pipe treatment to resource-oriented conversion techniques. Water Science and Technology 57, 1137–1148.

Voronov, R.S., VanGordon, S.B., Sikavitsas, V.I., Papavassiliou, D.V., 2011. Efficient Lagrangian scalar tracking method for reactive local mass transport simulation through porous media. International journal for numerical methods in fluids 67, 501–517.

Wang, B., Wu, D., Ekama, G.A., Tsui, T.H., Jiang, F., Chen, G.H., 2018. Characterization of a new continuous gas-mixing sulfidogenic anaerobic bioreactor: Hydrodynamics and sludge granulation. Water Research 135, 251–261. doi:10.1016/j.watres.2018.02.013.

Wang, X., Ding, J., Guo, W.Q., Ren, N.Q., 2010. A hydrodynamics-reaction kinetics coupled model for evaluating bioreactors derived from CFD simulation.

Bioresource Technology 101, 9749–9757. URL: http://dx.doi.org/10.1016/j.biortech.2010.07.115, doi:10.1016/j.biortech.2010.07.115.

Wang, X., Ding, J., Ren, N.Q., Liu, B.F., Guo, W.Q., 2009. CFD simulation of an expanded granular sludge bed (EGSB) reactor for biohydrogen production. International Journal of Hydrogen Energy 34, 9686–9695. URL: http://dx.doi.org/10.1016/j.ijhydene.2009.10.027, doi:10.1016/j.ijhydene.2009.10.027.

Wei, G., Yang, J.Q., 2023. Microfluidic investigation of the impacts of flow fluctuations on the development of Pseudomonas putida biofilms. npj Biofilms and Microbiomes 9. doi:10.1038/s41522-023-00442-z.

Weissbrodt, D.G., 2024. Engineering Granular Microbiomes.

Welch, P.D., 1967. The use of fast Fourier transform for the estimation of power spectra: A method based on time averaging over short, modified periodograms. IEEE Transactions on audio and electroacoustics 15, 70–73.

Wiederseiner, S., Andreini, N., Epely-Chauvin, G., Ancey, C., 2011. Refractive-index and density matching in concentrated particle suspensions: A review. Experiments in Fluids 50, 1183–1206. doi:10.1007/s00348-010-0996-8.

Wieneke, B., 2008. Volume self-calibration for 3D particle image velocimetry. Experiments in fluids 45, 549–556.

Wieneke, B., 2013. Iterative reconstruction of volumetric particle distribution. Measurement Science and Technology 24. doi:10.1088/0957-0233/24/2/024008.

Wilén, B.M., Liébana, R., Persson, F., Modin, O., Hermansson, M., 2018. The mechanisms of granulation of activated sludge in wastewater treatment, its optimization, and impact on effluent quality. Applied Microbiology and Biotechnology 102, 5005–5020. doi:10.1007/s00253-018-8990-9.

Willett, M.R., Codd, S.L., Seymour, J.D., Kirkland, C.M., 2024. Relaxation-weighted MRI analysis of biofilm EPS: Differentiating biopolymers, cells, and water. Biofilm 8, 100235.

Wright, S.F., Zadrazil, I., Markides, C.N., 2017. A review of solid–fluid selection options for optical-based measurements in single-phase liquid, two-phase liquid–liquid and multiphase solid–liquid flows. volume 58. Springer Berlin Heidelberg. doi:10.1007/s00348-017-2386-y.

Wu, J., Bi, L., Zhang, J.B., Poncin, S., Cao, Z.P., Li, H.Z., 2012a. Effects of increase modes of shear force on granule disruption in upflow anaerobic reactors. Water Research 46, 3189–3196. URL: http://dx.doi.org/10.1016/j.watres.2012.03.042, doi:10.1016/j.watres.2012.03.042.

Wu, J., Bi, L., Zhang, J.B., Poncin, S., Cao, Z.P., Li, H.Z., 2012b. Effects of increase modes of shear force on granule disruption in upflow anaerobic reactors. Water Research 46, 3189–3196. URL: http://dx.doi.org/10.1016/j.watres.2012.03.042, doi:10.1016/j.watres.2012.03.042.

Wu, J., Lu, Z.Y., Hu, J.C., Feng, L., Huang, J.D., Gu, X.S., 2006. Disruption of granules by hydrodynamic force in internal circulation anaerobic reactor. Water Science and Technology 54, 9–16. doi:10.2166/wst.2006.868.

Wu, J., de los Reyes, F.L., Ducoste, J.J., 2020. Modeling cell aggregate morphology during aerobic granulation in activated sludge processes reveals the combined effect of substrate and shear. Water Research 170. doi:10.1016/j.watres.2019.115384.

Wu, J., Zhang, J., Poncin, S., Li, H.Z., Jiang, J., Rehman, Z.U., 2015. Effects of rising biogas bubbles on the hydrodynamic shear conditions around anaerobic granule. Chemical Engineering Journal 273, 111–119. URL: http://dx.doi.org/10.1016/j.cej.2015.03.057, doi:10.1016/j.cej.2015.03.057.

Wu, Y., Liu, H., Dang, W., Li, M.L., Lv, G., Chen, Y., Liu, X., Wang, Z., 2021. Effect of calcification on anaerobic granular sludge: Micro-morphological structure and microbial community. Journal of Water Process Engineering 41, 102046. URL: https://doi.org/10.1016/j.jwpe.2021.102046, doi:10.1016/j.jwpe.2021.102046.

Xia, H., Francois, N., Punzmann, H., Shats, M., 2013. Lagrangian scale of particle dispersion in turbulence. Nature Communications 4, 1–8. doi:10.1038/ncomms3013.

Xu, X., Gao, F., Guo, X., Hao, X., Xu, Y., Zhang, P., Chen, G., 2025. Effects of particle concentration and diameter on hydrodynamics and mass transfer under a wire mesh-coupled solid particles reinforcement approach. Chemical Engineering Research and Design 219, 344–356. URL: https://doi.org/10.1016/j.cherd.2025.06.013, doi:10.1016/j.cherd.2025.06.013.

Yang, H., Chen, A., Geng, S., Cheng, J., Gao, F., Huang, Q., Yang, C., 2022. Influences of fluid physical properties, solid particles, and operating conditions on the hydrodynamics in slurry reactors. Chinese Journal of Chemical Engineering 44, 51–71. URL: https://doi.org/10.1016/j.cjche.2021.03.045, doi:10.1016/j.cjche.2021.03.045.

Yang, J., Yang, Y., Ji, X., Chen, Y., Guo, J., Fang, F., 2015. Three-dimensional modeling of hydrodynamics and biokinetics in EGSB reactor. Journal of Chemistry 2015, 14–16. doi:10.1155/2015/635281.

You, G., Wang, C., Wang, P., Hou, J., Xu, Y., Miao, L., Feng, T., 2020. Insights into spatial effects of ceria nanoparticles on oxygen mass transfer in wastewater biofilms: Interfacial microstructure, in-situ microbial activity and metabolism regulation mechanism. Water research 176, 115731.

Yu, H.Q., Fang, H.H., 2001. Inhibition by chromium and cadmium of anaerobic acidogenesis. Water Science and Technology 43, 267–274. doi:10.2166/wst.2001.0691.

Yu, T., Tian, L., You, X., Wang, L., Zhao, S., Kang, D., Xu, D., Zeng, Z., Zhang, M., Zheng, P., 2019. Deactivation mechanism of calcified anaerobic granule: Space occupation and pore blockage. Water Research 166, 115062. URL: https://doi.org/10.1016/j.watres.2019.115062, doi:10.1016/j.watres.2019.115062.

Zeng, Y., Mu, S.J., Lou, S.J., Tartakovsky, B., Guiot, S.R., Wu, P., 2005. Hydraulic modeling and axial dispersion analysis of UASB reactor. Biochemical Engineering Journal 25, 113–123. doi:10.1016/j.bej.2005.04.024.

Zhang, J.B., Poncin, S., Wu, J., Li, H.Z., 2011. A multiscale approach for studying an anaerobic multiphase bioreactor. Chemical Engineering Science 66, 3423–3431. doi:10.1016/j.ces.2011.01.021.

Zhang, J.B., Wu, J., Poncin, S., Hamelin, M., Li, H.Z., 2012. Microscale investigation of anaerobic biogas production under various hydrodynamic conditions. Environmental Science and Technology 46, 8698–8704. doi:10.1021/es3013722.

Zhou, J., McCreanor, P.T., Montalto, F., Erdal, Z.K., 2011. Sustainability. Water Environment Research 83, 1414–1438.

Zima-Kulisiewicz, B.E., Díez, L., Kowalczyk, W., Hartmann, C., Delgado, A., 2008. Biofluid mechanical investigations in sequencing batch reactor (SBR). Chemical Engineering Science 63, 599–608. doi:10.1016/j.ces.2007.09.048.

Summary

Anaerobic granular sludge technology has become the cornerstone of high-rate anaerobic wastewater treatment, combining the removal of organic contaminants from wastewater streams with the productions of biogas. It has been successfully implemented for different types of industrial effluents across a wide range of sectors. Anaerobic granular sludge reactors (AGSRs) are characterized by a small footprint and the ability to operate at high volumetric organic loading rates. Maximum performance of these bioreactors is obtained when the reactor contains a high concentration of active granular biomass. This is achieved through the formation and development of anaerobic granules, which can be described as spherical biofilms formed without supporting carrier materials. These granules provide rich microbial diversity within a robust structure with good settling ability, high mechanical stability, and tolerance to environmental stresses (e.g., inhibitory compounds).

Among the many parameters influencing the formation and development of anaerobic granules, hydrodynamics plays a key role. During granule formation, hydrodynamic conditions control the hydraulic selection pressure, through which poorly structured flocs and dispersed biomass are washed out, while dense and well-settling aggregates are retained within the reactor. During granule development and maturation, local hydrodynamics in the vicinity of granules govern the shear stress and thereby abrasion and attrition and mass transfer at the granule surface. These phenomena affect the transport of substrates, nutrients, and metabolic products between the bulk liquid and the granule interior, thereby shaping the physical, chemical, and biological properties of granules.

Previous studies have suggested that specific hydrodynamic conditions enhance mass transfer and biogas production. However, hydrodynamics in AGSRs, which are three-phase systems, are not an independent phenomenon, but emerge from complex gas–liquid–solid interactions governed by multiple parameters. These parameters include wastewater characteristics, operational conditions, and reactor design. Therefore, before any optimization of hydrodynamics in AGSRs takes place, a mechanistic understanding of how these parameters affect reactor-scale hydrodynamics and how these conditions translate to granule-scale flow dynamics is required. Furthermore, the influence of local flow behavior on mass transfer

and shear stress at the granule surface needs to be understood. However, such understanding has been constrained by the lack of experimental techniques capable of resolving local flow dynamics in three-phase systems, particularly at high solid concentrations. In this PhD thesis, experimental approaches were developed and applied to characterize local liquid velocity in lab-scale AGSRs and to elucidate how different hydrodynamic conditions influence granule properties under calcium-rich wastewater conditions.

Chapter 1 provides an overview of the current understanding of hydrodynamics in different AGSRs and reviews the experimental and modeling approaches used to characterize flow dynamics in these three-phase bio-reactors. Based on this review, it identifies the knowledge gaps and defines the research objectives of this thesis.

Chapter 2 presents the literature-based theoretical background on turbulence and transport phenomena in multiphase flows. It introduces the statistical description of turbulence and the different scales of turbulent motion. The chapter also discusses the main sources of turbulent velocity fluctuations in multiphase systems, including shear-induced turbulence and bubble- or particle-induced turbulence. This theoretical framework provides a basis to explain how turbulent velocity fluctuations influence mixing, mass transfer, and shear stress in anaerobic granular sludge reactors.

Chapter 3 evaluates the feasibility of experimentally resolving local flow dynamics in dense liquid–solid systems representative of the sludge bed/blanket region of AGSRs. To overcome the optical limitations caused by high solid concentrations, transparent hydrogel beads were used as model granules. A combined approach of refractive index matching (RIM), which completely eliminates the opaqueness of the suspension, and three-dimensional particle tracking velocimetry (3D-PTV) was successfully applied. This approach enabled non-intrusive measurement of three-dimensional liquid velocity fields within a reactor operated at model-granule volume fractions of up to 50%. The results demonstrated that the method can successfully capture local liquid flow dynamics under dense two-phase conditions, which were previously difficult to access experimentally. This enables us to investigate the effect of key influential parameters (e.g., granular sludge concentration) on the liquid velocity field and mixing performance in these reactors.

Chapter 4 extends the RIM–3D-PTV approach to gas–liquid–solid three-phase flow conditions by using the same model granules as in **Chapter 3** and by

introducing controlled gas flow through the reactors. These three phase conditions are characteristic of AGSRs. The study systematically investigated how gas superficial velocity, representing different biogas production rates, and model-granule volume fraction influence liquid velocity fields and mixing behavior. Flow measurements were conducted in a reactor operated at gas superficial velocities ranging from 0.01 to 0.1 cm/s and solid volume fractions ranging from 0 to 50%. The results showed that increasing gas flow generally enhanced the mean liquid velocity and increased the occurrence of extreme instantaneous velocities in both the axial and lateral directions. In contrast, increasing the solid volume fraction had a dual effect: both the mean liquid velocity and the likelihood of instantaneous high-velocity events initially increased to a peak value and subsequently decreased. Notably, the critical solid volume fraction and the corresponding peak mean velocity depended on the gas superficial velocity. For each tested operating condition, the axial dispersion coefficients, ranging from 4.1×10^{-5} to 2.4×10^{-3} m^2/s, were higher than the radial dispersion coefficients, which ranged from 8.1×10^{-6} to 2.3×10^{-4} m^2/s. Increasing GSV enhanced both axial and radial dispersion coefficients for all solid VOFs. At a constant GSV, the effect of increasing solid VOF on the dispersion coefficients varied with the applied GSV and differed between the axial and radial directions.

Chapter 5 investigates how local flow dynamics influence the evolution of anaerobic granule properties under calcium-rich wastewater conditions (400 mg/L Ca^{2+}) as found in paper mills. Granule development was studied in two low-seeded, lab-scale reactors operated under distinct hydrodynamic conditions controlled by gas sparging, namely a high-shear reactor (HSR) and a low-shear reactor (LSR). The results were compared with granules developed in slow-mixing (shear-free), continuous reactors with all reactors operated under calcium-rich conditions. Three-dimensional liquid velocity fields in the reactors were quantified using 3D-PTV, allowing time-averaged velocity and shear fields, as well as turbulence characteristics, to be related to the evolution of granule properties, including size, morphology, mechanical strength, internal structure, calcification, and methanogenic activity. The flow measurements showed average liquid velocities of 0.075 and 0.043 m/s in the HSR and LSR, respectively, with corresponding average shear rates of 0.25 and 0.125 1/s. The average methanogenic activities of the developed granules were 0.65, 0.38, and 0.10 g CH_4-COD/g VSS/day in the HSR, LSR, and shear-free reactors, respectively, suggesting considerably reduced intragranular mass transfer efficiency for granule

developed under shear-free conditions. Although smaller granules were expected in the reactor with higher meso-scale shear (HSR), granules developed in the LSR were smaller (1–1.5 mm) than those developed in the HSR (1.5–2 mm) and exhibited a higher degree of calcification, with calcium contents of approximately 185 and 83 g Ca/kg dry weight, respectively. Statistical analysis of the turbulence characteristics showed that, although the HSR exhibited stronger velocity fluctuations and higher overall kinetic energy, the dominant turbulent eddy size at the granule scale was smaller in the LSR. These small-scale flow structures likely generated higher-frequency velocity fluctuations, resulting in increased mechanical stress at the granule surface and enhanced Ca^{2+} transport into the granule structure. The results indicate that turbulence characteristics within the reactor play a more decisive role than the mean bulk flow in determining granule properties. Moreover, beyond the intensity of turbulent fluctuations, their temporal frequency was identified as a critical parameter governing both shear stress and mass transfer at the granule scale.

Chapter 6 integrates the findings of this thesis with state-of-the-art advances in multiphase flow research and recent insights into how biofilm-flow interactions influence biofilm properties. The chapter identifies key hydrodynamic variables in three-phase AGSRs and discusses the potential mechanisms by which they govern granule properties and reactor performance. It focuses on the main parameters that can affect hydrodynamics in these systems, including the physicochemical characteristics of wastewater, operational conditions, and reactor design. The chapter explains how these parameters can influence key hydrodynamic variables, including mean liquid velocity, gas holdup, bubble characteristics and dynamics, and turbulence, through direct and indirect mechanistic pathways. Particular attention is given to turbulence as a key hydrodynamic variable that can regulate both mass transfer and shear stress at the granule surface. The chapter further emphasizes that hydrodynamic conditions at the reactor scale do not always represent the mechanical stresses experienced by granules. Therefore, studying the effect of hydrodynamics on granule development requires multiscale approaches.

Acknowledgements

Looking back on my PhD journey, I realize that what I will remember most are the people I met along the way. Behind this thesis are many conversations, collaborations, friendships, and moments of laughter. I was fortunate to be surrounded by people who supported me both scientifically and personally, and I would like to thank them.

First and foremost, I would like to express my gratitude to my promotor, **Huub Rijnaarts**. **Huub**, thank you for your guidance, encouragement, and support. I learned much from our regular meetings and particularly valued the thoughtful discussions you initiated, which helped me look beyond the details and develop a broader perspective on my research.

To my co-promotor, **Dainis Sudmalis**, thank you for supporting me through the many challenges I encountered during my PhD. You were always willing to think through a problem with me, and your creativity in finding solutions helped us move forward on many occasions. I have learned so much from your critical thinking, your eye for detail, and your openness to new ideas and approaches, even when doing so meant building something from scratch or taking a more demanding path. I appreciate the trust you placed in me and the freedom you gave me to explore my own ideas.

To my co-promotor, **Harry Bruning**, thank you for the thoughtful perspective you brought to our meetings. Your questions and comments often encouraged me to look at my results from a different angle and helped me see possibilities I might otherwise have missed. I was always impressed by how quickly you could work through even complex calculations without reaching for a calculator.

Vinnie and Michiel, this work would not have been possible without your expertise, experience, and practical support. I would also like to thank **Ilse, Julian, and Bert** for their help along the way. My sincere thanks go to the analytical team: **Katja, Livio, Nick, Beatriz, Lucian, Pieter and Thomas**, for helping me and my students with the analytical methods and equipment and for making the lab such a friendly and welcoming place. To **Katja**, thank you for your patient support, whether helping me work through a practical problem or explaining a procedure. The care and guidance you offered the students who contributed to this thesis meant a great deal to me.

I would also like to thank the staff of Environmental Technology (ETE). **Liesbeth, Petra, and Wies**, I am grateful for all the work you did behind the scenes to keep

things running smoothly. **Shabab**, thank you for your advice and our many pleasant conversations. **Mirijam** and **Thomas**, thank you for bringing humor and laughter to our chats at the coffee corner. **Annemerel**, being team captains together at the Battle of WUR remains a wonderful memory of my time at ETE. **Annemiek**, thank you for creating a supportive atmosphere in the group. **Jan** and **Kasper**, it was a pleasure to share an office with you. Thanks for the friendly conversations and helpful advice.

Sanne, thank you for the office chats, after-lunch walks, and for organizing dinners and Prison Breaks. Your enthusiasm and competitive spirit in games always added to the fun. I am grateful for all the moments we have shared.

Silvana, thank you for the warmth and energy you bring to every gathering. I especially enjoyed the two weeks we spent together during the PhD trip, and I will fondly remember our runs and gym sessions. Thank you for hosting dinners. You have a wonderful way of making people feel welcome.

I would like to thank all my colleagues for making ETE an enjoyable place to work: **Milan, Kaiyue, Koen, Dilan, Jinsong, Amin, Anran, Xiaofang, Alessia, Merel, Zhaolu, Rik, Elizabeth, John, Yujun, Rikke, Lidya, Ralf, Alessio, Yulian, Selina, Pim, Yme, Shuhao, Claudia, Paulien, Tim, Nena, Dalia, Alaaeldin, Sha, Margo** and **Weishen. Selin,** I enjoyed working with you to chair the PhD meetings. **Chang**, thank you for always being willing to help with the bioreactors and for the great time we shared at the AD conference. **Jorn**, thank you for bringing humor to our days in the office. **Anne**, thank you for you kindness, I cherish the moments we shared and conversation we had. **Marko**, thank you for bringing us together through so many games and gatherings. **Halimat**, thank you for the chats and for sharing the joys and challenges of this journey. I am also grateful to my students, **Mordem, Gamma, Erfan, Hector, and Aron**, for their valuable contributions to this thesis.

To my friends outside work, **Dani, Annika, Kazem, Aref, Babak, Amin, Moein, Mehrdad, Saeid, Poorya and Reza**, thank you for good times, laughter and shared moments that made these years so much richer.

To my family, **Mom, Dad, Benyamin,** and **Niusha**, thank you for your love throughout these years. Even from afar, knowing you were there for me made the difficult moments easier. You give me so many reasons to keep moving forward.

Finally, I would like to give special thanks to **Yasmin**, my girlfriend. Your love, care, and support made the long days of writing this thesis filled with warmth.

About the Author



Born on 13 May 1993 in Ahvaz, southwestern Iran, Hooman Eslami found joy in learning and discovering how things work. His interest in mathematics and physics led him to study this subject in high school, where he graduated at the top of his class. Like other students hoping to enter university in Iran, he sat the nationwide entrance examination. He ranked among the top 1% of approximately 284,000 candidates.

In 2011, Hooman began a bachelor's degree in petroleum engineering at the Petroleum University of Technology (PUT) in his hometown. For his BSc graduation project, he worked on gas lift optimization in oil and gas production process. In 2015, he moved to Tehran to pursue a master's degree at Amirkabir University of Technology (Tehran Polytechnic). He worked on gas hydrate dissociation and two phase flow in porous media using ANSYS FLUENT for his master thesis, which he completed cum laude.

Curious about life beyond university, after graduation in 2018, Hooman joined Petroservices, a drilling company. Over the next year and a half, to discover what interested him most, he experienced four roles: research and development engineer, data analyst, field engineer, and contract management officer. Each offered something he enjoyed and opportunities to learn from colleagues with diverse expertise. When technical problems called for deeper scientific insight, Hooman sometimes sought advice from university professors. These conversations helped him clarify the direction he wanted to take: deepening and applying his knowledge in fields where he could contribute to renewable energy development and address environmental challenges.

In 2021, he began his PhD in the Department of Environmental Technology (ETE), investigating the hydrodynamics of anaerobic granular sludge reactors through experimental fluid flow measurements. Alongside his research, he supervised three master's students and two bachelor's students and contributed to building the department's flow measurement laboratory.

Netherlands Research School for the
Socio-Economic and Natural Sciences of the Environment

D I P L O M A

for specialised PhD training

The Netherlands research school for the
Socio-Economic and Natural Sciences of the Environment
(SENSE) declares that

Hooman Eslami

born on 13-05-1993 in Ahvaz, Iran

has successfully fulfilled all requirements of the
educational PhD programme of SENSE.

Wageningen, 4 November 2026

SENSE coordinator PhD education

Dr Ir Peter Vermeulen

The SENSE Director

Dr Jampel Dell'Angelo

The SENSE Research School declares that **Hooman Eslami** has successfully fulfilled all requirements of the educational PhD programme of SENSE with a workload of 33.7 EC, including the following activities:

SENSE PhD Courses

- A1: Environmental Research in Context (2021)
- A2 Research in context activity: 'Launching a community-driven digital platform for sharing the experimental protocols within and across departments' (2025-2026)

Other PhD and Advanced MSc Courses

- Experimental techniques in fluid mechanics, Twente/ J.M. Burgers Centrum (2021)
- Communication styles, How company (2021)
- Scientific Writing, Wageningen Graduate Schools (2022)
- Applied statistics, VLAG (2024)
- Career perspective course, Wageningen Graduate Schools (2025)

Management and Didactic Skills Training

- Organizing bi-Monthly ETE PhD and postdoc meetings (2024)
- Supervising 3 MSc students with thesis (2022-2025), and one BSc student with thesis and one BSc with internship (2025)
- Teaching assistant in introduction environmental technology (2022-2023)
- Teaching assistant in environmental process engineering (2023-2024)

External training at a foreign research institute

- Flow imaging, 3D-PTV, and shadowgraphy training, LaVision GmbH, Netherlands (2022)
- Tomo_PIV and 3D-LPT training/course, LaVision GmbH and Manchester university, United kingdom (2023)

Oral Presentations

- *Hydrodynamic shear effects on anaerobic granule properties: from bulk approaches to quantified details.* 18th IWA World Conference on Anaerobic Digestion, June 2 – June 6 2024, Istanbul, Turkey

Poster presentations

- *3D velocity measurement in dense two-phase flows using Particle Tracking Velocimetry (PTV) technique*. JMBC Symposium, May 29 – May 30 2024, Lunteren, Netherlands

This research was funded by the Dutch Ministry of Education, Culture and Science through Sector Plans for Scientific Research and University Education.

Financial support from Wageningen University for printing this thesis is greatly acknowledged.

Cover design concept by Hooman Eslami

Final cover design and artwork by Stefanie van den Herik

Printed by ProefschriftMaken

